Aix-Marseille Université
Università degli studi di Padova

ED 352

LAM/OAPD

Thesis submitted to obtain the degree of Doctor in

Field: Physics and Science of matter
Subfield: Astronomy & Cosmology

Alice Zurlo

Characterization of exoplanetary systems with the direct imaging technique: towards the first results of SPHERE at the Very Large Telescope

Defended in Marseille, the 01/06/2015, in front of the jury:

Niranjan THATTE	University of Oxford	Referee
Alessandro SOZZETTI	OATO/INAF	Referee
Gael CHAUVIN	IPAG	Examiner
Sascha HINKLEY	University of Exeter	Examiner
Magali DELEUIL	Aix-Marseille Université	Examiner
Pierpaolo PIOTTO	UNIPD	Examiner
Claire MOUTOU	LAM	Supervisor
Raffaele GRATTON	OAPD/INAF	Supervisor

Dedicated to everybody that
asked me to give his/her name
to the first exoplanet I will discover.

Acknowledgements

First of all I want to thank my supervisors Claire & Raffaele, to be with me always and help me achieving this important result. And, of course, the non-official (but fundamental!) ones: Arthur, Dino, and Silvano. Sorry for the multi-language acknowledgements but I find really impersonal to thank people in a language that I am not used to speak with.

Claire, merci pour être toujours disponible et présente (même si à Hawaii), pour être au même temps trop gentille mais dure quand il faut (jamais compris comment tu fais), je n'arrive pas à imaginer une directrice de thèse meilleure, t'es trop forte!

Grazie Raffaele per rispondere a qualsiasi mio dubbio, con chiarezza, precisione e una rapiditá impressionante.

Merci Arthur pour ton aide, sans toi mon travail aurait été 100 fois plus dur. Merci pour toutes les fois que je suis passée te voir et t'étais toujours disponible.

Dino, grazie per avermi aiutato ogni singolissimo giorno, soprattutto per le nostre chat skype che mi erano di compagnia e conforto.

Silvano, grazie per avermi dato questa bellissima opportunità e per essere sempre stato disponibile quando ne avevo bisogno.

Un grazie speciale alla mia famiglia che mi supporta (sopporta?) da anni e anni di studi, senza di voi non saremi mai riuscita ad arrivare fino a questo punto. Grazie per il vostro appoggio, fiducia e sostegno durante tutta la mia carriera accademica.

Grazie ai miei amici di Padova che hanno reso le mie permanenze laggiù momenti di divertimento; soprattutto grazie a Gre & Mastro per avermi sempre accolta amorevolmente!

Merci à Giovanni et Bastien pour partager avec moi le bureau, les cafés, et les milles et une conneries. Giovanni grazie per avermi sopportato anche a casa.

Gracias a Andi, el compañero de piso perfecto, y a nuestro grupo de amigos, gracias a vosotros el primer año de doctorado ha sido uno de los mejores de mi vida.

Gracias a mis amigos Javi, Rocío & Cris, por las noches de fiestas, las cenitas

y todo el tiempo estupendo que hemos pasado juntos. Os voy a echar mucho de menos!
Thanks to all the PASI group for the happy time together that makes work definitely better.
No te estoy olvidando Oscar, gracias por ser la persona que más me ha acompañado durante este camino, que ha estado a mi lado cada día en los últimos dos años y que ha hecho que este tiempo haya sido inolvidable. Gracias por hacerme feliz, ayer, hoy y mañana.

Abstract

In the year of the 20th anniversary of the discovery of the first extrasolar planet we can count more than 1800 companions found with different techniques. The majority of them are indirect methods that infer the presence of an orbiting body by observing the parent star (radial velocity, transits, astrometry). In this work we explore the technique that permits to directly observe planets and retrieve their spectra, under the conditions that they are bright and far enough from their host star.

Direct imaging is a new technique became possible thanks to a new generation of extreme adaptive optics instruments mounted on 8m class telescopes. On the Very Large Telescope two instruments dedicated to the research for exoplanets with direct imaging are now operative: NACO and SPHERE.

This thesis will describe the development and results of SPHERE from its predecessor NACO to its integration in laboratory and the final on sky results.

Chapter 1 gives a presentation of the exoplanet research, the formation mechanisms, and the characterization of planet atmospheres. Chapter 2 gives a general frame of the two instruments used for the results presented in this thesis: NACO and SPHERE. In Chapter 3 I describe an example of a false positive in the direct imaging technique, found during the survey NACO-Large Program. This work have been published in Zurlo et al. (2013). In Chapter 4 I present the performance of SPHERE, in particular of the subsystems IRDIS and IFS, deeply tested in the laboratory before the shipping to Paranal. This work has been published in Zurlo et al. (2014). Chapter 5 presents a work done to find special targets for the NIRSUR survey, these object are radial velocity long period planets which are observable with SPHERE. In Chapter 6 I present one of the first on sky result, the observations and analysis of the multi-planetary system HR 8799. In Chapter 7 I give the conclusions and future prospects.

Riassunto

Al giorno d'oggi più di 1800 pianeti sono stati scoperti orbitare attorno a stelle al di fuori del sistema solare. Le tecniche utilizzate per la ricerca di pianeti extrasolari sono molteplici: alcune, dette metodi indiretti, si basano sull'osservazione della perturbazione indotta dal pianeta orbitante sulla stella ospite, mentre altre si basano sull'osservazione diretta del pianeta stesso. La maggior parte dei pianeti scoperti attualmente é stata rivelata grazie ai primi. Specialmente il metodo delle velocità radiali e dei transiti hanno fornito il più alto numero si scoperte. Lo svantaggio di questo tipo di tecniche é che la caratterizzazione del pianeta non può essere completa a meno che non vengano usate simultaneamente più tecniche. Inoltre, per ottenere lo spettro del pianeta, quest'ultimo deve transitare e anche in questo caso il segnale é difficilmente estrapolabile. L'osservazione diretta di questi oggetti, detta *direct imaging*, é oggi possibile grazie ad avanzati sistemi di ottica adattiva installati su telescopi della classe 8m. Il direct imaging permette l'osservazione diretta di pianeti sufficientemente luminosi e distanti dalla stella ospite grazie ad una maschera che oscura la luce di quest'ultima. Questa tecnica quindi é particolarmente efficiente su sistemi giovani e vicini, dato che la luminosità intrinseca del pianeta diminuisce con l'età e che la separazione effettiva del pianeta dipende dalla distanza del sistema stesso. Sul Very Large Telescope a Paranal (Chile) due strumenti sono dedicati a questo tipo di ricerca: NACO e SPHERE. NACO é stato pensato come predecessore e prototipo di SPHERE, ma viene mantenuto grazie alle sue performance ancora competitive ed ad alcune caratteristiche che non sono presenti in SPHERE. SPHERE ha visto la sua prima luce in Maggio 2014 ed é ora pronto per cominciare una survey dedicata alla scoperta di pianeti attorno a sistemi giovani e vicini, NISUR. Questo strumento é composto da tre sottosistemi: IRDIS, IFS e ZIMPOL. IRDIS é una camera infrarossa cui detector é suddiviso in due porzioni uguali per sfruttare l'immagine simultanea del target in due filtri adiacenti. IFS é lo spettrografo di SPHERE, permette di estrarre lo spettro del pianeta con risoluzioni di 30 e 50 a seconda della banda spettrale utilizzata. ZIMPOL é l'unico sottosistema

che lavora nel visibile, viene utilizzato per osservare la polarizzazione dei sistemi planetari. In questo lavoro viene presentato lo strumento SPHERE e il suo predecessore NACO, focalizzando sui risultati e sulle performance nella caratterizzazione dei sistemi planetari. Nel Capitolo 1 si trova un'introduzione alla ricerca dei pianeti extrasolari, con una descrizione delle tecniche per la rivelazione, una spiegazione delle teorie di formazione planetaria e infine una descrizione della caratterizzazione dei pianeti extrasolari. Nel Capitolo 2 vengono descritte le caratteristiche tecniche degli strumenti NACO e SPHERE. Nel Capitolo 3 viene presentato un caso di falso positivo incontrato durante la survey NACO-Large Program, una nana bianca scambiata per pianeta a causa di una errata previsione dell'età. Una versione adattata di questo capitolo é stata pubblicata in Zurlo et al. (2013). Nel Capitolo 4 vengono descritte le performance di SPHERE, dedotte dai test di laboratorio che si sono tenuti prima dell'invio a Paranal dello strumento. Per poter al meglio predirre le capacità di SPHERE nella caratterizzazione dei pianeti extrasolari, sono stati inseriti dei pianeti artificiali nelle immagini di laboratorio e grazie a simulazioni si é potuto calcolare la precisione e gli errori sulle misure previsti per gli strumenti IRDIS e IFS, il ramo infrarosso di SPHERE. Questo lavoro é stato pubblicato in Zurlo et al. (2014). Nel Capitolo 5 viene presentato una lavoro preparativo per la selezione dei target della survey NIRSUR. Si tratta di oggetti scoperti tramite le velocità radiali che hanno una separazione angolare tale da essere osservabili con SPHERE. Grazie ad una simulazione Monte Carlo sono stati selezionati alcuni oggetti che al momento delle osservazioni potrebbero soddisfare le condizioni di separazione angolare e luminosità tali da poter essere rivelati. Nel Capitolo 6 viene presentato uno dei primi risultati di SPHERE in cielo: l'osservazione del sistema attorno HR 8799. Questo sistema costituito da 4 pianeti é il primo sistema multiplanetario mai rivelato dal direct imaging. Grazie a SPHERE é stato possibile estrarre il primo spettro per HR 8799e in banda YJH e uno spettro di qualità nettamente superiore agli altri strumenti per HR 8799d. Sono stati misurati i flussi di tutti i pianeti del sistema nella bande J, $H2H3$ e $K1K2$. Nuovi punti astrometrici sono forniti grazie alle osservazioni con SPHERE. Infine, nel Capitolo 7 vengono presentate le conclusioni e prospettive future.

Résumé

Aujourd'hui, plus de 1800 planètes qui orbitent autour d'étoiles en dehors du système solaire ont été découvertes. Les techniques utilisées pour trouver les planètes extrasolaires sont variées: certaines, appellées méthodes indirectes, sont basées sur l'observation de l'influence induite par la planète autour de l'étoile hôte, tandis que d'autres sont basées sur l'observation directe de la planète elle-même. La plupart des planètes découvertes actuellement a été révélée grâce aux méthodes indirectes. Surtout la méthode de la vitesse radiale et du transit ont fourni le nombre le plus important des découvertes. Par contre, avec ce type de techniques, la caractérisation des planètes ne peut pas être complète si on n'utilise pas plusieurs tecniques simultanément. Aussi, pour obtenir le spectre de la planète, il doit y avoir un transit et même dans ce cas là, le signal est très faible par rapport au signal de l'étoile. L'observation directe de ces objets, appelée *imagerie directe*, est maintenant possible grâce à des systèmes très avancés d'optique adaptative installés sur des télescopes de classe 8m. L'imagerie directe permet l'observation des planètes suffisamment lumineuses et éloignées de l'étoile principale en utilisant un masque qui cache la lumière de la dernière. Cette technique est donc efficace en particulier pour des systèmes jeunes et voisins car la luminosité intrinsèque de la planète diminue avec l'âge et la séparation réelle de la planète dépend de la distance du système. Dans le Very Large Telescope au Paranal (Chili), deux instruments sont dédiés à ce type de recherche: NACO et SPHERE. NACO a été considéré comme le prédécesseur et prototype de SPHERE, mais il est encore utilisé grâce à ses performances toujours compétitives et certaines caractéristiques qui ne sont pas présents dans SPHERE. SPHERE a vu sa première lumière en Mai 2014, et est maintenant prêt à commencer une enquête consacré à la découverte de planètes autour de systèmes jeunes et voisins, NIRSUR. Cet instrument se compose de trois sous-systèmes: IRDIS, IFS et ZIMPOL. IRDIS est une camera dont le détecteur infrarouge est divisé en deux parties égales pour exploiter simultanément l'image de la cible en deux filtres adjacents. IFS est le spectrographe de SPHERE, il permet d'extraire le spectre d'une planète avec des résolutions de 30 et 50 en fonction de la bande spectrale utilisée. ZIMPOL est

le seul sous-instrument qui fonctionne dans le visible. Il est utilisé pour observer la polarisation des systèmes planétaires. Dans ce travail sont présentés l'instrument SPHERE et son prédécesseur NACO, en mettant l'accent sur les résultats et la performance dans la caractérisation des systèmes planétaires. Dans le Chapitre 1 on trouve une introduction à la recherche de planètes extrasolaires, avec une description des techniques pour la détection, une explication des théories de formation planétaire et enfin une description de la caractérisation de planètes extrasolaires. Le Chapitre 2 décrit les caractéristiques techniques des instruments NACO et SPHERE. Dans le Chapitre 3, je présente un cas de fau positif rencontré lors de l'enquête NACO-Large programme, une naine blanche prise pour une planète à cause d'une mauvaise prédiction de l'âge. Une version adaptée de ce chapitre a été publié dans Zurlo et al. (2013). Dans le Chapitre 4, je décris le performances de SPHERE, déduites pendant les tests au laboratoire qui sont nécessaires avant d'envoyer l'instrument à Paranal. Pour mieux prédire la capacité de cet instrument dans la caractérisation des planètes extrasolaires, j'ai injecté des planètes synthetiques dans les images du laboratoire. Avec ces simulations j'ai pu calculer la précision et les erreurs sur les mesures prévues pour les instruments IRDIS et IFS, le bras infrarouge de SPHERE. Ce travail a été publié dans Zurlo et al. (2014). Un travail de préparation pour la sélection des cibles por l'enquête NIRSUR est présenté dans le Chapitre 5. Ce sont des objets découverts par vitesse radiale ayant une séparation angulaire qui leur permet d'être observables avec SPHERE. Grâce à une simulation Monte Carlo nous avons choisi les objets qui, au moment des observations, pourraient répondre aux conditions de séparation angulaire et luminosité telle qu'elles peuvent être révélées par SPHERE. Dans le Chapitre 6 je présente un des premiers résultats de SPHERE dans le ciel: l'observation du système autour de HR 8799. Ce système se compose de quatre planètes et il est le premier système multi-planétaire jamais révélé par imagerie directe. Grâce à SPHERE il a été possible d'obtenir le premier spectre dans la bande YJH pour HR 8799e et un spectre de qualité nettement supérieure aux autres instruments pour HR 8799d. Nous avons mesuré les flux de toutes les planètes du système dans les bandes J, $H2H3$ et $K1K2$. Nouveaux points d'astrométrie sont donnés grâce aux observations avec SPHERE. Dans le Chapitre 7 je présente les conclusions et les perspectives futures.

Contents

List of Figures

List of Tables

Chapter 1

Introduction

Since the discovery of the first exoplanet around a main sequence star by the radial velocity (RV) technique (Mayor & Queloz 1995) more than 1800 of these objects have been detected up to now (see, e.g., the Extrasolar Planets Encyclopaedia[1], Schneider et al. 2011).

Characterizing small objects far from us is a big challenge, nevertheless each day new planets are detected. Instrumentation from the ground and the space dedicated to the research of extrasolar planets is in continuous evolution, permitting us the discovery of objects similar to our Jupiter, and very soon to our Earth. Techniques used are various: radial velocity measurements of the host star, light curve during transits, transit time variation (TTV) and transit duration variation (TDV), astrometry, microlensing and direct imaging.

Those techniques explore different zones of the exoplanetary systems. Also, the information that we can recover with these techniques and the biases are different, as shown in the next Sections.

In this Chapter we will describe the indirect and direct methods of exoplanet detection, a description of the current theories of planet formation, and an introduction to planet atmospheres.

1.1 Indirect methods of detection

We present in this Section a review of methods used to discover and study extrasolar planets; I will give more details in the next Chapters.

The majority of the exoplanets have been detected by the radial velocity technique. With today's instrumentation we are capable to measure the relative velocity between a host star and the barycenter of the system down to 0.5-1.0 ms^{-1}. This permits us to find a

[1] http://exoplanet.eu/

possible perturbing body and to research for its characteristic, orbital elements and minimum mass.

Another method is the study of transit light curve. When a planet orbit is seen edge-on, part of the light of the host star is masked during the passage of the planet in front of it. These occulting bodies can give us a lot of information, such as the radius of planet, the orientation of the orbit and the period, the characteristics of the scanned surface of the host star, the presence of other companions, TTV, or moons, TDV, the characterisation of the atmosphere, etc.

Microlensing provides information on the mass and projected distance from the star, but there is no information on the other orbital parameters. Astrometry can provide all the orbital elements of the orbit of a planet. Direct imaging permits the study of massive planets at wide separations. Also, as the intrinsic luminosity of a planet depends on the age of the system, and planets are brighter at the very first stages after the formation (see Sec. 1.4), the best candidates for this technique are very young systems.

A picture of the state-of-art exoplanet detection is shown in Fig. 1.1.

1.1.1 Radial velocity

Radial velocity (RV) technique plays a major role in the discovery of planets around Sun-like stars and in the characterisation of planetary systems. Using this technique the first exoplanet was discovered around a solar type star (Mayor & Queloz 1995).

This technique reveals the presence of a perturbing body from the motion of a star with respect to the barycenter of the common system (as described in Sec. A.0.4).

† Having the astrocentric velocity vector of the planet in the desired reference frame, we can pass to barycentric coordinates. Calling V the barycentric velocity vector of the planet, and V_* that of the star, we have that $v = V - V_*$. The barycenter is fixed in this reference frame, we have $m_0 V_\star + mV = 0$. Solving for $V_\star$, we obtain:

$$V_\star = -\frac{m}{m_0 + m} v \tag{1.1}$$

which represents the velocity of the motion of the star around the center of mass of the system. To calculate the velocity actually detected by the observer, we must add the velocity V_0 of the barycenter itself with respect to background stars. It is useful to decompose this observable velocity into the tangential velocity component V_t and the radial velocity $v_r = V_\star z + V_0 z$. The former is the motion on the plane of the sky, detectable by astrometry. The radial velocity v_r is detectable by ground-based instruments, measuring the *Doppler*

†Formulas taken from Murray & Correia (2011)

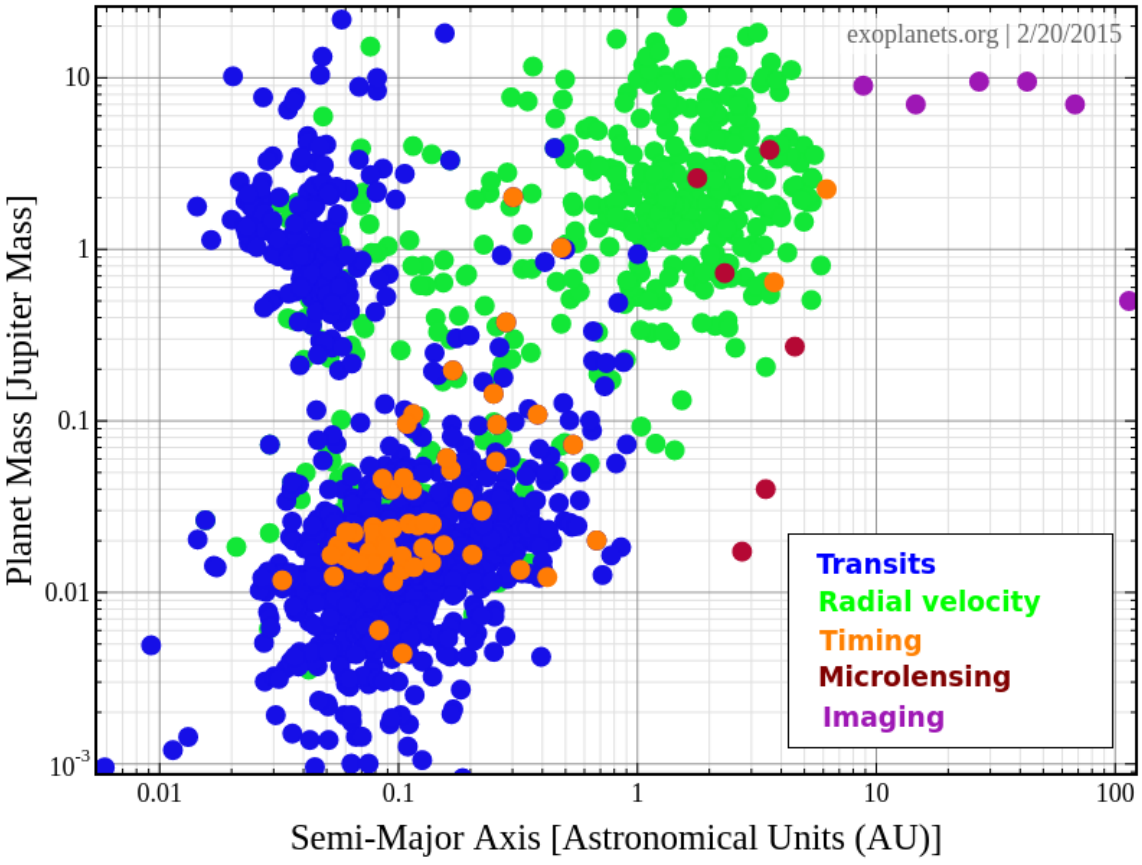

Figure 1.1: All the planets detected so far as function of their semi-major axis (projected for direct imaging) and mass. Different colors represent different detection techniques. The different methods are located in different zones of the mass/semi-major axis parameter space. Created on the webpage *exoplanets.org*.

shift of spectral lines in the star's spectrum. The best candidates are stars of spectral type F or G, as they have the right temperature to have a fair amount of absorption lines bright enough so that high signal to noise ratios (S/N) can be obtained.

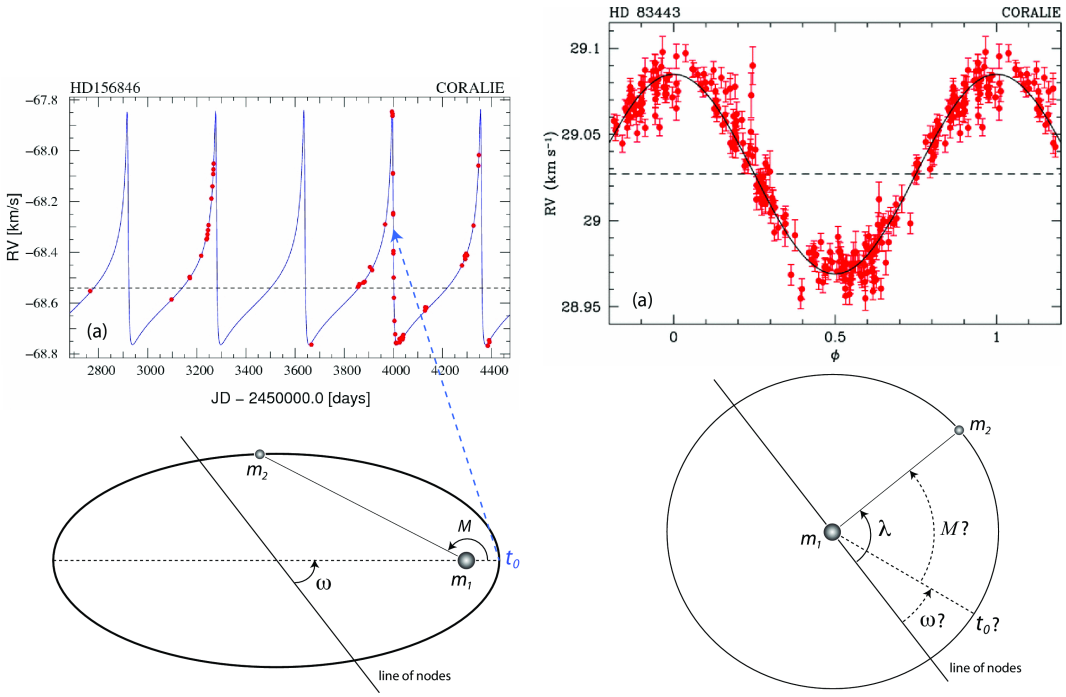

Figure 1.2: Hight eccentricity planet (left panel) and low (right panel) RV plots from Murray & Correia (2011).

Radial velocity precision has steadily improved toward and below 1 m s^{-1} with High Resolution Echelle Spectrometer (HIRES) at the Keck Observatory and with the High Accuracy Radial velocity Planet Searcher North and South (HARPS-N/S) installed at La Palma and La Silla.

With RV measurements it is possible to determine five spectroscopic orbital elements. The effects of most of these parameters are neither orthogonal nor linear, so finding a best solution for the orbit is difficult, especially if we are dealing with multi-planetary systems. Planets in mean motion resonances can be particularly difficult to identify from radial velocity curves because of degeneracies among the best-fit orbital parameters (Santos et al. 2007). The stability of the system is an additional constraint that multi-planet fits must satisfy (see, e.g., Gozdziewski et al. 2008). Also, this technique is extremely sensitive to the activity of the star, that can cause a *jitter* in the RV measurement (Tingley et al. 2009; Cegla et al. 2012).

A major limitation of this technique is that as we measure just one component of the velocity along the line-of-sight, we can only estimate the "projected mass" of the companion,

that represents as the minimum mass $m \sin i$.

Fortunately, it can be shown that for orbits randomly oriented in space it is much more likely to have a $\sin i$ close to unity, this means that the minimum masses obtained are statistically very close to the real masses (Correia et al. 2010). To find the true mass of the object RV measurements have to be coupled with other techniques (e.g. through an astrometric detection, a transit measurement or, in the case of very young planetary systems, if the disk inclination if measured, and a hint of the inclination is given) (Ohta et al. 2005).

1.1.2 Transits and timing variation

When a planet lies in a nearly edge-on orbit we could use the method of transit. Planets that eclipse their stars can give us a huge quantity of information: the relative dimension planet-host star, the orientation of the orbit relative to the sky plane and to the stellar rotation motion axis. These parameters can not be obtained from other techniques. The orientation of the orbit can in principle be obtained for directly imaged planets and for planets detected by astrometry, but after numerous observation epochs.

A transit is defined as the passage of a celestial body in front of a larger one, while the occultation occurs when the smaller body passes behind (Fig. 1.3). During a transit the planets passing in front of the star blocks a fraction of the light. Then the flux drops again when the planet is occulted by the star. In this way we can write the flux $F(t)$ as:

$$F(t) = F_\star(t) + F_p - \begin{cases} k^2 \alpha_{tra}(t) F_\star(t) \\ 0 \\ \alpha_{occ} F_p(t) \end{cases} \tag{1.2}$$

where $F_\star(t)$ and $F_p(t)$ are respectively the flux of the star and the planet and α are a dimensionless parameter depending on the overlap area between the stellar and planetary disks (Winn 2011). The flux of the star may vary in time due to stellar activity (spots, flares, ...), or for other mechanisms as pulsation or convection, but it is considered constant during the time of the transit. From the ratio of the fluxes $f(t) = F(t)/F_\star$ we can derive information on the transiting planet.

If I_p and $I_\star$ are the disk-averaged intensities of the planet and star, respectively, then $F_p/F_\star = k^2 I_p/I_\star$ and

$$f(t) = 1 + K^2 \frac{I_p(t)}{I_\star} - \begin{cases} k^2 \alpha_{tra}(t) \\ 0 \\ k^2 \frac{I_p(t)}{I_\star} \alpha_{occ}(t) \end{cases}, \tag{1.3}$$

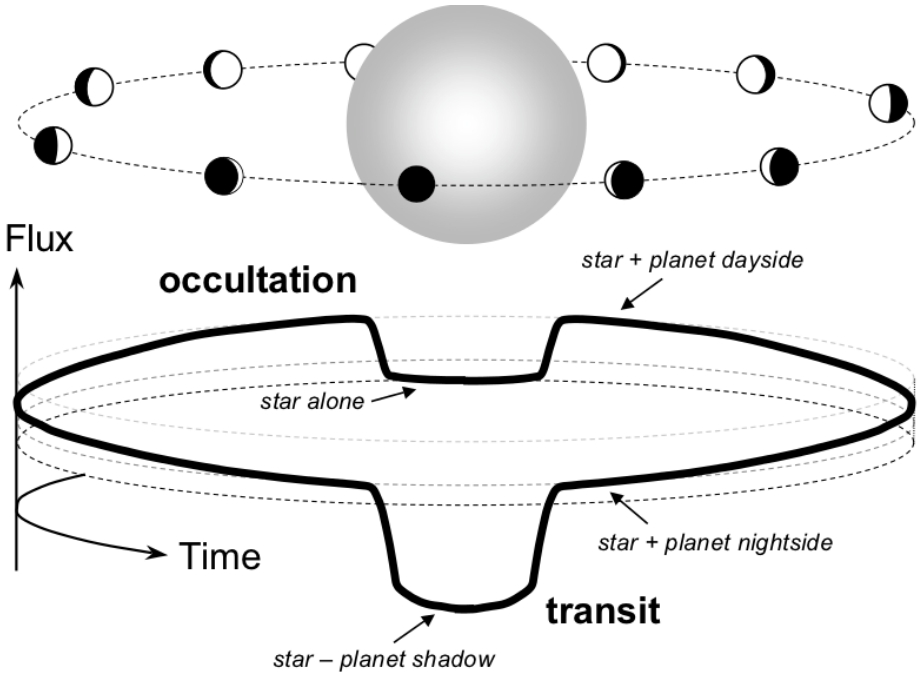

Figure 1.3: Cartoon of a transit and occultation from Winn (2011). Flux variations are simply illustrative: the shape of the curve depends on the ratio between the temperature of the star and that of the planet.

using the formalism of Winn (2011).

The α functions could be derived from the shape of the transit and the occultation. In this way, it is possible to derive the ratio of the radii of the star and the planet. When transits and occultations are both seen, a powerful constraint on the shape of the orbit is available. The timing of transits and occultations gives an estimate of $e \cos \omega$. Likewise the relative durations of the transit and the occultation depend on the complementary parameter $e \sin \omega$, as T_{occ}/T_{tra} can be approximated to the ratio between $1 + e \sin \omega$ and $1 + e \cos \omega$ (Winn 2011).

Two methods that naturally derive from the study of the transiting planets are the transit timing variation (TTV) and transit duration variation (TDV). The orbital period P of a transiting planet can be determined by timing a sequence of transits, or a sequence of occultations, and fitting a linear function:

$$t_c[n] = t_c[0] + nP \tag{1.4}$$

where $t_c[n]$ is the time of conjunction of the nth event.

It may occur that the period of the planet is not constant in time, this may be due to the perturbation of additional bodies in the system. The accuracy of the measurements

between successive transit (or occultation) events is typically of 0.1 sec, but depends on the instrument and the system configuration.

The interaction of other bodies in the system, greatest at each planetary conjunction, results in short-term oscillations of the semimajor axes and eccentricities of the planets, which in turn alter the interval between successive transits (Press & Rybicki 1989).

The TTV is correlated to the eccentricity of the perturber and its mass. This technique may be the only meant to estimate the mass and density of terrestrial-mass planets (Press & Rybicki 1989). Also, it can provide detection of non-transiting planets, just from the study of the perturbation induced by the object to the star.

1.1.3 Gravitational Microlensing

The gravitational microlensing is produced by the general relativistic bending of the light from a distant star by a stellar object (lens) that crosses the line-of-sight. The flux of the distant star could be magnified by a substantial factor, and the magnification of the light in function with time is a smooth and symmetric function. If the lens is constituted by a star which hosts a planet, the light of the background star will be magnified at different times by the star and the planet, as the light is perturbed first by the primary and then by the planet (Mao & Paczynski 1991).

To characterize a microlensing event caused by a lens at a distance = d_l to a source at a distance d_s we need a fundamental parameter, β, which is the angular separation between the lens and the background source (Einstein 1936):

$$\beta = \theta - \frac{4GM_\star}{c^2 d_{rel}\theta} \tag{1.5}$$

where θ is the angular separation of the two images created by the lens and $d_{rel}^{-1} = d_l^{-1} - d_s^{-1}$. The image produced is represented in Fig. 1.4. If β is null, i.e. the two objects are in the line-of-sight, the formula can be written as:

$$\theta_E = (\frac{4GM_\star}{c^2 d_{rel}})^{1/2}. \tag{1.6}$$

The parameter θ_E is known as the *Einstein radius*.

Microlensing has the advantage to permit the detection of very low-mass planets on large orbits, like in the example shown in Fig. 1.5. Moreover, free floating planets or objects widely separated from their primary can also be detected as isolated, short timescale microlensing events (Wright & Gaudi 2013).

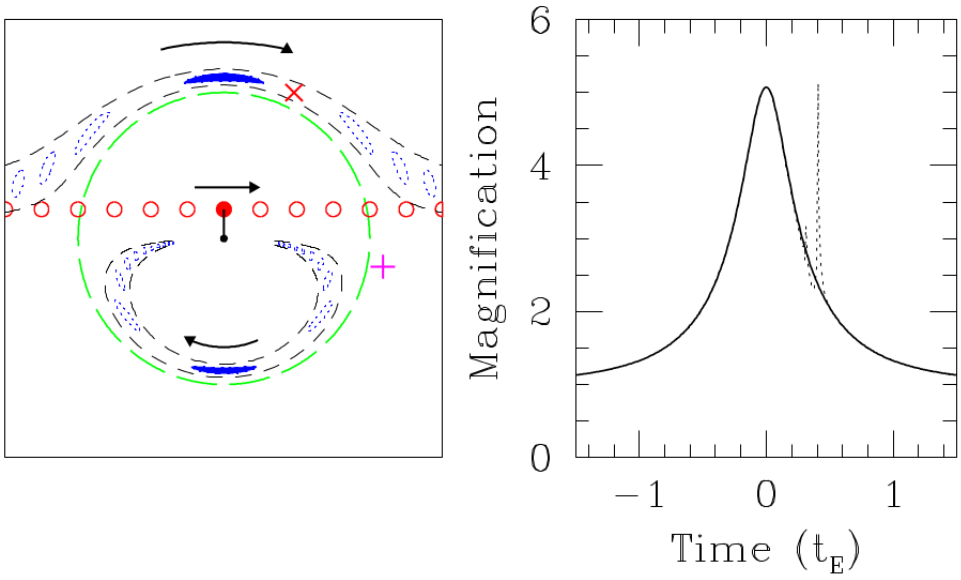

Figure 1.4: Figure and caption taken from Wright & Gaudi (2013). The left panel shows the images (dotted ovals) for several different positions of the source (solid circles) for a microlensing event with an impact parameter of 0.2 Einstein ring radii. The primary lens is indicated as a small black dot, and the primary lens Einstein ring is indicated as a green long-dashed circle. If the primary lens happens to have a planet near the path of one of the images (roughly within the short-dashed lines), then the planet will perturb the light from the source, creating a deviation to the single lens light curve. Right: The magnification as a function of time is shown for the case of a single lens (solid) and accompanying planet (dotted) located at the position of the X in the left panel. If the planet was located at the + instead, then there would be no detectable perturbation, and the resulting light curve would be essentially identical to the solid curve.

The inconvenient of this technique is that every event is unique (not reproducible) and rare. Also, the parameters of the planet have to be found with complex statistical assumptions used to modelize the system.

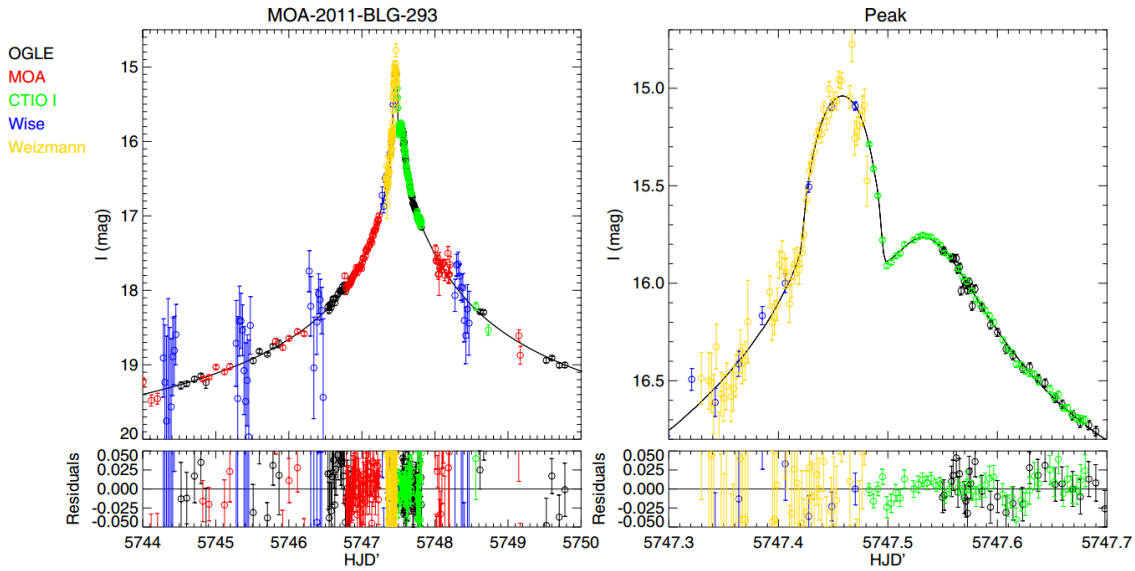

Figure 1.5: Example of the event that led to the discovery of the first microlensing planet in the habitable zone (from Batista et al. 2014). The planet has a mass $M_p = 4.8 \pm 0.3$ M_{Jup}, and projected separation of $\rho = 1.1 \pm 0.1$ AU.

A next generation of wide-field instruments will provide new detections by microlensing. For example, the Large Synoptic Survey Telescope (LSST) from the ground, and Euclid and the Wide-Field Infrared Survey Telescope (WFIRST) from space, will play a major role.

1.1.4 Astrometry

The principle of planet detection with astrometry is similar to that behind the RV technique: the presence of a planet is inferred from the motion of its host star around the barycenter. In the case of astrometry the observable is the motion of the parent star on the plane of the sky. This information can provide all the six parameters of the orbit, including the inclination. The amplitude θ in arcsec of the movement of the star with respect to the barycenter is:

$$\theta = \frac{M_p}{M_\star} \frac{a}{d} \tag{1.7}$$

where a is the semi-major axis in AU and d is the distance of the system in pc.

An example of detection by astrometry technique is shown in Fig. 1.6. This technique is sensitive to planets with large semi-major axis and has the advantage to be applicable to all types of stars (with increasing sensitivity with low mass stars), including active stars. Space missions will push astrometric precision well beyond the current state-of-art.

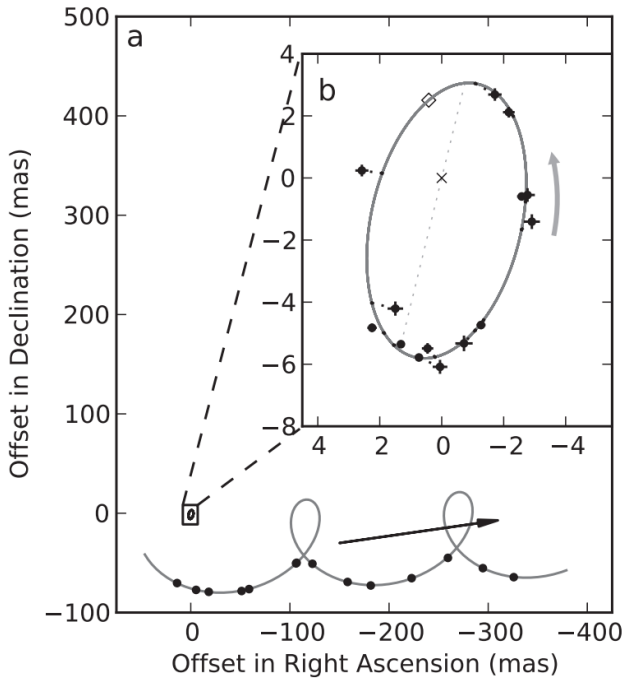

Figure 1.6: Example of astrometry detection of a low mass companion to an ultracool dwarf (Sahlmann et al. 2013).

To avoid false positives a long baseline of observations is required for this technique, coupled with an high precision measurement of the astrometric motion of the star. Dramatic progress is indeed expected from *Gaia*, which will be capable of detecting giant planets within 2–3 AUs thanks to its micro-arcsecond (μas) sensitivity (Sozzetti 2014), as shown in Fig. 1.7 .

1.1.5 Conclusions on the indirect methods

The indirect methods of exoplanet detection explore different zones of the mass/semi-major axis parameters space (Fig. 1.1) at different distances from the Earth (Fig. 1.8). These methods are complementary, and together they can span a huge region of the parameters

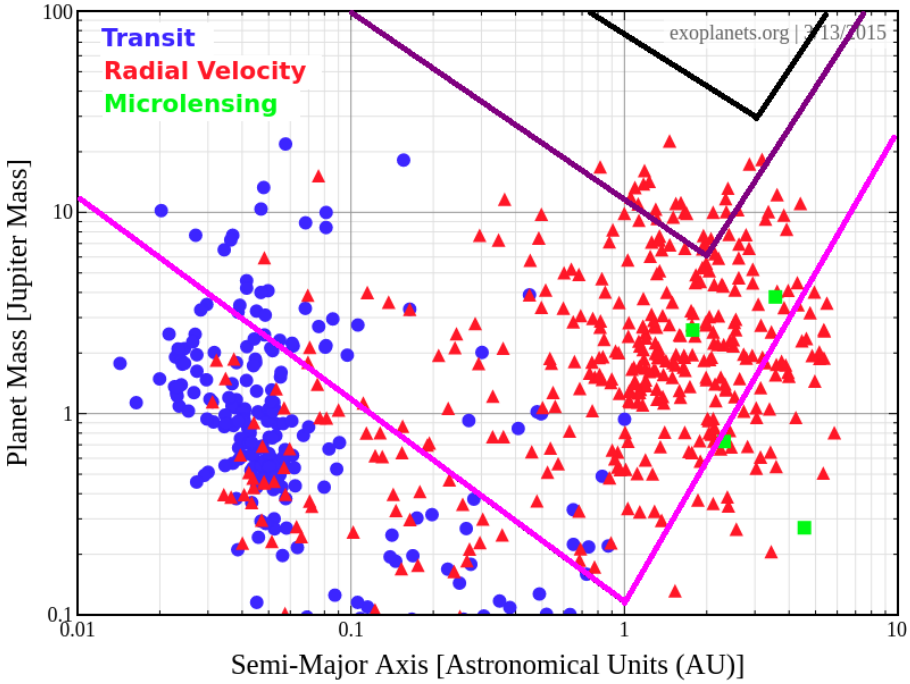

Figure 1.7: The Gaia sensitivity (pink, purple, and black curves). The values for the curves overplotted are taken from Sozzetti (2014). The upper black and purple curves are for Gaia astrometry with σ_A = 120 μas, assuming a 0.8 $M_\odot$ primary at 300 pc and for σ_A = 400 μas, assuming a 0.2 $M_\odot$ primary at 30 pc, respectively. The lower pink curve is for σ_A = 500 μas, assuming a 0.050 $M_\odot$ primary at 2 pc (appropriate for Luhman 16A). The survey duration is set to 5 yr. Planets detected by transit, RV, and microlensing techniques are shown.

space, and with the forthcoming instruments they will populate even more zones of these diagrams.

The inner zones of the planetary systems can be studied with the method of the transits, as the possibility to detect a planet passing in front of its host decreases with the separation from the star. The bias of this technique is that it privileges old systems, as young and active stars can mimic the presence of a companion when spots appear on the surface. The best targets for this technique are main-sequence stars, especially low mass, which yield larger transit signals (Wright & Gaudi 2013). Typically the targets are F and G stars in optical surveys (Pepper et al. 2003) while near IR surveys target lower mass stars (Wright & Gaudi 2013).

The S/N depends on the distance and luminosity of the host star, nevertheless the transit technique is sensitive to targets which are less than 4000 pc away (see Fig. 1.8). All the planets discovered by transit are closer that 1 AU to their host star (see Fig. 1.1). This means that they are all inside the snow line, defined as (see, e.g., Kennedy & Kenyon 2008):

$$a_{snow} = 2.7 \frac{M_\star}{M_\odot} AU. \tag{1.8}$$

The snow line delimits the zone of the protoplanetary disk where the water condenses, outer this radius the formation of gas giants is more favorable, due to the larger surface density of solids (see, e.g., Mordasini et al. 2009). Since the majority of the planets discovered by the transit technique are gaseous giant, the so-called "hot-Jupiters", this means that these planets migrated from the position where they were formed, as we will see in the next Section.

Radial velocity technique is also more efficient with planets close to the host star, but the sensitivity can span to massive planets separated by 10 AU. As shown in Sec. 1.1.1, the RV signal is proportional to the ratio between the mass of the planet and its semi-major axis, so that planets detected with long period are also more massive. Radial velocity technique also targets old star, as activity can strongly bias the signal or mimik the presence of a companion. RV and transits can be complementary techniques in the study of the closest zone of planetary systems, in fact many transiting planet candidates are followed-up by radial velocity campaigns to confirm the nature of the companion. RV tend to favor late G or early K quiet main-sequence stars (e.g., Pepe et al. 2011).

Microlensing explores the zone of the planetary system beyond the snow line. This technique is the only one that could detect planets of the size of the Earth at such a distance from the host star. Even if it seems to overlap with RV space in the mass/semi-major axis for massive planets, those targets cannot be followed-up because targets of microlensing are too far away. As Fig. 1.8 shows, this technique is the one that explores the furthest

stars. The preferable pointing direction is the galactic bulge, where the density of stars on the FOV is higher and thousand of targets are observed simultaneously. Also, as low mass stars are more frequent, so far microlensing detected planets around distant, low mass stars. This is just a statistical bias not correlated to the sensitivity of the technique.

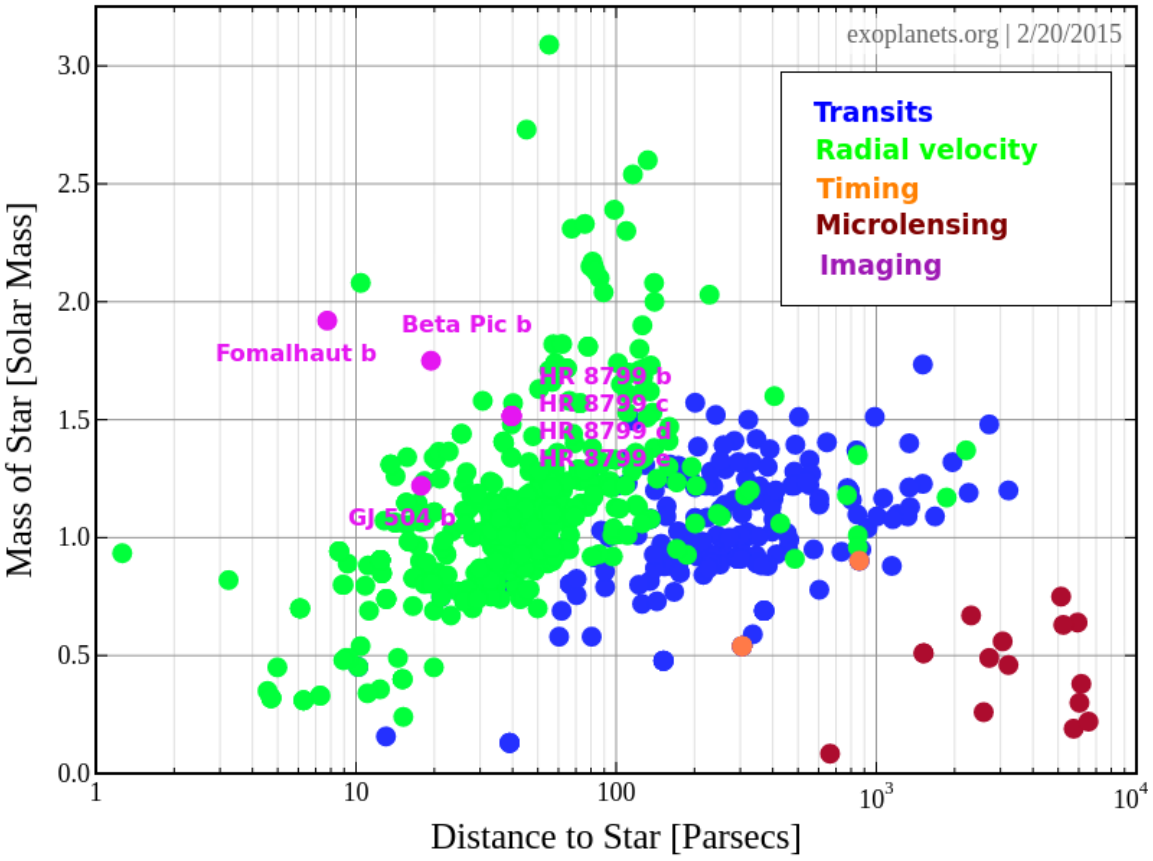

Figure 1.8: Sensitivity of imaging techniques: the distance of the system vs the mass of the hosts star. Each technique explores a different volume of the galaxy and privileges low mass or massive stars. Each technique is represented in a different color.

Astrometry is sensitive to massive planets in long period orbits. Contrary to transit and RV, it is not biased by stellar activity and can target stars with spots (Lanza et al. 2008). The S/N of the detection is strongly dependent with the brightness of the host star, while the amplitude of the induced movement of the planet decreases for massive stars. This means that the best targets for astrometry are bright low mass stars. Astrometry will detect planets more likely in the solar neighborhood.

All the indirect techniques complement each other and fill parts of the mass/separation parameters space. The technique that explores the outer part of planetary systems, beyond

$\sim$ 10 AU from the host star, is the direct imaging. Direct imaging will eventually overlap with astrometry and microlensing, as the instrumentation is constantly evolving, and the sensitivity through fainter stars and smaller separations is increasing. For a detailed description of this method, we refer the reader to the next Section.

1.2 The direct imaging technique

Direct imaging (DI) is the only technique that can directly show the presence of giant gaseous exoplanets at wide separations from their host stars. This powerful technique permits to have a huge amount of information on the atmosphere of these objects, thanks to the possibility of recovering their spectra. It is a unique technique to have a picture of the planetary system at its very first stages, giving clues to the study of formation mechanisms (as we will see in Sec. 1.4).

Direct imaging consists in masking the light of the host star with a coronagraph to reveal what there is around it. It is a challenging technique, as the contrast between the planet and its host star is of the order of 10^{-6} even in rather favorable cases, and the residual light of the star is brighter.

In the following Section I give a general frame of the optical principles involved in high-contrast imaging, presenting the fundamental concepts needed to the comprehension of the direct imaging method, and listing the instrumental formalism which will be used in the next Chapters.

1.2.1 Limitations and instrumentation

To exploit the DI we first need a proper instrumentation: adaptive optics (AO) and coronagraphs. The principles of the AO are that to attenuate the impact of the atmosphere we predict its behavior and correct for it. The light of the stars, which by appoximation arrives from an infinite distance, is a perfect plane wave when entering the pupil of the telescope. Following the law of the diffraction by a circular aperture, the angular resolution of a telescope with an aperture size D is defined as:

$$\theta_{diff} = 1.22\frac{\lambda}{D}, \tag{1.9}$$

where λ is the wavelength of the observation. θ_{diff} is the radius of the inner Airy disk, of the order of 30 mas for $\lambda = 1$ μm and $D \sim 8$ m. What is observed on the focal plane of a telescope is essentially the Fourier transform of the wavefront impinging on the pupil plane multiplied by the pupil shape (Fraunhofer approximation: see, e.g., Oppenheimer &

Hinkley 2009). The intensity of the Airy function is mostly concentrated in the first peak, inside θ_{diff}, then has secondary rings separated by minima of the function, with decreasing energy.

For ground based telescopes the light from the stars passes through the atmosphere. This latter is formed by layers of turbulent "bubbles", of size r_0 (Fried parameter), within which the wavefront remains coherent. The bubbles have different diffraction coefficients, so that the wavefront is corrugated before entering the pupil of the telescope. The variation of the refraction index is larger (causing larger deviations of the beam) at shorter wavelengths. For this reason, the wavefront error WFE (measured in units of the wavelength) is larger at shorter wavelengths.

These bubbles act as subpupils of aperture r_0 which form PSFs with dimension $\theta_{atm} = 1.22\frac{\lambda}{r_0}$. Having two bubbles at a distance $\sim D$ constitutes a two-beam interferometer which creates a pattern of linear interference fringes (Racine et al. 1999). Before the pupil telescope there are subapertures of size r_0 and their fringes interfere constructively: these fringes constitute the variable "speckle pattern". The speckles have a size of $\sim \lambda/D$, for the distance of the two sources of interference. The speckles have the same dimension of the PSF of the star, so that it is impossible to distinguish them from a real source.

To try to minimize this variable speckle noise, the AO uses a deformable mirror (DM) which permits to correct quasi-instantaneously the wavefront corrupted by the atmosphere. The DM has actuators which deform its shape as the wavefront sensor sends the correction to be applied. In order to model the atmospheric behavior a point source, typically a star, is taken as a reference source. It has to be bright enough to permit a high S/N in the wavefront sensor. Many instruments have the possibility of using an artificial reference in addition to natural point-sources, the laser guide star (LGS), when a bright star is lacking. Currently DI instruments use the host star itself as a reference for the AO.

To commensurate the goodness of the AO, a parameter defined as Strehl Ratio (SR) is used. It defines the ratio between the peak of the PSF measured in the detector and the theoretical diffraction limited PSF. In Fig.1.9 the differences between the performance with and without the AO are shown. A perfectly flat wavefront corresponds to the theoretical diffraction limit, and then has SR= 1. A corrugated wavefront has a SR < 1. The largest the wavefront error, the lower is the SR; for this reason, the Strehl ratio provided by an AO system is higher at longer wavelengths. Also, as the Airy pattern dimension increases as λ, and the image flux is being conserved, the higher Strehl (longer wavelength) PSF has a brighter Airy pattern (core and inner rings) and a correspondingly lower intensity in its halo (Marois et al. 2000). While low-order AO can achieve SR of $20 - 60\%$, in the 1-2 μm wavelength range, extreme AO (ExAO) can reach more than 90% SR, almost a diffraction

limited PSF, in the same wavelengths. This improvement does not come for free, brighter star are needed for the ExAO, as the wavefront is more finely sampled. The ExAO provides a stabilized, quasi-diffraction limited beam, which is centered in the coronagraph.

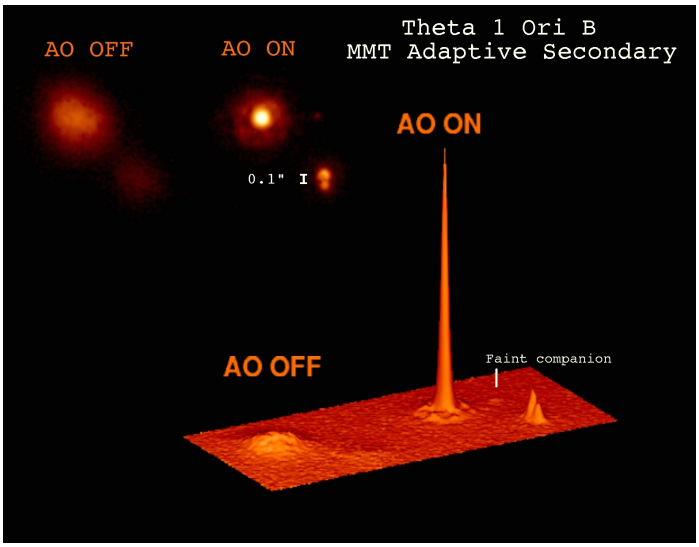

Figure 1.9: Differences between the performance with and without the AO. Without the AO we can see just two object, very blurred, when the AO is working, we can easily distinguish four objects. Credit: Laird Close, CAAO, Steward Observatory.

The AO can correct the wavefront errors till a separation defined as the outer working angle (OWA). It is the angular distance corresponding to spacial frequencies above $N_{act}\lambda/2D$ where N_{act} is the number of actuators along a linear dimension of the AO and D the telescope aperture. Higher frequencies cannot be corrected for the Nyquist criterion of sampling.

In addition to that due to the atmosphere, a second type of speckle pattern has to be taken into account: the quasi-static speckle pattern. The quasi-static speckles are due to the imperfections of the optics of the telescope, and they are mostly permanent during the exposure with typical lifetimes of tens of minutes. To attenuate this pattern, post-processing techniques are needed, as we will see in the next Sections. The variable speckle pattern attenuated by the AO can be further suppressed during the post-processing by averaging the images during a long exposure.

The speckles are brighter going closer to the host star and this is a limitation for the DI, as the majority of the planets detected are close to their host, as seen in Chapter 1. Also, the coronagraph has a physical dimension, and the region around the star which is behind

it is not visible. The major limitations for the DI techniques are the high contrast between the primary and the companion and the small angular separation.

1.2.2 Coronagraphs

DI exploits different types of coronagraphs to attenuate the light of the primary, which are divided in two categories: coronagraphs with occulting masks and phase masking coronagraphs. While the first class of coronagraphs uses an opaque mask which attenuate the first peak of the Airy function, the second class of coronagraphs exploits the principle of the destructive interference of the on-axis light. The most used coronagraphs are:

- apodized Lyot coronagraph (ALC): It is part of the first class of coronagraphs. It includes three optical elements: the occulting mask in the focal plane stops the light within a short separation from the center (typically $\sim 0''.1$ in 8-10 m telescopes); an apodizer located on a pupil plane (generally in front of the focal plane) limits the diffraction of the light with a gradual transmission function. A Lyot stop after the focal plane improves the contrast by masking the shadow of the spiders, that act as source of undesired additional diffracted light. It has then a shape similar to the occulting mask of the pupil plane, as shown in Fig. 1.10 (see, e.g., Guerri et al. 2009). The suppression of light achievable with this coronagraph is shown in Fig.1.11 (left part).

- four quadrant phase-mask (4QPM): It is part of the second class of coronagraphs. The mask (located in the focal plane) has a π phase shift in each quadrant. When the beam of light is centered there is destructive interference that suppresses the light. This type of coronagraph is reasonably achromatic (see, e.g., Rouan et al. 2000). The suppression of light achievable with this coronagraph for different filters is shown in Fig.1.11 (right part).

- vortex coronagraph: It is part of the second class of coronagraphs. The phase mask has different phases from 0 to 2π which creates destructive interference of the light (see, e.g., Mawet et al. 2009).

One of the principal parameters of the coronagraphs is the inner working angle (IWA) which is the radius where half of the light of the star is suppressed. The goal of new coronagraphs is to decrease as much as possible this value, to be able to detect planets orbiting at small separations.

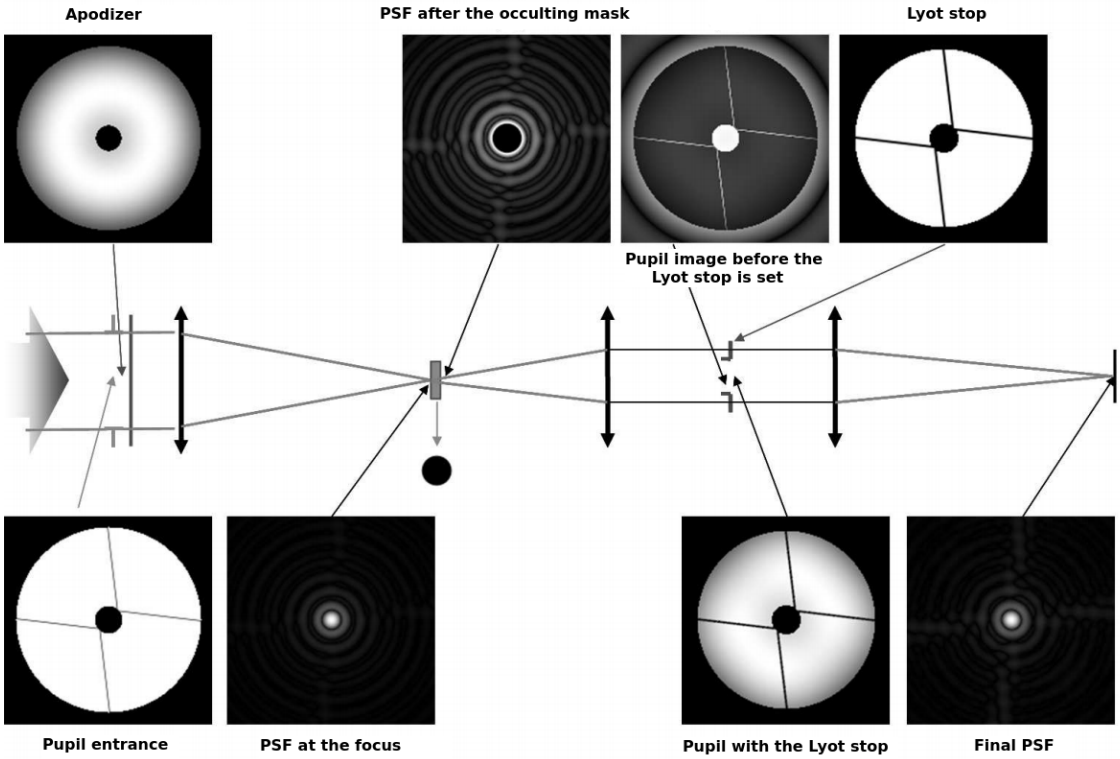

Figure 1.10: Principles of the ALC for SPHERE. Image adapted from Guerri et al. (2009).

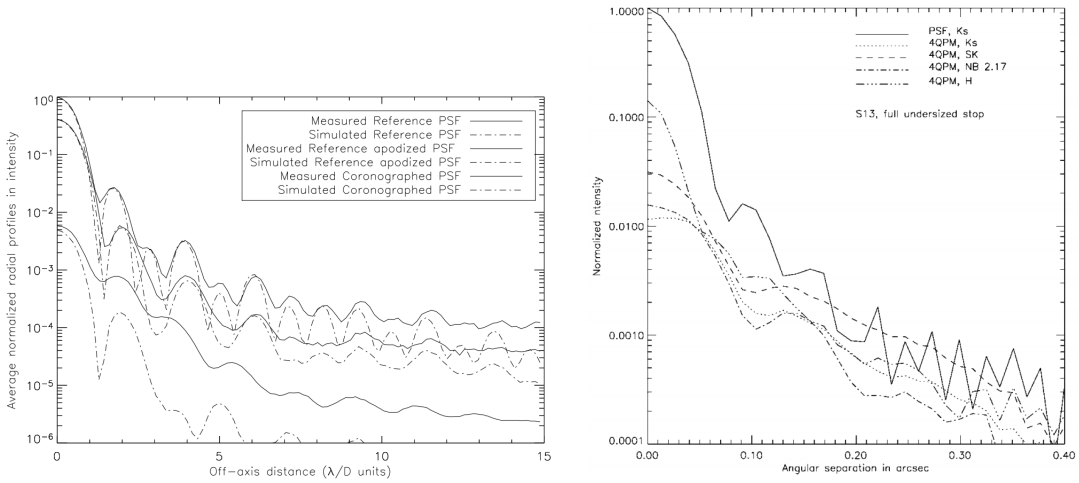

Figure 1.11: Light suppression achievable with the Lyot (left) and the 4QPM (right) coronagraphs of SPHERE. Images taken from Guerri et al. (2009) and Boccaletti et al. (2004).

1.2.3 Post-processing techniques

To attenuate the quasi-static speckle pattern various techniques can be applied, that will be widely mentioned in this thesis.

1.2.3.1 The SDI technique

One of the techniques more used exploits the fact that the speckle pattern, which is a diffraction pattern, rescales with the wavelength, while planets remain in the same position independently from wavelength. The spectral differential imaging (SDI, Racine et al. 1999) exploits this property to suppress the speckle pattern. The principle is to take simultaneously two coronagraphic images in two different bands with close wavelength λ_0 and λ_1. In this way the speckle pattern is almost identical in the two filters. We rescale the image at longer wavelength λ_1 to have the speckles at the same position in both images with respect to the center of the image. On the other hand, the planet is shifted from the original coordinates, according to the wavelength, and has different position in the two images. The two images are then subtracted according to the formula:

$$I_{diff} = I_{\lambda_0} - k(I_{\lambda_1})_{resc}, \tag{1.10}$$

where k is a factor to correct for the flux amplitude. A cartoon of the SDI method is represented in Fig. 1.12. This technique permits a reduction of the speckles noise that improves with the number of images at different wavelength that we have.

Also, this technique permits to distinguish a flat spectrum, where the fluxes are roughly the same in all the filters, from a spectrum which presents strong absorption in one of the channels, which will present different peak intensities in function of the wavelength. As we saw in Sec. 1.4, planetary spectra, especially T-type objects, present strong absorption in the bands of methane and water. For this reason, to observe in those bands, especially J and H, is convenient to distinguish a planet from a star with a flat spectrum, as shown in Fig. 1.13.

When the SDI is performed on two close filters we use the term Dual Band Imaging (DBI; Vigan et al. 2010a). An example of the contrast that we can reach with a DBI reduction with IRDIS/SPHERE is shown in Fig. 1.14. To compare, another technique that I will present in Sec. 1.2.3.3 is overplotted. The contrast achievable with the DBI alone reaches 5×10^{-5} at $0''.5$ of separation. This is just using a datacube of $\sim$ 30 sec.

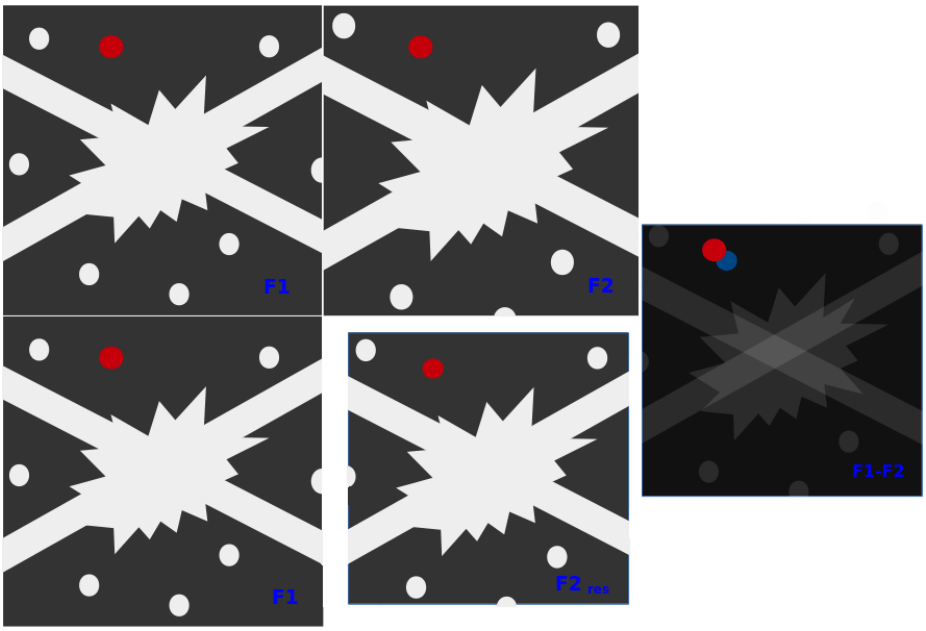

Figure 1.12: Images combination to exploit the SDI technique. The companion is represented in red, while its negative flux is represented in blue.

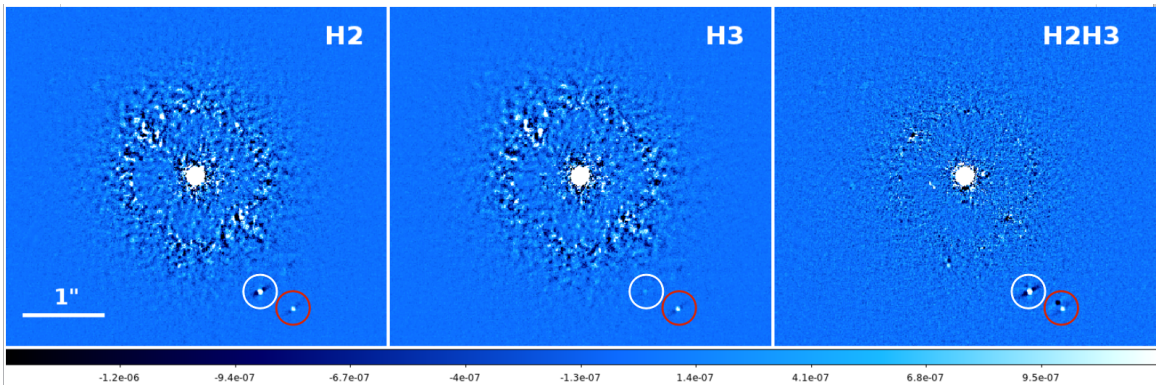

Figure 1.13: Images of the system around GJ 758. The object in the white circle, GJ 758 B, is a late T-dwarf. In the red circle, a background star. The methane absorption in the *H*3 filter is evident, as the flux of the object is lower. In the SDI combination of the two filters the difference between the T-dwarf and the background star close to it is clear, the T-dwarf has two different peaks, while the star has equal peaks. Reduced images kindly provided by A. Vigan.

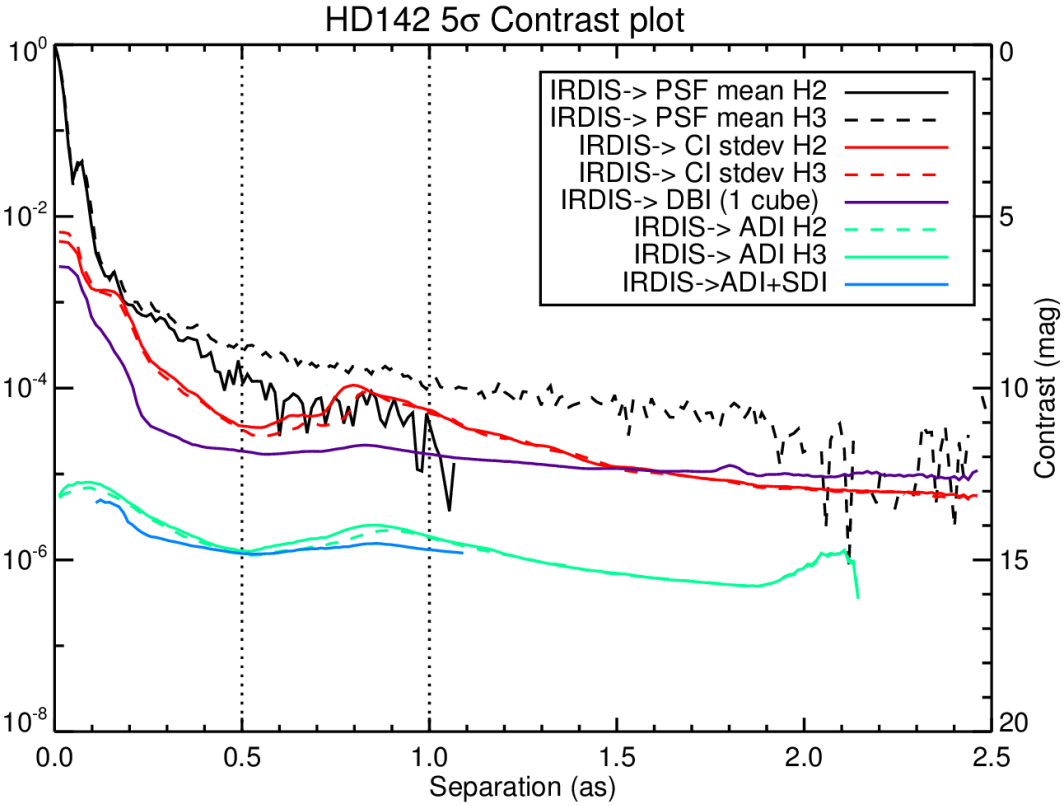

Figure 1.14: Different methods of reduction compared together. The SDI is performed using just one datacube over 128 (corresponding to 1h observation), as the FOV is moving during the sequence and there is no sense in combining more than one cube. The ADI reduction is performed in all the 128 datacubes. An improvement is seen when we combine ADI and SDI together.

1.2.3.2 The SD technique

The spectral deconvolution (SD) technique has been introduced by Sparks & Ford (2002) in the reduction of spectroscopic data of exoplanets. Subsequently, Thatte et al. (2007) proposed an improved version of the SD that is currently used in the reduction of IFS datacubes. The principle of the SD technique is based on the fact that the speckle pattern scales with wavelength, while the distance of a planet with respect to the center of the image is fixed in every channel.

After a proper rescaling, inversely proportional to the wavelength, the speckles are in the same position in the slices (i.e. frame at a given wavelength) of the IFS datacube, while the companion is located in different positions (see Fig. 1.15). For every spatial pixel, or *spaxel*[*] we can fit a low-order polynomial function of the wavelength which describes the profile of the residual light from the star along the channels. In this fit the signal of the planet is not recorded, as it is a high-frequency modulation. The polynomial fit is then subtracted from the rescaled channels of the datacube, and finally the slices are rescaled back to have the planet at the same position along the slices.

This technique is applicable outside a region delimited by the bifurcation radius, concept introduced by Thatte et al. (2007). Consider an object at a distance r (expressed in angular units) from its host star, the PSF of the object have the size of:

$$\theta_0 = 1.22\frac{\lambda_0}{D} \tag{1.11}$$

where D is the aperture of the telescope and λ_0 is the shortest wavelength of the datacube. The total shift of the planet after rescaling of the slices is:

$$\Delta r = r - r\frac{\lambda_0}{\lambda_1} = 2\epsilon \times 1.22\frac{\lambda_0}{D} \tag{1.12}$$

where λ_1 is the longest wavelength and ϵ is a parameter slightly greater than 1, explained in Fig. 1.15. In the separation for which $\epsilon = 1$, which is the bifurcation point, the projection of the PSF center of the planet at the mean wavelength is always inside the projection of the PSF in all the other channels.

[*]The spaxel is represented by all the corresponding pixels in all the other channels of an Integral Field Spectrograph (IFS) datacube of a same spatial pixel.

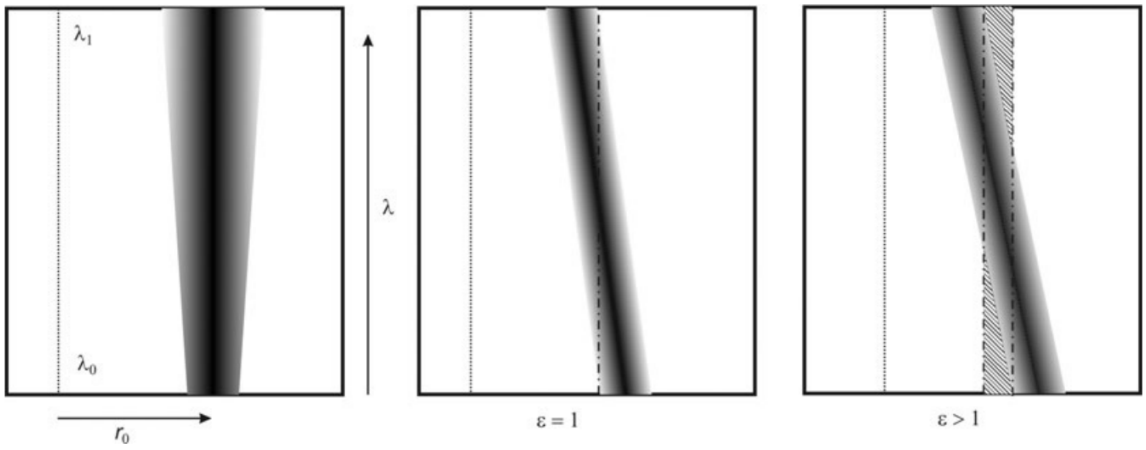

Figure 1.15: Figure from Thatte et al. (2007). A slice of an IFS datacube is schematized in the left-part of the Figure. In the x axis is represented the distance from the center of the image, while in the y axis we go along the channels, with increasing wavelength. In the center of the Figure the PSF of the object is shown after rescaling when the parameter $\epsilon = 1$, i.e. when the object is at the bifurcation radius and it is not possible disentangle the light of the speckles from the signal of the companion. The right-hand panel illustrates the situation after rescaling for $\epsilon > 1$, where the hatched areas are not contaminated by light from the companion.

1.2.3.3 The ADI technique

Another important technique is the angular differential imaging (ADI; Marois et al. 2006a). This technique uses the intrinsic field of view (FOV) rotation of altitude/azimuth telescopes, to rotate the companions of the target around the center of the image, and the speckles as stable as possible. For an instrument at the Cassegrain focus [†], the detorator of the telescope is switched off and the telescope pupil is fixed on the science camera. To exploit the maximum FOV rotation, the target are observed during the meridian passage. The rotation rate ψ (in degrees per minute) of the FOV is calculated as (McLean 1997):

$$\psi = 0.2506 \, \frac{\cos A \cos \phi}{\sin z}, \tag{1.13}$$

where A is the target azimuth, z the zenith distance and ϕ the telescope altitude.

In Fig. 1.16 the combination of the images is shown: the first step is to collect the images of the sequence, where the planet is slowly moving through the detector, while the speckles and the spiders are fixed (A_j); second we combine the images with the median

[†]For an instrument at Nasmyth focus, the field rotates as the sum of the parallactic and altitude angle, while the pupil rotates as the altutude angle. A suitable optical element (e.g. a K-mirror) derotating the image as wished may then be located in front of the instrument, allowing stabilizing the image of the pupil on the detector; in this case the field will rotate on the detector as the parallactic angle, as it is observed at the Cassegrain focus.

or other techniques to evaluate the speckles halo (B); then we subtract this product to the original images of the sequence (C_j); and derotate the images to have the planet at the same position (D_j); the result (E) is the combination of the detorated images.

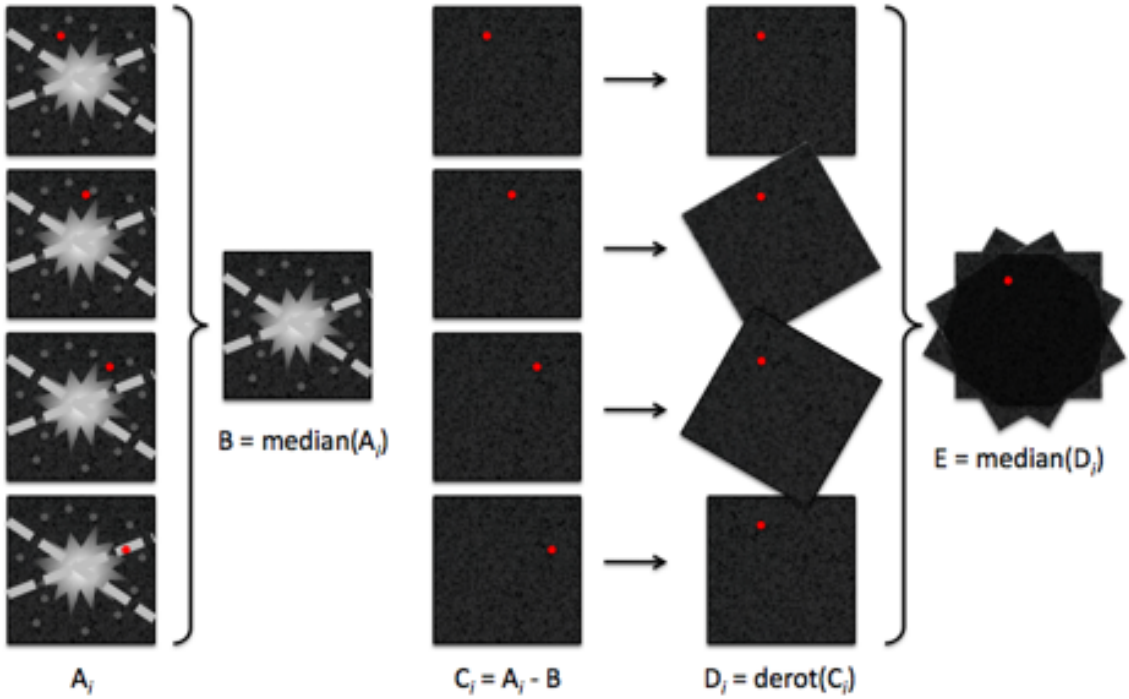

Figure 1.16: Images combination to exploit the ADI technique. The companion is represented in red. Credit: C. Thalmann.

The efficiency of this technique improves for greater and faster angular rotation of the FOV during the exposure. It is widely used by mostly every direct imaging instrument. ADI can be combined with SDI to go deeper in contrast. One example is shown Fig. 1.14. The contrast achievable with the ADI alone reaches 10^{-6} at $0''.5$ of separation. Combining SDI and ADI gives a further slight improvement.

Currently three flavours of ADI are used:

- classical ADI (cADI; Marois et al. 2006a): as explained above;
- smart ADI (sADI; Lagrange et al. 2010): a selection of the reference images which reconstructs the speckles halo is performed. While in the cADI all the images are taken in consideration and median-combined, in the sADI the closest-in-time frames to the reference image are excluded. This avoid the self-subtraction of the signal of the planet;

Table 1.1: Planetary companions detected so far by direct imaging technique.

Planet	M (M_{Jup})	R (R_{Jup})	P (yr)	a (AU)	Ref.
2M1207 b	6-10	1.5	1620	46	Chauvin et al. (2005)
Fomalhaut b	< 2	1.6	20	113	Kalas et al. (2008)
β Pic b	~ 8	-	20	8-15	Lagrange et al. (2010)
1RXS 1609 b	8-14	1.7	6518	331.1	Lafrenière et al. (2008)
HR 8799 b	~ 5	1.2	474	69.2	Marois et al. (2008b)
HR 8799 c	~ 7	1.3	189	37.4	Marois et al. (2008b)
HR 8799 d	~ 7	1.3	100	24.5	Marois et al. (2008b)
HR 8799 e	~ 7	1.3	49	14.5	Marois et al. (2010b)
Ross 458 c	8.5	1.8	33081	1167.7	Burgasser et al. (2010b)
2MJ044144	5-10	-	-	15	Todorov et al. (2010)
WD 0806-661 b	7-13	-	-	2500	Luhman et al. (2011)
HD 95086 b	~ 5	-	-	56	Rameau et al. (2013a)
GJ 504 b	3-7	-	-	43.5	Kuzuhara et al. (2013)
FW Tauri b	6-14	-	-	300	Kraus et al. (2014)
HD 106906 b	9-13	-	-	650	Bailey et al. (2014)
GU Piscium b	9-13	-	163000	2000	Naud et al. (2014)
ROXs 42 Bb	9	-	-	157	Currie et al. (2014b)

- radial ADI (rADI; Marois et al. 2006a): it is a procedure similar to the sADI. This time the selection of the frames is optimized for the separation of the object, as the signal of the planet rotates along the frame at different angles as a function of the radius planet-center of the image. The PSF of the planet moves faster along the images for larger separations (i.e. we can reject less frames).

1.2.4 Direct imaged systems

Direct imaging technique provides us discoveries since already twenty years, when the first brown dwarf companion, GI 229 B has been found with this method (Nakajima et al. 1995; Oppenheimer et al. 1995). In Table 1.1 I list some of the more important results of the direct imaging technique, while in the following paragraphs I will give more details for particular objects discovered so far.

The first companion in the planetary mass regime ever imaged has been detected by Chauvin et al. (2005). This object has been observed with NACO (see Sec. 2.1). The first epoch has been obtained in 2004, when they detected a promising object around the star 2MASSW J1207334-393254 (Fig. 1.17), a M8 type star of the TW Hydra association (age $\sim$ 8 Myr). The object, called for simplicity 2M1207 b, is separated from the host star of

about 0″.78 (= 55 AU). To confirm that the object is comoving, a second epoch has been taken one year later, and the nature of the planet has been confirmed. Following evolutionary models presented in Sec. 1.4, a mass of M = 5 ± 2 M_{Jup} and an effective temperature of T_{eff} = 1250 ± 200 K is found. The nature of this object is particular, as it is very unlikely that the planet has been formed in the protoplanetary disc, given the distance from the host star. It is considered more a binary system of low mass objects, rather than a planetary system.

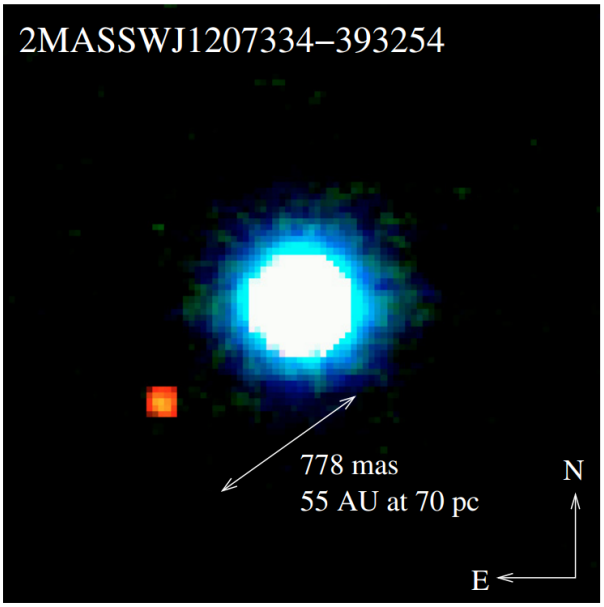

Figure 1.17: The first planet ever imaged: 2M1207 b (Chauvin et al. 2004).

High-contrast observations with the Keck and Gemini telescopes have revealed in 2008 the first multi-planetary system ever imaged: four planets orbiting the star HR 8799 (Marois et al. 2008b, 2010b). An image of the system is shown in Fig. 1.18. This system is the most observed target of the direct imaging technique, and a benchmark for the study of planetary atmospheres and formation. I present in more details this system and SPHERE results that we obtained in Chapter 6.

Kalas et al. (2008) discovered the lowest mass planet ever imaged, Fomalhaut b (Fig. 1.19). The planet has been imaged in visible light using Hubble Space Telescope (HST) Advanced Camera for Surveys (ACS), and it appears in the dust belt surrounding the brightest star of

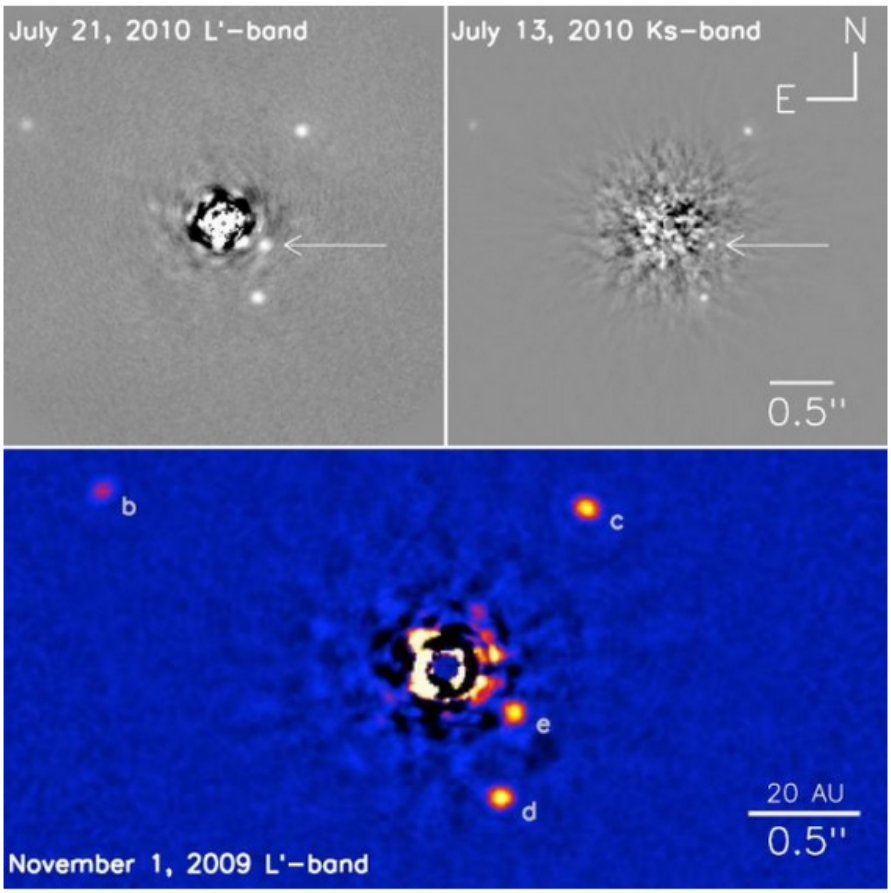

Figure 1.18: The first multi-planetary system ever imaged: HR 8799 bcde (Marois et al. 2010b).

the constellation Piscis Austrinus. Fomalhaut is a A4 type star, 7.7 pc away, aged $\sim$ 400 Myr. The planet is not detected in IR light. Neither Keck (L' band) nor Gemini (H band) have been able to detect it. This can suggest that the planet is (a) low mass and (b) detected in the visible through reflected light more than thermal emission. Its presence was predicted by the unusual sculpturing of the disk, that is highly inclined and off-centered. The origin of the planet is accepted to be in the debris disk, as it is still surrounded by it. Dynamical studies put an upper limit for the mass of the object of 3 M_{Jup}. Fomalhaut b is on a very eccentric (0.8) orbit, with a semi-major axis of 177 AU (Kalas et al. 2013).

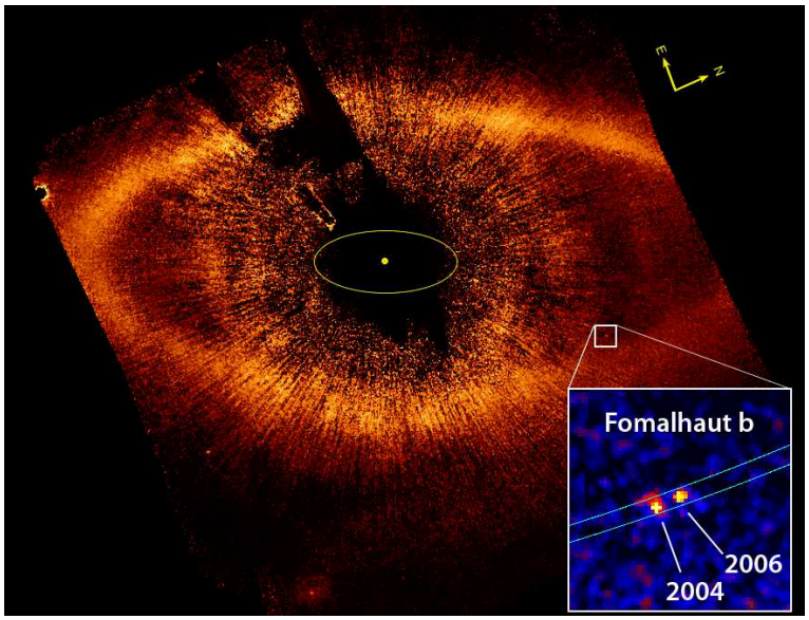

Figure 1.19: Image of the debris disk surrounding the star Fomalhaut. The planet Fomalhaut b is seen in two different epochs confirming its association to the system (Kalas et al. 2008).

Around the star β Pic, a planet has been discovered by Lagrange et al. (2009). The system also hosts an edge-on debris disk, as shown in Fig. 1.20. This planet has the closest semi-major axis for a direct imaging planet, 8 – 10 AU, that corresponds to the snow line of the system, as the primary star is of A type. As for Fomalhaut planetary system, upper limits on the mass of the companion can be calculated from dynamical constraints. The mass of β Pic b has been estimated of $\sim$ 8 M_{Jup}. The age of the system is assumed to be of 21 Myr, as Binks & Jeffries (2014) reported a lithium depletion boundary age for the β Pic moving group. The projected separation of the system, 0$''$.4, is not anymore an issue

for the new generation instruments, which are finally able to extract the spectrum of the companion. The first GPI results are presented in Bonnefoy et al. (2014). SPHERE results on the system are presented in Appendix B.

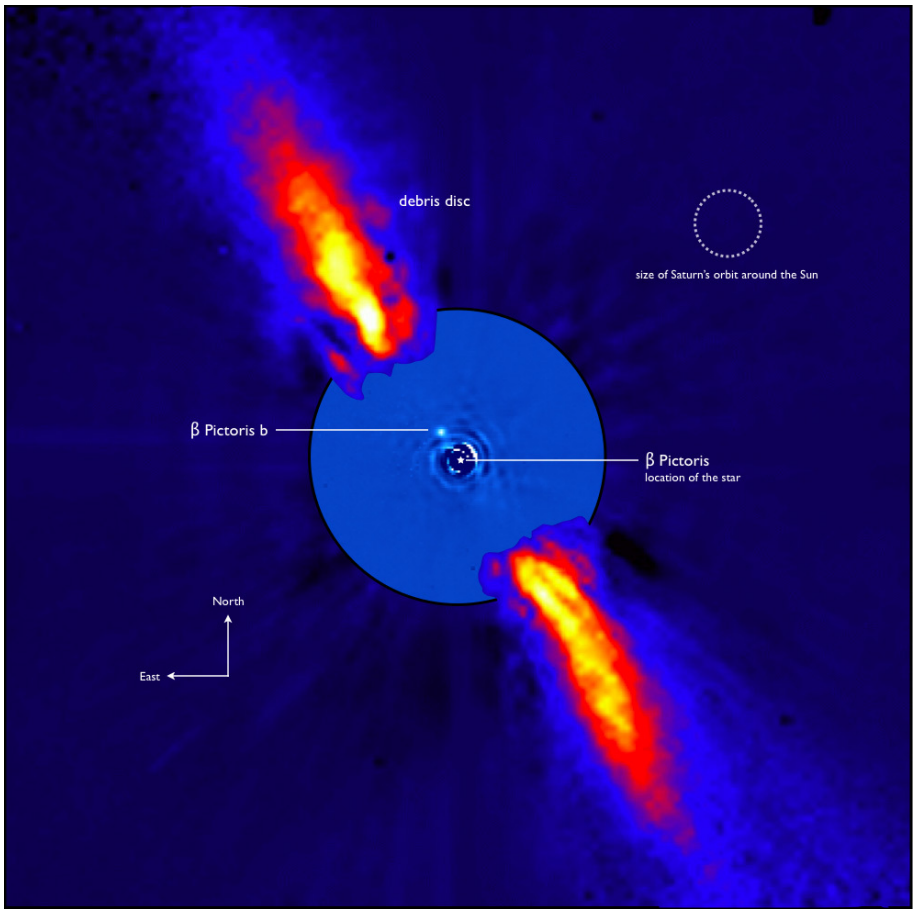

Figure 1.20: Image of (Lagrange et al. 2009).

1.3 Mechanisms of giant planet formation

1.3.1 Core accretion model

One of the theories of planet formation most widely accepted is the so-called *core accretion* model (Mizuno 1980; Pollack et al. 1996). It is the mechanism mostly accepted for the formation of giant gas planets in our solar system and in exoplanetary systems, at least for objects orbiting closer than 10-50 AU (Perryman 2014). This scenario is based on the fact that in the protoplanetary disk solid objects, called *planetesimals*, are present. These

objects can collapse on a solid core, created from dust, if located inside a zone where the protoplanet has gravitational influence. The solid cores can be formed more easily in the outer part of the disk, beyond the snow line, where the temperature is low enough for the formation of water ices. The feeding zone can extend over a few Hill radii ($R_H = a(M_p/3M_\star)^{1/3}$, where a is the planet orbital radius, M_p and $M_\star$ is the protoplanet and star mass respectively) (Baraffe et al. 2010). When the solid core (ice and rock) has reached a mass of ~ 0.1 $M_\oplus$ it starts to gather an envelope of nebular gas. In this phase there is a quasi-static balance between radiative loss and accretion energy. When the gas accretion has reached a critical mass M_{crit} a gravitational contraction occurs to compensate the radiative loss. The critical mass is reached when the mass of the core and the envelope are roughly equal (Mordasini et al. 2008). The critical mass can be estimated to be in the range 5-15 $M_\oplus$ depending on physical conditions and assumptions about grain opacity (see, e.g, Pollack et al. 1996; Papaloizou & Nelson 2005). When the critical mass is reached, the envelope can stay no longer in hydrostatic equilibrium. It begins to contract and the gas falls in free fall onto the core. The radius of the new born planet is fixed by the conditions of this radiative shock. The accretion process terminates when the planetesimals and gas supplies end, as a gap in the disk may be created or because the disk gas dissipates at some point.

An example of simulation of Solar system giant planets formation is given by Pollack et al. (1996). The process is divided in three phases: (i) the embryo of the protoplanet accumulates planetesimals in the first 5×10^5 yr, and there is a depletion of its feeding zone; (ii) the accretion rate remains constant during ~ 7 Myr, and the growth accelerates during the beginning of the phase (iii) with a runaway accumulation of gas. The results of these simulations are shown in Fig. 1.21. During the first years, the planet accumulates solids by rapid runaway accretion; this "phase 1" ends when the planet has severely depleted its feeding zone of planetesimals. The accretion rates of gas and solids are nearly constant during most of the duration of phase 2. The planet's growth accelerates toward the end of phase 2, and runaway accumulation of gas characterizes phase 3. The simulation was stopped when accretion became so rapid that the model breaks down. The endpoint was thus an artifact of the technique. As expected, the final mass of the planet is proportional to the density of planetesimals of the feeding zone, even if the core is initially of the same dimension. The core of Jupiter predicted by these simulations is more massive that the estimate (see Section 1.4.1). This is one of the issues which has to be explained by the core accretion models.

The major problem of this theory is that the protoplanetary disk lifetime, few Myr (Haisch et al. 2001), is shorter than the time needed to a core to grow. The growth timescale is proportional to $a^{3/2}M_\star^{-1/2}$, for that planets far away from the host star cannot be formed

there (D'Angelo et al. 2011). To solve this issue, Hourigan & Ward (1984) first proposed the mechanism of migration. In this way planets can move from their formation position. Migration occurs when the torques exerted by the different parts of the disk interact with the planet. It reacts in adjusting its semi-major axis to compensate the forces (Mordasini et al. 2009). There are two types of migration: type I, the migration of low mass planets (see Goldreich & Tremaine 1980; Tanaka et al. 2002), and type II, where massive planets open a gap in the protoplanetary disk and migrate (Lin & Papaloizou 1986). This mechanism permits the core to accrete on different zones where it can find new planetesimals as the lengthy phase II is skipped (Alibert et al. 2004).

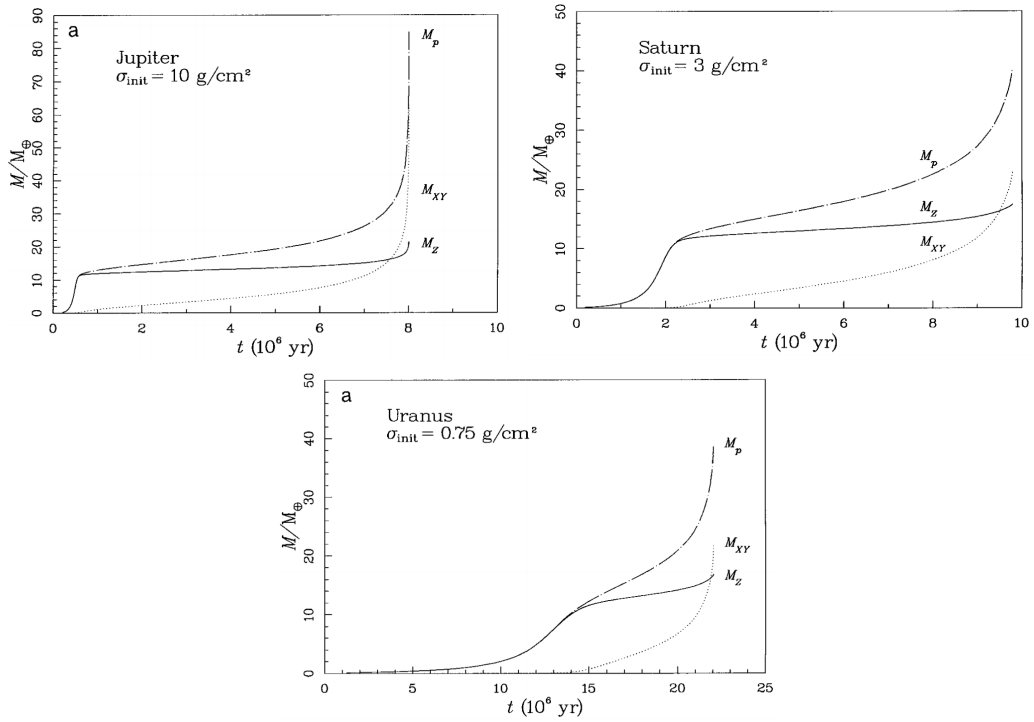

Figure 1.21: Figures 1, 4, and 5 from Pollack et al. (1996). Results on the simulations performed on the formation of the solar system giant planets. The initial planetesimal surface density, σ_{init} is shown for each planet. The initial embryo has nearly the mass of Mars, and planetesimals have a radius of 100 km. The solid line represents accumulated solid mass, the dotted line accumulated gas mass, and the dot-dashed line the planet's total mass.

The Solar system can be at the same time a good evidence for the core accretion model and against it. The outer Solar system is consistent with the trend of time scale/radius. The less massive planets could have been formed during the beginning of the dissipation of

the gas. Also, Jupiter has the closest Solar composition, while the other giants planets are poorer in gas (Armitage 2007).

Against the model there is the difficult explanation of the Neptune time scale. To obviate this problem, migration of the planet is proposed. Also problematic is to explain the small core of Jupiter, as we saw before, even if a core erosion may have occurred.

Concerning exoplanets, the correlation between the frequency of planets and the metallicity of the host (Fischer & Valenti 2005) seems to confirm the core accretion scenario, as it is more probable to form planets faster around high metallicity stars. On the other hand one should consider that this statistical analysis is biased by the high number of close-in planets discovered so far, and it could be different for long period planets.

To obviate the problems aroused by the core accretion model and to explain exceptions found in the exoplanets population, another scenario has been proposed, presented in the next Section.

1.3.2 Gravitational instability

An alternative theory to the core-accretion model, suggested especially to obviate the timescale problem, is the *gravitational instability* scenario (Cameron 1978; Boss 1997). Following this theory it is possible to explain the formation of massive planets, far from their host star. A condition for this scenario is that the disk is massive. Instability perturbations may occur in a disk if the Toomre stability condition falls: $Q = c_s\kappa_e/\pi G\sigma \sim T^{1/2}\Omega/\Sigma \sim (M_{star}/M_d)(H/r) < 1$, where κ_e is the epicyclic frequency in one point of the disk, $\Sigma \sim M_d/r^2$ is the surface density, $H \sim c_s/\Omega$ is the disk vertical scale height and M_d is the mass of the disk within the radius r (Toomre 1964). If this occurs, the disk fragments into pieces and from the clumps that they cause, future giant gas planets can form.

A steady-state disk becomes less stable at large radii (Armitage 2007). If the mass accretion rate increases, the radius decreases (Zhu et al. 2012). Examples of simulations performed to predict the formation of planets by gravitational instability are shown in Fig. 1.22. Three out of four synthetic disks presents clumps at the end of the simulation.

Another parameter that plays an important role is the temperature of the disk, lower temperature disks may be more likely unstable. This mechanism is faster than the core-accretion one, taking time in less than 1 Myr. This is due to the fact that disk fragmentation is possible if cooling time is shorter than the orbital period (Gammie 2001).

The planets formed by gravitational instability are expected to be far away from the host star and with great radii. Also, differently from the core accretion model, no core is expected. This model predicts that planets have a high initial entropy, while for the core accretion model the entropy is low, as entropy is lost during the cooling process of the gas.

For this reasons we define as “hot-start” the birth of planets in the gravitational instability scenario, and “cold-start” the one of the core accretion. This is crucial when we want to assume a mass for planets during the first stages of its life, as the “hot-start” planets are much more brighter for a fixed mass.

This scenario has been proposed to explain some of the direct imaged systems as Fomalhault (Kalas et al. 2008) and HR 8799 (Marois et al. 2010b), or planets around multiple systems (Kratter et al. 2008, 2010a,b).

Also, it could explain the fact that Jupiter has a smaller core than the expected from core accretion.

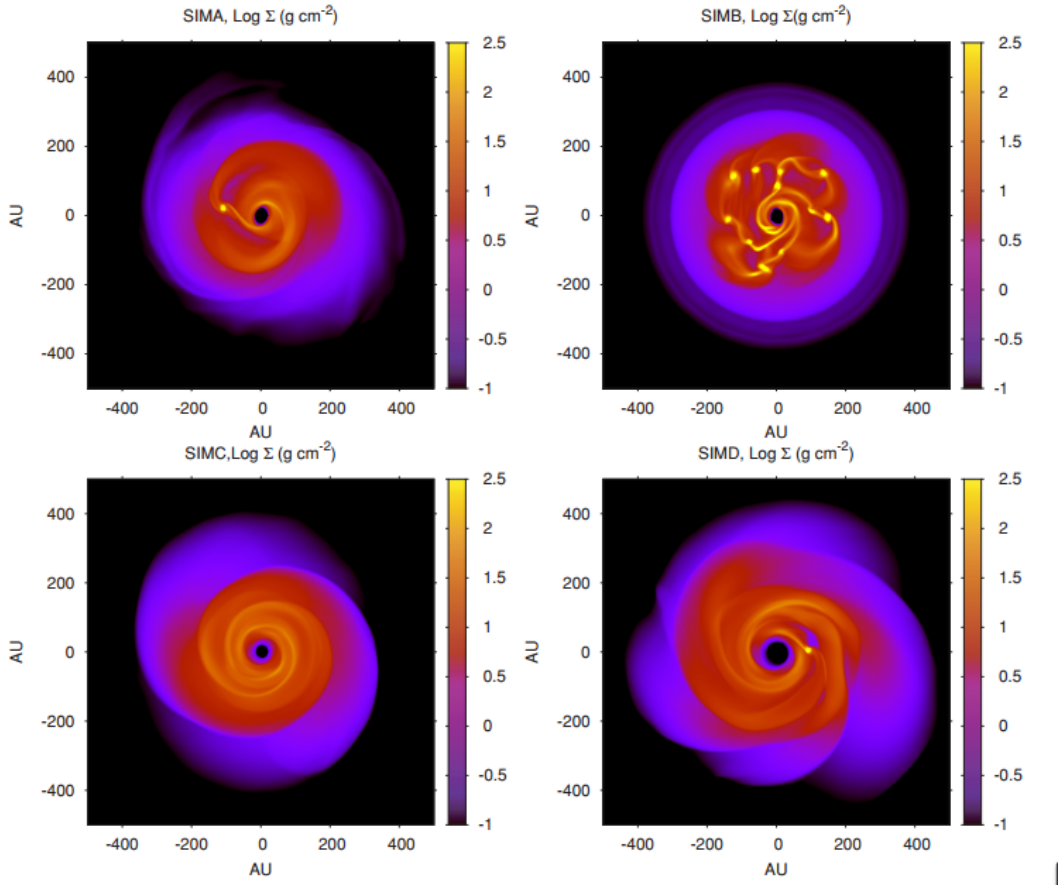

Figure 1.22: Figure taken from Boley (2009). Snapshots of the surface density of the disk at the end of different simulations to predict gravitation instability formation. In three out to four cases the gravitational instability bursts lead to fragmentation and formation of clumps.

Boley (2009) proposed to unify these two theories that can coexist, saying that the core accretion can operate in the internal part of the disk ($\sim$ 100 AU) while gravitational instability clumps form planets in the outer region.

Direct imaging method will help us to speculate on the formation of planets at wide orbits, which are not explored by the other indirect techniques. Also, measuring the luminosity of planets during the first stages of their life will help us in understanding which is the scenario that better describe the formation of planetary system. Coupling the estimated mass from "hot-start" and "cold-start" models and dynamical information on the mass will be fundamental to comprehends how giant planets form.

1.4 Giant planets atmosphere

During these last 20 years we collected a huge population of exoplanets that permits us investigate their properties and composition. Comprehending their nature could also help us in understanding the mechanisms which caused their formation. Giant planets are very complex objects where hydrogen (H) and helium (He) are pressed together under megabar to gigabar pressure, at the temperature of 10^4 K. To derive properties of the observed companions we first try to extrapolate the information from the giant planets of our solar system and combine them with the knowledge derived from exoplanets spectra extracted. The new generation of planets hunters presented in Chapter 2 will provide high S/N spectra, fundamental to improve our knowledge on exoplanets atmospheres.

1.4.1 Solar system giant planets

The giant planets of our solar system help us understanding the nature of extrasolar planets. The giant planets of the solar system are Jupiter, Saturn, Uranus, and Neptune; all located beyond the snow line, situated at 2.7 AU from the Sun. A snapshot of these planets is shown in Fig. 1.23.

A scheme of the interior of Jupiter and Saturn is shown in Fig. 1.24, while a cartoon of the interior of Uranus and Neptune is shown in Fig. 1.25..

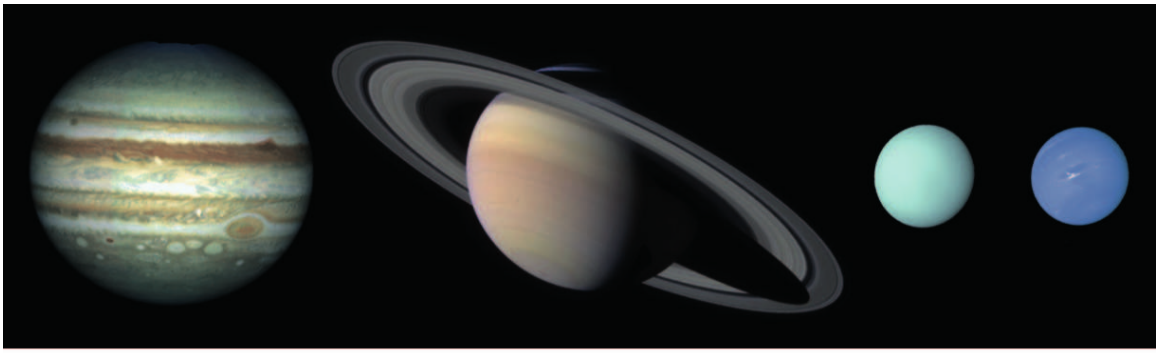

Figure 1.23: Image of the giant planets of our solar system, taken from Voyager 2 (Jupiter, Uranus, and Neptune) and Cassini (Saturn). Figure taken from Guillot & Gautier (2014).

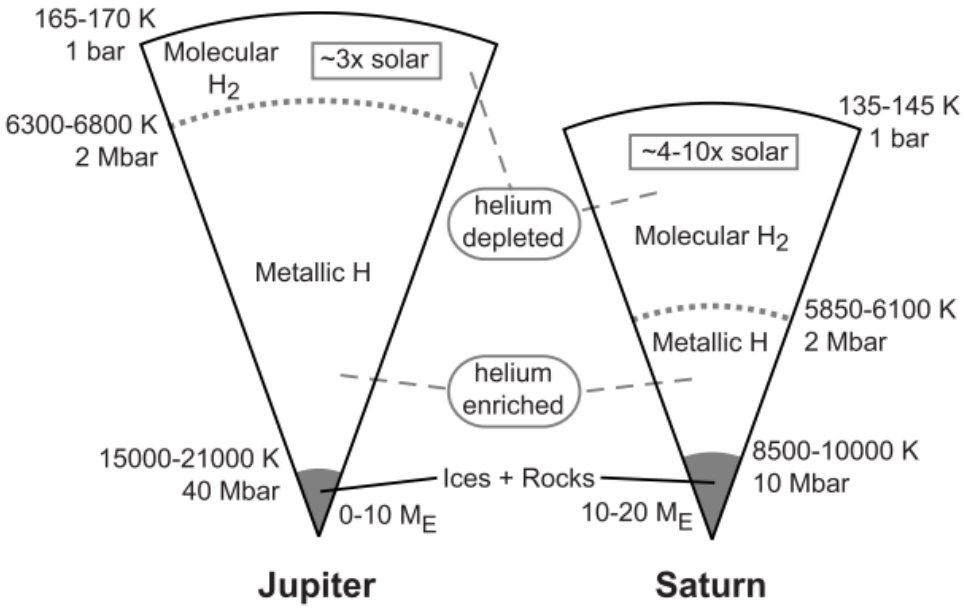

Figure 1.24: Figure and caption taken from Fortney et al. (2011) . Interior views of Jupiter and Saturn, from calculations with the Saumon et al. (1995) "chemical picture" H/He equation of state (EOS). Jupiter is more massive, which leads to a greater fraction of its mass in the high-pressure liquid metallic phase. It also has a higher temperature at a given pressure. Interior temperatures are taken from Guillot (2005).

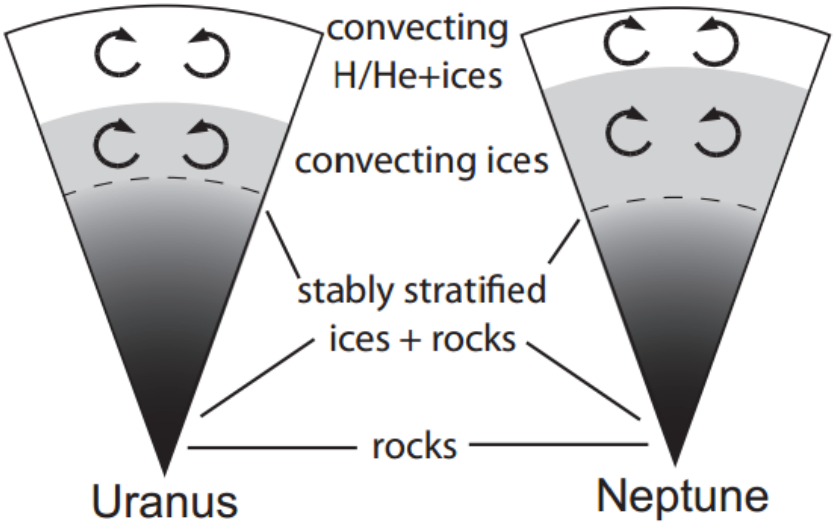

Figure 1.25: Figure and caption taken from Fortney et al. (2011) . Possible interior views of Uranus and Neptune. White indicates a composition of predominantly H_2/He gas (with smaller amounts of heavy elements mixed in), solid gray is predominantly ices, and black predominantly rock. The gray-to-black gradient region in each planet shows where the interior may be statically stable due to composition gradients. Circles with arrow heads indicate convection. Neptune appears to be composed of a greater fraction of heavy elements and it may have a larger freely convective region. This and other inferences are, however, uncertain.

Jupiter is the biggest planet and it is widely studied to unveil all the questions on gas giant planets atmospheres. As the Sun, Jupiter is composted mostly by H and He, even if, given its radius and mass, heavier elements are present, too. Podolak & Cameron (1974) proposed that Jupiter and Saturn have a core made of heavier elements. The observed heat flux can be carried by convection, and the interior is fluid. The mass of the core of Jupiter has been estimated for some equations of state to be below 5 $M_\oplus$ (Armitage 2007). Guillot (2005) gives an upper limit to the mass of the core of 10 $M_\oplus$. The core of Saturn has been estimated to be of 10-20 $M_\odot$ (Saumon & Guillot 2004; Militzer et al. 2008). This suggests that the second has formed by core accretion, while Jupiter should have a more massive core following the same formation theory.

Saturn has a similar structure of Jupiter, it is 3.3 times less massive and 50% more luminous than expected, due probably to an additional source of energy. While most of the hydrogen mass of Jupiter is fluid metallic, for Saturn it is fluid molecular, H_2 (Fortney et al. 2011). Both planets are covered with clouds.

Uranus and Neptune are the so-called "ice giant" planets. Unfortunately, the amount of data that we have on these planets is significantly less than what we have for Jupiter and Saturn. The first thing that has been noticed is that these planets are denser than Jupiter and Saturn, suggesting a composition where H and He are not predominant. Uranus and Neptune likely have a core composed of a mix of fluid ice and solid rock. The fully adiabatic model that describes Jupiter cannot be applied to Uranus and Neptune, which are underluminous. The interior is predominantly stratified, with only the outer 1/3 of the heavy elements interior region freely convecting (Hubbard et al. 1995). The energy is then "locked" in between the interior layers.

All the giant planets of the solar system are emitting more light than the one they receive from the Sun (Guillot & Gautier 2014). This can be due to the progressive contraction and cooling of the planets (proposed for the case of Jupiter in Hubbard 1968). The interior of these planets has to be fluid at such an high temperature ($\sim$ 10000 K). The interior temperature profile is close to adiabats.

1.4.2 Brown dwarfs and exoplanets

Similar properties of the giant planets of the solar system are found in the so-called "substellar objects": brown dwarfs (BDs) and planets. This class is composed by objects that are not massive enough to host nuclear fusion of hydrogen in the core. The upper limit of the mass for a substellar object is then $\sim$ 0.08 $M_\odot$. Objects heavier than 13 M_{Jup} can fuse deuterium (Saumon et al. 1996; Burrows et al. 1997; Chabrier et al. 2000), and those above $\sim$ 65 M_{Jup} can fuse lithium (Lodders & Fegley 2006).

The boundary between a brown dwarf and a giant planet is still on debate. More studies will permit to know whether the mechanisms of formation and/or the physics of the interior are different. Generally the limit is imposed by the mass of the object.

The class of substellar objects includes spectral types from late M to Y. The spectral types L and T were introduced by Kirkpatrick et al. (1999), for objects cooler than M-dwarfs. Then, Cushing et al. (2011) introduced the class of Y-type dwarfs, the coolest objects ever observed. The main features of substellar objects of the spectral sequence from M to T are shown in Fig. 1.26. The main properties of the spectral classes are:

- **M-dwarfs**. This spectral type is the link between stellar objects and BDs. The latest types of the M sequence includes young objects which are considered BDs. The spectrum is characterized by the presence of TiO and VO. TiO bands increase in strength up to spectral type M6, and VO becomes strong in the latest types (Bailey 2014). Broad absorptions due to H_2O are found around 1.4 and 1.9 μm, especially in later spectral types. Other molecules with strong absorption are FeH, CrH, and MgH.

- **L-dwarfs**. In this type of dwarfs the TiO and the vanadium monoxide are increasingly disappearing. At their places the band of CrH, FeH, and alkaline metals are appearing in the optical. In the near-infrared the bands of CO, CrH and FeH are strong till the mid-L and then become weaker. The sequence of the L-dwarfs is redder than the others in the NIR mag/color diagram (see Fig. 1.27). This is due to the dusty clouds of species such as enstatite, forsterite, spinel, and solid iron which condense in the upper layers of the atmosphere (see, e.g., Allard et al. 2001).

- **T-dwarfs**. The T-dwarf class is characterized by the presence of methane (CH_4) absorption features in the near-IR region (1-2.5 μm) and water absorption bands. The methane absorptions at 1.6 and 2.2 μm (H and K bands) cause the blue shift of the sequence in the mag/color diagram (see Fig. 1.27). They have a closer resemblance to solar system giant planets. Burgasser et al. (2002) estimate that, at birth, Jupiter had a T_{eff} near 600-1000 K and the appearance of a T-dwarf.

- **Y-dwarfs**. These objects lack water absorption bands, because the H_2O condensates with temperatures around 500 K and it is not present in their clouds (Ackerman & Marley 2001; Burrows et al. 2003). .

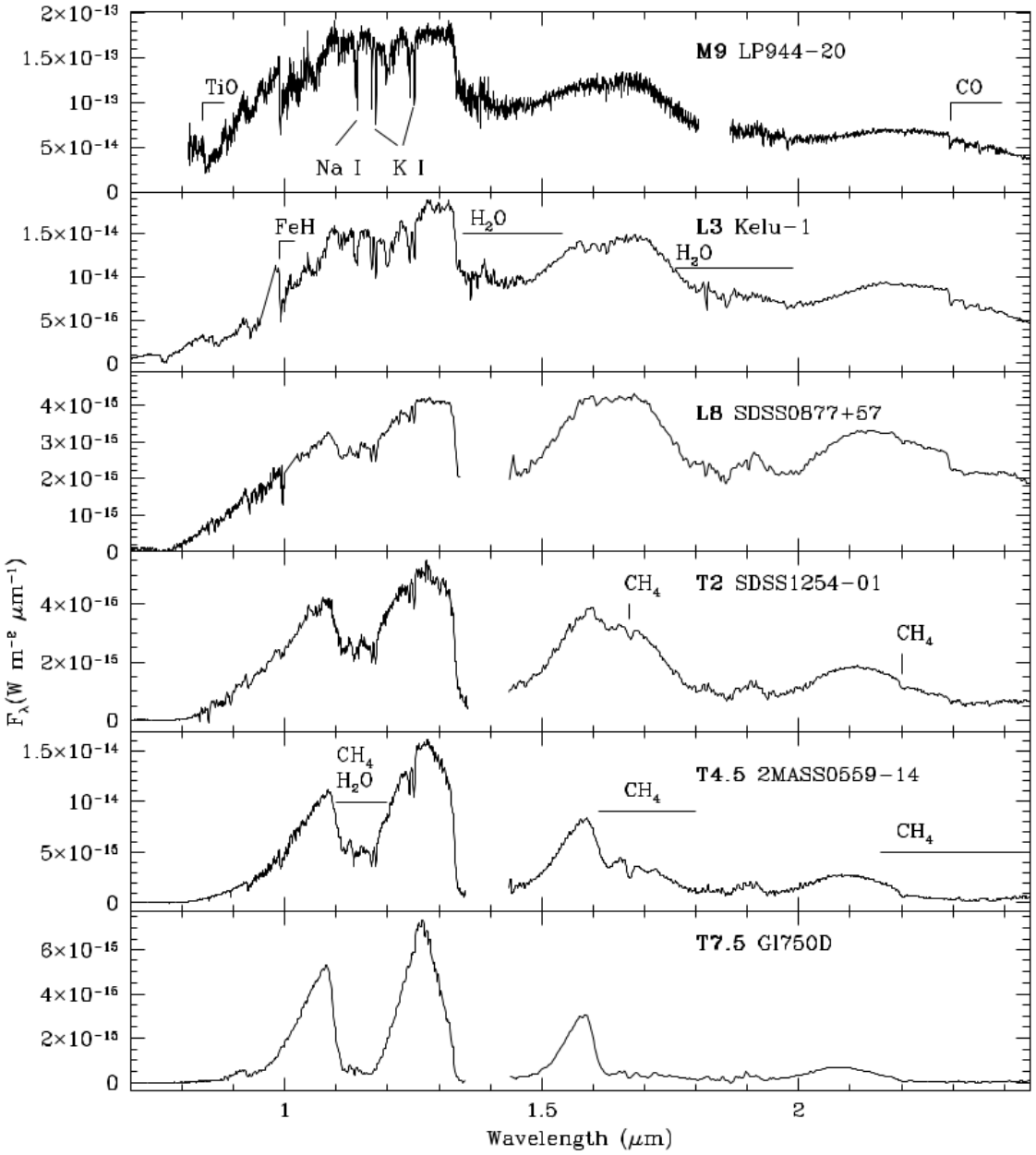

Figure 1.26: Figure and caption taken from Bailey (2014). Spectra of ultracool dwarfs from M9 to T7.5. The species responsible for the main absorption features are indicated. Spectral data is from Burgasser et al. (2003); Cushing et al. (2005); Geballe et al. (2001); Geballe et al. (2002); Leggett et al. (2000, 2001, 2002); Rayner et al. (2009); Ruiz et al. (1997).

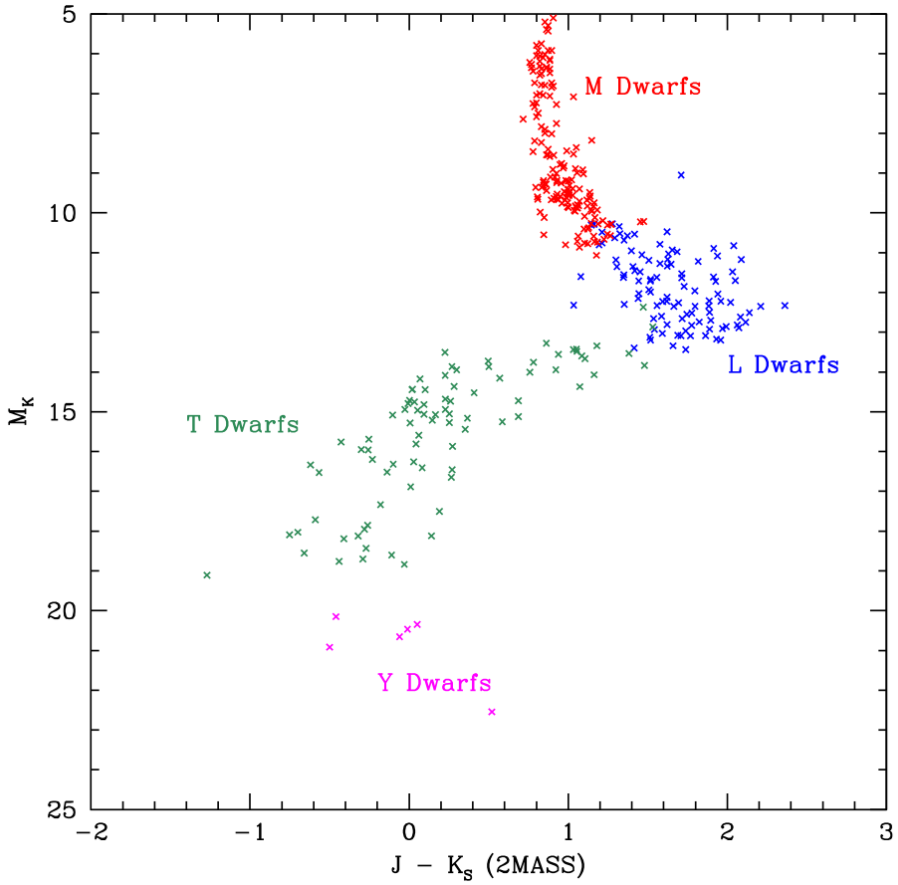

Figure 1.27: Figure and caption taken from Bailey (2014). Colour magnitude diagram ($J-K$ against M_K) for late type dwarfs. Most of the data is taken from Dupuy & Liu (2012). Data on late T and Y dwarfs is from Dupuy & Kraus (2013) and has been roughly converted to the 2MASS system according to Stephens & Leggett (2004). Additional data on earlier type M dwarfs has been added from the compilation of Reid (http://www-int.stsci.edu/lnr/cmd.html) based on photometry from Leggett (1992) and converted to the 2MASS system using relations in Carpenter (2001).

An example of the information that we can extract from planetary spectra will be presented in Chapter 6.

Substellar objects are known to evolve with time more rapidly than low mass stars. This is a fundamental propriety of these objects for the direct imaging technique, as in the first stages of their formation they are much more brighter and hotter. Since they do not have any significant internal source of energy, planets cool down gradually with time. The evolution in time of the temperature for different masses is shown in Fig. 1.28. Brown dwarfs have an initial temperature of ~2500 K during the first 10 Myr, than they cool rapidly and the temperature can drop till 500 K after 10 Gyr. On the other hand, planets cool-down since the beginning, reaching a final temperature of ~ 200 K after 1 Gyr. At the first stages, substellar objects are bright, large in radius, and usually fully adiabatic (as Jupiter).

More important for what concerns direct imaging observation is the luminosity evolution with time, shown in Fig. 1.29. The luminosity of substellar objects generally decrease with a power-law (roughly $L \sim 1/t$).

If we combine the information on the luminosity to the estimated age of the system, we can derive a mass for the companion. This value is not an observable quantity till is not coupled with dynamical information. Especially at young ages models are not fully tested. Marley et al. (2007) proposed models were the initial conditions were not arbitrary but assumed by the core accretion scenario: the "cold-start" models. As we saw in the previous Section, the two different formation scenarios lead to different predictions on the luminosity of planets at the first stages. Planets formed by gravitational instability are expected to have large radii and high temperatures. The entropy of these objects is high. In the core accretion scenario, the birth of planets is more gentle, they have low entropy, small radii and low T_{eff}. The evolution of the three parameters are shown in Fig. 1.30 for both models. The plots show that planets keep the information of their formation just in the first Myr of their life, for old object the two models are coincident.

Direct imaging campaigns will provide soon luminosities of new born planets that will help to constrain and test these evolutionary tracks and better understand the mechanism of formation and evolution of substellar objects.

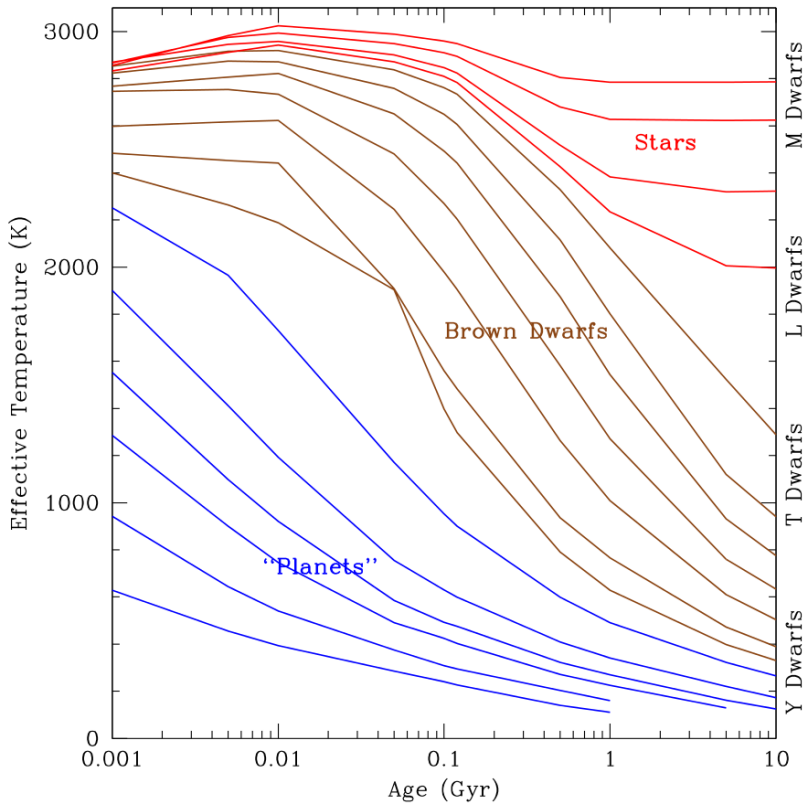

Figure 1.28: Figure taken from Bailey (2014). Evolution of effective temperature for sub-stellar objects. The range of mass represented goes from 0.0005 to 0.1 $M_{\odot}$ based on the models of Baraffe et al. (2003a). The red tracks are for stars with masses above the hydrogen burning limit. The magenta tracks are for brown dwarfs, and the blue tracks are for objects below the deuterium burning limit (planets or sub brown dwarfs) The tracks plotted from top to bottom are masses of (Stars: 0.1, 0.09, 0.08, 0.075 $M_{\odot}$) (Brown Dwarfs: 0.07, 0.06, 0.05, 0.04, 0.03, 0.02, 0.015 $M_{\odot}$), (Planets: 0.01, 0.005, 0.003, 0.002, 0.001, 0.0005 $M_{\odot}$).

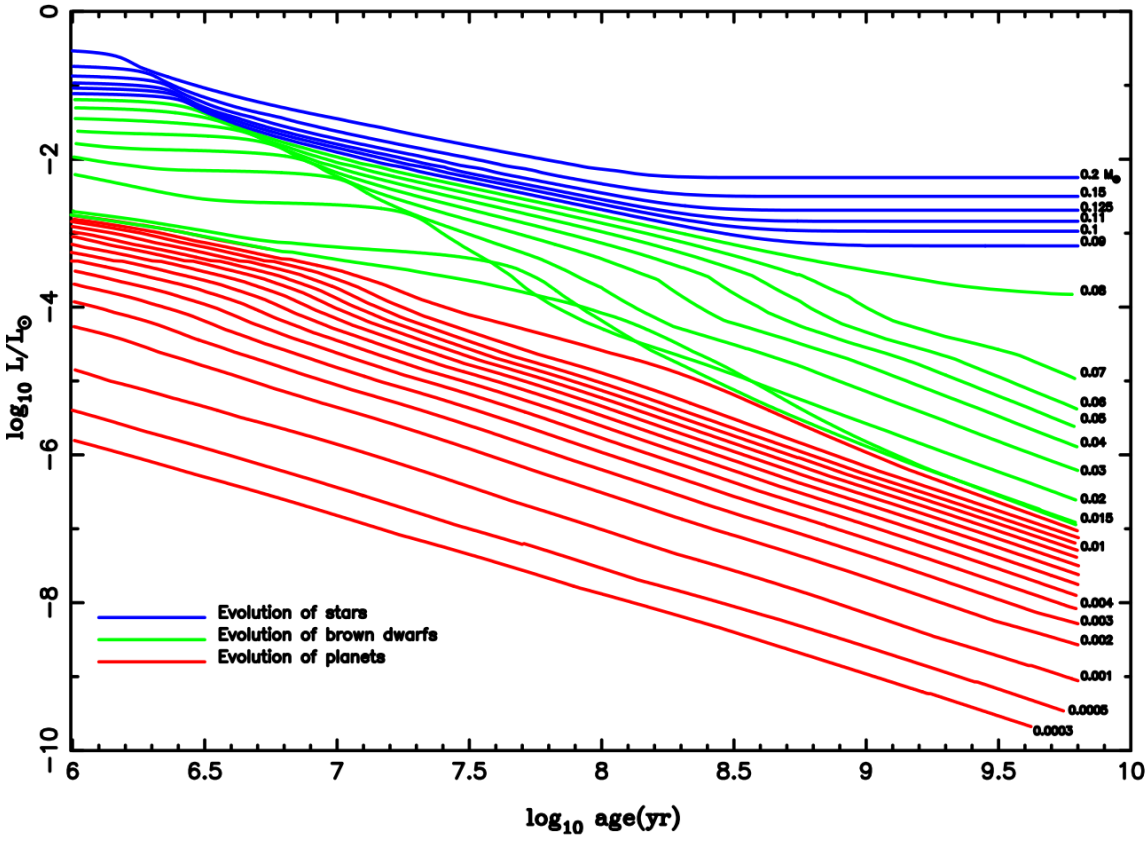

Figure 1.29: Figure taken from Burrows et al. (1997). Evolution of the luminosity of sub-stellar objects in function of their age. The distinction of the planetary/brown dwarf/stellar regime is represented by red/green/blue colors. The mass is labeled in the right edge of each evolutionary track.

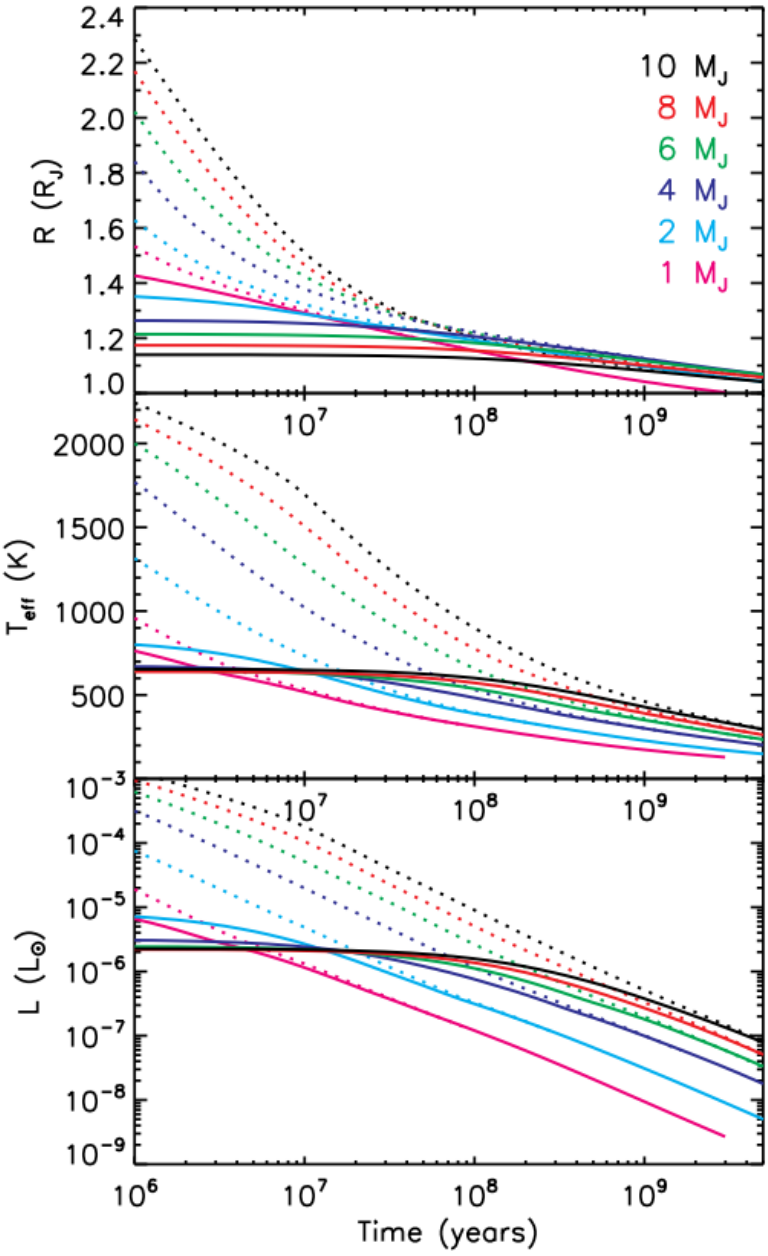

Figure 1.30: Figure taken from Marley et al. (2007). Evolution of the parameters of radius, R, temperature, T_{eff}, and luminosity, L, for planets with different masses. "Hot-start" models are represented in dotted lines. The parameters for the two models converge for older ages. The moment when the planet looses the information on its birth depends on its mass.

Chapter 2

NACO & SPHERE

The high-contrast imaging technique permits the direct detection of the exoplanets, masking the light of the primary star with a coronagraph. Up to date, many new planet hunter instruments are at disposal of the astronomic community to detect objects by direct imaging: SPHERE, GPI, ScEXAO, Project 1640, NACO (Beuzit et al. 2008; Macintosh et al. 2014b; Martinache & Guyon 2009; Hinkley et al. 2011b; Chauvin 2010). I present in this Chapter two powerful instruments dedicated to the research of exoplanets by direct imaging: the NAOS-CONICA (NACO) and the Spectro-Polarimeter for High-contrast Exoplanets Research (SPHERE). Both of them are installed at the Very Large Telescope (VLT) in Paranal, Chile. They have different possibilities of observation and capabilities. NACO is still very competitive and continues the observations as it has a wider FOV and it is equipped with a detector sensitive to longer wavelengths and with filters that are not present in SPHERE. Also, it permitted the use of the laser guide star.

2.1 NACO

NACO is short for NAOS-CONICA. It was installed at the Nasmyth B focus of UT4 (Unity Telescope number 4) of the VLT from 2001 through 2013. It is currently on UT1 at the Nasmyth A. NACO is an imager and spectrograph equipped with an adaptive optics (AO) system that performs coronagraphic imaging, imaging polarimetry, and spectroscopy in the range $1 - 5\ \mu$m.

The Nasmyth Adaptive Optics System (NAOS), is equipped with both visible and infrared wavefront sensors. The deformable mirror contains 14×14 actuators. It is based on the Shack-Hartmann wavefront sensor. The magnitude limits for the guide stars are $V = 16.7$ and $K = 12$. It contains 5 dichroics which split the light from the telescope between the COudé Near-Infrared CAmera (CONICA) and one of the NAOS wavefront sensors.

The corrected beam enters CONICA, the infrared camera and spectrograph. It contains different coronagraphic masks, filters, grisms, and polarizing elements. The detector has a size of 1024×1024 pixels and the maximum FOV is $56'' \times 56''$.

CONICA is equipped with J, H, K_s, L', and M' broad band filters, plus 12 narrow band filters. With respect to SPHERE, NACO offers the possibility to observe at longer wavelengths, the L', and M' bands which are not available on SPHERE. On the other hand SPHERE, differently from NACO, has the possibility to observe in visible light as described in the next Section.

Further information can be found in Lenzen et al. (2003) and Rousset et al. (2003).

A plot with examples of the contrast limits achievable with NACO is shown in Fig. 2.1. The contrast begins to drop down considerably for separations greater then $1''$. In the best of the cases the contrast reached is about 3×10^{-6}, while in the worst it is 5×10^{-4}. After $2''$ of separation, the curve remains constant and in the best case we are able to get a contrast of 10^{-6}.

NACO was exploited to perform several surveys aimed to image exoplanets: among them we cite the NACO-Large Program (NACO-LP*; Chauvin 2010). The results of this survey are presented in Desidera et al. (2014) and Chauvin et al. (2015). A case of false positive, a white dwarf around HD 8049, is presented in Chapter 3. The survey, which was conducted around 86 young solar-type stars, did not provide any new discovery of planetary companions. The non-detection constrained the occurrence of planets more massive than 5 M_{Jup} to less than 15% between 100 and 300 AU, and less than 10% between 50 and 300 AU for exoplanets more massive than 10 M_{Jup} (Chauvin et al. 2015).

Other important surveys are: a Search for Hot Massive Extrasolar Planets around Nearby Young Stars (Masciadri et al. 2005), a high contrast survey for extrasolar giant planets with the Simultaneous Differential Imager (Biller 2007), the International Deep Planet Survey (Vigan et al. 2012a), and a survey of young, nearby, and dusty stars conducted to understand the formation of wide-orbit giant planets (Rameau et al. 2013b).

2.2 SPHERE: a new planet hunter for the VLT

The new planet-finder instrument at VLT in Chile, SPHERE, had its first light during the spring 2014. The principal goal of the instrument is to find and characterize giant, gaseous, long-period planets within the solar neighborhood. As atmospheric models predict, young

*ESO program 184.C-0567, PI J.-L. Beuzit, "Probing the Occurrence of Exoplanets and Brown Dwarfs at Wide Orbits".

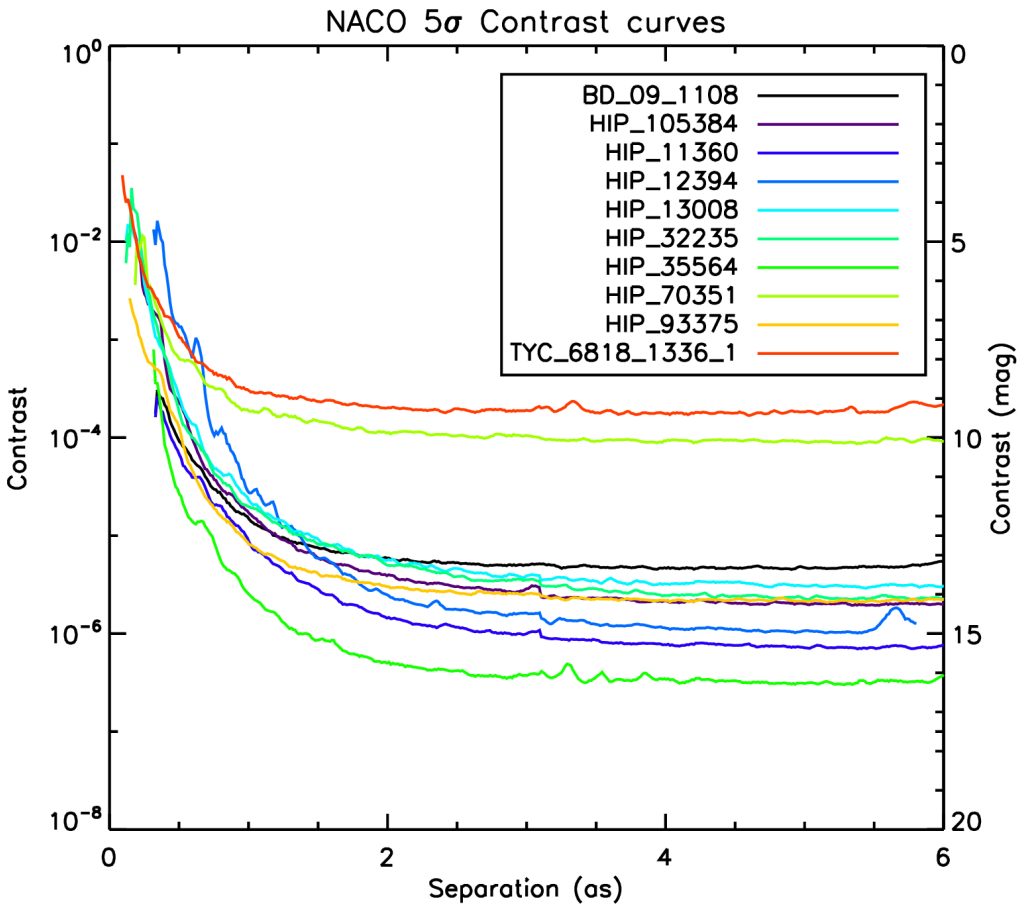

Figure 2.1: Some examples of contrast curves, including the worst and the best, of deep ADI observations with NACO. The names of each targets are labeled in the legend. Contrast values for NACO targets kindly given by A. Vigan.

planets are hot and self-luminous in the IR, making their direct detection possible in favorable cases by masking the primary star with a coronagraph (see Sec. 1.4). Evolved systems can also be detected in visible light through their reflected polarized light. From the ground, ExAO systems are required to correct for the atmospheric turbulence at very high frequency.

SPHERE is composed of the following subsystems, as shown in Fig. 2.3:

- an ExAO system called SAXO (SPHERE AO for eXoplanet Observation, Petit et al. 2012) that produces a highly stabilized beam with a SR of more than 90% (see Fig. 2.2);
- the Common Path and Infrastructure (CPI) that brings the telescope light to the three scientific modules. The CPI contains the DM, relay optics such as toric mirrors (Hugot et al. 2012), derotator, atmospheric dispersion compensators, ALC and 4QPM coronagraphs (Dohlen et al. 2011);
- the three science subsystems working in the visible or the near-infrared. The Infra-Red Dual-beam Imager and Spectrograph (IRDIS, Dohlen et al. 2008a) and the Integral Field Spectrograph (IFS, Claudi et al. 2008a) can operate in parallel on infrared light in the range 0.95–2.32 μm, while the Zurich IMager POLarimeter (ZIMPOL, Thalmann et al. 2008) operates in the visible (0.60–0.90 μm). The three instruments cannot all work at the same time.

Representations of IRDIS, IFS, and ZIMPOL are shown in Fig. 2.4, 2.5, and 2.6 respectively.

2.2.1 IRDIS

IRDIS allows for a wide range of observing modes, including:

- dual-band imaging (DBI),
- long-slit spectroscopy (LSS),
- classical imaging (CI), and
- dual-polarimetric imaging (DPI).

IRDIS FOV is $12\farcs5 \times 11''$, with a pixel scale of $12\farcs25$/px. There is a selection of 12 filters available for imaging, in broad-, medium- or narrow-band, and five different filter

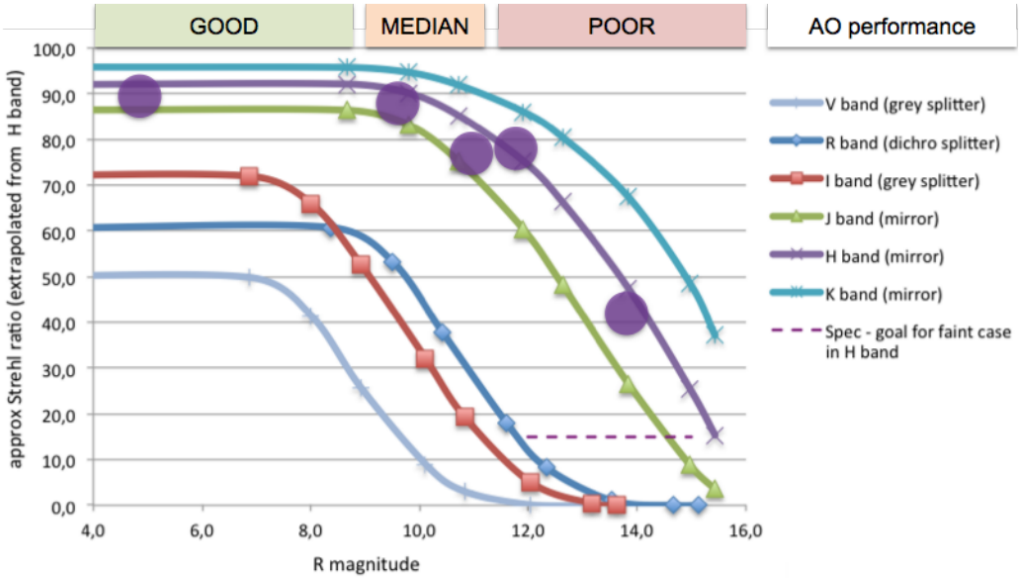

Figure 2.2: Expected Strehl Ratio, extrapolated from *H*-band values, as a function of the *R* magnitude value of the guide star. The purple circles represent measured values from commissioning. Picture taken from the SPHERE User manual.

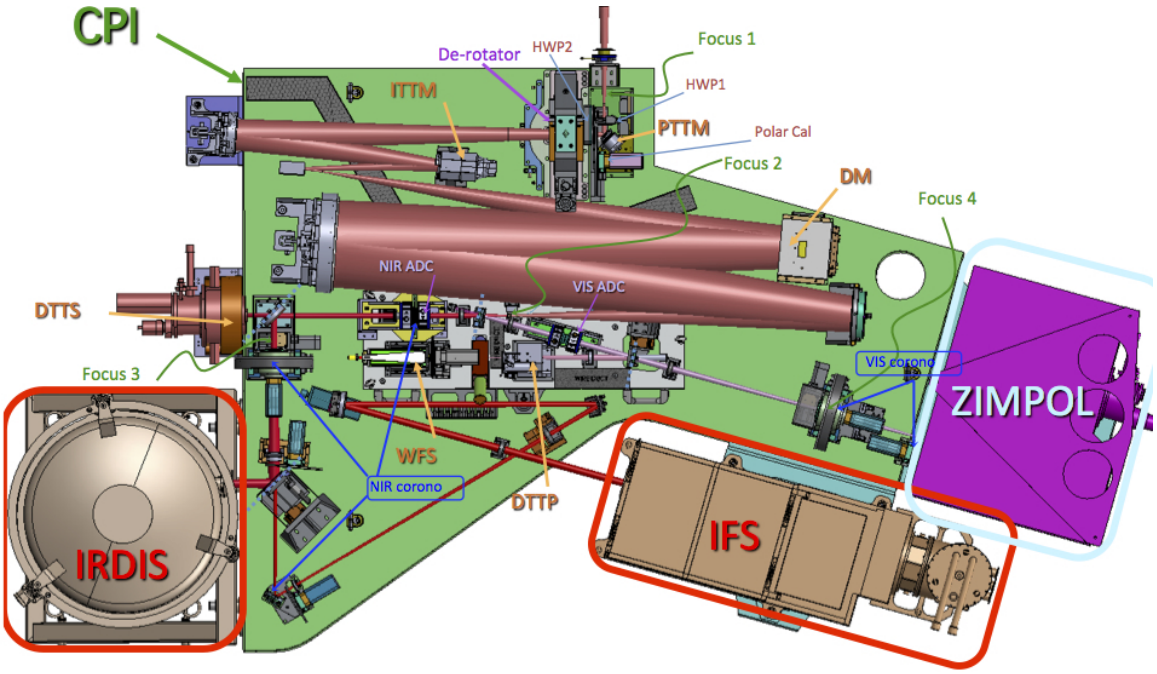

Figure 2.3: Schematic representation of the SPHERE with its 3 subsystems and the CPI.

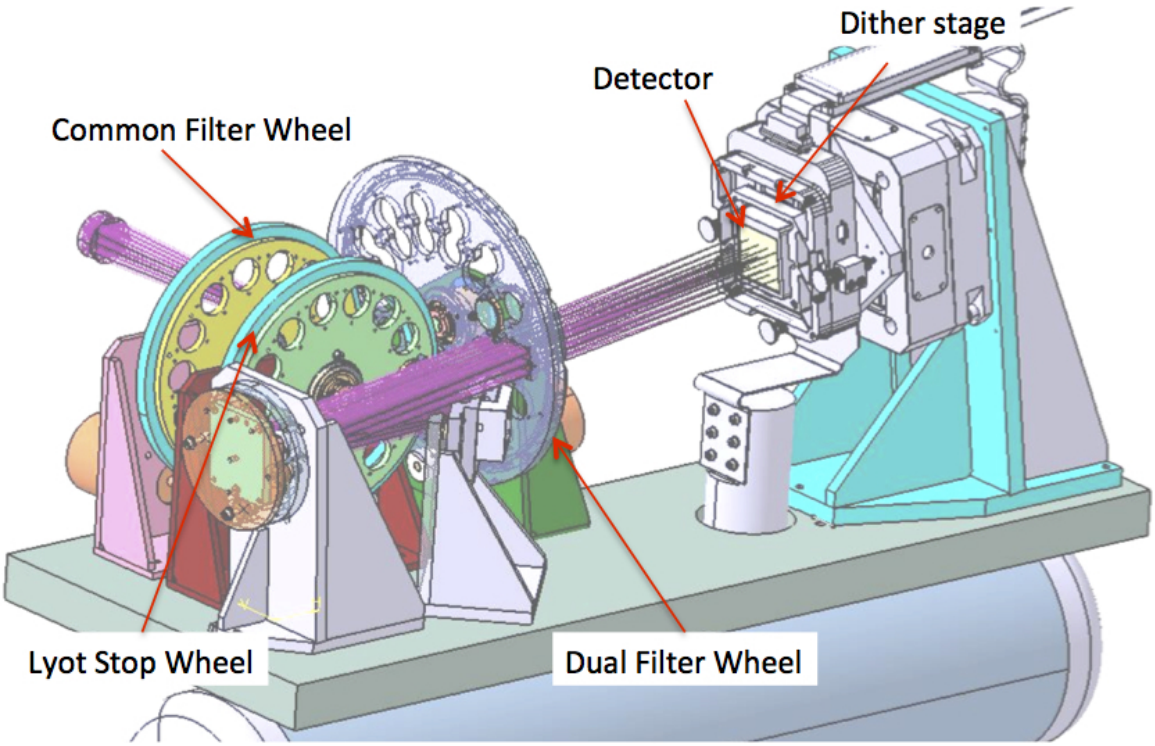

Figure 2.4: Schematic representation of the SPHERE subsystem IRDIS.

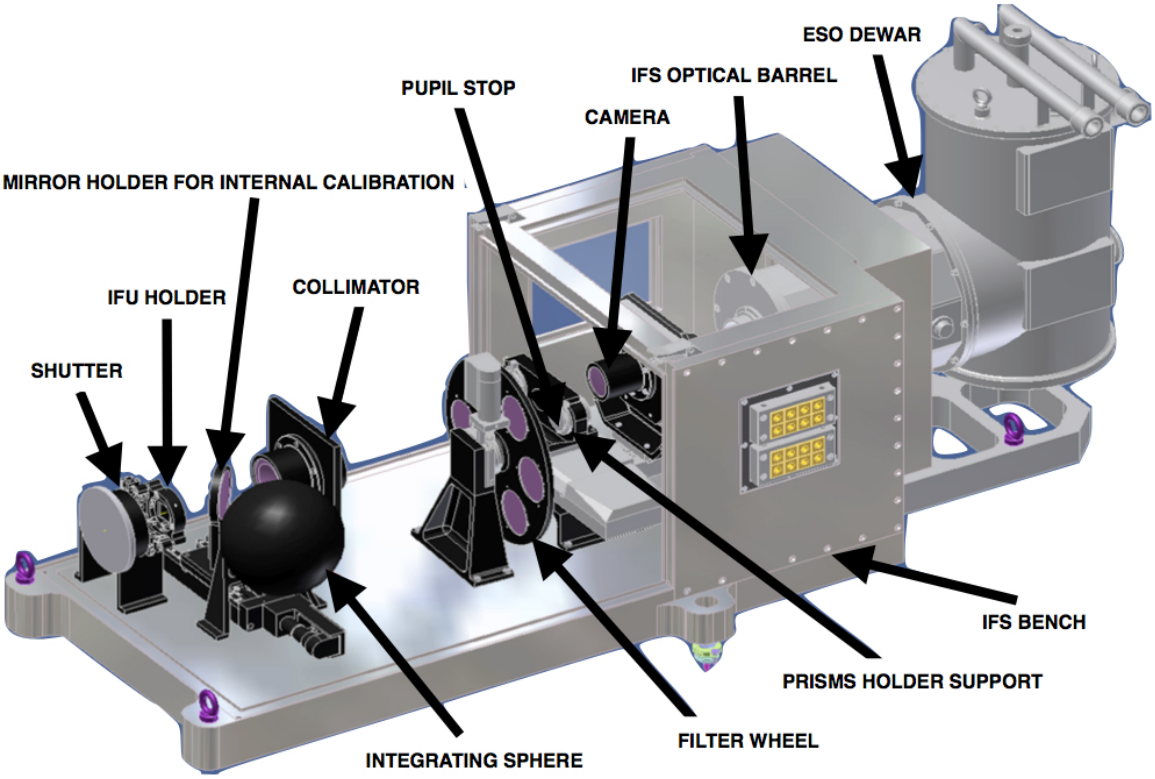

Figure 2.5: Schematic representation of the SPHERE subsystem IFS.

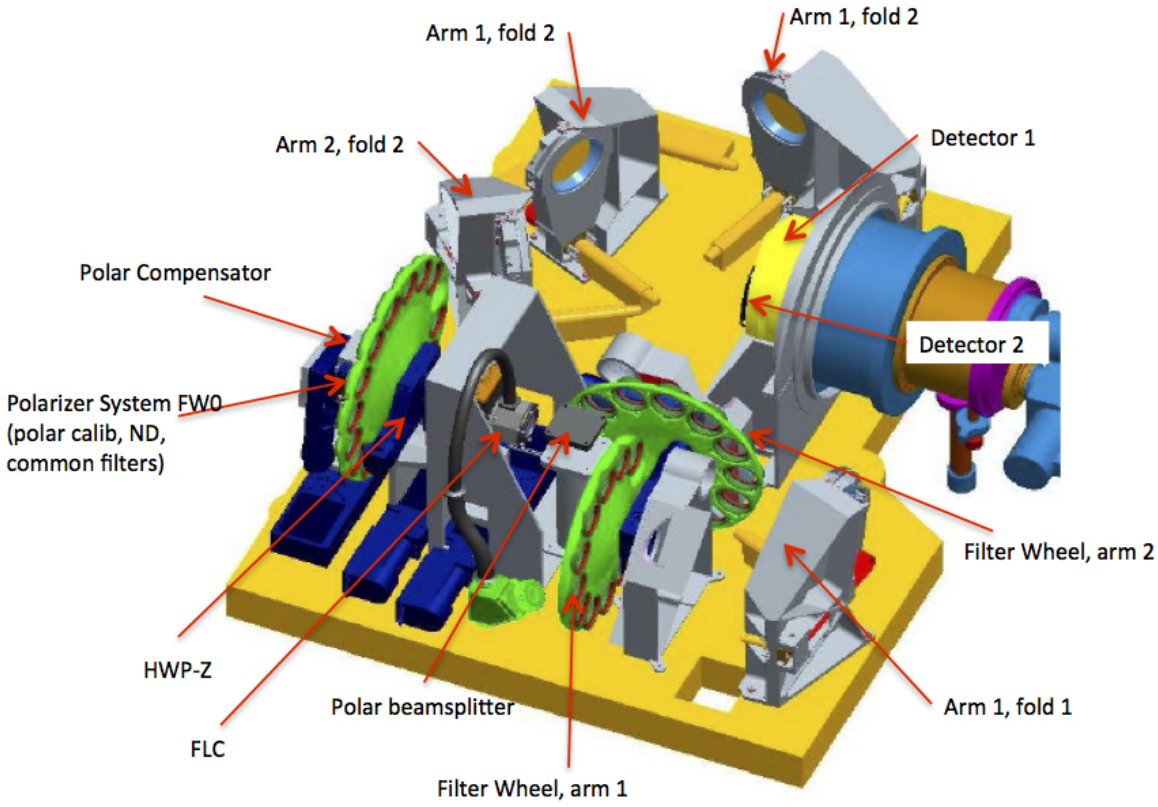

Figure 2.6: Schematic representation of the SPHERE subsystem ZIMPOL.

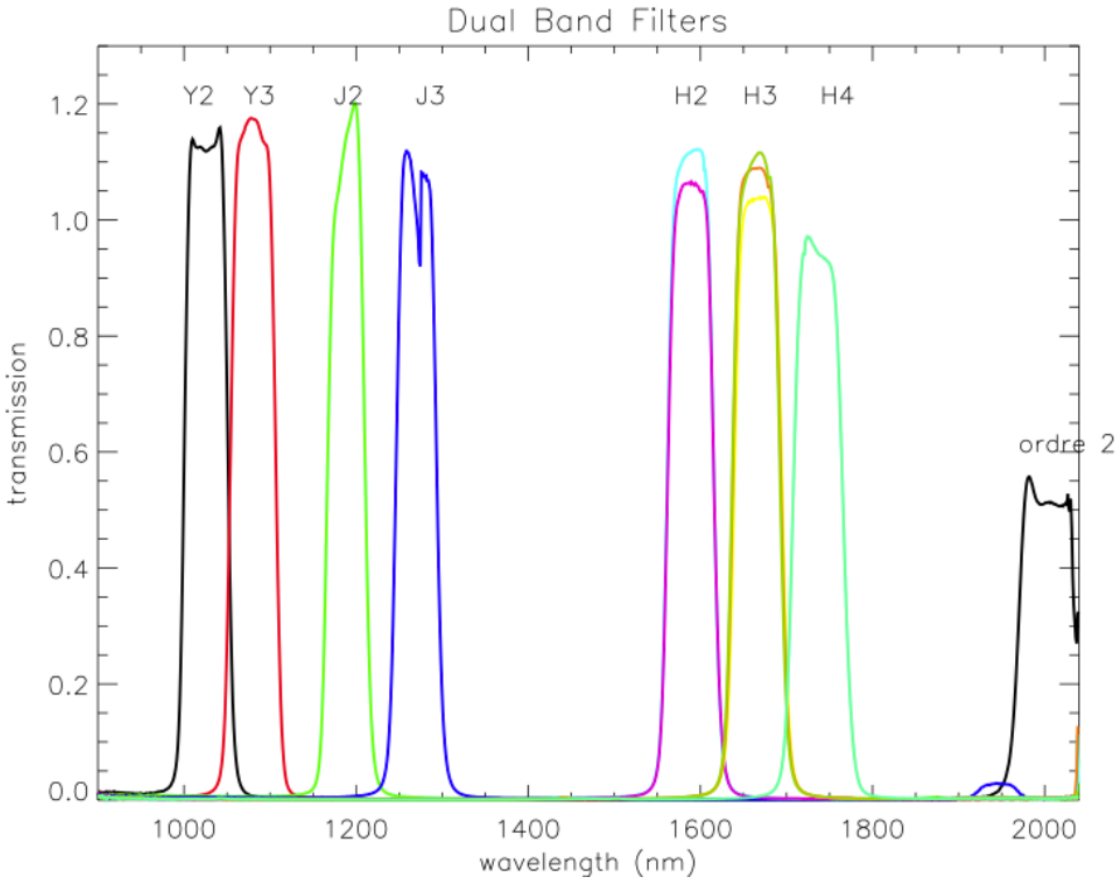

Figure 2.7: Transmission curves of the IRDIS dual-band filters.

pairs are dedicated to the DBI mode. IRDIS dual-band filters transmission curves are shown in Fig. 2.7.

The LSS mode with resolving powers of $\sim$ 50 and $\sim$ 350 is coupled to simple Lyot coronagraphy for the characterization of detected companions (Vigan et al. 2008). The CI and DPI observing modes can also be used for the study of extended objects such as disks. The differential aberrations are less than 10 nm between the two channels, for this reason IRDIS is a powerful instrument to perform high contrast differential imaging (see Sec. 1.2.3.1).

An example of IRDIS raw image is shown in Fig. 2.8. The speckle pattern extends from the center of the coronagraph, where there is a concentration of brighter speckles, which are corrected till the OWA. In the case of SPHERE, the OWA $\sim 20\ \lambda/D$ (see Sec. 1.2).

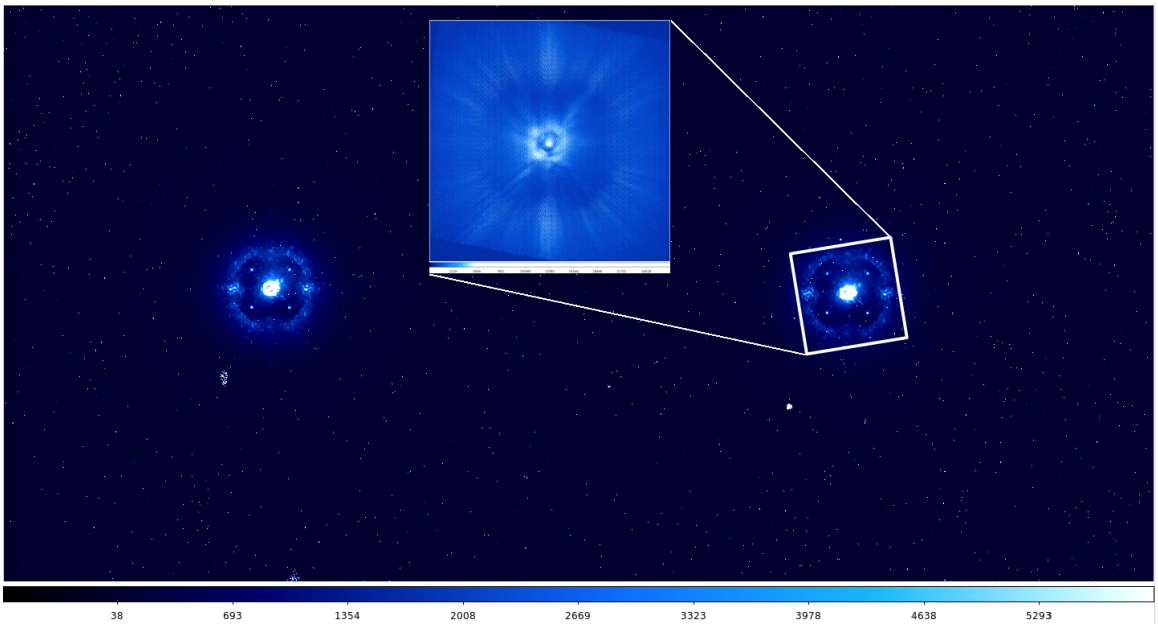

Figure 2.8: IRDIS and IFS raw images. The four satellite spots used for the fine centering of the image are also shown. In the detector there is a dual-band $H2H3$ coronagraphic image. The IFS FOV is represented, on the detector is divided in thousands of tiny spectra, the light is dispersed along the vertical direction.

2.2.2 IFS

The subsystem IFS is an integral field spectrograph with a lenslet-based integral field unit (BIGRE, Antichi et al. 2009). It allows for two spectral ranges (Claudi et al. 2008a):

- YJ-mode (0.95 – 1.35 μm) with a two-pixels resolving power of $\sim$ 50;

Table 2.1: Technical description of the subsystems IRDIS and IFS, the IRDIFS and IRDIFS_EXT modes.

	IRDIS	IFS
FOV[a]	12.″5×11.″0	1.″77×1.″77
Pixel scale	12.25 mas/px	7.46 mas/px[b]
Spectral range	0.95–2.32 μm	0.95–1.65 μm
Channels	2	39
IRDIFS mode	$H2H3$[c]	YJ
IRDIFS_EXT	$K1K2$[d]	YJH

[a]Field of view
[b]After the pipeline resampling
[c]λ_{H2} = 1.59 μm, λ_{H3} = 1.66 μm
[d]λ_{K1} = 2.10 μm, λ_{K2} = 2.24 μm

- YJH-mode (0.95 – 1.65 μm) with a two-pixels resolving power of ~ 30;

IFS FOV is smaller than IRDIS one: 1.″77 × 1.″77, with a pixel scale of 7.″46/px. The IFS is aimed to explore the inner regions of planetary systems. Its 39 spectral channels enable a better speckle subtraction, allowing us to reach contrasts about 10^{-6} at small angular separation. An example of IFS raw image, where the tiny spectra are visible, is shown in Fig. 2.8.

To allow for a parallel operation of the two NIR instruments, the light entering the telescope is split in two beams downstream of the coronagraphic mask, each instrument having its own set of Lyot stops. Two dichroic plates are available to allow for two different observing modes: IRDIFS mode, where IRDIS performs DBI observations in H band, while IFS works in YJ mode; and IRDIFS_EXT mode, where IRDIS performs DBI in $K1K2$ band, and IFS observes in YJH mode (Beuzit et al. 2006). A general description of the two modes is found in Table 2.1. It is expected that the IRDIFS mode will be predominantly used during the giant planets survey, to exploit the IRDIS DBI on the methane absorption bands. For this reason, we aim to present results obtained exploiting this particular observing mode (Chapters 4 and 6).

2.2.3 ZIMPOL

ZIMPOL is designed as high contrast imaging polarimeter with very high polarimetric sensitivity for the visual range. It has a small FOV (3.″5×3.″5) and a limited absolute polarimetric accuracy (0.5 %) due to the fact that it is a Nasmyth focus instrument. The relative polarization is measured with respect to the host star, assumed as a zero-polarization reference. This instrument is strongly affected by the seeing, and to obviate this fact we perform

differential measurements with fast (kHz) polarization modulation. The great innovation introduced in ZIMPOL is that the polarisation is switching with each polarisation being recorded on alternative columns (or rows) of the CCDs. The two arms of ZIMPOL are independent: while one is used for the polarization analysis, the second can perform polarimetry with the same or with different filters. Each one can provide a full polarimetric measurement. Also, ZIMPOL will permit to perform classical imaging in visible light, with narrow- and broad-band filters. An example of ZIMPOL raw image, where the jets of R Acq are visible, is shown in Fig. 2.9.

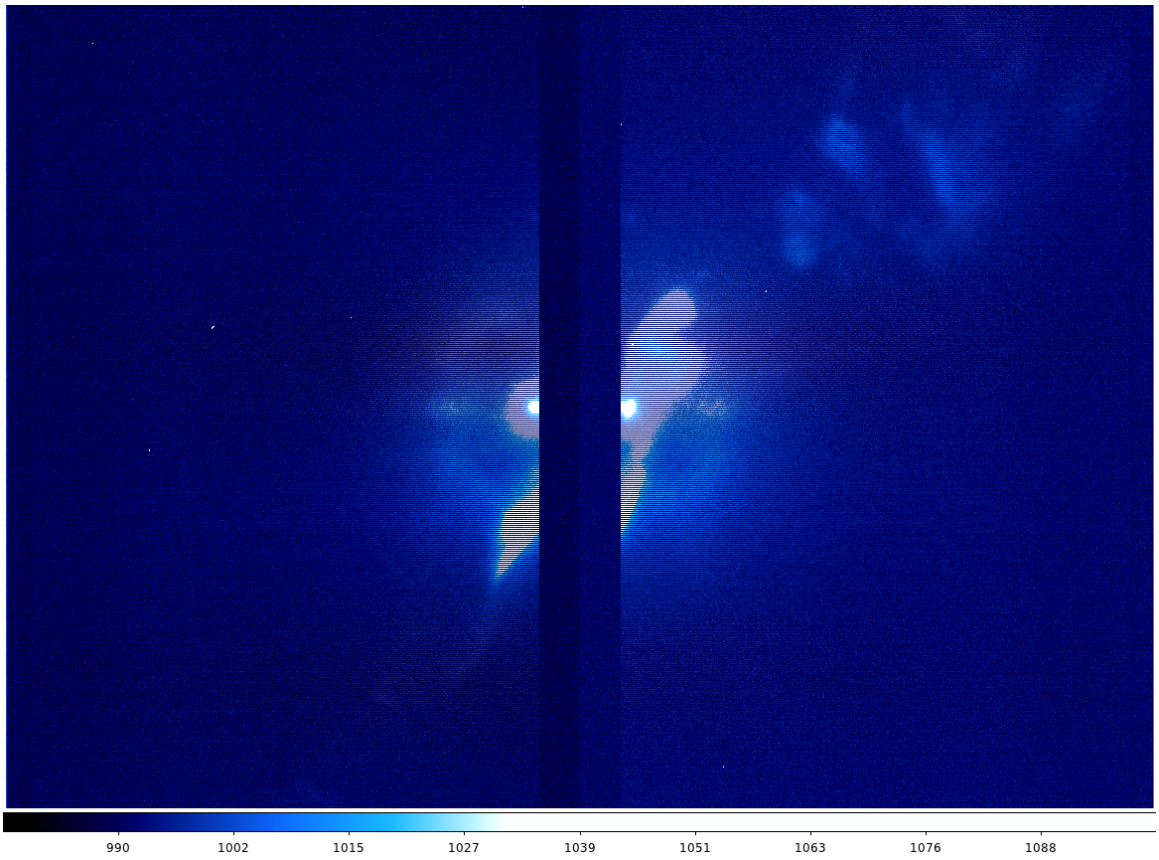

Figure 2.9: ZIMPOL raw image. The object seen on the detector is R Acq.

The performance and capability of SPHERE are discussed in more details in Chapters 5 and 4.

2.2.4 Comparison with NACO

We present in this Section a comparison between the instruments NACO and SPHERE. Table 2.2 shows the technical description of the two instruments, while in Fig. 2.10 is

shown the achievable contrast of NACO and SPHERE in H-band, underlining the progress made with the new generation instrument SPHERE.

The AO system of SPHERE is equipped with a DM with 41×41 actuators, where NACO has 14×14. As the gain in SR is substantial, the performance of the AO system of SPHERE are not comparable to the one of NACO, and the contrast achievable is indeed very different. At a separation of $0''.5$ the contrast of SPHERE is ~ 100 times better. On the other hand, NACO has a larger FOV and can explore more extended objects/systems.

Table 2.2: Table of comparison between the two instruments NACO and SPHERE.

	NACO	SPHERE
Number of actuators	14×14	41×41
Best SR (K_S-band)	50%	96%
Spectral range	1.0–5.00 μm	0.50–2.32 μm
Maximum FOV	$56'' \times 56''$	$12''.5 \times 11''.0$
Best contrast at $0''.5$	12 H-band mag	15.5 H-band mag
Observing modes	Imaging, LSS, Polarimetry	Imaging, LSS, Polarimetry, IFS

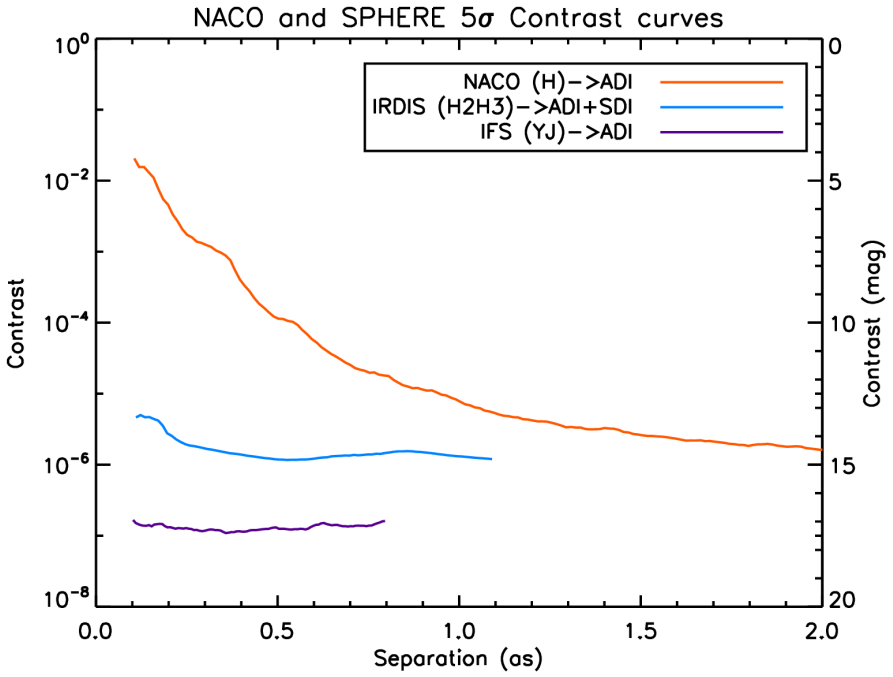

Figure 2.10: Contrast achievable with NACO and SPHERE. The curve of NACO is the best contrast obtained with deep ADI observations. Values for SPHERE/IRDIS and SPHERE/IFS are related to one observation during the commissioning.

2.3 Objectives of the thesis

As we saw in these first Chapters, DI technique is a powerful instrument that permits the study of the external zone of planetary systems. Thanks to the current generation of instruments, we are capable of distinguish photons from companions 10^6 times fainter than their host stars. The advantages of this method are numerous and the information that we will collect in the incoming years is extremely important for our knowledge on exoplanets. DI is the unique technique that explores planets at wide orbits (> 10 AU), which is fundamental to span all the separations of planetary systems. Also, it is the only technique sensitive to massive stars, that cannot be studied by the other techniques.

This technique is capable of retrieving all the orbital parameters of companions, including the inclination. This fact is fundamental to study the formation of planets via the mutual inclinations between disk/planets or the relative inclinations in a multi-planetary system. If planets are generally co-planar, it probably means that they have formed in a disk. Imaging planets embedded in their disk will be of great help in understanding formation mechanisms.

DI is the only technique that can permit to retrieve spectra from planets which are not strongly irradiated from the host star. The spectra extracted will tell us the chemical composition of planets atmospheres, the abundances and the presence of dust, and even the surface gravity of the planets can be retrieved. Having empirical spectra of planets will help us improving our models and understanding if planets presents similarities in between them and with the planets of our Solar system. Finally, the study of the variability of their luminosity tells us about the presence of clouds and dust in the upper layers of the atmosphere.

Nevertheless, DI presents difficulties that we have to be aware of. The presence of the diffracted light of the primary star, and the speckle pattern, limits the detection of companions fainter that $\sim 10^6$ times the host star, with the current instrumentation. This means that today we are capable of studying Jupiter like planets, even if in the next future instrumentation might provide an upgrade in sensitivity till detecting Earth like planets.

The self-luminosity of a planet is dependent with its age, as in the first stages of its life a planet is hot and luminous, then it starts to cool down rapidly. This fact implies that DI is more sensitive to young targets, and it is a limitation to find exoplanets around old stars.

The estimate of the mass of a companion is dependent with the evolutionary model we choose, so it is not straightforward to give a value to it. Also, the estimation of the age of the system is fundamental to avoid an incorrect value of the mass of the companion, and falling into false positives.

The objective of this thesis is to characterize planetary companions with DI, in particular exploiting the instrument SPHERE. First, I understood the important lesson given by the NACO-LP survey: if we want to characterize a companion, we first have to deal with its parent star. Knowing the characteristics of the host star is essential to understand the nature of the system. For the NACO-LP it happened that a target labeled as a young star, turned out to be an older object. Discrepancies on the ages indicators made us suspect about an incorrect estimate on the age of the star, and indeed the companion detected by NACO was a white dwarf which accelerated the rotation of the parent, rejuvenating it. This lesson will be useful for next DI surveys, where targets will be carefully studied to give a correct estimation on the mass of the companion and avoid false positives.

During the SPHERE GTO, a survey dedicated to the research of exoplanets will be performed: The Near-Infrared Survey for Exoplanets (NIRSUR). The survey will target 400 to 600 young stars in the solar neighborhood during 200 nights of observations. During my thesis, which has mostly developed before the starting of this survey, I tried to test the capabilities of the instrument and foreseen how NIRSUR will contribute to the knowledge on exoplanets.

During most of the time of my thesis, the instrument SPHERE was located in the Grenoble laboratory, before the shipping to the VLT at Paranal. A long experience of observations in the laboratory, both for IRDIS and IFS side, gave me ideas to future proposals and reduction methods. During this period, I conducted a study on the expected photometry and astrometry accuracy for the IRDIFS mode: I injected in the laboratory data synthetic planets at different separations and position angles and measured the differences between the input and measured values. I tried to improve the SDI technique, as in the laboratory the ADI could not be performed because of limitations of the telescope simulator. This work, presented in Chapter 4, showed us what we are capable in term of spectrophotometric and astrometric accuracy. I took advantage of the simulations to test new techniques of suppressing the speckle pattern which I am currently using to reduce data and that were applied to obtained all the results presented in this thesis.

Having in mind the performance of SPHERE, I proposed a challenging group of targets that will be observed during NIRSUR: the RV targets. With a Monte Carlo simulation I selected the RV long period planets which are observable with SPHERE (see Chapter 5). All these targets could give us information in both cases of detection or non-detection. If the object is not found, an upper limit to its mass can be given, if the object is detected, we will have the predicted and the dynamical mass of the object. This will be a great advantage to prove the goodness of evolutionary models.

Finally, during the last months of my thesis, SPHERE begun to operate in Paranal. First on-sky data arrived, and the results are, as expected, very impressive. I obtained results on the system around HR 8799 (presented in Chapter 6), and I had the opportunity of studying planetary objects with such a powerful instrument as SPHERE. This was the perfect opportunity to test my routines on real data, to prove my estimations on the instrument capabilities and to deal with models of planetary atmosphere. The objective of the thesis has been achieved.

Chapter 3

False alarms in direct imaging surveys

[*] In the search for extrasolar planets, we are frequently faced with objects or physical phenomena that mimick the signature of a substellar object — the so-called astrophysical *false positives*. The most commonly used techniques in the search for exoplanets are the radial velocity, transit, TTV (transit timing variation), microlensing, and direct-imaging techniques. A large portion of the planets discovered so far has been detected through the radial velocity technique. Rotational modulations of star spots and magnetic activity cycles may produce spurious periodic radial velocity signals that mimic planet signatures (see e.g. Queloz et al. 2001; Lovis et al. 2011). A number of controversial cases have been reported in the literature (e.g. Setiawan et al. 2008; Huélamo et al. 2008; Hernán-Obispo et al. 2010; Figueira et al. 2010). Simultaneous monitoring of activity indicators, spectral line profile changes, and photometric variations may allow one to recognize the true origin of the radial velocity variations and to at least partially account for them (see e.g. Boisse et al. 2011; Lanza et al. 2010; Dumusque et al. 2012).

Transit searches are even more heavily plagued by false positives. Various kinds of eclipsing binaries can mimick a transiting planet's photometric curve. Such false positives can often outnumber the true exoplanet detections (Brown 2003). The phenomenon of blended eclipsing binaries is the most severe, as described in O'Donovan et al. (2006). To help mitigate these adverse effects, various observational diagnostics, based on the photometric light curves or on additional spectroscopic or photometric observations, have been developed. Statistical tools can also be exploited to explore all possible scenarios of binary systems and the probability of their occurrence (e.g. BLENDER code, PASTIS code; Torres et al. 2011; Díaz et al. 2014).

Timing variations in eclipsing binaries can be signatures of circumbinary planets, but alternative explanations cannot be firmly ruled out (Zorotovic & Schreiber 2012). A recent

[*] An adapted version of this work has been published in Zurlo et al. (2013).

case of TTVs induced by stellar activity (star spot features modulating the brightness of the host) instead of the gravitational influence of a planet is described in Barros et al. (2013). Finally, a case of a possible microlensing planet-detection was recently revealed to be a false positive, resulting from the variability of the lensed star (Gould et al. 2012).

Concerning the direct imaging technique, the subject of this work, it may occur that the detected candidate companion is not gravitationally bound to the host star. Detection of unbound objects is frequent since direct-imaging surveys typically have better sensitivities to planets far from the host star, where a higher contrast can be reached (see e.g. Chauvin et al. 2010; Vigan et al. 2012b). If the follow-up observation is close in time to the first epoch and the displacement of the star on the sky due to proper motion is small, it may be challenging to determine with a high probability whether an object is bound. One example is given in Metchev & Hillenbrand (2009), where an object that was originally thought to be compatible with being bound, based on the proper motion test, was determined through spectroscopy to be a background M-star. Moreover, the case of the false positive object around IM Lupi (Mawet et al. 2012) teaches that, when the distance determination is complex, it is possible to miscalculate the relative certainties of a bound versus unbound interpretation. Secondly, even after a candidate companion is shown to be bound, the system might prove to be a stellar binary, which is the case of the object of our study.

Finally, to meaningfully characterize the companion, the system age must be accurately determined, because the luminosity of substellar objects depends strongly on the age of the system (younger age corresponds to a brighter companion magnitude, see e.g. Baraffe et al. 2003b; Madhusudhan et al. 2011a); spurious young stars might therefore lead to poorly classified companions.

3.1 The case of HD 8049

I present the case of such a spurious young star, along with an originally misidentified substellar candidate, found in the NACO-LP.

The object of our study, HD 8049, was observed in July 2010. The target is a solar neighborhood K2-star, with a distance of 33.6 pc.

A promising exoplanet candidate was detected around the target. Its contrast of ΔH = 7.05 at 1.57 arcsec allowed us to assume a 35 M_{Jup} companion at 50 projected AU, for the nominal system age and heliocentric distance. To check whether it was gravitationally bound to the host star, as opposed to an unrelated background object, we re-observed the system one year later and concluded a high probability of a bound system. We also used radial velocity measurements of the host star, spanning a time range of $\sim$ 30 yr, to constrain

the companion's mass and orbital properties, as well as to probe the host star's spectral age indicators and general spectral energy distribution. We also obtained U-band imaging with EFOSC and *NIR* spectroscopy for the companion.

However, combining all these information we conclude that the companion of HD 8049 is a white dwarf (WD) with temperature $T_{\rm eff}$ = 18800 ± 2100 K and mass $M_{\rm WD}$ = 0.56 ± 0.08 $M_{\odot}$. The significant radial velocity trend combined with the imaging data indicates that the most probable orbit has a semi-major axis of about 50 AU. The discrepancy between the age indicators speaks against a *bona-fide* young star. The moderately high level of chromospheric activity and fast rotation, mimicking the properties of a young star, might be induced by the exchange of mass with the progenitor of the WD. This example demonstrates some of the challenges in determining accurate age estimates and identifications of faint companions.

The case is similar to that of the object orbiting Gliese 86 (see Mugrauer & Neuhäuser 2005), initially considered a brown dwarf in Els et al. (2001). Other cases of close WD companions around HD 147513 and HD 27442 are described in Porto de Mello & da Silva (1997) and Chauvin et al. (2007), respectively.

Sometimes, as in the case presented here, a false positive turns out to be an interesting object: among the known nearby WD this target is one of the hottest. Because it is part of a close binary system, it yields insights into how these types of objects interact with their companions.

3.2 Observations and data reduction

HD 8049 was observed with several instruments and techniques. All data I collected for this analysis are listed in Table 6.1 along with the related instrumentation, date of observation, and technique.

3.2.1 NACO observations

HD 8049 was observed as part of the NACO Large Program (NACO-LP) imaging survey. We used the VLT/NACO (Lenzen et al. 2003; Rousset et al. 2003) high-contrast Adaptive Optics (AO) system with the H-band (1.33–1.99 μm) and the S13 camera, which provides a spatial sampling of ∼13 mas/pixel and a field of view (FoV) of $14'' \times 14''$. The target was observed in pupil-tracking mode to allow implementation of angular differential imaging (ADI, Marois et al. 2006b) data analysis techniques. The observing sequence consisted of a series of unsaturated images of the point spread function (PSF), which served as reference for differential photometry and astrometry, and a series of deep saturated exposures

Table 3.1: Summary table of the observations of HD 8049.

Instrument	Date	Type of Data
CORAVEL	June 14 UT, 1983	1 RV p.,V spectrum
	December 31 UT, 1983	1 RV p.,V spectrum
	November 30 UT, 1985	1 RV p.,V spectrum
CORALIE(98)	from December 26 UT, 2000	43 RV points
	to January 21 UT, 2007	
HARPS	September 15 UT, 2004	1 RV p.,V spectrum
CORALIE(07)	from July 3 UT, 2007	20 RV points
	to July 8 UT, 2012	
NACO	July 30 UT, 2010	H-band imaging
	July 28 UT, 2011	H-band imaging
EFOSC	December 21 UT, 2011	U-band imaging,
		V spectrum
SINFONI	August 28 UT, 2012	JHK spectra
GPI	November 16 UT, 2013	JH spectrum
	December 10 UT, 2013	HK spectrum

optimized for the detection of faint companions. Data reduction for saturated and unsaturated sequences followed standard procedures (flat-fielding, sky subtraction, bad-pixel correction). The saturated sequence was then analyzed with two methods: (1) the LOCI algorithm (Lafrenière et al. 2007) with the separation criterion $N_\delta = 0.75$ FWHM, and (2) a spatial filtering of all images in a 5×5 FWHM box followed by de-rotation and median-combination. Differential astrometry was performed using fitting of a 2D Gaussian profile on the primary star and on the point sources detected in the reduced images.

The target was first observed on July 30 UT, 2010. A faint point source (hereafter HD 8049 B) at a separation of $\rho = 1.566 \pm 0.006$ ″ and with a position angle of $\theta = 118.4 \pm 0.2$ deg was detected with a magnitude difference $\Delta H = 7.1 \pm 0.1$ mag (see Figure 3.1). Follow-up observations on July 28 UT, 2011 revealed that the point source was co-moving with the primary. Thanks to the high proper motion of the central star ($\mu_\alpha = 65.99 \pm 1.18$ mas/yr and $\mu_\delta = -240.99 \pm 0.98$ mas/yr), a χ^2 probability test on $\Delta\alpha$ and $\Delta\delta$ with respect to the star at two epochs rejected the possibility (at 99% certainty) that the object was a background source. The measured contrast, along with our original age estimate and the measured astrometry, led us to conclude that this was a 35 M_{Jup} companion at 50 AU projected separation.

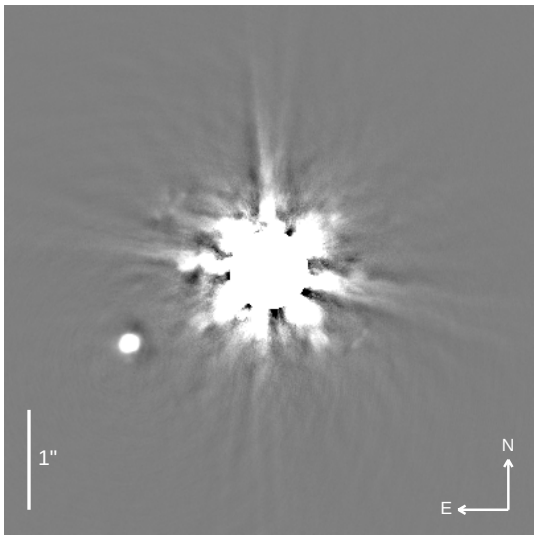

Figure 3.1: VLT/NACO, H-band image (1.65 μm) of the companion. The frame was generated from the median combination of processed images after spatial filtering ($5\times5\lambda/D$ box) and de-rotation. The central core of the PSF is saturated and has been masked in this image.

3.2.2 CORAVEL, CORALIE, and HARPS high-resolution spectroscopy

HD 8049 was observed as part of a long-term extra-solar planet search program begun in June 1998 with the CORALIE high-resolution fibre-fed echelle spectrograph mounted on the 1.2 m Euler Swiss telescope at La Silla (ESO, Chile). In addition to the CORALIE data, we obtained a spectrum with HARPS. Finally, we used the CORAVEL database (Baranne et al. 1996) and extracted three radial velocity (RV) observations with a 300 m/s precision (Baranne et al. 1996). This yielded a total time-span of nearly 29 years.

For these three instruments, radial velocities were computed by cross-correlating the observed stellar spectra with a binary mask, whose non-zero zones correspond to the theoretical positions and widths of stellar absorption lines at zero velocity. For HARPS and CORALIE, the instrumental velocity drifts were monitored and corrected for using the "simultaneous thorium referencing technique" with dual fibres (more details in Baranne et al. 1996), whereas for CORAVEL a standard radial velocity star (HD 168454) was used for calibration. Radial velocity points are shown in Figure 3.2. The trend in the radial velocity points is likely produced by the influence of an object more massive than a brown dwarf. Additionally, activity indicators (S index, $\log R_{\rm HK}$) and the projected rotational velocity were also measured on the CORALIE and HARPS spectra.

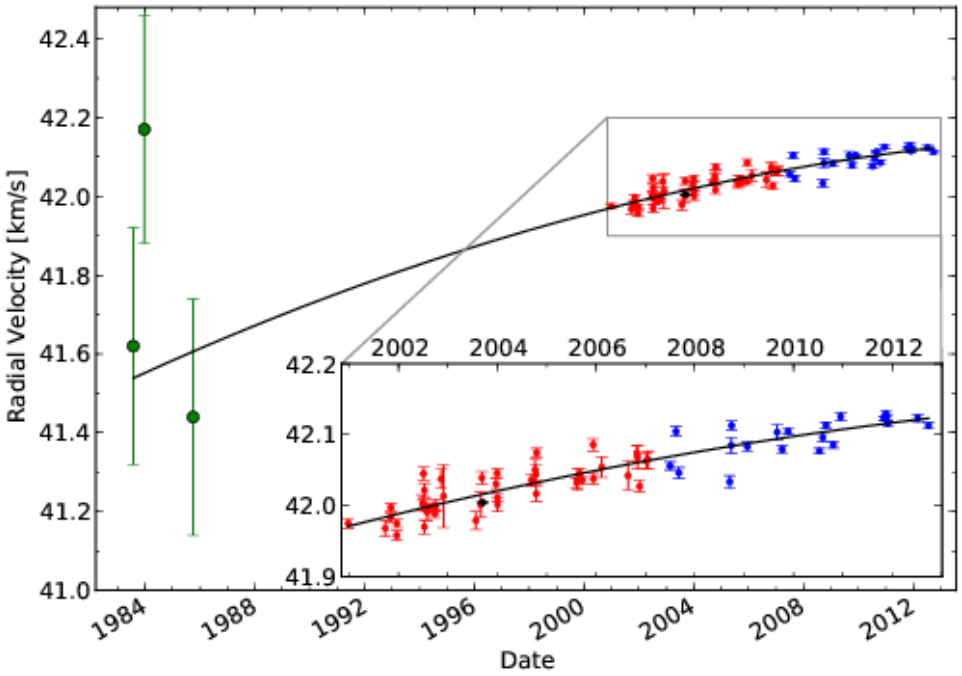

Figure 3.2: Radial velocity of the star measured with four instruments: CORAVEL (green), CORALIE98 (red), CORALIE07 (blue), and HARPS (black). The solid black line is a least-squares fit of a quadratic RV trend. While the drift information alone is consistent with either a BD or WD interpretation, the inclusion of the separation information, as gathered from NACO, allows us to rule out the BD possibility.

3.2.3 NTT/EFOSC

We obtained ten images of HD 8049 on December 21 UT, 2011, with EFOSC2 at the NTT (ESO, Chile). Each frame was taken with the Johnson U filter, a 0.2 s exposure to avoid saturation, 2×2 binning and seeing of 0.8″. I reduced the U-band images with standard IRAF* tasks. I fitted the two objects with Moffat profiles and performed aperture photometry on each star after subtracting contributed flux from the neighbor star. The resolved binary system had a magnitude difference of $\Delta U = 1.714 \pm 0.023$ mag, as shown in Figure 3.3. The difference was calculated taking into account the correction for the $U - B$ color index

*IRAF is distributed by the National Optical Astronomy Observatory, which is operated by the Association of Universities for Research in Astronomy (AURA) under cooperative agreement with the National Science Foundation.

of the two stars using equation (9) of the EFOSC2 manual[†]. I used for the K star the value listed in Table 15.7 of Allen (1977) and for the WD I considered the colors in the range of effective temperature, $T_{\rm eff}$, from 15000 K to 25000 K (see Sec 3.3.2). The measured values of the projected separation, $\rho = 1.56 \pm 0.02''$, and the position angle, $\theta = 118 \pm 0.5$ deg, were compatible with NACO measurements.

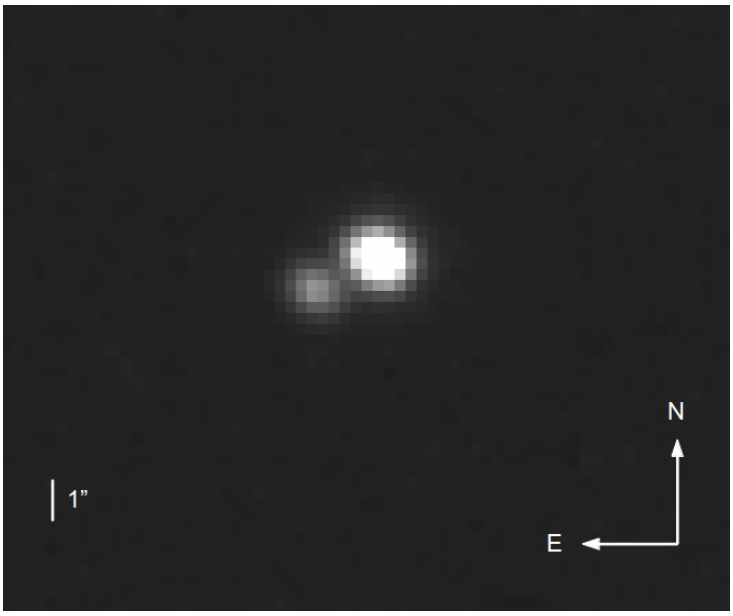

Figure 3.3: U-band EFOSC image of the binary system. HD 8049 B, in the south east side, is 1.7 mag fainter.

During the same night, we performed spectroscopy of the system. The n.11 grism and the 1″ slit were used, providing a resolution R ∼ 360 over the range between 3500–7400 Å. The slit was oriented along the two stars (i.e., PA = 121 deg). We obtained two frames of 8 s exposure.

The spectral reduction was performed using standard IRAF tasks. The raw data were bias subtracted and flat-field corrected. The spectra were extracted with the IRAF task *apall*, wavelength calibrated using arc lamp exposures, and cross-correlated with the sky lines. The relative flux calibration was performed by deriving the sensitivity curve for the instrument set-up from the spectroscopic standard star L745-46A (Hamuy et al. 1994).

We found that a low signal to noise ratio (S/N) signature of HD 8049 B was present in the blue part of the spectrum; its contribution is completely blended with that of the primary star.

[†]EFOSC2 manual, version 3.6. ESO user facilities.

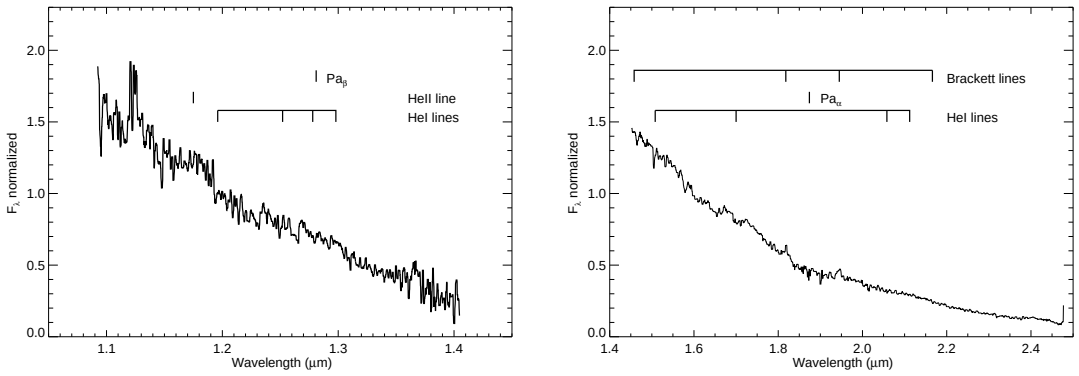

Figure 3.4: SINFONI spectrum of HD 8049 B in J-band (left) and HK-band (right).

3.2.4 VLT/SINFONI

The companion was further characterized on August 28 UT, 2012 using the Spectrograph for INtegral Field Observations in the Near Infrared (SINFONI, see Eisenhauer et al. 2003; Bonnet et al. 2004b,a) mounted at the VLT/UT4. SINFONI provides AO assisted integral field spectroscopy in the near-infrared. It is composed by the SPectrograph for Infrared Faint Field Imaging (SPIFFI) fed by a modified version of the Multi-Applications Curvature Adaptive Optics system (MACAO, see Bonnet et al. 2003). We used the gratings J and $H + K$ to cover the 1.1–1.4 and 1.45–2.45 μm ranges at a spectral resolution of ∼2000 and ∼1500, respectively. The smallest plate scale (12.5 mas) was used, enabling Nyquist sampling of the PSF. The primary served as a reference for the AO wavefront sensor and was kept outside the instrument field of view ($0.8'' \times 0.8''$). Each sequence was composed of 12 acquisitions on the source with small dithering and one acquisition on the sky. Immediately after observing our science targets, we observed the standard star HIP 17280 (B5V) following an AB pattern to correct our spectra for telluric features. HD 8049 and the standard were both observed under poor atmospheric conditions with a seeing of 1.3–1.5″, although the AO loop remained stable, and airmass was lower than 1.1.

We homogeneously reduced our dataset with the ESO data reduction pipeline version 1.9.8 (Abuter et al. 2006). The pipeline successfully carried out bad-pixel detection, flat-fielding, distortion coefficient computation, and wavelength calibration using calibration frames acquired the day after the observations. Individual datacubes were reconstructed from sky-subtracted object frames and merged into a final mosaicked datacube. Datacubes of telluric standard stars were obtained in a similar way. Finally, we integrated the source flux in each final datacube over selected apertures to optimize the S/N without introducing differential flux losses. The spectra of the standard star were corrected from their intrinsic

features and divided by a black body at the appropriate temperature (Pickles 1998). The SINFONI near-infrared spectrum of the object is shown in Figure 3.4.

3.3 Nature and properties of HD 8049 B

3.3.1 Early discovery

HD 8049 was identified as a binary system by van den Bos (1929) in 1928. A projected separation $\rho = 3.19''$ and a position angle $\theta = 153.1$ deg were measured at epoch 1928.81. We corrected for the precession effect as listed in Heintz (2000) and found $\theta = 153.6$ deg. The original paper did not provide any error bar on the measurement, just a note that there were good observing conditions. I assumed an error of 100 mas on $\Delta\alpha$ and $\Delta\delta$. The magnitude resulting from the visual observations was 13.5 mag (rounded to 0.5 mag) and a bluish color was reported; the assumed error is 0.5 mag. This is the only available measurement of the pair listed in the Washington Double Star (WDS) Catalog (Mason et al. 2001) before our observations. This position is possibly compatible with the one measured in our EFOSC U-band images and with the NACO results, once the time lapse is considered. Table 3.2 summarizes the available astrometry, including the two epochs from NACO.

From NACO observations spanning over 1 yr, I derive a relative motion of 2.7 mas/yr in α and 30.4 mas/yr in δ. Repeating this for 1928 vs 2010 observations, I obtain a motion of 0.4 mas/yr in α and 26 mas/yr in δ. These determinations are obviously much smaller than the proper motion of the star ($\mu_\alpha = 65.99 \pm 1.18$ mas/yr and $\mu_\delta = -240.99 \pm 0.98$ mas/yr), supporting the physical association of the faint companion. The motions with respect to the central star derived from 1928 to 2010 and from 2010 to 2011 are consistent within their errors, which makes it very likely that the companion detected in 1928 in the optical range is the same as we found with NACO, and that we are indeed tracking the orbital motion of HD 8049 B around HD 8049 A. The characterization of the orbital properties of the binary is discussed in Section 3.5.1.

Table 3.2: Astrometry of candidate(s) around HD 8049

Epoch	$\Delta\alpha$ (mas)	$\Delta\delta$ (mas)	Reference
1928.81	1417 ± 100	-2858 ± 100	van den Bos (1929)
2010.58	1378 ± 7	-744 ± 7	NACO
2011.58	1382 ± 10	-705 ± 10	NACO
2011.97	1373 ± 24	-734 ± 24	EFOSC

3.3.2 HD 8049 B, a new nearby WD

Considering the combined optical and NIR photometry of HD 8049 B (U, V, and H bands) from EFOSC, the WDS Catalog and NACO observations, the hypothesis of a substellar companion is unambiguously excluded. The combined visible and NIR photometry indicate that HD 8049 B is most likely a WD. The SINFONI spectrum indeed confirms this assumption as the observed spectral energy distribution shows a hot and dense atmosphere that can be associated with that of a WD. The NIR spectrum is rather featureless because we detected no hydrogen or helium lines over the whole 1.0–2.5 μm spectral range. Despite the low-S/N, it could indicate a featureless helium-rich nature (DB WD) or a hydrogen-rich white dwarf (DA) with a relatively hot atmosphere and therefore less contrasted hydrogen lines (see Dobbie et al. 2005). Visible band spectroscopy should enable a better characterization of the WD nature of HD 8049 B, but unfortunately, the low quality EFOSC spectrum does not provide such additional information due to the blend with the much brighter primary spectrum.

To further constrain the physical properties of HD 8049 B, I used the emitted fluxes in the FUV and NUV listed in the GALEX Catalog (Martin et al. 2005). In the ultraviolet, I applied the correction for the chromospheric emission of the primary as described in Sect. 3.5.2. I refer to that section for an exhaustive summary of the photometry for the two objects.

As a preliminary analysis of the object properties, I created empirical sequences using the catalog of nearby WDs by Giammichele et al. (2012). When required photometry was unavailable there, I supplemented it with available GALEX FUV and NUV magnitudes, and 2MASS J, H and K_S magnitudes. The final sample consisted of 107 nearby ($\leq$ 51 pc) WDs: 22 with FUV magnitudes, 18 with NUV magnitudes and 84 with J, H, K_S magnitudes calibrated by Giammichele et al. (2012).

The catalog of observed WDs listed mass, $T_{\rm eff}$, $\log g$ (logarithm of the surface gravity) and $t_{\rm cool}$, all measured from spectroscopy. As a check, I overplotted these object parameters with the expected values from theoretical sequences of Vennes et al. (2011), and confirmed that they fit perfectly, as shown in Figure 3.5.

We noticed that the $FUV - NUV$ color of HD 8049 B did not fit with theoretical or empirical models. The NUV magnitude is more affected by the chromosphere of the K star, but if we considered the corrected value, the discrepancies were even greater.

To fit our photometry measurements with the spectral energy distribution (SED) of a white dwarf object, we used the Markov Chain Monte Carlo (MCMC) based code PASTIS (Díaz et al. 2014). To extract characteristics of the WD atmosphere, we used models by Koester (2010); these models predict the mean intensity of the stellar disk and depend on

$\log g$, $T_{\rm eff}$, and the atmosphere composition; the latter is assumed to be of pure H in this case. To calculate the observed flux measured from our viewpoint on Earth, we multiplied the intensity by the solid angle of the star, calculated using the distance and the radius of the WD. The latter was obtained from the $T_{\rm eff}$–$\log g$–$t_{\rm cool}$–mass relation from Holberg & Bergeron (2006); Kowalski & Saumon (2006); Tremblay et al. (2011); Bergeron et al. (2011)[‡] (used also below to compute the derived parameters).

The synthetic spectrum was then corrected for interstellar extinction using the relations of Fitzpatrick (1999) with $R_V = 3.1$, and an assumed reddening value of $E_{(\rm B-V)} = 0.0106$, as listed in the GALEX catalog. Finally, the spectrum was integrated in the bandpass listed in Table 3.4 as described in Bayo et al. (2008). We did not consider the NUV point for the reason listed previously. We also omitted the U point because it can be affected by the cut-off of the atmosphere; the V point was rejected because the observation was made by eye and there is no associated error.

The SEDs of the system and its components are shown in Figure 3.6. The fitted parameters are the distance, $\log g$, and $T_{\rm eff}$. As priors, we assumed a normal distribution with a mean distance of 33.6 pc and a standard deviation of 1.4 pc (based on the Hipparcos parallax of 29.79 ± 1.21 mas, van Leeuwen (2007); for $\log g$ we used a uniform distribution in the range 7.0–9.0; for $T_{\rm eff}$ we used a uniform distribution in the range 10000–40000 K.

We ran 50 chains of 5×10^5 steps starting from random values of the priors. After removing the *burning phase* (steps before convergence), we merged all chains, taking into account the correlation lengths. The results of the fitted parameters are $\log g = 7.86 \pm 0.16$ and $T_{\rm eff} = 18800 \pm 2100$ K. The distance remained equal to the prior. The derived parameters were $M_{\rm WD} = 0.56 \pm 0.08\ M_\odot$, $R_{\rm WD} = 0.0145 \pm 0.0016\ R_\odot$, and cooling time $t_{\rm cool} = 63^{+23}_{-17}$ Myr (see Figure 3.6). Note that the errors of the values are the 68.3% confidence interval of the fit, and they do not take into account possible model errors.

The cooling time calculated using the empirical sequences is 98^{+28}_{-40} Myr (see Fig. 3.7), in agreement with the SED fit. To estimate the age of the system we added the main-sequence lifetime to the cooling age of the WD. This is discussed in Sec. 3.5.3.

3.4 Nature and properties of HD 8049 A

We exploited the spectroscopic data described in Sec. 3.2.2 and additional data from public archives with the aim of improving the age determination and other stellar parameters of the primary.

[‡]http://www.astro.umontreal.ca/~bergeron/CoolingModels

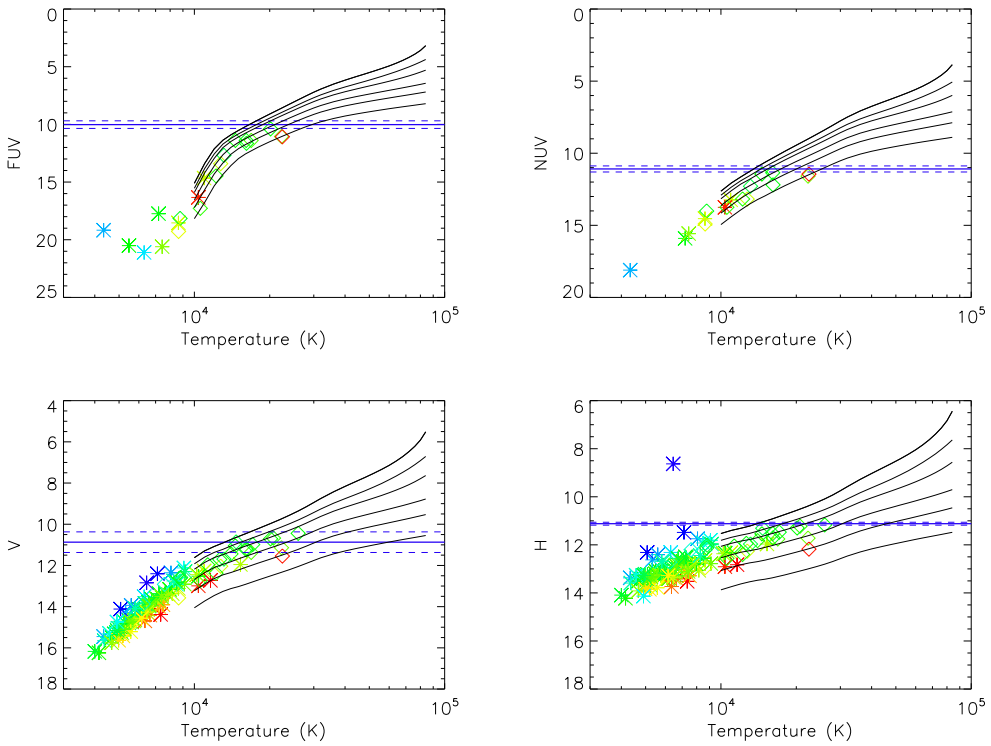

Figure 3.5: Absolute magnitude in different bands (from top-left FUV, NUV, V and H) versus effective temperature for the white dwarf models of Vennes et al. (2011) (black lines) and a sample of nearby dwarfs collected by Giammichele et al. (2012). Stars represent objects with all magnitudes available and diamonds represent the other. Colors indicate the mass from the lowest (blue) to the highest (red ones) white dwarfs. The continuous blue horizontal line represents the magnitude of HD 8049 B. The corresponding error bars are plotted as dashed blue lines. The plots show that the objects of the Giammichele et al. (2012) catalog are not peculiar and are well described by the theoretical models of Vennes et al. (2011).

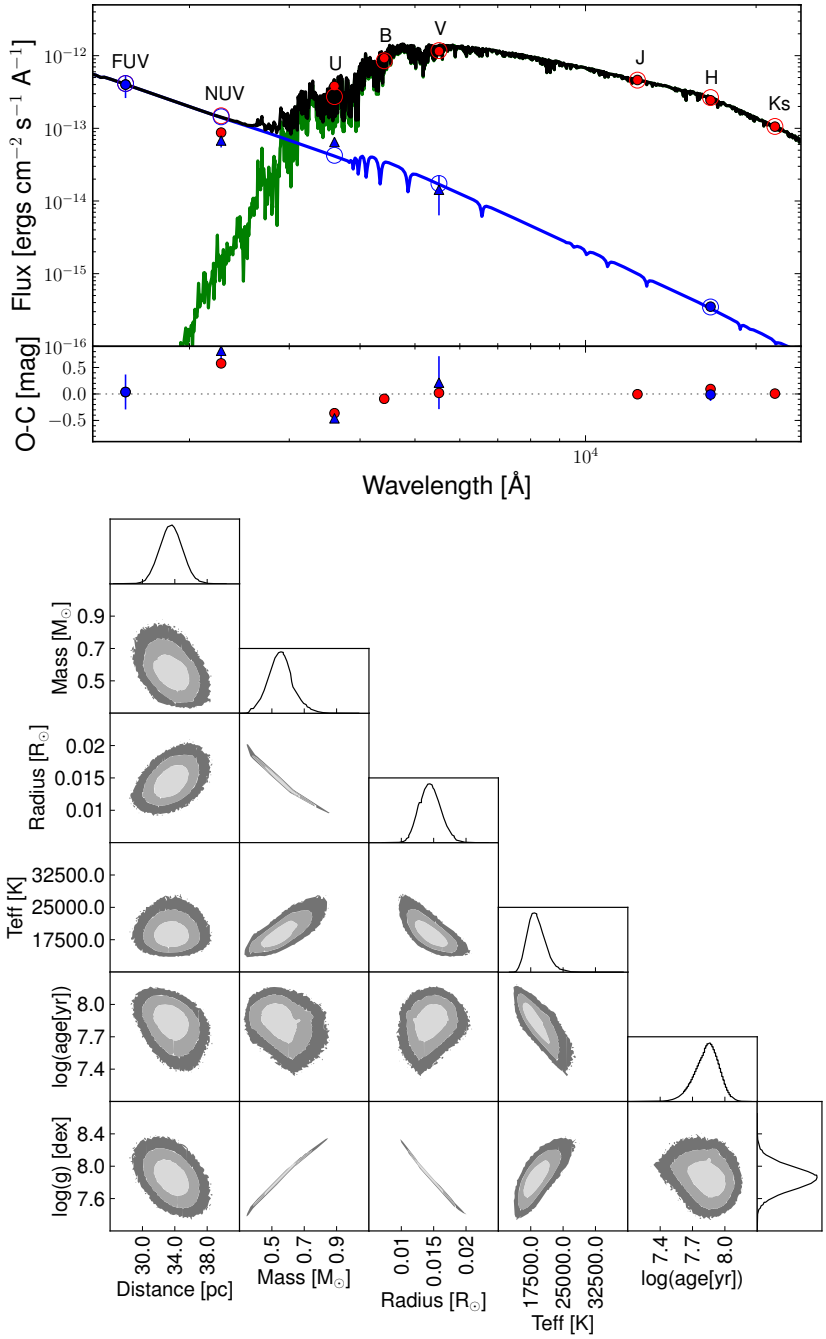

Figure 3.6: Top: Observed magnitudes of the system plotted over the synthetic spectra. Blue points are those taken in consideration during the SED fitting of the WD. Triangle-shaped ones are not considered during the PASTIS integration. Values of the magnitudes of the integrated system are represented in red and the SED in black. The primary star SED is represented in green. Bottom: Two parameters joint posterior distributions for HD 8049 B. The 68.3%, 95.5% and 99.7% confidence regions are denoted by light gray, dark gray and black areas, respectively. Single PDF of each combination is shown along the sides.

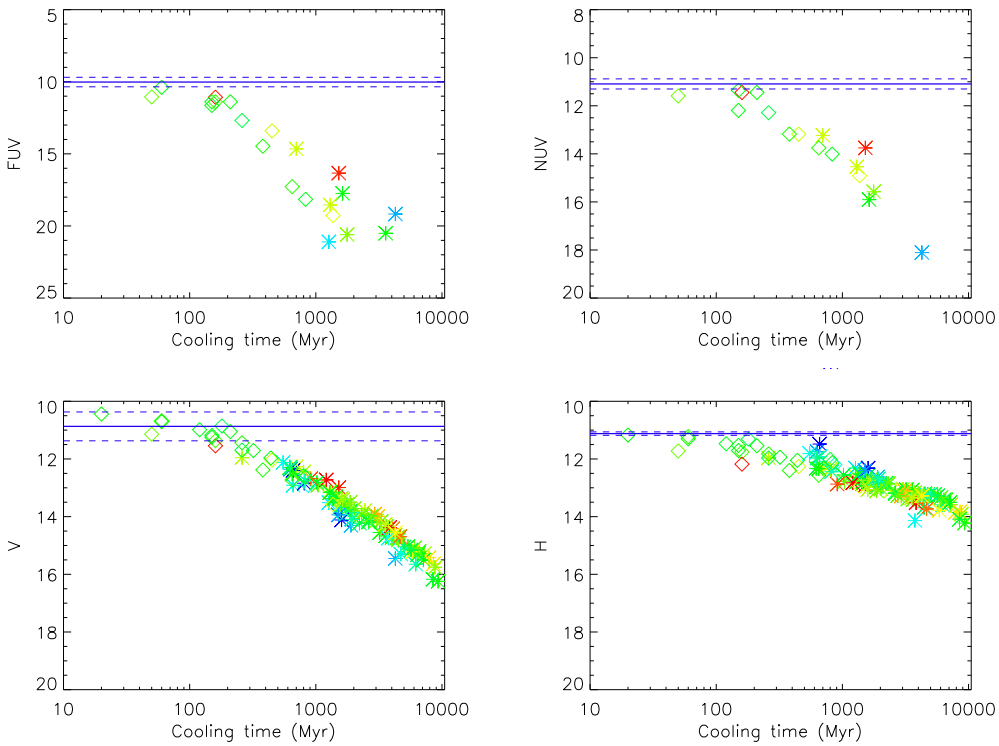

Figure 3.7: Absolute magnitude in different bands (from top-left FUV, NUV, V and H) versus cooling age for the white dwarf models of Vennes et al. (2011) (black lines) and a sample of nearby dwarfs collected by Giammichele et al. (2012). Stars represent objects with all magnitudes available and diamonds represent the other. Colors indicate the mass from the lowest (blue) to the highest (red ones) white dwarfs. The continuous blue horizontal line represents the magnitude of HD 8049 B. The corresponding error bars are plotted as dashed blue lines. The plots show that the objects of the Giammichele et al. (2012) catalog are not peculiar and are well described by the theoretical models of Vennes et al. (2011).

3.4.1 Rotation period

HD 8049 was observed in the All Sky Automated Survey (ASAS[§] Variable star catalog; Pojmanski 2002). Archive observations span from November 20 UT, 2000 to October 28 UT, 2009. After removing outliers and averaging observations collected within short-time intervals (less than 2 hr), we were left with 583 data points for the rotation period search. The average photometric accuracy was 0.02 mag. The brightest V magnitude was $V = 8.68 \pm 0.02$ mag. To minimize the effects of active region growth and decay on the periodograms, we sectioned the data time series into 14 light curves. The light curve amplitude was variable, with values up to $\Delta V = 0.04$ mag. A Lomb-Scargle analysis (Scargle 1982) was carried out on the complete time series data as well as on each of the 14 light curves. We found a rotation period of $P = 8.3 \pm 0.1$ days in the complete time-series data, and the same period in 4 out of 14 time intervals (with a false alarm probability, FAP $\leq 1\%$). The light curve amplitude was larger than the photometric accuracy σ in 13 out of 14 time segments.

HD 8049 was also observed by SuperWASP (Pollacco et al. 2006; Butters et al. 2010). The public archive permitted us to retrieve data for the 2006 and 2007 seasons[¶]. We carried out an analysis similar to that described for the ASAS data. After outlier removal, averaging, and data series sectioning, we found a rotation period $P = 8.5 \pm 0.1$ days for the complete series and for the 2006 and 2007 seasons, with a confidence level higher than 99%. This is consistent with the period determination from ASAS data. The highest light curve amplitude was 0.02 mag, whereas photometric accuracy was 0.01 mag. In Fig. 3.8 we show a summary of the period search on Super WASP data. I refer the reader to Messina et al. (2010) for a more detailed description of the photometric data analysis methods. According to the criteria adopted in Messina et al. (2011) for assigning a confidence level to the rotation period, the period of HD 8049 can be considered *confirmed*. The $P = 8.3$ days rotation period is compatible with the projected rotational velocity (3.5 ± 1.2 km/s, see Torres et al. 2006) for stellar radii $R \geq 0.6\ R_{\odot}$.

3.4.2 Age indicators

Table 3.3 summarizes the measurements and corresponding ages as derived from the different indicators. From our analysis of the HARPS spectrum, we confirm that no lithium is detectable, as found by Torres et al. (2006). Two sets of $\log R_{\rm HK}$ measurements are available: those from our CORALIE spectra and that by Gray et al. (2006). Within the

[§]http://www.astrouw.edu.pl/asas/
[¶]http://www.wasp.le.ac.uk/public/

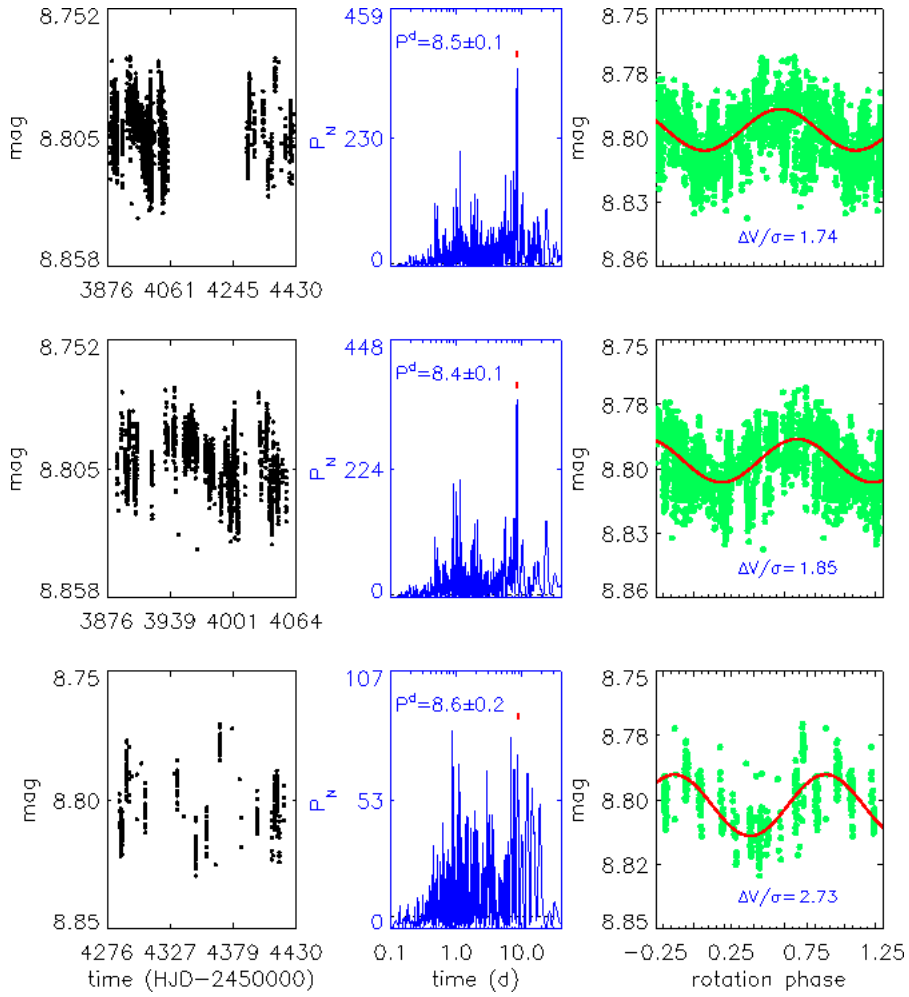

Figure 3.8: Photometry time-series of HD 8049 from SuperWASP: left columns display time segments of magnitudes versus Heliocentric Julian Days (HJD) (the first panel only shows the complete series). The middle columns display the Lomb-Scargle periodograms with an indication of the rotation period. The right columns display the light curves phased with the rotation period and the first HJD as initial epoch. Solid curves represent the sinusoidal fit with the rotation period. The labels report the ratio of average residual from the fit and the rotational modulation amplitude.

uncertainties they give the same value ($\log R_{\rm HK} = -4.25$). The logarithm of the ratio of X-ray and bolometric luminosity $\log L_{\rm X}/L_{\rm bol}$ was derived from the ROSAT All-Sky Bright Source Catalog (Voges et al. 1999) assuming the source 1RXS J011915.1-433803 is the X-ray counterpart of HD 8049 A. The X-ray emission should be dominated by the active K dwarf primary because HD 8049 B is cooler than WDs that show significant X-ray emission ($T_{\rm eff} > 25000$ K, Vennes 1999). The U, V, and W heliocentric space velocities (given in a right-handed coordinate system with U toward the galactic center) are taken from Holmberg et al. (2009) adopting the trigonometric parallax of 29.79 ± 1.21 mas (van Leeuwen 2007). The uncertainty in the center of mass velocity due to orbital motion spans from a lowest value of 200 m/s to a maximum of 3 km/s, as determined from the simulations described in Sec. 3.5.1.

The age estimates provided from these various indicators are quite discordant. Chromospheric HK emission, coronal emission, and rotation period indicate an age between 100–400 Myr. On the other hand, the lack of lithium indicates an age older than about 500 Myr. Additionally, the kinematic parameters are quite far from the typical locus of young stars (Montes et al. 2001). The galactic orbit as given in Holmberg et al. (2009) has $e = 0.19$ and $z_{max} = 0.33$ kpc. These properties are more typical of stars with age of about 3 Gyr, as estimated from the galactic orbits of stars with small age uncertainty in the Holmberg et al. (2009) catalog. These discrepancies strongly suggest that HD 8049 A is not a bona-fide young star but is instead a peculiar object.

I identify the source of these anomalies to be the WD companion detected through direct imaging. The accretion of some amounts of mass and angular momentum by the central star at the time of mass loss from the WD progenitor might have spun-up the star, while increasing the level of magnetic activity. The presence of the WD cannot significantly alter the measurement of the rotation period and X-ray flux. Only minor effects on the $\log R_{\rm HK}$ measurement are expected from the contamination of the spectrum.

I conclude that the young rotation-activity age is not spurious. The central star should have been rejuvenated by the accretion of some amount of mass and angular momentum at the time of mass loss from the WD progenitor. This scenario is investigated more thoroughly in Sec. 3.5.3.

3.4.3 Mass determination

Using our spectroscopic temperature and metallicity results, I employed the PARAM interface[‖] (da Silva et al. 2006) to conclude a mass of 0.804 ± 0.023 $M_{\odot}$. The mass of the

[‖] `http://stev.oapd.inaf.it/param`

Table 3.3: Age indicators of HD 8049 A. The second column lists the adopted value for the various parameters, and the third column lists the corresponding reference; the fourth column contains the resulting age, and the last column has the calibration adopted for age determination.

Indicator	Measure	Ref	Age (Myr)	Ref.
Li EW (mA)	0	1,2	>500	1
$\log R_{\rm HK}$	-4.25 ± 0.05	1,3	90	4
$\log L_{\rm X}/L_{\rm bol}$	-4.24	1	182	4
$P_{\rm rot}$ (d)	8.3 ± 0.1	1	360	4
$P_{\rm rot}$ (d)			380 ± 30	5
U, V, W (km/s)	18,−47,−28	6	old (few Gyr)	1

References. 1: this work; 2: Torres et al. (2006); 3: Gray et al. (2006); 4: Mamajek & Hillenbrand (2008); 5: Delorme et al. (2011) 6: Holmberg et al. (2009)

convective envelope of the star, following Murray et al. (2001), is 0.086 $M_{\odot}$.

3.4.4 Abundance analysis

It is well known that a considerable amount of mass can be transferred to a companion in close binary systems. This is the explanation for blue stragglers in clusters (McCrea 1964), Ba-stars, and extrinsic C-stars (McClure et al. 1980; McClure 1984; McClure & Woodsworth 1990). Different signatures can be observed, depending on when and how much mass was transferred from the donor (in our case the white dwarf). The surface chemical composition of the current primary can therefore be used to better constrain the history of this system.

To better characterize the primary and explore possible signatures of accretion of material processed by the WD progenitor, we derived the stellar spectroscopic parameters and measured the abundances of several elements. To this aim, we used the HARPS high-resolution spectrum of HD 8049 A (Sec. 3.2.2) and adopted the prescriptions of Biazzo et al. (2012). For a detailed description of the method, I refer to that paper.

The derivation of the iron abundance of our target was performed differentially with respect to the Sun. To this purpose, we analyzed a Ganymede spectrum acquired with HARPS at high S/N, obtaining $\log n({\rm FeI})_{\odot} = \log n({\rm FeII})_{\odot} = 7.53 \pm 0.05$. In the end, we found the following stellar parameters and iron abundance for HD 8049 A: effective temperature $T_{\rm eff} = 5050 \pm 50$ K, surface gravity $\log g = 4.50 \pm 0.10$ dex, microturbulence velocity $\xi = 1.42 \pm 0.05$ km/s, [FeI/H] = -0.10 ± 0.02 dex, and [FeII/H] = -0.10 ± 0.05 dex.

Looking for potential evidence of pollution by the ejecta of the precursor of the WD, we

derived abundances of the s-process elements** Y, Ba, and La, which are mainly produced by low-mass AGB stars (~ 1.5–3 $M_\odot$, e.g., Busso et al. 1999). The abundances of Y, Ba, and La were derived as in D'Orazi et al. (2012). We also gathered Cu abundances, whose 70–80% abundance in the solar system is ascribed to massive stars (Käppeler et al. 2011). We adopted the hyperfine splitting from Steffen (1985) and the isotopic mixture from Simmerer et al. (2003) (69% for ^{63}Cu and 31% for ^{65}Cu. We found [Y/Fe] = -0.15 ± 0.10, [Ba/Fe] = -0.10 ± 0.10, [La/Fe] = -0.12 ± 0.10, and [Cu/Fe] = 0.00 ± 0.07. Errors are those derived from the spectral synthesis.

We also measured the abundances of Na and Al because these elements are expected to be overabundant in the ejecta of intermediate-mass AGB stars (Ventura et al. 2001), which is another potential precursor of HD 8049 B. We found [Na/Fe] = 0.05 ± 0.04 and [Al/Fe] = 0.13 ± 0.03, indicating no significant pollution from this type of star.

3.5 System properties

3.5.1 Orbital properties

To constrain the possible orbit of the object I performed a Monte Carlo simulation following the example of Desidera et al. (2011). The simulation steps through 1.8×10^6 random orbital elements and rejects all orbits that do not fit both the RV trend and the astrometric data. I adopted $M_A = 0.804 \pm 0.023\ M_\odot$ and $M_B = 0.56 \pm 0.08\ M_\odot$ as described in Sec. 3.4.3 and 3.3.2. The simulation found ~28000 orbits consistent with the observational data. I present the allowed orbital elements in Fig. 3.9.

The distribution of each element is shown in the histograms of Figure 3.10. The distribution of the inclinations is bimodal and peaks on the values of 5 deg and 65 deg. The argument of periastron ω and the longitude of the node Ω have the highest probability around values of 180 deg and 250 deg, respectively. The most probable period is around 300 yr, corresponding to a semi-major axis of ~ 50 AU. Among the possible configurations of the orbit, there is a lack of edge-on inclinations that can produce the correlation plots of ω and Ω. This is consistent with the RV trend. The orbit is very likely eccentric, with a most probable value $e = 0.55$.

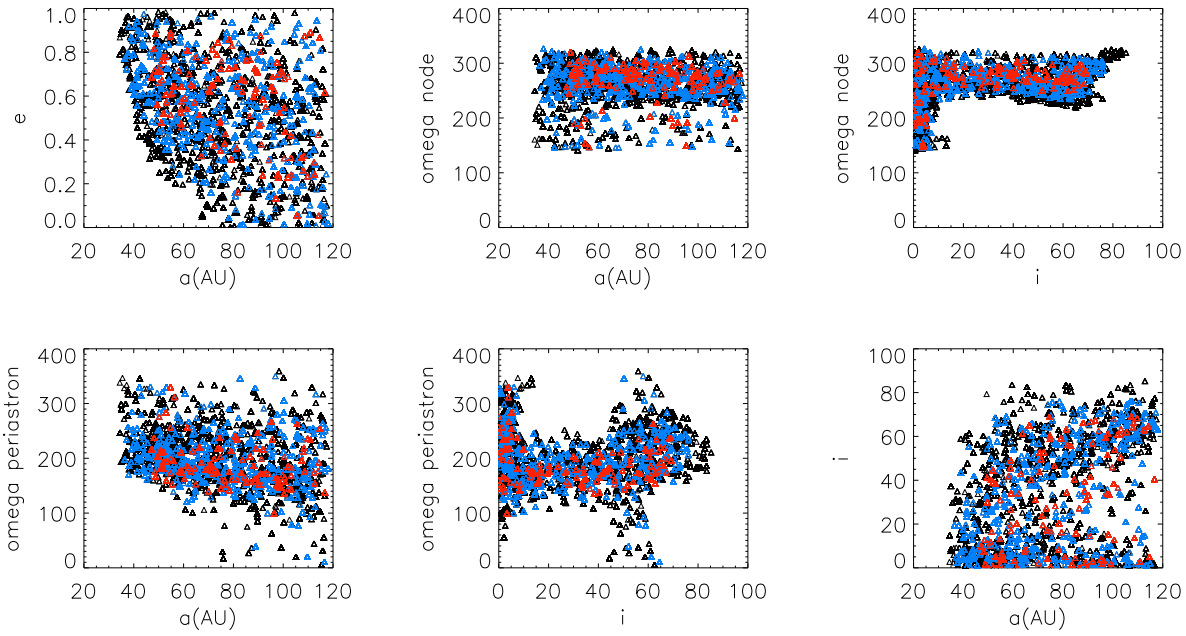

Figure 3.9: Monte Carlo simulation results showing orbital parameters for orbital solutions compatible with the observational data. Colors indicate different levels of χ-squared values (decreasing from black to blue and finally red). The plots show that some parameters are well constrained in a region of parameters space while others can span all possible values. See 3.5.1 for information on the Monte Carlo procedures.

3.5.2 Broad band photometry

Table 3.4 lists the available broad band photometry for the system. A very bright FUV magnitude is listed in the GALEX catalog. The offset between the optical and GALEX position of 1.67″ along the SE direction indicates that the FUV source is better coincident with the WD than with the K2 star. Such a bright FUV magnitude is not expected from the primary, even taking into account the star's high level of chromospheric activity (see e.g. Fig. 6 in Smith & Redenbaugh 2010). Corrections for chromospheric contribution of the primary were calculated using equations 2 and 4 of Findeisen et al. (2011); I assumed a $B - V$ color for the K star as given in Table 15.7 of Allen (1977); I assumed $\log R_{\rm HK} = -4.25$. The final derived errors take into account the dispersion of the points used to derive the mentioned relations.

Based on the composite U magnitude of the unresolved system, I determined an individual U magnitude following the procedures described in Sec. 3.2.3. H magnitude was

**Elements heavier than iron are mostly synthesized via neutron-capture processes, which can be slow (s) and rapid (r), where slow and rapid is meant compared with the the β-decay timescale (Burbidge et al. 1957).

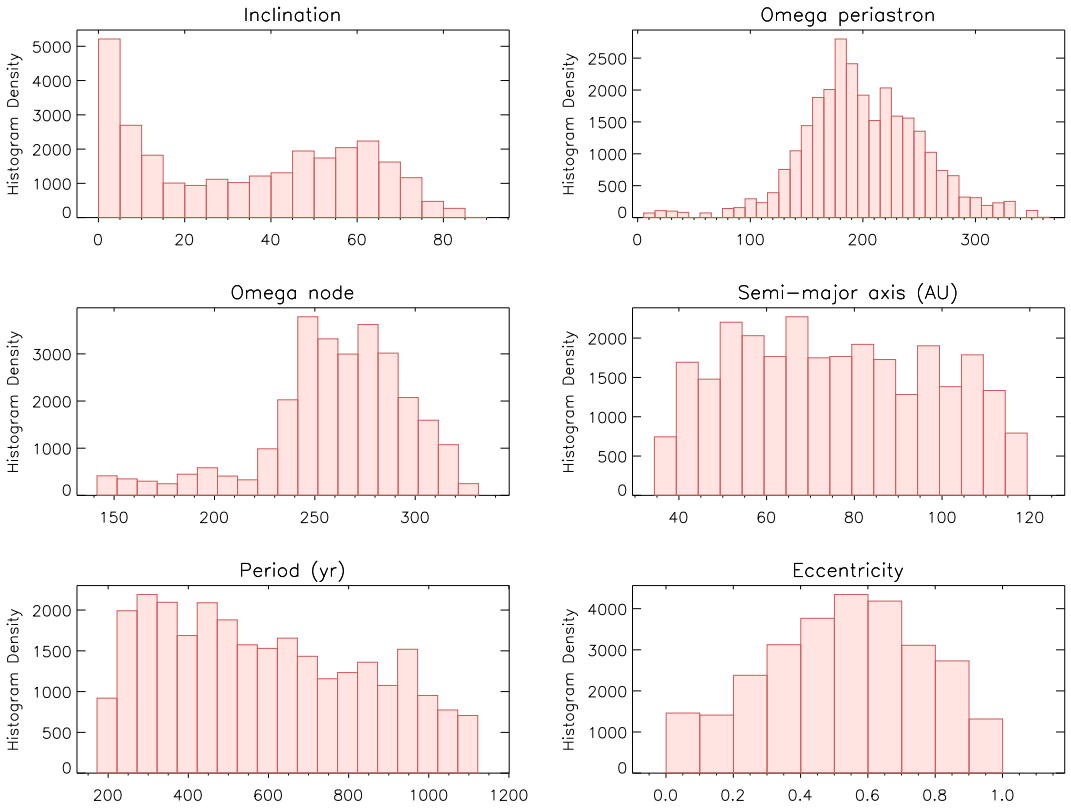

Figure 3.10: Histograms of orbital parameters derived with a Monte Carlo simulation following the example of Desidera et al. (2011).

obtained with NACO observations (see Sec. 3.2.1).

3.5.3 System history

As mentioned in Sec. 3.4.2, the discrepant results of various age indicators for HD 8049 A might be qualitatively explained by the accretion of some amounts of mass and angular momentum from its WD companion HD 8049 B. Comparable cases have been discovered in the past. Jeffries & Stevens (1996) showed that the accretion of slow wind from the AGB progenitor of the WD can transfer sufficient angular momentum to speed up the companion even for orbital separations up to 100 AU. Cases of pairs formed by a WD and a fast rotating, barium-rich star have been reported by Jeffries & Smalley (1996). Another case is represented by the binary GJ86, which is known to host a giant planet and a WD companion (GJ86B; Els et al. 2001; Mugrauer & Neuhäuser 2005). GJ86 also shows anomalies in the age indicators that are similar, even if less extreme, than those I found for HD 8049; the GJ86 age indicators yield a younger age from X-ray and H&K than from kinematic (see

Desidera & Barbieri 2007, App. B). Another more direct indication of wind accretion onto a companion during the AGB phase is represented by the accretion disk around Mira B (Karovska et al. 1997; Ireland et al. 2007), which lies at a projected separation of about 70 AU, which is slightly larger than the most probable value for HD 8049.

Following these works, we can speculate that part of the material lost through stellar wind by the WD progenitor was accreted by HD 8049 A, increasing its rotation rate and mimicking a young age for indicators that are directly or indirectly tied to stellar rotation (rotation itself, X-ray and H&K emission). Specifically, we expect that the activity and rotation age of the system is related to the time elapsed since the accretion event, i.e., the cooling age of the WD. However, the activity-rotation age might be larger than the cooling age of the WD if the primary was not spun-up to the fast rotational velocity typical of a very young star. In this scenario, increasing the mass of the WD progenitor allows for larger amounts of accreted material, both because of large amounts of mass loss due to stellar wind at the end of AGB phase, and also because of the larger widening of the binary orbit due to mass loss. A more massive progenitor also implies a younger age for the system. On the other hand, the lack of significant abundance anomalies on HD 8049 A (Sect. 3.4.4) indicates that either the s-process enhancement of the material lost by the AGB progenitor is small, which may arise only for masses lower than 1.5 $M_\odot$, or that the amount of accreted material is small with respect to the heavy element content of the convective zone.

To explore the possible original configuration of the system, we used the BSE package (Hurley et al. 2002), evolving binary systems with different primary masses and orbital parameters. We used their adopted initial-final mass relationship for the WD and default parameters to take into account mass loss and wind accretion. These elements have significant uncertainty, therefore the results are intended only for a qualitative view of the possible configuration.

A system with a 1.2–1.5 $M_\odot$ star initially at 30 AU will produce a WD of roughly the correct mass with a semi-major axis close to the most probable value, for current orbits presented in Sect. 3.5.1. The resulting age of the system (3-6 Gyr) is compatible with the kinematic properties of HD 8049. About 0.005 $M_\odot$ are accreted by the other component in this case, which is about 5% of the mass of the stellar convective zone as derived following the prescriptions by Murray et al. (2001).

We checked that the results using the more recent semi-empirical relationship by Salaris et al. (2009) are fully consistent with those derived using BSE. Salaris et al. (2009) found that WDs with masses in the range 0.56–0.64 $M_\odot$ are found in NGC 7789 (estimated age of 1.5 Gyr) and older clusters while those in younger ones, like the Hyades and Praesepe (age of about 0.65 Gyr), are more massive.

3.6 GPI observations

After our analysis on the system HD 8049 AB, new observations have been performed by the Gemini Planet Imager (GPI, Macintosh et al. 2014a). The white dwarf companion has been used as a spectrometric calibrator for the instrument. The object has been observed in J, H, $K1$, and $K2$ bands (see Table 6.1). I analyzed the H band data to compare the value of the photometry with NACO results. One of the GPI H-band channel is shown in Fig. 3.11. The sequence, following the observation method of the GPI consortium, has been obtained with four replicae of the central PSF (satellite spots) to calibrate the flux of the central star. Measuring the flux of the four satellite spots and the PSF flux of the white dwarf, I was able to retrieve the broad-band H photometry. The transmission of the four satellite spots is provided in the documents of the GPI consortium.

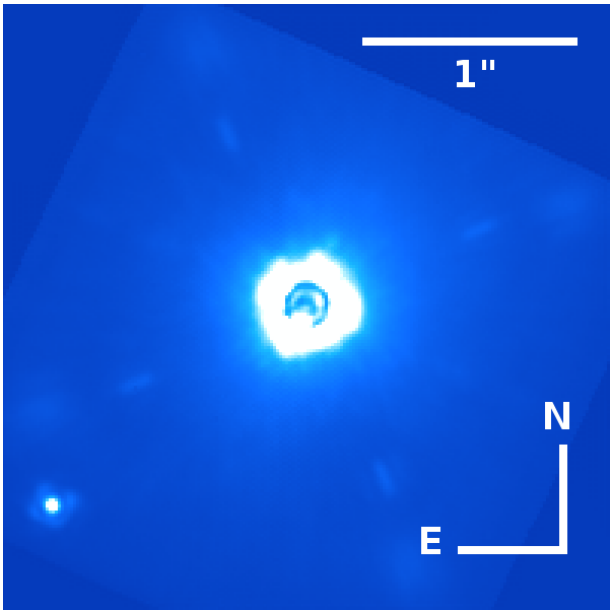

Figure 3.11: Median of the GPI channels in H band showing HD 8049 AB.

The value for the contrast in magnitude that I found is slightly different from the one obtained with NACO: $\Delta H = 7.02 \pm 0.15$. This is probably due because the transmission of the spots has not been re-calibrated on sky. I performed the same analysis for $K1$ filter, finding $\Delta K1 = 7.15 \pm 0.15$.

3.7 Conclusions

The substellar candidate around HD 8049 A, initially suspected based on NACO H-band

photometry and astrometry, turned out to be a WD companion instead of a BD.

With direct imaging, second-epoch observations of the object, we confirmed a bound companionship and determined the WD mass through its luminosity.

The M/L relation for exoplanets strongly depends on the age of the system (see e.g. models from Baraffe et al. 2003b; Madhusudhan et al. 2011a). For this reason, samples of stars scrutinized for low-mass companions through high-contrast imaging usually include a high fraction of presumably young stars. However, a misinterpretation of the age of the host star may produce false alarms and/or an erroneous calculation of the mass of the companion. This was the case of HD 8049 A, a star that appears rejuvenated by the accretion of significant angular momentum from the ejecta of the progenitor of a WD. The faint companion was confused with a 35 M_{Jup} brown dwarf when the age indicated by rotation and activity was considered.

From radial velocity analysis we found a trend that was compatible with a more massive object rather than a brown dwarf. Indeed, a comprehensive analysis of age indicators revealed inconsistencies. The final clue that unequivocally confirms the WD hypothesis is the observation of the system in U- band. At this wavelength, a bright object is observed at the same astrometric position as the NACO candidate. The ultraviolet magnitude of this object is 1.7 mag fainter than that of the host star.

We found parameters for the WD assuming an atmosphere made of pure hydrogen and fitting photometry observation points. The results are $T_{\rm eff} = 18800 \pm 2100$ K, $M_{\rm WD} = 0.56 \pm 0.08\ M_{\odot}$, $\log g = 7.86 \pm 0.16$, and age $t_{\rm cool} = 63^{+23}_{-17}$ Myr.

We made a Monte Carlo simulation, following the example of Desidera et al. (2011), to constrain the orbital parameters. We found that the WD very likely moves in a eccentric orbit with a most probable period of 300 yr ($\sim$ 50 AU).

In our scenario, the existence of the WD companion (with H-band magnitude compatible with a sub stellar object) and the spurious young age of the star, as derived from rotational period, $\log R_{\rm HK}$ and X-ray emission, are intrinsically linked. As discussed in this chapter, a way to identify the spurious young stars that have been affected by wind accretion is to compare the ages resulting from several age indicators, paying attention to discrepancies between rotation-activity ages and lithium and kinematic ages. If the sample is focused on young stars, such a false alarm is related to a WD with a short cooling age, which explains a young rotation-activity age for the companion. Such objects are most easily identified in the UV bandpass, as done in our study exploiting archive GALEX observations.

Resolved systems with white dwarf companions close enough to have harbored some accretion phenomena are interesting targets for additionally constraining the wind accretion

occurring in moderately wide binaries during the asymptotic giant branch (AGB) phase of the WD progenitor. They also enable investigations of the maximum binary separation at which Ba-stars can be observed. Finally, our results confirm that there is a population of WD companions awaiting discovery even at small distance from the Sun, as suspected by Holberg (2009), and that AO imaging can play a relevant role for unveiling it.

Because nearby young stars are prime targets for direct imaging planet searches, and new instrumentation optimized to this science goal is about to start operations, one might wonder about the expected frequency of the kind of false alarm we have found in NACO-LP. To this purpose, we may first consider the frequency of Ba-stars, which are systems similar to those considered here, but with initially smaller separation and shorter period. Ba-stars are the result of mass transfer from an AGB companion (the original primary of the system) to the small-mass star that is currently observed. For our considered scenarios, the system is observed at a late stage in its development, when the AGB star has evolved into a WD. From a survey of ∼200 slightly evolved F dwarfs, Tomkin et al. (1989) discovered two barium dwarfs, and derived a rough frequency of ∼1% Ba-stars among F dwarfs; Edvardsson et al. (1993) found 6 dwarf barium stars among 200 F stars (i.e., 3%), but their binary nature remains to be proven. North & Duquennoy (1991) found a frequency of 0.5 to 1.0% Ba dwarfs among FV stars. McConnell & Gast (1972) estimated that 1% of the G and K giants in the vicinity of the Sun are Ba-stars. From a 200 star sample, Williams (1975) derived a frequency of Ba-stars among G-K giants between 1 and 4%. Bidelman (1985) obtained a frequency between 0.5 and 1%. Most Ba-stars are in binary systems with orbital periods typically longer than 100 days but shorter than 10 years (McClure et al. 1980; McClure 1984; McClure & Woodsworth 1990), though Jorissen et al. (1998) reported a few cases with periods outside this range. Orbits typically have low but non-zero eccentricity, because they are most likely not produced by Roche-lobe overflow; the origin is probably due to stellar wind. This is also supported by evolutionary models (Han et al. 1995).

We may consider the period and secondary mass distribution of binary stars, and estimate the fraction of systems that are of potential interest. Integrating the distribution of binary separation by Duquennoy & Mayor (1991) yields that at least half of the binaries containing a WD have a separation large enough that the star does not become a Ba-star. Hence, the fraction of G-K stars with a WD companion should be on the order of a few percent. This is consistent with arguments based on the initial mass function: roughly a few percent of the G-K stars should have a companion originally more massive if we assume that the mass of the two stars is independent of each other, which is probably a good approximation at least for solar-type stars. Objects like HD 8049 A are therefore most likely G-K stars with a WD companion and an original separation typically slightly higher than

that required to become a Ba-star. They should also have experienced some mass and angular momentum transfer. Hence there should be no large separations.

Objects like HD 8049 A may very well pass through the pre-selection of the direct imaging candidates, failing to show up as spectroscopic binaries. Periods are long enough that RV variations are very small. Furthermore, they will not show up in astrometric binary catalogs, because the periods are so long that orbital motion is not distinguished from proper motion. Finally, they might also be overlooked as visual binaries because the contrast is high. Inclusion in the sample of direct-imaging planet searches also depends on the adopted age limits. For surveys focused on young stars, such as our NACO one, only companions of WDs with short cooling times might be selected.

Table 3.4: Broad band photometry of HD 8049

Band	Mag	Ref.
	A+B	
FUV	12.645 ± 0.004	1
NUV	13.454 ± 0.003	1
$FUV - NUV$	−0.809 ± 0.005	1
U	10.098 ± 0.031	2
B	9.626 ± 0.028	2
V	8.734 ± 0.027	2
$B - V$	+0.892 ± 0.007	2
$V - I$	+0.95 ± 0.02	3
$U - B$	+0.472 ± 0.013	2
J	7.077 ± 0.027	4
H	6.649 ± 0.059	4
K	6.523 ± 0.031	4
$V - H$	+2.04 ± 0.06	2,4
$V - K$	+2.17 ± 0.04	2,4
	A	
FUV	19.68 ± 0.57	5
NUV	15.12 ± 0.22	5
U	10.30 ± 0.03	5
V	8.747 ± 0.030	5
H	6.65 ± 0.07	5
	B	
FUV	12.65 ± 0.33	5
NUV	13.72 ± 0.21	5
U	12.02 ± 0.04	5
V	13.5 ± 0.5	6
H	13.75 ± 0.12	5

References. 1: GALEX, AB magnitude system (Martin et al. 2005) 2: Cousins (1983); 3: Perryman et al. (1997); 4: 2MASS (Skrutskie et al. 2006) ; 5: this work; 6: van den Bos (1929);

Chapter 4

Astrometry and Photometry precision with IRDIS and IFS in laboratory

[*] Nowadays, more than 1000 extrasolar planets are known. The majority of these discoveries has been performed exploiting the RV and the transit techniques. These two techniques are biased toward planets in close orbits. For this reason, the mass vs. semi-major axis parameter space is not homogeneously covered, and at the moment, just 70 planetary mass objects have been found at a separation larger than 5 AU. Among these long period objects, 40 have been found using the direct imaging technique, and 23 using the RV technique. For the latter objects, the orbital parameters are not well constrained when they show only long-term trends rather than a full orbital period. Direct imaging is then a complementary technique to explore the outer separations of the exoplanetary systems. In particular, this technique allows us to study the regions beyond the snow line around young stars. Also, taking advantage of the intrinsic luminosity of young giant gaseous planets in the first phases of their evolution, we can infer their masses (see, e.g., evolutionary models by Chabrier et al. 2000; Baraffe et al. 2002, 2003a; Fortney et al. 2005; Burrows et al. 2006). However, the mass determination is subject to unconstrained physics and unknown initial conditions at very young ages (Marley et al. 2007; Spiegel & Burrows 2012) and large discrepancies on the derived mass are expected between the "hot-start" and "warm-start" models.

Direct imaging provides insights on formation and migrations mechanisms for planetary systems. Moreover, this technique allows us to obtain photometric, spectroscopic, and astrometric measurements of the detected companions, and for this reason it is a fundamental technique to study the atmosphere of the known objects, their mass-luminosity function and their orbits (see, e.g, Rameau et al. 2013a; Kuzuhara et al. 2013; Esposito et al. 2013; Currie et al. 2013) . However, direct detection of extrasolar planets is challenging for two

[*] An adapted version of this work has been published in Zurlo et al. (2014).

reasons: (1) the large luminosity contrast with respect to the star, which is of the order of 10^{-6} for giant young planets with high intrinsic luminosity, and 10^{-8}–10^{-9} for old planets seen in reflected and intrinsic light; and (2) the small separation between the star and the planet, of the order of a few tenths of arcsec for planets at few AUs around stars at a distance up to 100 pc from the Sun. As a result, the light from the companion objects is completely overcome by the light of the host star. These difficulties explain why, at the moment, not a large number of exoplanets have been discovered through direct imaging.

Despite the challenging nature of this technique, several different surveys have been performed in the past decade to search for extrasolar planetary systems. The main objectives of these surveys were to populate the mass vs semi-major axis diagram at large separations, and to clarify the mechanisms of planetary formation. Among the most recent of these surveys I can cite the NACO-Large Program at the Very Large Telescope (Desidera et al. 2014; Chauvin et al. 2014), the Strategic Exploration of Exoplanets and Disk with Subaru (SEEDS) at the Subaru Telescope (Janson et al. 2013; Brandt et al. 2014), the Near-Infrared Coronagraphic Imager (NICI) campaign at the Gemini South Telescope (Nielsen et al. 2013; Biller et al. 2013), the International Deep Planet Survey (Vigan et al. 2012a) at the Very Large Telescope (VLT) and Gemini North, and a survey of young, nearby, and dusty stars to understand the formation of wide-orbit giant planets (Rameau et al. 2013b) at VLT.

A new generation of high-contrast imaging instruments specifically designed for direct imaging of extrasolar planets is now operational, such as the Project 1640 at the 5 m Palomar Telescope (Crepp et al. 2011) which provides important science results (see, e.g, Oppenheimer et al. 2013), or the Gemini Planet Finder (GPI, Macintosh et al. 2014a) at the Gemini South Telescope that just concluded its commissioning phase and already provides scientific results (Galicher et al. 2014). A fourth instrument, the Coronagraphic High Angular Resolution Imaging Spectrograph (CHARIS, Peters-Limbach et al. 2013), is expected to be operative at the Subaru Telescope at the end of 2015. In Europe, the Spectro-Polarimetric High-contrast Exo-planet REsearch instrument (SPHERE, Beuzit et al. 2006) just had the science verification (SV) phase at VLT.

I present in this chapter the expected performance, as deduced from the laboratory experience, for the characterization of extrasolar planets using the two instruments composing the near-infrared (NIR) arm of SPHERE, IRDIS and IFS.

4.1 Acquisition of the data in laboratory

During the Assembly, Integration and Testing (AIT) phase, SPHERE was located at Institut de Planétologie et d'Astrophysique de Grenoble (IPAG). During a period of more than a year, both IRDIS and IFS subsystems were tested in various configurations.

A telescope simulator (TSIM) with central obstruction and spiders matching that of the VLT was installed at the entrance of SPHERE to produce a realistic pupil and generate turbulent conditions. The turbulence is simulated by the use of rotating reflective phase screens, which allows us to tune the seeing and windspeed to recreate typical observing conditions in Paranal. One of the limitations of the TSIM is that the VLT pupil it contains is fixed (or rotated by 90 degrees steps) with respect to the instrument, which means that the SPHERE derotator has to remain fixed during the observations to avoid misalignment of the pupil with the Lyot stops. The main consequence is that angular differential imaging (ADI; Marois et al. 2006a) could not be simulated properly in laboratory.

During IRDIFS tests, the calibration sequence of the instrument typically includes the acquisition of:

- dark frames for IFS;
- flat-field frames for both instruments;
- a spectra position calibration for IFS;
- a wavelength calibration for IFS;
- an instrument flat for IFS that evaluates the response of all the lenslets of the integral field unit (IFU);
- IRDIS backgrounds taken in the same conditions (optical setup and exposure time) as the scientific images (off-axis point spread function (PSF) and coronagraphic images); and
- two images of four symmetric replicae of the central PSF to calibrate the center of the star behind the coronagraph.

The acquisition of scientific data generally follows the scheme described below. First, the fine centering of the star on the coronagraph is performed using an automated procedure that ensures both centering and focusing on the coronagraphic mask. This procedure is used for all coronagraphs available in SPHERE: three apodized Lyot coronagraphs (Carbillet et al. 2011) of different dimensions (145, 185, and 240 mas of diameter), two

4-quadrants phase mask coronagraphs (see Boccaletti et al. 2008), as well as two classical Lyot coronagraphs.

In order to get a precise measurement of the star center behind the coronagraphic mask, a reference image with waffle spots is acquired immediately before or after the scientific sequence. Just one acquisition was needed as the tests confirmed that the system remained stable in the laboratory during the entire observation sequence. When observing on the sky, we will take one at the beginning and one at the end if proven necessary. The waffles are four replicae of the central PSF, placed in symmetrical positions around the center of the star. Waffles are introduced by the use of a small periodic offset on the deformable mirror in closed-loop operations, by an appropriate modification of the adaptive optics (AO) reference slopes (as proposed in Sivaramakrishnan & Oppenheimer 2006; Marois et al. 2006c; Langlois et al. 2013; Wang et al. 2014). The waffle pattern introduced has a spatial frequency of 10 cycles/aperture, and an amplitude of 74 nm, to create well illuminated but not saturated spots.

Before or after the coronagraphic sequence, an off-axis image of the PSF of the star is acquired by introducing an offset on its position. This off-axis PSF is acquired with the same configuration of the instrument to be able to perform flux calibration of the coronagraphic images. To avoid saturation we use a neutral density (ND) filter in the CPI to attenuate the flux of the beam. This filter attenuate the flux of the simulated star by a factor of $10^{3.5}$.

For the coronagraphic sequence of images, exposure times are adapted to the simulated conditions of seeing and stellar magnitude. To improve the flat-field accuracy from 0.5% to 0.1%, both instruments have the possibility of dithering their detector in the focal plane on a square grid of a few pixels (up to 10), by steps of one pixel. By this procedure, the scientifically useful signal falls on different physical pixels throughout the observing sequence, which results in averaging flat-field variations after the images are aligned and combined during the data analysis (Rohloff et al. 2008). For IRDIS, the improvement in flat field accuracy is expected to play a role in small separations ($\lesssim 0''.5$) for contrasts below a few 10^{-6}, levels, which could not be reached in the laboratory because of the lack of ADI. Nonetheless, the dithering was used to be representative of a normal on-sky observing sequence.

In the case of IFS, dithering was thought to improve the instrument performance for contrasts better than 10^{-7} that cannot be reached in laboratory. However, previous tests have demonstrated that the use of dithering can degrade the final contrast obtained by IFS. This is given by the difficulties in defining in a precise way the spectra positions once dithering is implemented.

For IFS, the results discussed in this chapter are obtained without dithering.
In general, the noise sources on the final raw images are:

- the readout noise, which depends on the readout mode chosen;
- the thermal background, which varies with the temperature of the instrument and is homogeneous over the whole image;
- the photon noise, which follows $\sqrt{N}$, where N is the number of detected photons; and
- the speckle noise, which decreases with the separation from the star;

To improve performance and limit as much as possible the instrumental noise level, a specific reduction process is required, as described in the following section.

4.2 Data reduction and detection limits

I selected an observation sequence acquired in October 2013 at IPAG during the Preliminary Acceptance in Europe (PAE). The observing conditions of the instrument were as close as possible in terms of system calibration and performance when observing on sky. Moreover, we simulated a typical atmospheric condition of Paranal*, where the median value of the wind speed is $\sim 6m/s$ and the median seeing value is around $0.69''$. This sequence includes calibrations and scientific datacubes as described in Sec. 4.1. Information on the selected datasets are listed in Table 6.1.

The sequence we performed simulates an observation of a bright star with $J = 2.6$. The IRDIS raw images were prereduced performing background subtraction, bad-pixels correction, and flatfielding. The precise star center was measured on the waffle images acquired right before the coronagraphic sequence. This calibration measurement was used to deduce the coordinates of the center of the star for each frame taking the detector dithering positions into account.

After the preprocessing of each frame, spectral differential imaging (SDI, Racine et al. 1999) was performed. The general principle of SDI is that two images of the star acquired simultaneously at close wavelengths can be subtracted to remove most of the stellar halo and speckle pattern. To ensure optimal rejection of the speckle noise, the images must be aligned, resampled on the same spatial scale, and scaled in intensity to account for any filter transmission and stellar flux variation. For this work, I implemented an optimized SDI

*http://www.eso.org/gen-fac/pubs/astclim/paranal/

Table 4.1: Observation sequence characteristics used for the characterization analysis after the injections of the synthetic planets. The data were taken in the laboratory in IRDIFS-mode (see Table 2.1).

	IRDIS	IFS
Simulated seeing	0.85″	
Simulated wind speed	5 m/s	
Coronagraph type	Apodized pupil Lyot coronagraph	
Coronagraph diameter	185 mas	
IRDIFS-mode	*H2H3*	*YJ*
DIT[a]	1.6 s	2.0 s
NDIT[b]	20	50
Total exposure time	512 s	100 s
Image size	2048×1024	2048×2048
Dithering	4×4	None
FoV rotation	None	None
ND[c]	0.0	0.0

[a]Detector Integration Time
[b]Number of frames per dithering position
[c]Neutral Density filter

procedure designed to minimize the speckle noise in the subtracted image between 0.″25 and 0.″65. The parameters that were optimized by the minimization routine are the amplitude scaling factor, and the differential shift between the images at the two wavelengths. The spatial scaling factor remain identical for all images, and equal to $\lambda_{H2}/\lambda_{H3}$. Because SPHERE images are at least Shannon-sampled, the spatial rescaling of the images acquired in H3 was performed accurately using a Fast Fourier Transform (FFT). The scaling consists of zero-padding the image both in direct space and in Fourier space in order to obtain the zoom factor of our choice (Vigan et al. 2010c).

After averaging all SDI-subtracted frames, the final data product was used to calculate noise level as the residual standard deviation in the SDI image. The IRDIS DBI 5σ noise level is plotted in Fig. 6.3; red color represents the 5σ noise level of individual channels, and green color the DBI curve. All the reductions of IRDIS images were done using custom IDL routines. The level of residual noise that I can obtain exploiting only SDI analysis are satisfactory, reaching a contrast of 2×10^{-5} at 0.″5 and 4.5×10^{-6} at 1.″5 from the primary at 5σ. Following the simulations presented in Vigan et al. (2010a), with the addition of the ADI technique, the contrasts will be of the order of 5×10^{-7} and 2.5×10^{-7} at the same separations.

For IFS, the following calibrations were performed using the Data Reduction and Handling (DRH, Pavlov et al. 2008) software, the official pipeline for the SPHERE instrument:

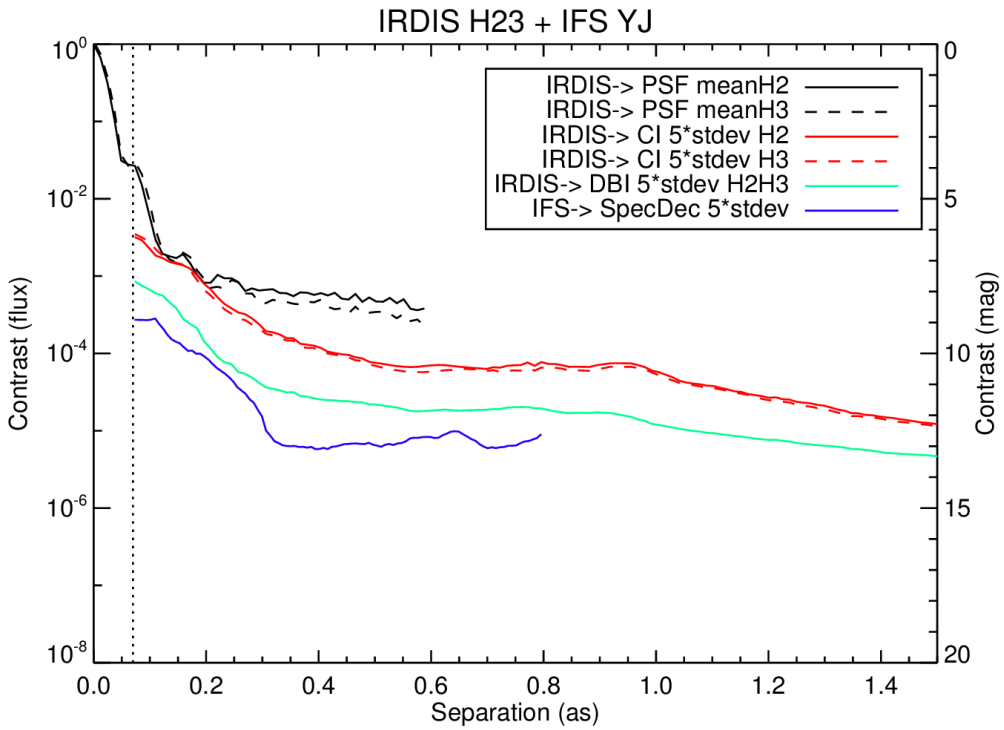

Figure 4.1: 5σ residual noise levels, without ADI reduction, for the two science modules of SPHERE, IRDIS and IFS, in IRDIFS mode. The curves refer to the dataset described in Table 6.1, where I injected the synthetic planets. The vertical dotted line represents the radius of the coronagraph, i.e., the zone where the detectors are blind. The mean azimuthal profile of the off-axis PSF (black), the coronagraphic profile (red) are shown for the two IRDIS channels $H2$ (continuous line) and $H3$ (dashed line). The contrast results after the SDI reduction (green) and SD reduction for IFS (blue) are shown.

- dark subtraction;
- bad-pixels correction;
- detector flat-fielding;
- determination of all the spectra positions;
- wavelength calibration; and
- instrument flat correction to account for the different response of each lenslet.

After these calibrations, a scientific DRH recipe (module of the pipeline that performs a particular task) is applied to produce a three-dimensional datacube composed of 39 monochromatic images of 291×291 pixels.

On this datacube I used both the spectral deconvolution (SD, see, e.g, Sparks & Ford 2002; Thatte et al. 2007) and the principal component analysis (PCA, see, e.g, Amara & Quanz 2012; Soummer et al. 2012; Oppenheimer et al. 2013) reductions methods. For more details, regarding the first method applied on SPHERE-IFS data I refer the reader to Mesa et al. (submitted).

Here I list the most important steps needed to implement the SD. First, each monochromatic frame in the datacube is rescaled according to its wavelength in such a way that the speckle pattern is at least ideally the same while the position of an eventual companion is different from frame to frame. After that a fit is performed along the rescaled datacube wavelength direction for each pixel. The fitting function is then subtracted from the rescaled datacube. The degree of the fitting function can be selected in such a way to maximize the speckle noise subtraction and, in the meantime, to avoid subtracting signal from the companion. Finally, each frame is rescaled back to its original dimension so that the companion is always in the same position. At separation less than the bifurcation radius ($\sim 0\farcs15$) (Thatte et al. 2007) the spectrum is completely covered by an eventual companion that, for this reason, would be completely canceled so that the method is not effective at these small separations. The SD method can provide good results on SPHERE data as the instrument meet some particular characteristics: the speckles do scale linearly and the chromaticity of the speckles can be completely described by a low order polynomial.

The method based on PCA, that I used for the characterization of the detected objects is presented in more details in Sect. 4.2.1.

The procedure (following Masciadri et al. 2005) that I have used to calculate the contrast is the following:

- the standard deviation into a box centered on each pixel and with a side corresponding to $1.5\lambda/D$ is calculated for each pixel in the image;
- a median of the standard deviation obtained as described in the previous point is made for all the pixels at the same separation from the central star;
- the contrast is defined by the ratio between the flux in the coronagraphic images and the flux of the central star. To calculate it we measured the flux of the off-axis PSF of the star after normalization for the value of the detector integration time (DIT) and the transmission of the neutral density (ND) filter used during the exposure, as mentioned in Sec. 4.1. The same normalization for exposure time and ND filter was also applied to the coronagraphic images.

The contrast limit curve for IFS obtained exploiting the SD method described above is presented in Fig. 6.3. In this case, I used a fitting function with degree of 1 because I found that in this manner I could obtain a good speckle subtraction simultaneously avoiding self-cancellation of the companion.

In this analysis the cancellation that the SD could cause is not taken into consideration and I refer the reader to Mesa et al. (submitted) for more details. The contrast obtained with the SD reduction is of the order of 1×10^{-5} at a separation of $0\farcs5$ and 1×10^{-5} at a separation of $0\farcs8$. With the addition of the ADI, we expect the contrast to reach 1.5×10^{-7} and 5×10^{-8} at the same separations, as resulted from the simulations presented in Mesa et al. (2011).

The contrast curves presented in Fig. 6.3 have been calculated on a short temporal sequence, so the speckles noise dominates over the other sources of noise described in Sect. 6.3. We expect that longer sequences when observing on sky will improve the detection limits, as in the laboratory the TSIM reproduced identical speckles patterns with a given frequency.

4.2.1 The KLIP method

To improve our capability on the characterization of the planetary candidates that will be detected by IFS, I implemented a PCA method that performs the Karhunen–Loève Image Projection (KLIP) algorithm, following the model of Soummer et al. (2012), with improvements dedicated to the spectral extraction from IFS datacubes developed for Project 1640 data (Pueyo et al. 2014). Our code was implemented in IDL language and is suitable to work with IFS datacubes.

The KLIP method takes advantage of the multiple channels of the IFS to create the reference library for the basis of the Karhunen–Loève matrix. The principle is that the signal of the planet after the spatial rescaling of the IFS datacube is in different positions with respect to the center of the image while the speckles pattern remains fixed. If we take a small portion of the image around the position of the planet in a specific spectral channel, it is possible to create a reference library using a characterization zone that is included in the projection of this portion on all the other channels that contain no signal from the planetary candidate, or at least or a very small quantity of this signal.

Using as a PCA library a set of portions of the frames that do not contain much astrophysical signal attenuates the typical flux losses induced by the SD technique. I used the forward modeling method presented in Soummer et al. (2012) to get our results in KLIP photometry, as I will show in Sect. 4.4.4. On-sky observations are expected to produce even better results, as the construction of the PCA library will exploit the FoV rotation.

4.3 Synthetic planets injection

To estimate the errors on photometry and astrometry of future candidates, I injected synthetic planets in the set of data presented in Sect. 6.2. The synthetic planets consist of a small portion of the off-axis PSF acquired during the scientific sequence (see Sect. 4.1). In this manner, the light diffracted by the spiders and the secondary ring of diffraction are taken into account. While for IRDIS it was possible to insert the planets directly into the raw data, for IFS I had to inject them in the datacube after the scientific recipe as described in Sect. 6.2. This is due to the fact that it is extremely difficult to inject the simulated objects into the IFS raw data, which is constituted by the thousands spectra created by all the IFS lenslets.

The flux in each spectral channel was calculated to reproduce L and T-type spectra. The libraries of field brown dwarfs used for the L-type spectra are taken from Testi et al. (2001), while the T-type spectra are from Looper et al. (2007), Burgasser et al. (2004) and Burgasser et al. (2006). The flux ratio between the fluxes of the two IRDIS band ($H2/H3$) in the different spectral types ranged from a minimum value of 0.85 (L4-type, the flattest one) to a maximum of 7.46 (T8-type).

Five simulated planets were injected simultaneously at five different separations (0″.20, 0″.35, 0″.50, 0″.65, 0″.80) and position angles with respect to the star. The procedure was repeated 30 times with position angles rotated by steps of 12 degrees each time to improve the statistical significance of the results. The flux of the planets was scaled for five different contrast levels (10^{-3}, 3×10^{-4}, 10^{-4}, 3×10^{-5} and 10^{-5}) with respect to the host star. The contrast was defined as the ratio between the integrated flux of the planet over that of the star, over the whole band covered by the two instruments (0.8–1.8 μm). This means that for a given contrast the flux collected by IFS is greater than for IRDIS, especially for T-type objects. Overall, the statistics of our results is based on a total of 750 injected planets (five planets each image, five contrasts, 30 different rotation angles) of the same spectral type.

After the injection, the raw IRDIS images were pre-reduced (background subtraction, flat-fielding, recentering, median recombination of the datacube, and rescaling) and the SDI was applied to minimize the speckles noise as described in Sect. 6.2. An image of the planets after injection and SDI reduction is shown in Fig. 4.2 (top). For the IFS, an example of the simulated planet inserted in the scientific datacube, after SD reduction, is also shown in Fig. 4.2 (bottom).

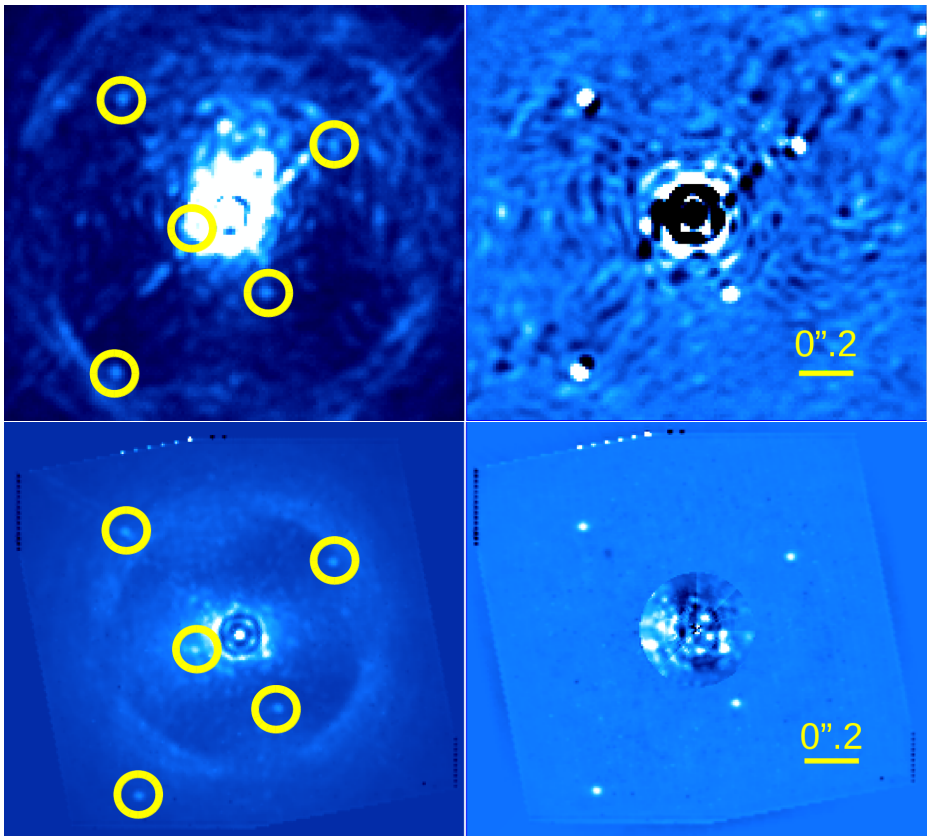

Figure 4.2: *Top:* Map of the synthetic T5-type planets (T∼2000 K) of $1{\times}10^{-4}$ after injection in *H*2 filter (left) and SDI reduction (right) of IRDIS data. A slight misalignment of the Lyot stop causes the oblique stripe going through the image. *Bottom:* Simulated T5-type (T∼1100 K) planets at a contrast of 3×10^{-5} injected in the IFS pre-reduced datacube (left) and after the SD reduction (right). In the central part of the image, the SD cannot work properly for the reasons explained in Sec. 6.2. The images show the 15th channel of IFS at $\lambda = 1.09\ \mu$m.

4.4 Results

4.4.1 Signal-to-noise ratio

First, I determined in which cases the planets are detectable. I assumed that a planet was detectable if its signal-to-noise ratio (S/N) is above the value of 5[†], with the S/N defined in this way:

[†]The values of 5, commonly used as a good false alarm rejector, will be effective in retrieving real detections with the addition of the ADI, while for this set of data I estimated that a level of 5 times the standard deviation of the signal still includes some false alarms, especially along the spiders projection. I empirically observed that the distribution of the S/N level of the pixels of our data is represented by an exponential function, while the expected distribution for an ADI processed image is expected to be Gaussian (Marois et al. 2008a).

- for each pixel p I calculate the integrated flux (F_A) in an aperture of radius $0.6\lambda/D$ centered on p, and normalize it by the area of the aperture;
- I consider an annulus centered on p with an inner radius of $3\lambda/D$ and an outer radius of $5.5\lambda/D$, to be close enough to the object and without including its flux;
- I consider another annulus centered on the star with inner and outer radii of $r-0.6\lambda/D$ and $r + 0.6\lambda/D$, where r is the distance between the star center and p;
- I calculate the background (median of the values) bkg_B and the standard deviation σ_B on two areas (B) that are the intersection of the two rings described above; and
- I define the S/N as: $S/N = (F_A - bkg_B)/\sigma_B$.

A cartoon describing the different areas defined for the S/N calculation is shown in Fig. 4.3. The values of the radii and the choice of the zones is made to have a local value of the S/N, as the speckles noise is not homogeneous on the whole FoV and the structure of the spiders is visible.

If I use the entire annulus centered on the star, the estimation of the S/N can change from some fraction of a percent to a maximum of 9% for planets fainter than 10^{-4}. I decided to use a local estimation of the background to avoid some instrumental features, such as the diffracted light from the spiders, which will have much less impact while exploiting the ADI technique. Once on the sky, especially for the cases close to the detection limits, I will explore different methods for the estimation of the S/N to reach the maximum rejection of the false alarms.

For IFS data, we had to distinguish the procedure used to find planets, where an aggressive method is used to create deep detection maps and the procedure to characterize them, where we know the position of the planet and we use optimized methods around the position of the object to recover its signal. This different approach between the detection part and the characterization of the detected object has to be kept in mind in general when dealing with direct imaging data (see, e.g, Pueyo et al. 2014). For the IFS detection maps, the aggressive method we used is the SD without any mask to protect the planet signal. The number of detected planets and the mean S/N is given for both instruments in Table 4.2 for each simulated separation and contrast. The optimized method to characterize the planets are the SD with a mask and KLIP, described in Sec. 6.2.

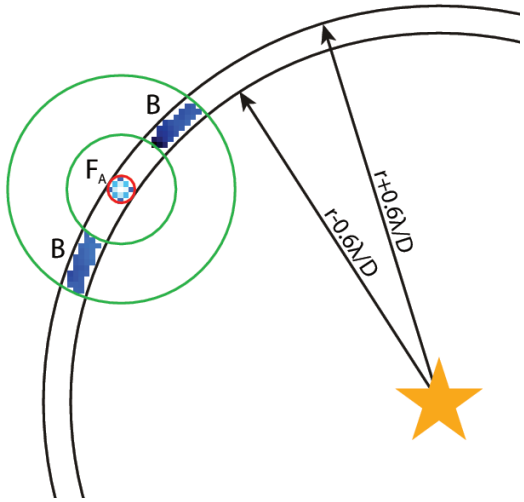

Figure 4.3: Representation of the areas where the signal of the planet and the local noise are calculated. The zone F_A (red circle) is the area where the signal is calculated, while the zone B (green circles) represents the area where the background and the standard deviation of the noise are calculated, as described in Sect. 4.4.1.

4.4.2 Photometry with IRDIS

Photometry on SDI data is difficult because, as shown in Fig. 4.2 (top, right), we have to deal with two peaks: one positive from the planet signal in $H2$ filter and one negative from the planet signal in $H3$ filter. The peaks can overlap and the *a priori* ratio between the fluxes in the two filters is unknown (see, e.g, Maire et al. 2014a). Instead of attempting to measure the planet signal in the final SDI image, where degeneracies will necessarily occur because of the partial subtraction of the two peaks (Maire et al. 2014a), I have adopted a method based on the introduction of "negative synthetic planets" into the raw data (see,

Table 4.2: Number of detected planets out of 30, in function of the contrast (columns) and the separation (lines) for IRDIS and IFS subsystems. The mean S/N value for the detected planets is given in parenthesis. The definition of the S/N and how it is calculated for our data is described in Sec 4.4.1.

	10^{-3}		$3{\times}10^{-4}$		10^{-4}		$3{\times}10^{-5}$		10^{-5}	
	IRDIS	IFS	IRDIS	IFS	IRDIS	IFS	IRDIS	IFS	IRDIS	IFS
0″.20	30 (20)	30 (70)	30 (9)	30 (22)	6 (7)	27 (7)	0 (-)	1 (6)	0 (-)	0 (-)
0″.35	30 (98)	30 (347)	30 (42)	30 (129)	30 (15)	30 (46)	18 (6)	30 (14)	0 (-)	14 (8)
0″.50	30 (171)	30 (238)	30 (64)	30 (114)	30 (22)	30 (43)	23 (8)	30 (12)	5 (8)	5 (7)
0″.65	30 (260)	30 (281)	30 (93)	30 (135)	30 (31)	30 (55)	29 (10)	30 (17)	6 (7)	6 (8)
0″.80	30 (272)	30 (285)	30 (104)	30 (130)	30 (36)	30 (50)	29 (12)	26 (17)	11 (7)	11 (8)

e.g, Bonnefoy et al. 2011), adapted for SDI data, for which we expect that the degeneracies will be less limiting. This method is similar to what the routine `fitstars`, presented in ten Brummelaar et al. (1996, 2000), does to calculate the photometry of binaries. In the following paragraphs I describe this method in more detail.

I note $\mathcal{P}_{H2}$ and $\mathcal{P}_{H3}$ the PSFs of the planet in filters H2 and H3, respectively. Similarly, I note $\mathcal{M}_{H2}$ and $\mathcal{M}_{H3}$ the off-axis PSFs in filters H2 and H3, which I use to model the planet PSFs. Finally, I note $\mathcal{F}_{H2}$ and $\mathcal{F}_{H3}$ the numerical factors by which we need to multiply our models to obtain a representation of the planet PSFs. I write:

$$\begin{aligned} \mathcal{P}_{H2} &= \mathcal{F}_{H2}.\mathcal{M}_{H2}, and \\ \mathcal{P}_{H3} &= \mathcal{F}_{H3}.\mathcal{M}_{H3}. \end{aligned}$$

Additionally, I assume that the planet PSFs are located at an unknown position (Δx,Δy) with respect to the star position. This value is independent from the filter.

The photometry and astrometry method for IRDIS attempts to determine the values of $\mathcal{F}_{H2}$, $\mathcal{F}_{H3}$, Δx and Δy by subtracting the planet signal from the raw data. For the practical implementation, I used the Levenberg-Marquardt least-squares fitting routine `MPFIT` (Markwardt 2009) with a custom function that takes as an argument the current values of the parameters being fitted: (f_{H2},f_{H3}) for the fluxes, and (δx,δy) for the position. The function performs the following steps:

1. creation of a model of the planet from the off-axis PSF, scaled with the current flux values:

$$\begin{aligned} m_{H2} &= f_{H2}.\mathcal{M}_{H2} \\ m_{H3} &= f_{H3}.\mathcal{M}_{H3}. \end{aligned}$$

2. subtraction of m_{H2} and m_{H3} in the raw H2 and H3 data, respectively, shifting them around the true position Δx,Δy at each iteration of the fit;

3. application of the SDI procedure described in Sect. 6.2 to obtain a final SDI image $\mathcal{I}_{SDI}$;

4. return the residual variance in a zone (C) made of the union of two circular apertures of diameter $1.5\lambda/D$ centered at the location of the planet in H2, and in H3 after the spatial rescaling. This residual variance is used for the least-squares minimization.

When a local or global χ^2 minimum is found, the current values of f_{H2}, f_{H3}, δx, and δy are assumed to represent good estimations of $\mathcal{F}_{H2}$, $\mathcal{F}_{H3}$, Δx, and Δy respectively, i.e., for the photometry I write:

$$\begin{aligned} \mathcal{P}_{H2} &\simeq f_{H2}.\mathcal{M}_{H2} \\ \mathcal{P}_{H3} &\simeq f_{H3}.\mathcal{M}_{H3}. \end{aligned}$$

As mention above, this method could be affected by degeneracies for planets very close to the central star, where the peaks at both wavelengths overlap significantly. Future work will be devoted to improving this technique and precisely identifing its limitations, but the results detailed below show that it is promising even for planets as close as 0$''$.2.

Photometry measurements were performed for all the synthetic planets introduced in the data, as detailed in Sect. 4.3. For the starting point of f_{H2} and f_{H3}, I assumed a value 10% above the true values $\mathcal{F}_{H2}$ and $\mathcal{F}_{H3}$. This choice is arbitrary, but I performed tests to verify that varying this starting point did not have significant impact on the result. I also tested the impact of varying the size of zone C for the minimization of the residual variance, and verified that there is no impact for the size between 1 and 2λ/D.

To have a realistic prediction of what we could measure when conditions would vary significantly, I performed this method using two different off-axis PSFs as a model:

- Ideal case: the PSF of the planets can be well represented by off-axis PSFs $\mathcal{M}_{H2}$ and $\mathcal{M}_{H3}$ acquired right after the coronagraphic sequence, which means that the system and the atmospheric conditions are stable during the sequence.

- Variable PSF case: the model used to represent the PSF of the planets is an off-axis PSF taken some months before the scientific exposure, which means that the system and the atmospheric conditions changed during the exposure.

The residual between the two PSFs are shown in Fig 4.4. The peak-to-peak variation of the difference between the two PSFs is about the 5-6% of the PSF flux and the standard deviation of the central zone (12×12 px) is 1%. A realistic case on the sky should lie in between the two boundaries, depending on the stability of the conditions during the scientific acquisition. Future on sky tests will be dedicated to the study of the variability of the PSF shape during the scientific exposures.

The offsets in magnitude between the nominal and measured flux versus the S/N of the planets are shown in Fig. 4.5 for the extreme case. The trend of the error for the different PSF case in function of the S/N is calculated as:

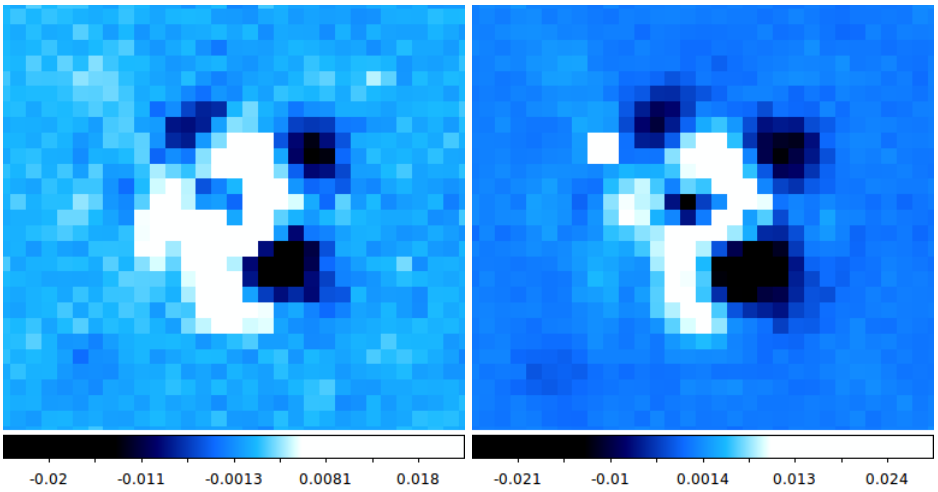

Figure 4.4: Residual from the subtraction of the off-axis PSF taken right after the sequence and a different PSF taken some months before for H2 filter (right) and H3 (left). The peak-to-peak variation is about the 5-6% of the PSF flux and the standard deviation of the central zone (12×12 px) is 1%.

$$\sigma = 0.07 + \frac{2.6}{S/N} mag \tag{4.1}$$

and is plotted as a solid line in Fig. 4.5, while for the ideal case is calculated as:

$$\sigma = \frac{2.8}{S/N} mag \tag{4.2}$$

and overplotted as a dashed line.

This can demonstrate that for the IRDIS photometric measurement, the variability of the PSF during the exposure does not have a big impact, as the photometric fit considers residuals inside an aperture.

Examples of the two IRDIS photometry channels measured with the different PSF as a model for a T5-type spectrum, for two different contrasts and three separations from the host star are shown in red in Fig. 4.6. The theoretical value of the photometry for each filter is also represented as a black horizontal line. The error bars are calculated as the standard deviation of the measurements of each planet in 30 different positions.

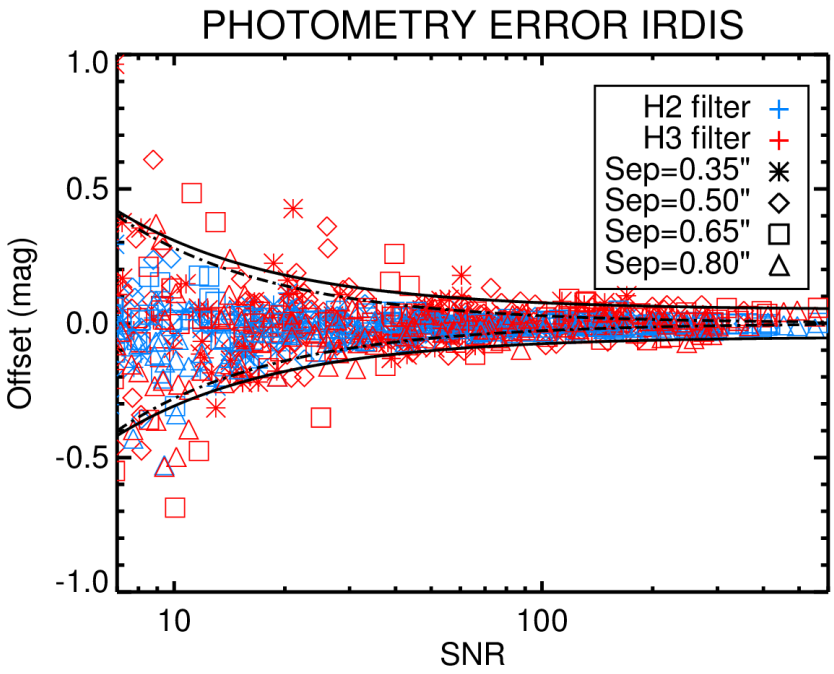

Figure 4.5: Plot of the difference between nominal and measured values of the magnitude versus the S/N of each planet with contrasts from 10^{-5} to 10^{-3} and different separations from the host star for the SDI image. The dashed black line represents Eq. 4.1. Different separations from the host star are represented with different symbols.

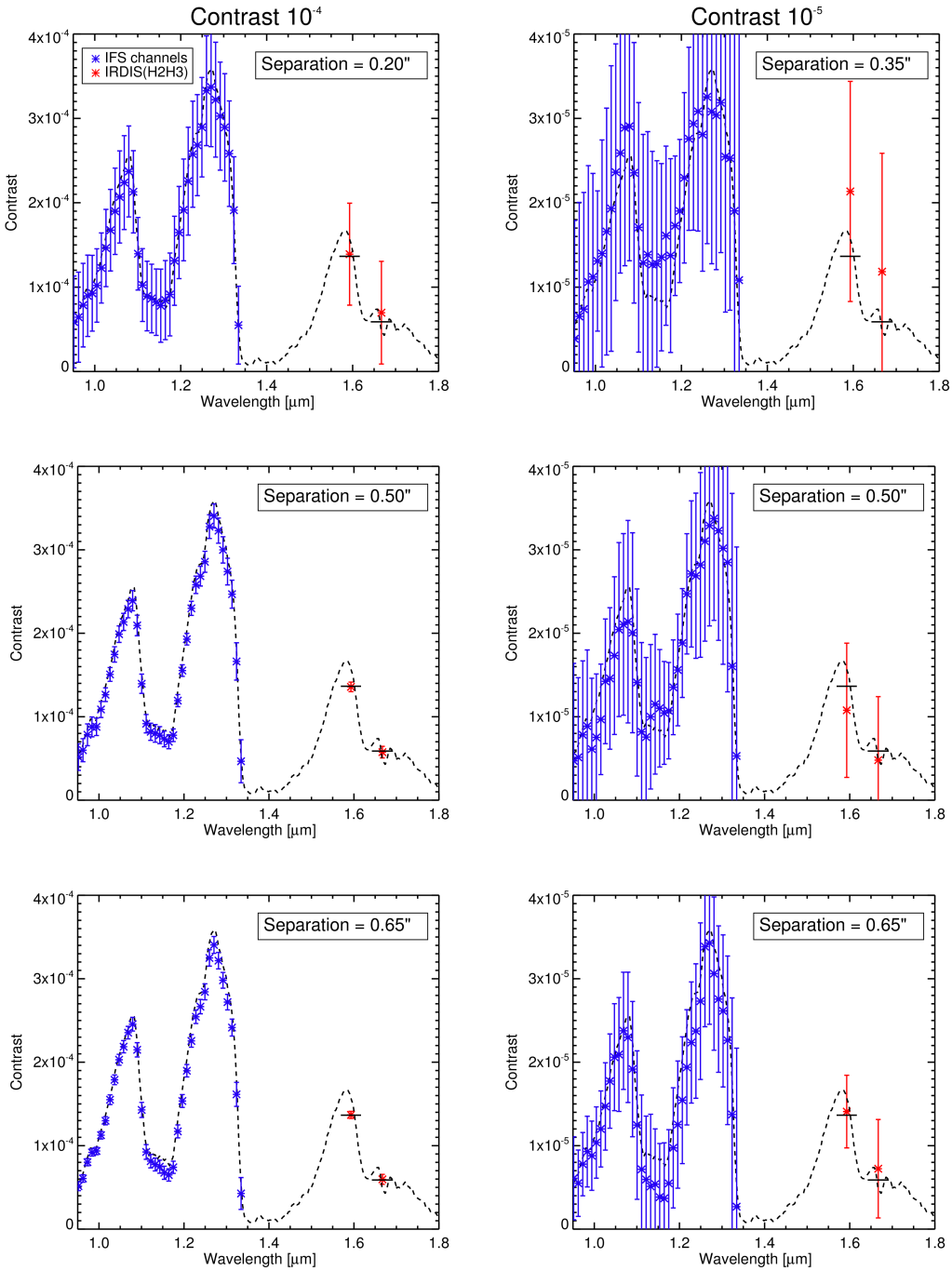

Figure 4.6: Spectral extraction of a T5 (T∼1100 K) model spectrum (black line) for planets at different separations (from top to bottom) and contrast from the star (10^{-4} on the left, 10^{-5} on the right). The blue points represent the IFS photometry for each channel (reduced with the SD technique), while the red ones represent the flux measurement in the two IRDIS filters $H2$ and $H3$. For IRDIS data, the black horizontal line represents the therotical value of the photometry; each line covers the bandpass of the filters.

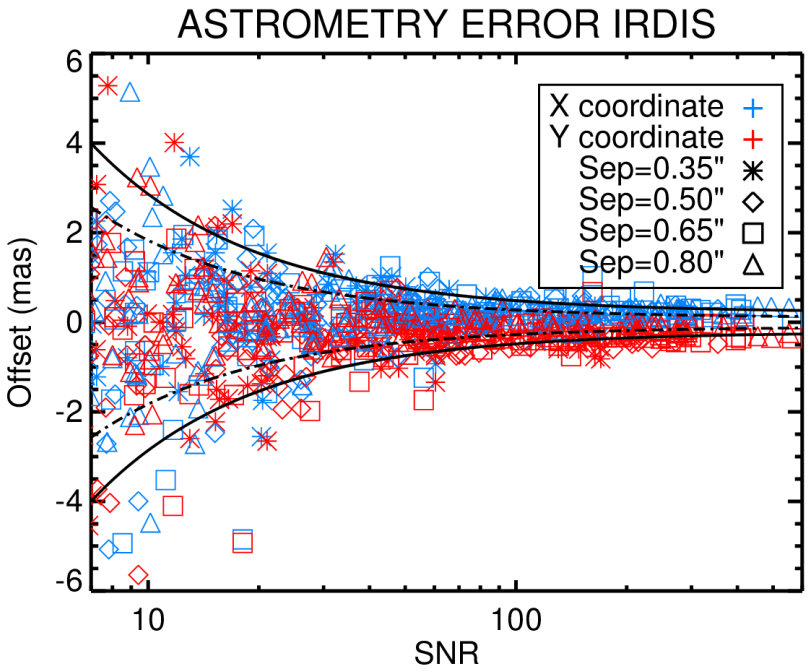

Figure 4.7: Plot of the difference between nominal and measured astrometric values for the two coordinates versus the S/N of each planet with contrasts from 10^{-5} to 10^{-3} and separations from 0″.35 to 0″.80 in the SDI image. The dashed black line represents Eq. 4.3. Different separations from the host star are represented with different symbols.

4.4.3 Astrometry with IRDIS

For the astrometric analysis, I used the same least-squares method presented in Sect. 4.4.2 to calculate the position of the simulated planets. The fit is done simultaneously with the photometric measurement, and the PSFs are shifted from their original position by 8 mas. The results for the case where the model PSF is different than the off-axis PSFs are presented in Fig. 4.7, where I plot the astrometric errors on both axes as a function of the S/N. In this figure, only detected planets (481 out of 600) are shown. Moreover, the planets at the closest separation of 0″.2 are not taken into consideration for this analysis because of the large uncertainties obtained for them.

To estimate the final error in the astrometry I calculated the standard deviation σ of these values and extrapolated their trend. The expected astrometric error for the relative planet-star position is shown in function of the S/N of the planets in Fig. 4.7. The curve overplotted (solid black line) is given by:

$$\sigma = 0.2 + \frac{26.4}{S/N}\ mas, \tag{4.3}$$

for the different PSF case, while for the ideal case is given by:

$$\sigma = 0.1 + \frac{17.3}{S/N}\, mas, \tag{4.4}$$

and plotted as a dashed line in Fig. 4.7. In this case, the minimization of the residuals is biased by the different shapes of the PSF and there is a rigid shift in the coordinates of the centroid found by the fit. A realistic case should fall in between the two boundaries described by Eq. 4.3 and 4.4.

From these results, I predict a relative astrometric precision for IRDIS from a few tenths to ~3 mas depending on the S/N of the candidate. This error also includes the error in the recentering introduced during the measurement of the waffle images and the shift of each frame, but it does not include the errors related to the absolute position of the planet (true north determination, distorsion, platescale orientation, ...).

4.4.4 Photometry with IFS

To estimate the errors on the photometry measurements with IFS after SD (as presented in Mesa et al., submitted) and KLIP reductions I performed PSF-fitting photometry on the data where I injected planets. I made this choice because there are 39 spectral channels for IFS, and a method similar to that used for IRDIS analysis would not easily converge. I first reduced the dataset presented in Sec. 4.3 with SD and KLIP method separately and then I applied the PSF-fitting on the planets. The position of the planets is found by `MPFIT`, as described in Sec 4.4.5.

The procedure consisted in comparing a different off-axis PSF for each spectral channel with the PSFs of the planets. The contrast is calculated pixel by pixel after the alignment of the centers of the PSFs of the star and the planet. The final result is calculated as the weighted median of all the pixels inside a radius of $1.2\lambda/D$, as described in the following equation:

$$Contrast = \iint \frac{\frac{flux(x,y)}{model(x,y)} \left(\frac{model(x,y)}{k}\right)^2}{noise_{bkg} + \frac{model(x,y)}{k}} dxdy. \tag{4.5}$$

Here k is a normalization constant, $noise_{bkg} = (bkg_B)^2/2$ (see Sect. 4.4.1), and $flux(x, y)$ is the value converted in ADU/s of the pixel (x,y) after subtraction of the background estimated in the same area B as described in Sect. 4.4.1 (Fig. 4.3). In this manner, the

central part of the PSF has a stronger impact than the wings. The same procedure was performed using a 2-d Moffat function that reconstructs the different off-axis PSF of the star, obtaining the same results.

As the procedures of the SD and the PCA generally cause a loss of flux of the planets, I tried to reduce this problem using a mask that protects the zones where the planets sit during the reduction. To calculate the errors on photometry for each channel of IFS, I calculated the standard deviation of the residuals of all the planets with the same separation, flux, and wavelength.

In order to improve KLIP results I used an implementation of the forward modeling presented in Soummer et al. (2012). To evaluate which method is better to use as a function of separation and contrast, I calculated the standard deviation of the photometry offsets obtained reducing the data with the SD and KLIP techniques. The results of this analysis are presented in Fig. 4.8. From this evaluation, I determined that in general KLIP works better for brighter objects and that its results are comparable with the results of the SD. Nevertheless, we expect that KLIP will greatly improve with the addition of the FoV rotation, which permits us to expand the part of the library without the signal from the object itself.

Examples of the extracted spectra for T5-type planets at contrasts of 10^{-4} and 10^{-5} and separations within the range of 0.2–0.8 arcsec are shown in Fig. 4.6, with error bars reflecting the dispersion of the results obtained with synthetic planets at different positions within the image.

As for IRDIS case, the use of a PSF taken in different conditions does not impact the spectrum extraction.

4.4.5 Astrometry with IFS

For astrometric measurements, I used the same procedures described as for IRDIS (see Sect. 4.4.3) with the only difference that the final step of the analysis, the minimization of the standard deviation in the aperture, is done on the median of all the IFS spectral channels.

After using the off-axis PSF taken right after the sequence and a PSF taken with different observation conditions as a model, as I did for IRDIS, I found that for the variable PSF case the method of the "negative synthetic planets" introduced larger error than finding the centroid of the planets with `MPFIT2DPEAK`, a routine that fit the image with a 2-D Gaussian profile. The difference of the two PSFs, for the case of IFS, has a peak-to-peak variation of 31% and a standard deviation of the 3%. Also, the wings of the PSFs are asymmetric and this fact could strongly affect the astrometry measurements. This is probably induced by the dependence of the IFS wavelength calibrations with time, as the two PSFs have been taken well separated in time (some months). As the IFS instrument is so sensitive to the

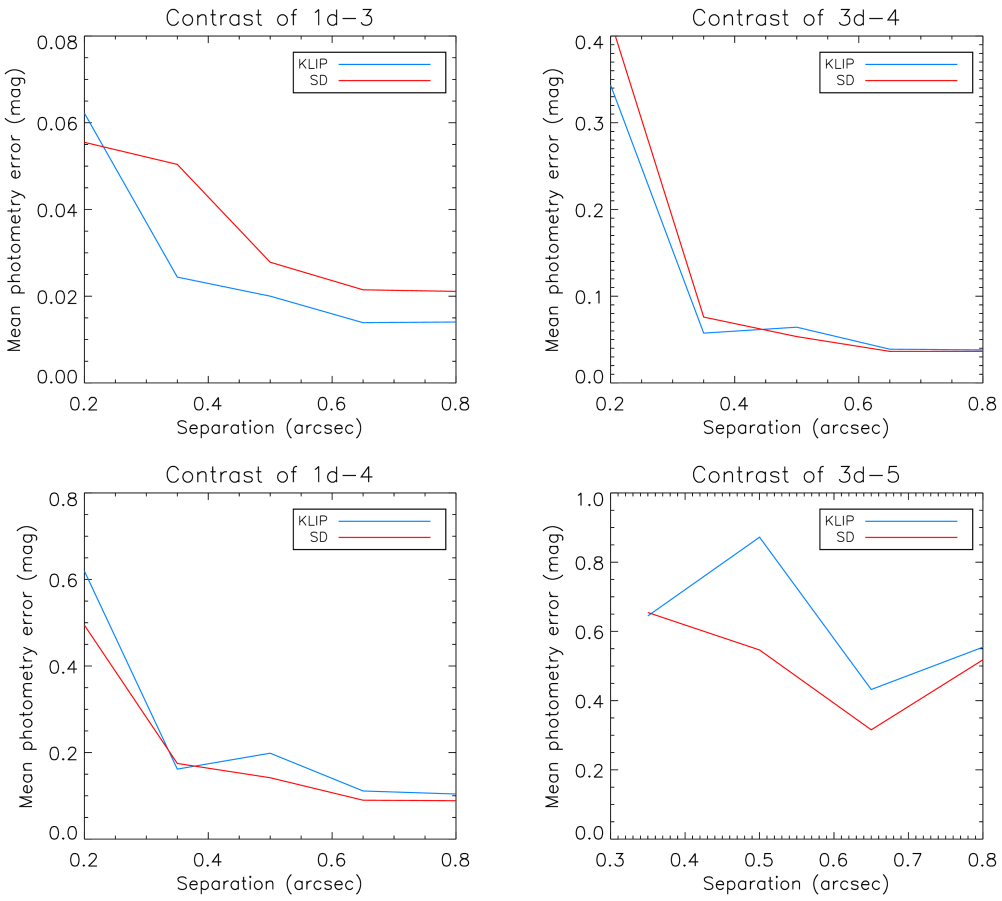

Figure 4.8: Plots of the expected photometric errors for different contrasts as a function of separation from the central star. Results obtained with KLIP (red line) and SD (blue line) are compared. Each point represents the median of the errorbar on the 39 IFS channels. Only detected planets are considered in this analysis. Very few planets with contrast of 10^{-5} are detected, as shown in Table 4.2, so the corresponding plot is not shown.

calibrations we expect that when observing on the sky, where calibrations are taken during the same night of the observation sequence, the shape of the PSF should be more stable.

I performed astrometric measurements both on SD and KLIP reduced datacubes. The expected error is calculated taking into account the dependency of the standard deviation of the offsets on the S/N of the candidates. The total numbers of detected planets (S/N > 5) are 523 and 441 out of 600 for the SD (with mask) and KLIP reductions, respectively. Planets with separation of 0″.20 are not considered in this analysis because of the very low number of detected planets at this separation.

I represent the astrometric offsets along the two cartesian coordinates for the SD analysis in Fig. 4.9, and for the KLIP analysis in Fig. 4.10.

I found that the trend of the standard deviation σ could be described by the following formulas for the SD:

$$\sigma_{SD} = 0.25 + \frac{34.26}{S/N}\ mas, \tag{4.6}$$

for the model-independent analysis, plotted as a solid line in Fig. 4.9, and for the ideal case is calculated as:

$$\sigma_{SD} = 0.15 + \frac{15.64}{S/N}\ mas, \tag{4.7}$$

and plotted as a dashed line. Concerning KLIP analysis, the error bar is given by:

$$\sigma_{KLIP} = 0.21 + \frac{28.94}{S/N}\ mas \tag{4.8}$$

for the model-independent analysis (`MPFIT2DPEAK`), plotted as a solid line in Fig. 4.10, and for the method of the "negative synthetic planets" with the same PSF is calculated as:

$$\sigma_{KLIP} = 0.05 + \frac{12.25}{S/N}\ mas, \tag{4.9}$$

and plotted as a dashed line.

I consider that trends represent the error on our relative astrometric measurements with IFS.

I can then predict that for a faint planet, with a contrast of 10^{-5}, the typical relative position error will be of the order of 3 mas at a separation of 0″.35 from the host star, while for a brighter planet with a contrast of $3{\times}10^{-4}$ will be of the order of 0.6 mas at the same separation. As discussed in the next Section, these results are comparable and even better to those obtained nowadays exploiting the ADI, even if they are obtained with only the use of SDI techniques.

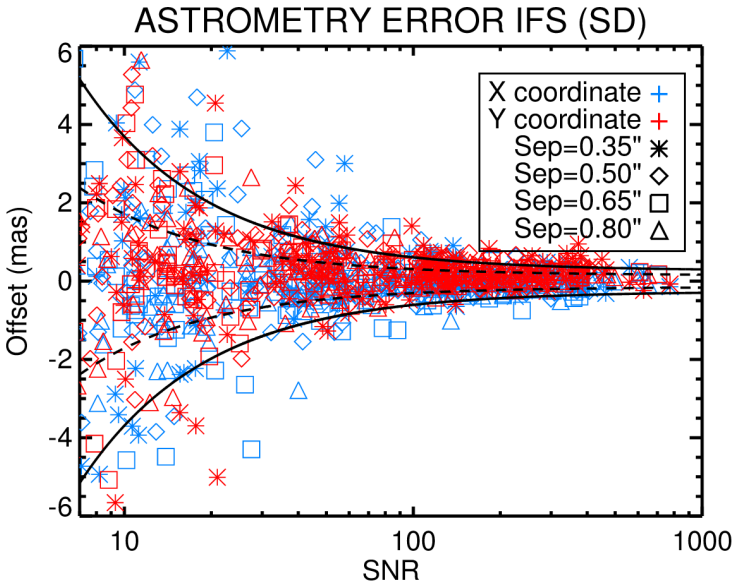

Figure 4.9: Plot of the difference between nominal and measured astrometric values for the two coordinates versus the S/N of each planet with contrasts from 10^{-5} to 10^{-3} and separations from 0″.35 to 0″.80 in the IFS datacube after SD reduction. The dashed black line represents Eq. 4.7. Different separations from the host star are represented with different symbols.

4.5 Conclusions

During the AIT phase of SPHERE, the new planet finder for the VLT, we had the opportunity of testing the instrument, acquiring data, and analyzing them, exploring the capabilities of the IRDIFS and IRDIFS_EXT modes. Using laboratory data and injecting synthetic planets into them, we were able to study the expected performance of these sci-

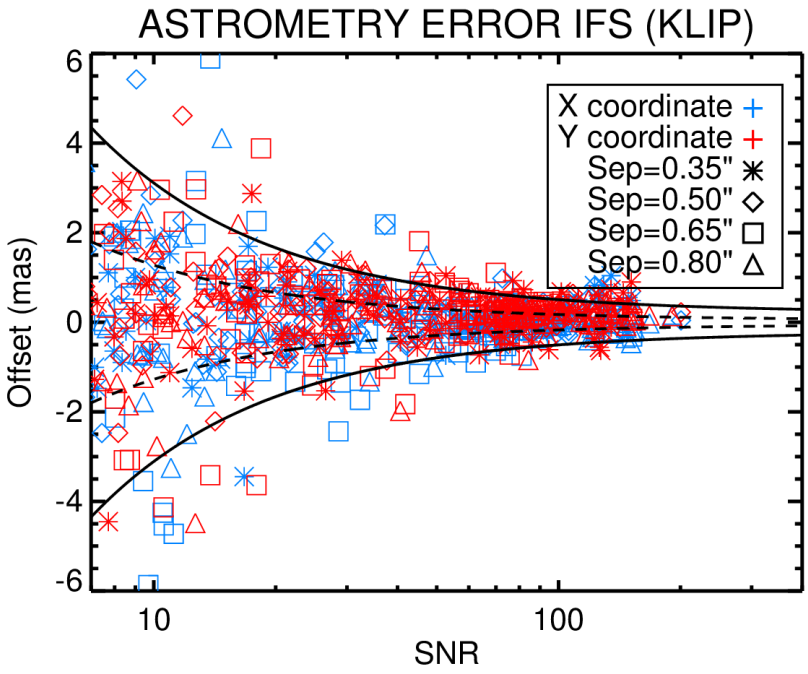

Figure 4.10: Plot of the difference between nominal and measured astrometric values for the two coordinates versus the S/N of each planet with contrasts from 10^{-5} to 10^{-3} and separations from 0″.35 to 0″.80 in the IFS datacube after KLIP reduction. The dashed black line represents Eq. 4.9. Different separations from the host star are represented with different symbols.

entific IRDIFS modules IRDIS and IFS, when working in parallel (IRDIS in $H2H3$ and IFS in YJ).

I performed the reduction of laboratory data using the SDI method for IRDIS, and the SD and KLIP methods for IFS. All of these methods provide good results in reducing the residual light from the primary star and detecting possible planetary candidates buried into the speckles pattern. As FoV rotation could not be simulated properly in the laboratory, our analysis does not include expected results using the ADI technique. Nonetheless, the 5-σ contrast limit that we can reach using only spectral diversity methods is around 14 mag for IRDIS at separation of 0″.5 from the host star, and 15 mag for IFS.

To study the photometric and astrometric accuracy, I injected 750 synthetic planets in the same set of raw data acquired in the laboratory in parallel with IRDIS and IFS. I calculated the expected errors on photometry, astrometry, and spectroscopy in function of the S/N of the recovered companions. When observing on the sky, together with these minimum expected errors, we will have to take into account the uncertainties related to calibrations (e.g., for astrometry the orientation of the platescale and the determination of

the true north). In order to reach these theoretical values of the errors accurate calibrations are needed.

Using IRDIS we expect to detect a bright object like the white dwarf around the star HD 8049, which has a H band contrast of $10^{-2.8}$ and a projected separation of 1″.56 (Zurlo et al. 2013), with a S/N of ∼270, an error on photometry of 0.045 mag and an error on the relative position of 0.2 mas. Using VLT/NACO, and exploiting the ADI, I have obtained errors of 0.12 mag on photometry and 7–10 mas on absolute astrometry.

The planet around β Pic is a 12 Myr old planet of ∼10 M_{Jup} and semi-major axis of 9–10 AU (Bonnefoy et al. 2013). If it would be detected with IRDIS, for a H band contrast of 10^{-4} and projected separation of 0″.5, the S/N would be of ∼22, the error on the photometry 0.16 mag and on the relative astrometric position the error would be of 1.1 mas. With VLT/NACO, typical errors are of the order of 0.2 mag for photometry and ∼13 mas for astrometry.

An error of 0.16 mag implies an uncertainty on the determination of the mass of the object of ∼0.5 M_{Jup} using COND or DUSTY models (Allard et al. 2000), or of the order of 1–2 M_{Jup} using core accretion models (Fortney et al. 2008). With IFS we would be able to retrieve a spectrum with error bars of the order of 0.15 mag on each channel and astrometric relative position error of 0.6 mas.

For fainter objects, such as the planets around the star HR 8799 (Marois et al. 2008b), SPHERE would be able to detect HR 8799d, 7 M_{Jup} planet at a distance of 27 AU (Marois et al. 2010b; Oppenheimer et al. 2013), with a relative astrometric error of 3 mas. Esposito et al. (2013), using LBT/PISCES, found an astrometric error of 10 mas.

All these results will be revisited, once we are observing on the sky, when we will also be able to take advantage of ADI techniques. In particular, we expect that the KLIP reduction will greatly improve with the FoV rotation because the condition of the signal-less library will be better satisfied (as described in Pueyo et al. 2014).

The possibility of having a precise photometry and astrometry will contribute to the rejection of false alarms and to the characterization of the candidates and their host stars. Photometry and spectrometry will help to determine the temperature, the spectral type (that could possibly exclude background stars with flat spectrum) and the chemical composition of the atmosphere for bright targets. Also, these data will make a great contribution to the study of the L-T transition (Best et al. 2013; Apai et al. 2013).

Astrometry with a precision of few mas will permit us to distinguish a background star from a comoving object over short temporal baselines for the follow-up. For example, the star β Pic has a proper motion of 83 mas/yr and the error bars on the position of the

companion would be 0.7% of the projected motion on the sky for one year. For HR 8799, that has a proper motion of 118 mas/yr error bars will be the 2% of the projected motion.

It is crucial to have high accuracy on the relative position of the planet to retrieve the orbital solution and discover possible perturbations due to other unseen planets. Astrometry could also give the possibility to calculate the mass of the companion by the motion of the primary with respect to the background object and it also opens the opportunity to determine the mass of stars in case of microlensing events (see, e.g., Sahu et al. 2014) in very favorable cases.

Chapter 5

Exploring the RV long period objects

So far, 592 planets have been discovered with the radial velocity (RV) technique*. Those objects' hosts have in general the common characteristics to be old and non-active stars, as this technique is hindered by the stellar activity. With this method both close planets and massive long period objects could be detected, but only the minimum mass could be determined. Surveys have been dedicated to the synergy between the RV technique and the direct imaging. We could cite three of them as examples: TRENDS (Crepp et al. 2012), the NICI follow-up on long period RV targets (Salter et al. 2014) and the Geneva follow-up of drift planets with direct imaging (Hagelberg 2010). The aim of these surveys is to follow up companions that show a RV drift. Objects with long periods are far from their host star and could be candidates for a direct imaging observation. In this Chapter we will consider a similar approach in view of an observing program planned for SPHERE.

First we selected all the RV planets with a projected angular separation (as listed in the input catalogues) from the host star greater than 0.″09 and with a declination lower than 40 degrees to be observable from the VLT. The sample includes nearly 60 objects from both *exoplanet.org* and *exoplanet.eu* databases (see plot in Fig. 5.1). Only planets with known parameters of the orbit have been included, objects with drift are not taken into account.

Using a Monte Carlo simulation we explored the intrinsic magnitude of the companion and its projected separation from the host star as function of its unknown orbital inclination. The projected separation of the targets at a given epoch is calculated with the Thiele-Innes formalism. Some of the objects of the sample have constraints on inclination from astrometry (see, e.g., Reffert & Quirrenbach 2011) that are included in the simulation. In order to predict the intrinsic magnitude of the planets we used the AMES-COND model of (Allard et al. 2003). As all the objects taken in consideration are not young ($>$ 1 Gyr) we do not expect the choice of the model to be crucial. The magnitude strongly depends on the age

*from exoplanets.eu

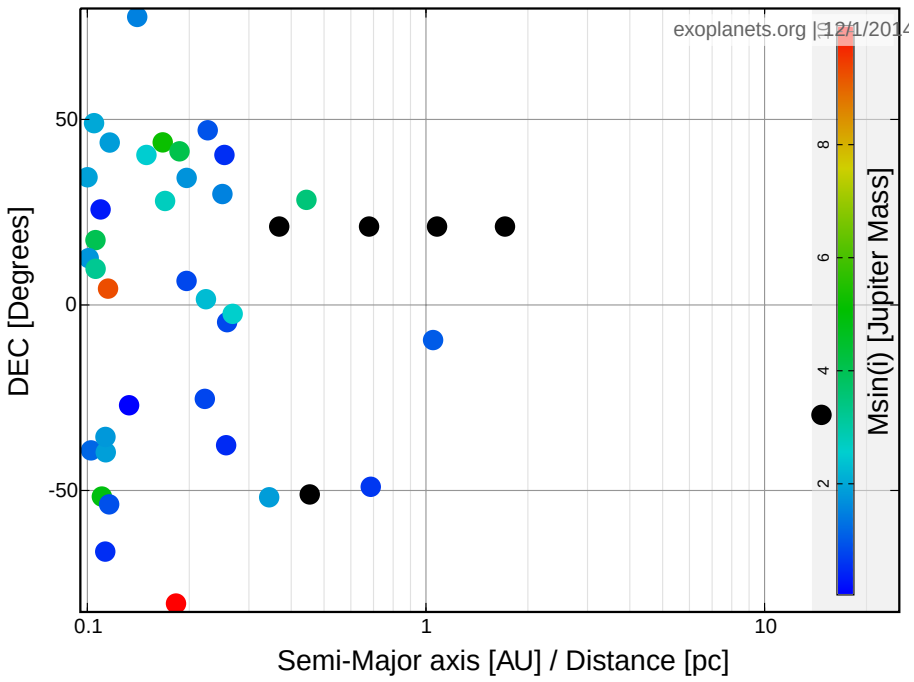

Figure 5.1: Current sample of long period objects from *exoplanet.org* database.

of the system, so the error bars are correlated to the uncertainty on the age of the host star. Most of the time we found the value of the age with error bars in the literature, where the age was not found we used the `PARAM` interface[†] (see da Silva et al. 2006, for details).

We explored the H, J, K_S bands contrast for each target that has points above the detection limit curve of the IFS instrument. To better understand the formalism used in the following Sections we refer the reader to Appendix A.

5.1 Best epoch of observation

I report some considerations about the best epoch of observation. Summarizing and recalling formulas from Sec. A.0.1 and Sec. A.0.2, the distance r planet-star is calculated using the equation:

$$r = \frac{a(1-e^2)}{1+e\cos(\theta-\varpi)}, \tag{5.1}$$

where θ is called the *true longitude*, a is the *semi-major axis*, e is the eccentricity and ϖ is the *longitude of the periastron*.

[†]http://stev.oapd.inaf.it/cgi-bin/param

We remember that from this Equation we derived the *Kepler's equation*, whose solution permits us to find the position of a planet given the time t:

$$n(t - T_P) = E - e \sin E. \tag{5.2}$$

Keeping in mind this formalism we can calculate the epoch of the maximum separation from a star.

It is quite intuitive that if the major axis lays on the line of the nodes the maximum distance will be the apoastron radius for all the inclinations. These cases are all the orbits with $\omega \approx 90°$ or $270°$. The projection of the apoastron radius on the line of the nodes is:

$$r_a = -a(1 + e)\cos(\omega) \tag{5.3}$$

as the *true anomaly* f of the descending node is $-\omega$, using Eq. A.10 and 5.3 we can deduce that the projected apoastron will be greater than the distance of the descending node for all the orbits with:

$$r_a > \frac{a(1 - e^2)}{1 + e\cos(-\omega)} \tag{5.4}$$

giving the result:

$$\frac{k\pi}{2} - \arccos(\frac{e - 1}{e} + k\pi) < \omega < \frac{k\pi}{2} + \arccos(\frac{e - 1}{e} + k\pi) \tag{5.5}$$

For all the orbits with ω that satisfies the latter equation the best epoch of observation is the apoastron passage. Otherwise the best epoch of observation will depend on the inclination of the system.

The projected apoastron radius on the plane of the sky is:

$$r_a = -a(1 + e)\cos i \tag{5.6}$$

so the best epoch will be the time of the descending node passage for:

$$\frac{k\pi}{2} - \arccos(\frac{e - 1}{e} + k\pi) < i < \frac{k\pi}{2} + \arccos(\frac{e - 1}{e} + k\pi) \tag{5.7}$$

In all the plots which will be presented in Sec. 5.3 both curves are shown. Depending on the value of the argument of the periastron we will find that the maximum separation is reached in one epoch or in the other.

5.2 Probability of detection

To predict the detection curve as a function of the projected separation for the IFS instrument we used the official ESO time calculator (ETC [‡]), assuming one hour of observation, the time we requested for the observations. We considered just the IFS curve as it can go deeper in contrast as small separations. One target could be detected if the contrast between its intrinsic luminosity and the magnitude of the host star is above the detection limits previously calculated.

Concerning the probability of detection, it is clear that massive objects, for a given age, have more chances of being detected. As we do not know the real inclination we just can infer which is the probability that the mass is greater than the minimum mass that permits the detection. For this aim, we used the *a posteriori* probability distribution of $sin(i)$ suggested by Ho & Turner (2011).

The inclination distribution *a priori* is isotropic with the constraints given by Reffert & Quirrenbach (2011).

The *a priori* probability distribution function of the observed mass M_0 given the real mass M_T is:

$$P(M_0 \mid M_T) = \frac{M_0/M_T^2}{\sqrt{1-(\frac{M_0}{M_T})^2}}. \tag{5.8}$$

If we want the *posterior* probability, using Bayes' theorem:

$$P(A \mid B) = \frac{P(B \mid A)P(A)}{P(B)}, \tag{5.9}$$

and assuming that

$$P(M_0) = \int P(M_0 \mid M_T)P(M_T)dM_T, \tag{5.10}$$

we finally obtain

$$P(M_T \mid M_0) = \frac{P(M_0 \mid M_T)P(M_T)}{\int P(M_0 \mid M_T)P(M_T)dM_T}, \tag{5.11}$$

that is the *posterior* distribution of the probability. We can write it as:

$$P(M_T \mid M_0) = \frac{\frac{M_0/M_T^2}{\sqrt{1-(\frac{M_0}{M_T})^2}}P(M_T)}{\int \frac{M_0/M_T^2}{\sqrt{1-(\frac{M_0}{M_T})^2}}P(M_T)dM_T}. \tag{5.12}$$

[‡]http://www.eso.org/observing/etc/bin/gen/form?INS.NAME=SPHERE+INS.MODE=IFS

If we want the probability of finding a mass greater than a value X:

$$P(M_T > X \mid M_0) = \frac{\int_{M_0}^{X} \frac{M_0/M_T^2}{\sqrt{1-(\frac{M_0}{M_T})^2}} P(M_T) dM_T}{\int_{M_0}^{M_{max}} \frac{M_0/M_T^2}{\sqrt{1-(\frac{M_0}{M_T})^2}} P(M_T) dM_T}. \tag{5.13}$$

Finally, to calculate the probability we need the distribution of the true mass $P(M_T)$. In this work we assumed that the distribution in the planetary regime is a power law function with index -1 (Heinze et al. 2010) and for the brown dwarf regime a power law with index approximately zero (Metchev & Hillenbrand 2009).

So, the function $P(M_T)$ is $\propto M^{-1}$ from M_0 to the upper limit of the brown dwarf desert and constant for greater values of the mass. The final function is the sum of the two different curves connected in the point where the mass is equal to the value of the upper limit of the brown dwarf desert. The boundaries of the brown dwarf desert are assumed to be 20-57 M_{Jup} (Grether & Lineweaver 2006).

If we want to know how many object we can detect with SPHERE in the substellar regime the upper limit of the mass is 80 M_{Jup}. If the physical maximum mass of the target is in the planetary regime we changed the upper limit of the integral.

In general we have to solve the integral:

$$y = \int_{M_0}^{X} \frac{M_0/M_T^2}{\sqrt{1-(\frac{M_0}{M_T})^2}} A M_T^{\alpha} dM_T \tag{5.14}$$

for $\alpha = -1$ and $\alpha = 0$.

$$y(\alpha = -1) = A \int_{M_0}^{X} \frac{M_0/M_T^3}{\sqrt{1-(\frac{M_0}{M_T})^2}} dM_T = A \frac{\sqrt{X^2 - M_0^2}}{M_0 X} \tag{5.15}$$

$$y(\alpha = 0) = A' \int_{M_0}^{X} \frac{M_0/M_T^2}{\sqrt{1-(\frac{M_0}{M_T})^2}} dM_T = A' \arccos(\frac{M_0}{X}). \tag{5.16}$$

We can split the two zones below and above the upper limit of the brown dwarf desert, $M_{des} = 57$ M_{Jup}, and the total area for the normalization is:

$$\Phi = A \int_{M_0}^{M_{des}} \frac{M_0/M_T^3}{\sqrt{1-(\frac{M_0}{M_T})^2}} dM_T + A' \int_{M_{des}}^{80 M_J} \frac{M_0/M_T^2}{\sqrt{1-(\frac{M_0}{M_T})^2}} dM_T, \tag{5.17}$$

where the constant $A' = A/M_{des}$ because we want the two curves to be connected in the value of M_{des}.

If the mass of detection is $M_0 \leq X \leq M_{des}$ then the probability is calculated through:

$$P(M_T > X \mid M_0) = 1 - \frac{A \int_{M_0}^{X} \frac{M_0/M_T^3}{\sqrt{1-(\frac{M_0}{M_T})^2}} dM_T}{A \int_{M_0}^{M_{des}} \frac{M_0/M_T^3}{\sqrt{1-(\frac{M_0}{M_T})^2}} dM_T + \frac{A}{M_{des}} \int_{M_{des}}^{80M_J} \frac{M_0/M_T^2}{\sqrt{1-(\frac{M_0}{M_T})^2}} dM_T} \tag{5.18}$$

that gives

$$P(M_T > X \mid M_0) = 1 - \frac{\frac{\sqrt{X^2-M_0^2}}{M_0 X}}{\frac{\sqrt{M_{des}^2-M_0^2}}{M_0 M_{des}} + \frac{1}{M_{des}} \arccos(\frac{M_0}{80M_J})}. \tag{5.19}$$

For $M_{des} < X \leq 80M_J$ in the same way we obtain:

$$P(M_T > X \mid M_0) = 1 - \frac{\frac{\sqrt{M_{des}^2-M_0^2}}{M_0 M_{des}} + \frac{1}{M_{des}} \arccos(\frac{M_0}{X})}{\frac{\sqrt{M_{des}^2-M_0^2}}{M_0 M_{des}} + \frac{1}{M_{des}} \arccos(\frac{M_0}{80M_J})}. \tag{5.20}$$

In this way we obtained the probability that an object is more massive than the minimum mass value for the detection and that it is not a stellar type companion.

5.3 Results

We present the final results. In the following plots I show the contrast between each target and its host star and the projected angular separation for the two epochs of the best epoch of observation (see Sec. 5.1) and the epoch of the observation (here assumed to be January 2015). The two passage times are shown in the upper part of the plot, with the corresponding probability of detection. The dashed green line is the detection limit of the IFS instrument in the JH configuration. All the results are summarized in Table 5.1. One of the RV selected targets has been observed during the early guaranteed time observing (GTO) in October 2014. Results on this target are presented in the dedicated Section 5.3.5.

5.3.1 Promising targets

- HIP 70849 Ab (Ségransan et al. 2011) is a 27 yr period, high eccentricity companion of the star HIP 70849 A. Its minimum mass is 9 M_{Jup}. The star is old, 1-5 Gyr, K7V type, at a distance of 24 pc. The minimum mass of detection is 26 M_{Jup}. There are no constraints from astrometry for this object. In the curve of Fig. 5.2 error bars include the incertitude on the age. Recently Lodieu et al. (2014) found a T4.5 brown

dwarf companion, HIP 70849 B, around the star. The separation is of 6.3 arcmin with a high probability of being bound to the system (false alarm probability of 0.027). This discovery makes the system a very interesting target for high-contrast imaging observations.

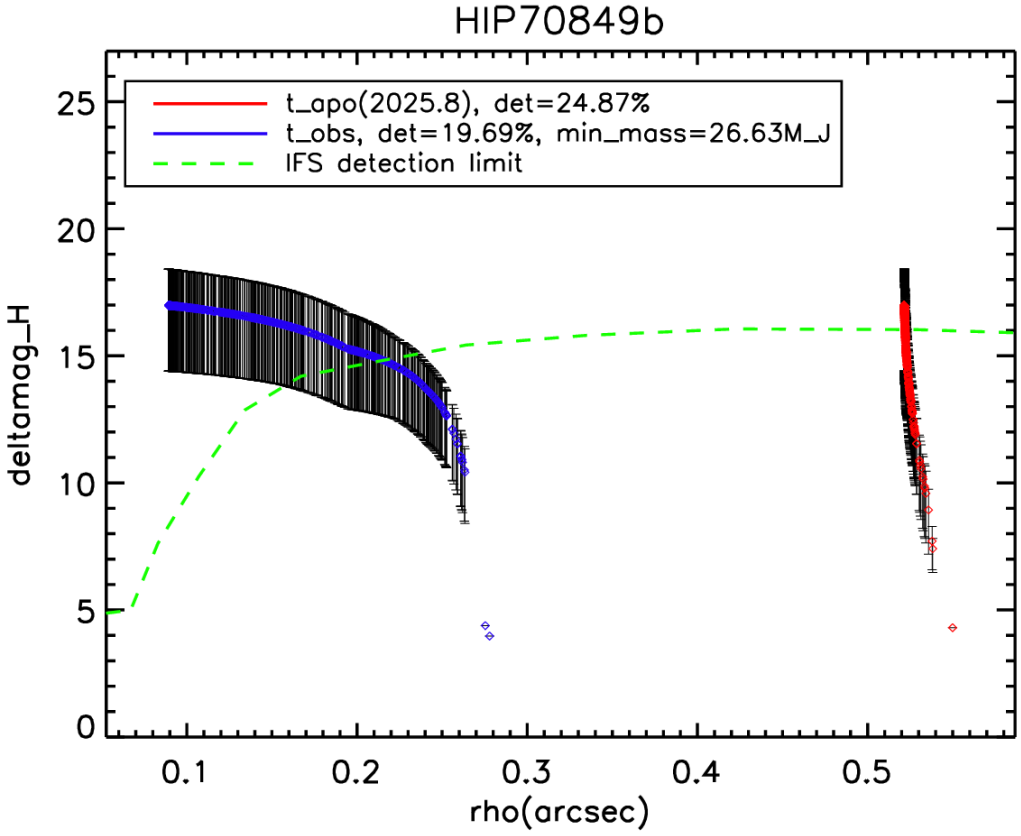

Figure 5.2: Contrast in *H* band of the planet HIP 70849 b. The green line shows the IFS detection limit. In the upper part of the plot are shown the probability of detection for the apoastron passage and the observation date (January 2015).

- GJ 676 Ab (Forveille et al. 2011) is a sub-stellar companion orbiting the binary star Gliese 676 A. The system is composed of two M stars, the primary has been classified as a M0V star (Koen et al. 2010). I calculated the age with the `PARAM` interface, as it is not available in the literature, which gives a value of 4 Gyr. I assumed an error of the 30% on this estimation. Its minimum mass is of 4.9 M_{Jup} and it has a period of 1056.8 days, low eccentricity and a distance of 16.4 pc. There are no constraints on inclination from astrometry. The minimum mass for the detection is 41 M_{Jup}

and the probability of detection is of the 10% (see Fig. 5.3). Anglada-Escudé & Tuomi (2012) rederived Doppler measurements in the HARPS South database for this system and found other planets candidates, GJ 676 A may host four sub-stellar companions. GJ 676 Ac, which shows a trend in the RV, could be also observable with SPHERE with a minimum mass of 19.3 M_{Jup}, as shown in Fig. 5.4. The orbital parameters are given by Forveille et al. (2011) but the incertitude is high.

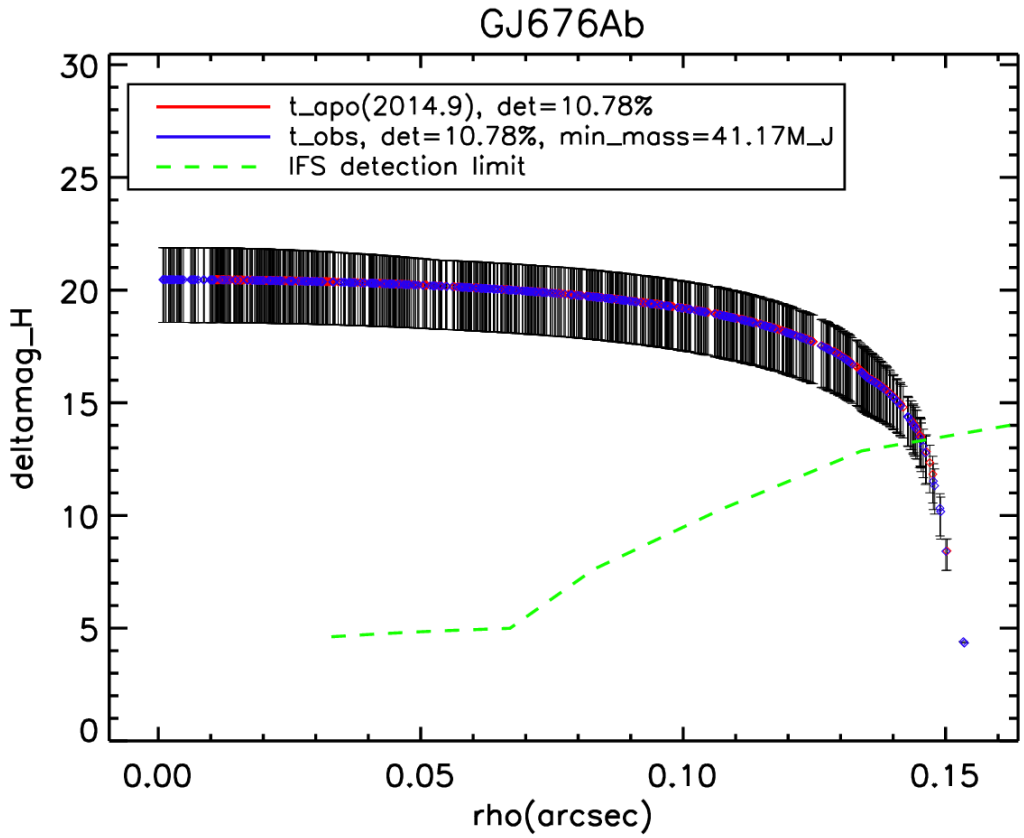

Figure 5.3: Contrast in *H* band of the planet GJ 676 Ab. The green line shows the detection limit. In the upper part of the plot are shown the probability of detection. The incertitude on the age is taken into consideration in the error bars. The observation time is consider to be January 2015.

- HD 217107 c (Vogt et al. 2005) is a 4270 days period orbit, minimum mass 2.62 M_{Jup} planet. Its host star is a 7.32 Gyr old G8IV star of the constellation of Pisces, 19.86 pc

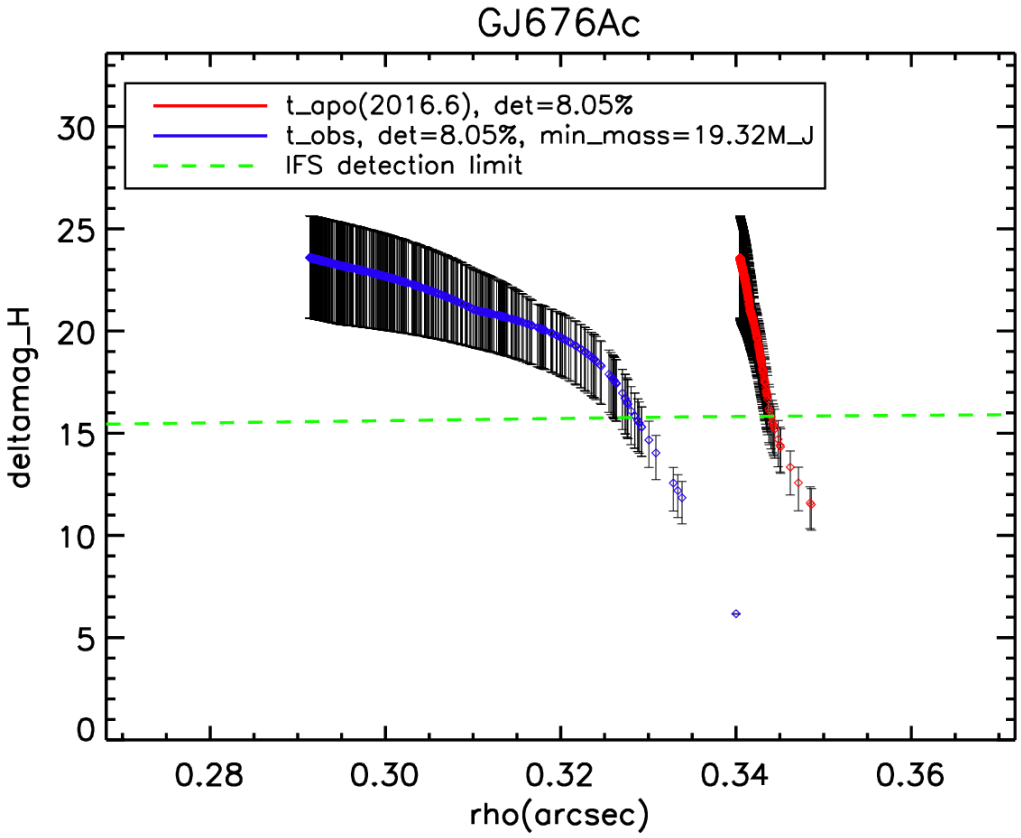

Figure 5.4: Contrast in H band of the planet GJ 676 Ac. The green line shows the detection limit. In the upper part of the plot are shown the probability of detection. As the planet shows just a trend in the RV, the orbital parameters are just indicative, the plot is preliminary. The observation time is consider to be January 2015.

away from us. The separation from its host star is always greater than 0.″1 (blind part of the detector behind the coronagraph), so the time of observation does not influence the probability of detection. The minimum mass for the detection is 42 M_{Jup} at the apoastron passage in 2016 (Fig. 5.5). The star also hosts a hot-Jupiter, HD 217107 b (Fischer et al. 1999).

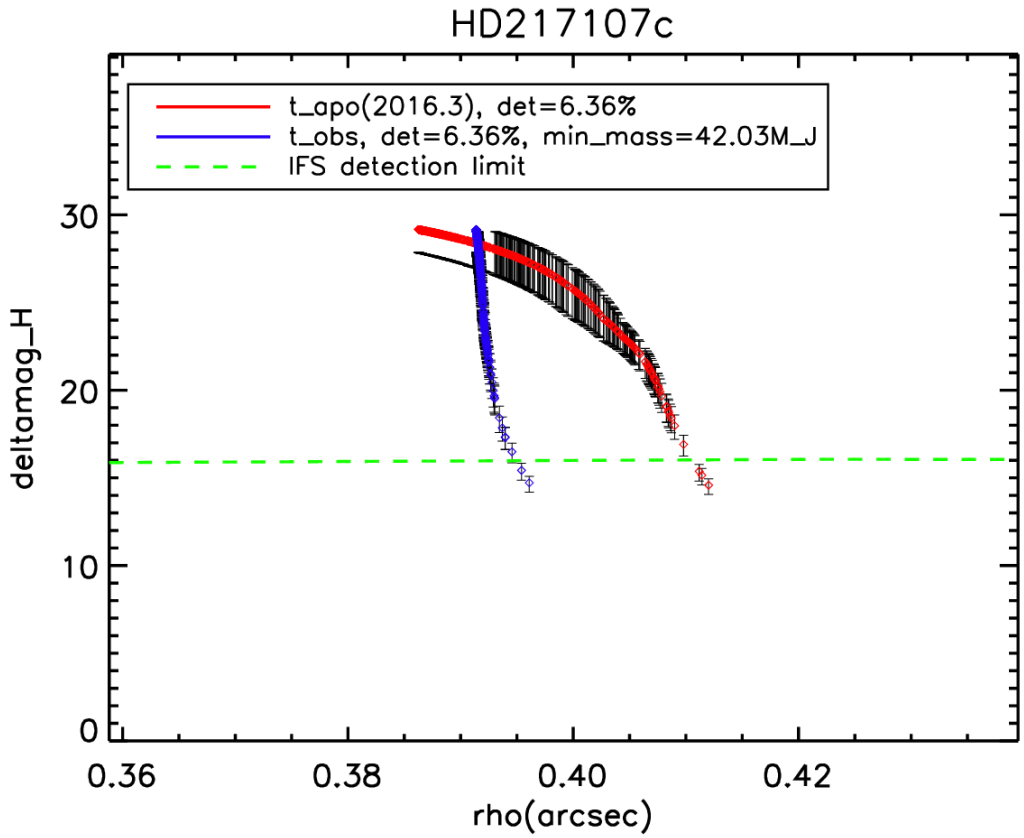

Figure 5.5: Contrast in *H* band of the planet HD 217107 c. The green line shows the detection limit. In the upper part of the plot are shown the probability of detection.

5.3.2 Stellar objects

- HD 33636 B (Vogt et al. 2002) was initially identified as a sub-stellar companion. The strong constraints on the inclination given by Bean et al. (2007) makes this object cataloged as a star. The orbit is nearly pole-on, with a period of 2127.7 days and an eccentricity of 0.48. Its mass is of 0.14 $M_{\odot}$ and it orbits around a 3.38 Gyr old, G0

star, 28.37 pc away from us. The target must be observed near the apoastron to be separated enough from the star, so the best epoch is during 2019 (see Fig. 5.6).

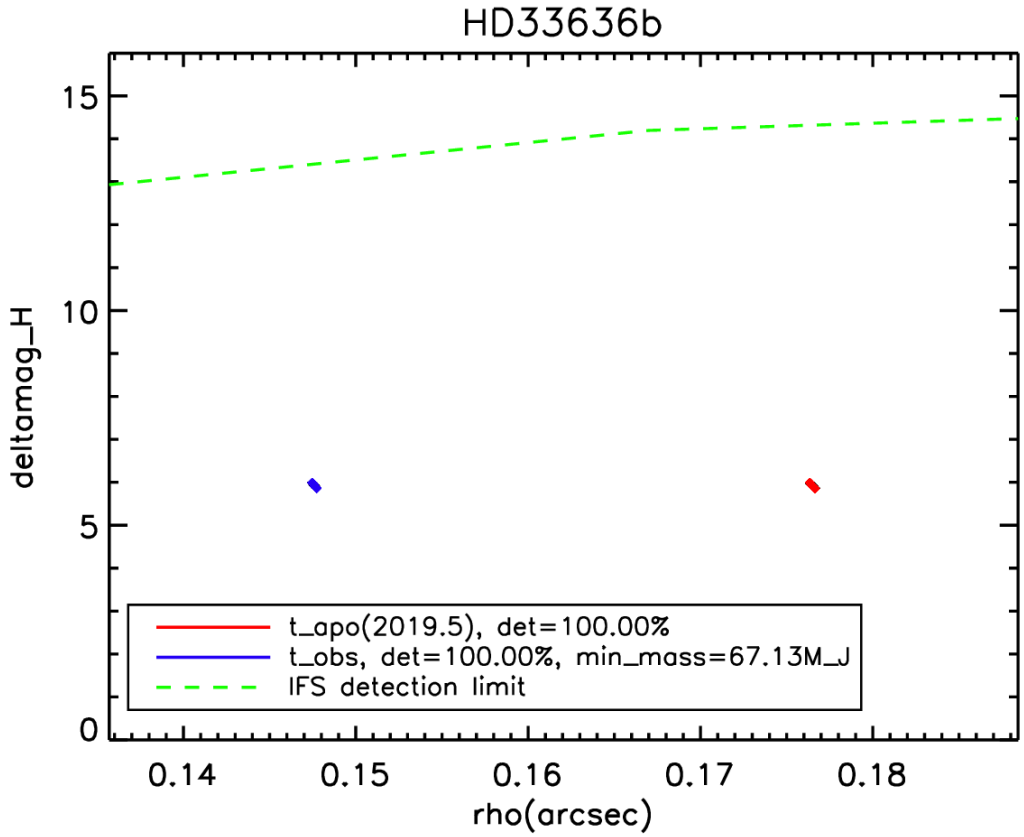

Figure 5.6: Contrast in *H* band of the stellar companion HD 33636 B. In the upper part of the plot are shown the probability of detection.

5.3.3 Low probability of detection (less than 5%)

- HD 7449 c (Dumusque et al. 2011) orbits a 2.1 Gyr old F8V star. The planet has a minimum mass of 2 M_{Jup} and a period of 4046 days, high eccentricity (0.53). The probability of detection is low, as shown in Fig 5.7. The star host also the inner companion HD 7449 b.

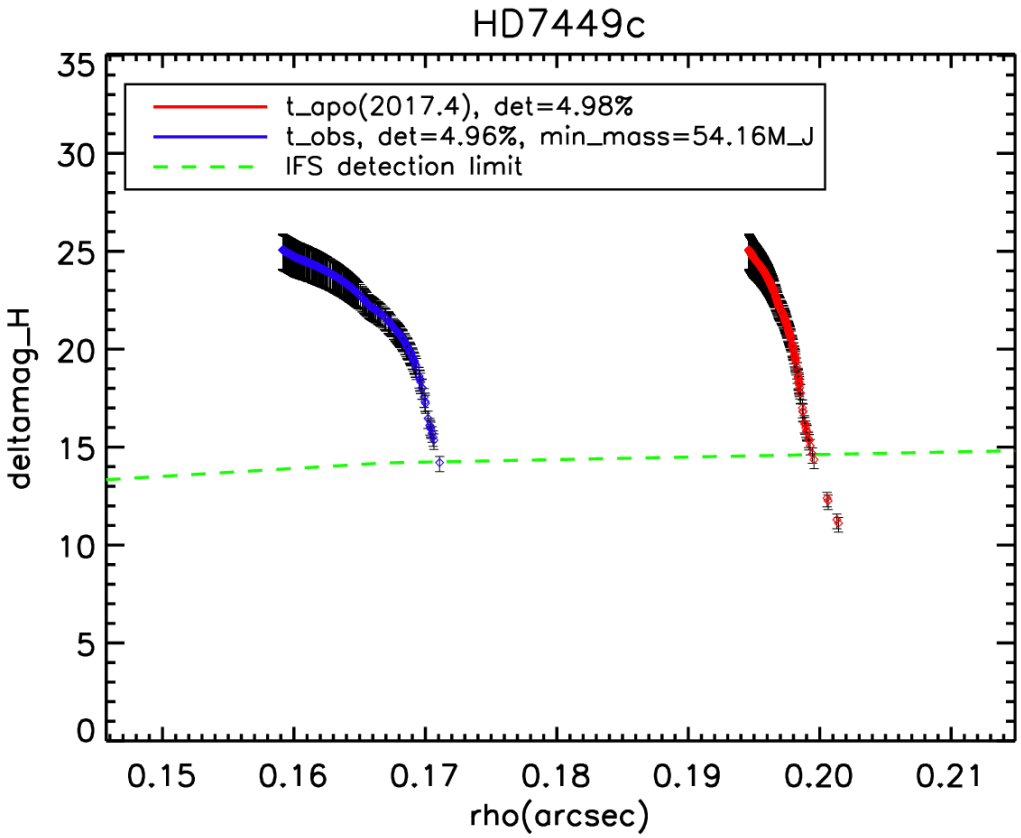

Figure 5.7: Contrast in *H* band of the planet HD 7449 c. The green line shows the detection limit. In the upper part of the plot are shown the probability of detection.

5.3.4 Non detectable targets

- HD 39091 b (Jones et al. 2002) is a massive object with a minimum mass of 10.09 M_{Jup}, long period (2151 days), very eccentric (0.641) orbit, 18.32 pc from us. It orbits a 3.83 Gyr old, G1 star. Given the strong astrometric constraints (Reffert & Quirrenbach 2011) the possibility of detection is zero, as shown in Fig. 5.8. The astronomical constraints are directly taken into account in the simulation, when generating all the possible random inclinations.

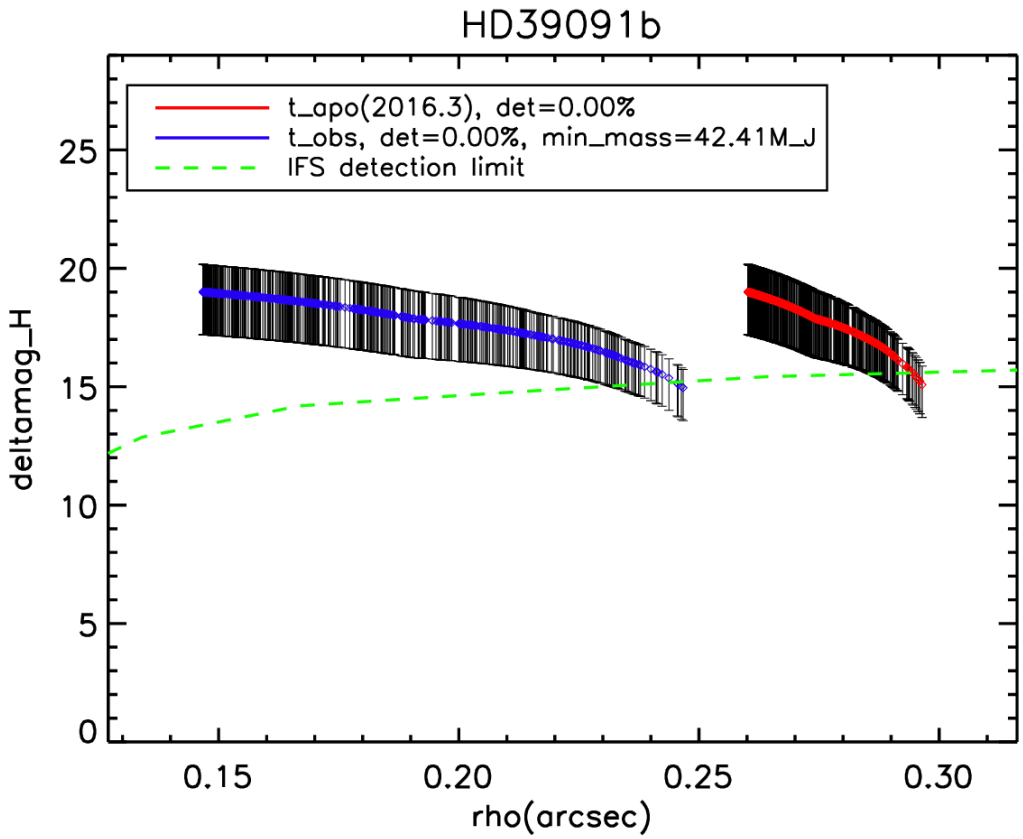

Figure 5.8: Contrast in H band of the companion HD 39091 b. The green line shows the detection limit. In the upper part of the plot are shown the probability of detection.

- ϵ Eri b (Hatzes et al. 2000), even if it is a very young planet (660 Myr), is not detectable by SPHERE according to the strong constraints in astrometry given by Benedict et al. (2006), as shown in Fig. 5.9.

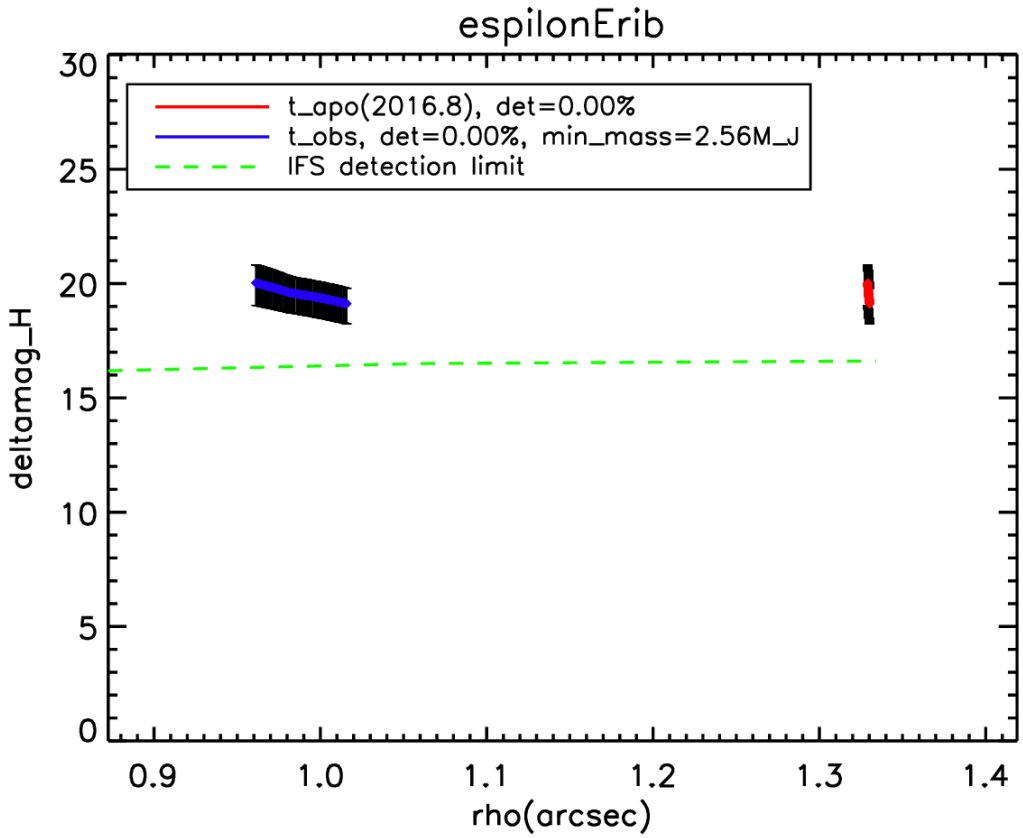

Figure 5.9: Contrast in H band of the planet ϵ Eri b. The green line shows the detection limit. In the upper part of the plot are shown the probability of detection.

Name	**msini**(M_{Jup})	**P**(days)	**e**	**d**(pc)	$\mathbf{i}_{min}(^{\circ})$	$\mathbf{i}_{max}$	**age**(Gyr)	**epoch**	**R.A.**	**Dec**	**mass det**(M_{Jup})	**prob**(%)
HIP 74849 b	9	10000	0.6	24	0	360	3	2025.8	14:29:19	-46:27:50	27	20
GJ 676 Ab	4.90	1057	0.3	16.45	0	360	4.00	2014.93	17:30:11	-51:38:11	41	11
GJ 676 Ac	3.0	4400	0.2	16.45	0	360	4.00	-	17:30:11	-51:38:11	41	8
HD 217107 c	2.62	4270	0.5	19.86	0	180	7.32	2016.34	22:58:15	-02:23:43	42	6
HD 33636 B	9.27	2128	0.5	28.37	3	177	3.38	2013.64	05:11:46	+04:24:13	-	100
HD 7449 c	2.00	4046	0.5	39.00	0	360	2.10	2017.42	01:14:29	-05 02 50	54	5
HD 39091 b	10.09	2151	0.6	18.32	20	150	3.83	2016.30	05:37:08	-80:28:18	42	0
ϵ Eri b	1.08	2500	0.2	3.22	26	34	0.66	2016.77	03:32:56	-09:27:29	-	0

Table 5.1: Summarizing table of the results found by the Monte Carlo analysis on the RV long period objects.

5.3.5 On sky data during pre-early GTO

During the early GTO of SPHERE one of the RV targets which I selected has been observed: HD 142 A (Wittenmyer et al. 2011). As the possibility of detection was quite high and the period was suitable to observe the target, I proposed it for the early observations of October. The expected possibility of detectability of HD 142 Ac is shown in Fig. 5.10. This target is particularly interesting because it is a binary star that hosts two planets, the distance of the system is 26 pc. HD 142 Ac has a minimum mass of 5.3 M_{Jup}, a low eccentricity of 0.21, and a period of 6005 days. HD 142 A has been observed during the night of the 13th of October 2014, in NIRSUR mode (IRDIS in H2H3, IFS in YH, see Chapter 2). The object has been observed during the meridian passage and the total FOV rotation was of 35.24 deg.

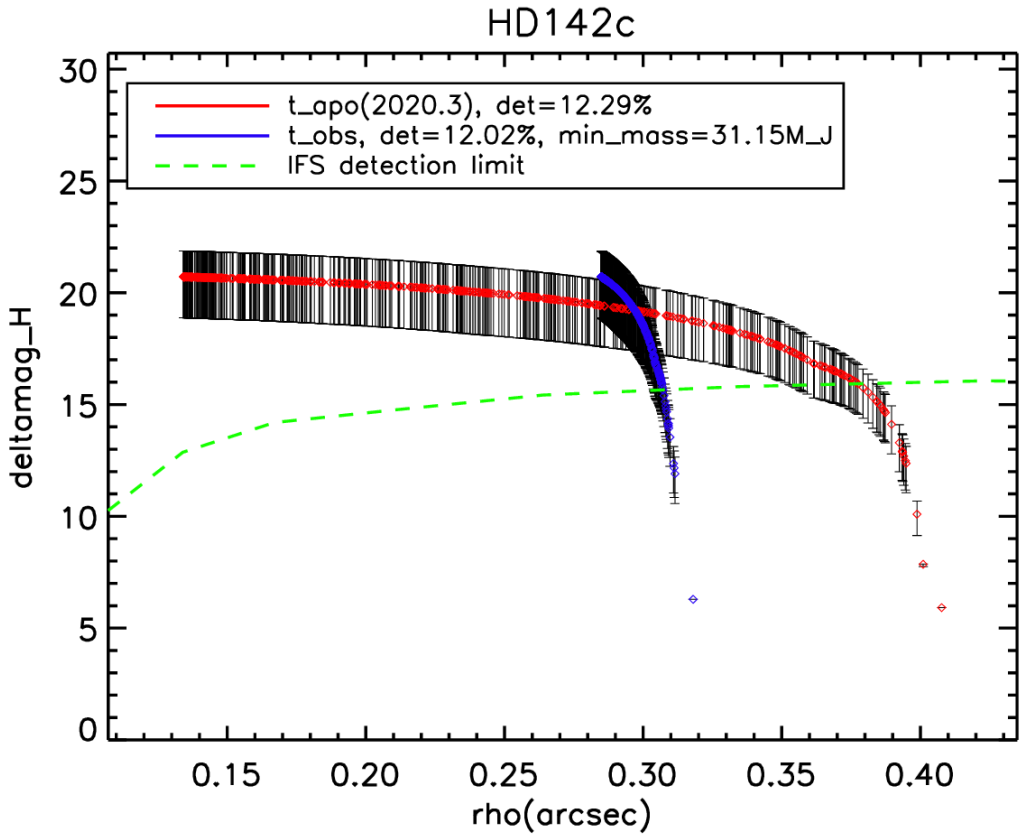

Figure 5.10: Contrast in *H* band of the planet HD 142 Ac. The green line shows the detection limit calculated with the ETC, as in the previous Section. In the upper part of the plot are shown the probability of detection.

We reduced and analyzed both IRDIS and IFS data. No object has been detected neither in the expected position of planet c, separation of 0.″3, nor at any other separations, see reduced ADI+SDI image in Fig. 5.11. To infer an upper limit on the mass of the companion we calculated the detection limits, shown in Fig. 5.12.

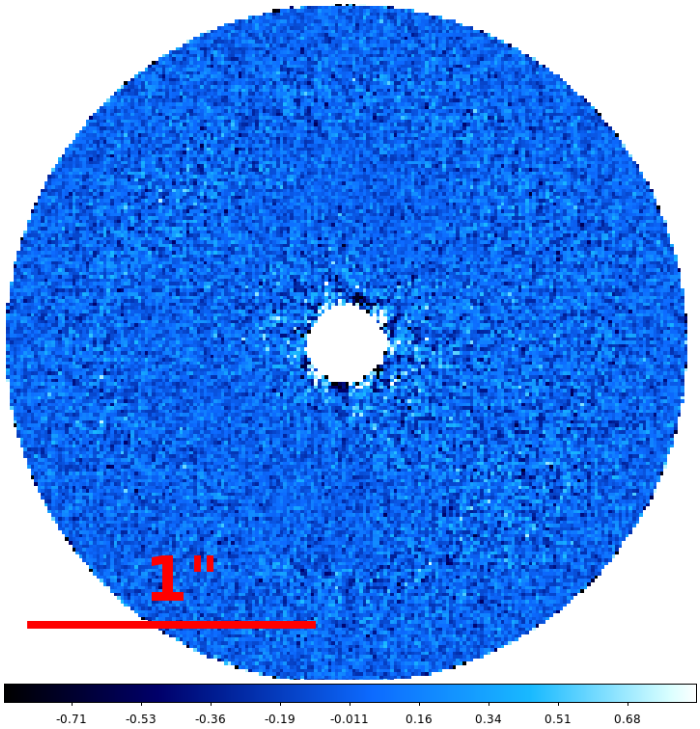

Figure 5.11: SDI+ADI reduction of SPHERE/IRDIS $H2H3$ channels for the object HD 142 A. In the detector no point above 5σ is detected.

Following this limits and attributing to this object the age of 2.6 Gyr, as recently estimated in Ramírez et al. (2014), we can put an upper limit for the mass of HD 142 Ac of $\sim$ 30 M_{Jup}, using AMES-COND models (Allard et al. 2000) and considering the planet at the expected separation. With respect to the expected curve calculated with the ETC we go slightly deeper, reaching a sensitivity to detect a 30 M_{Jup} object rather than 31.15 M_{Jup}. As seen in 5.12 the estimation of the ETC, used during the simulations, is pessimistic. This means that for good atmospheric conditions the probability of detecting low-mass objects increases.

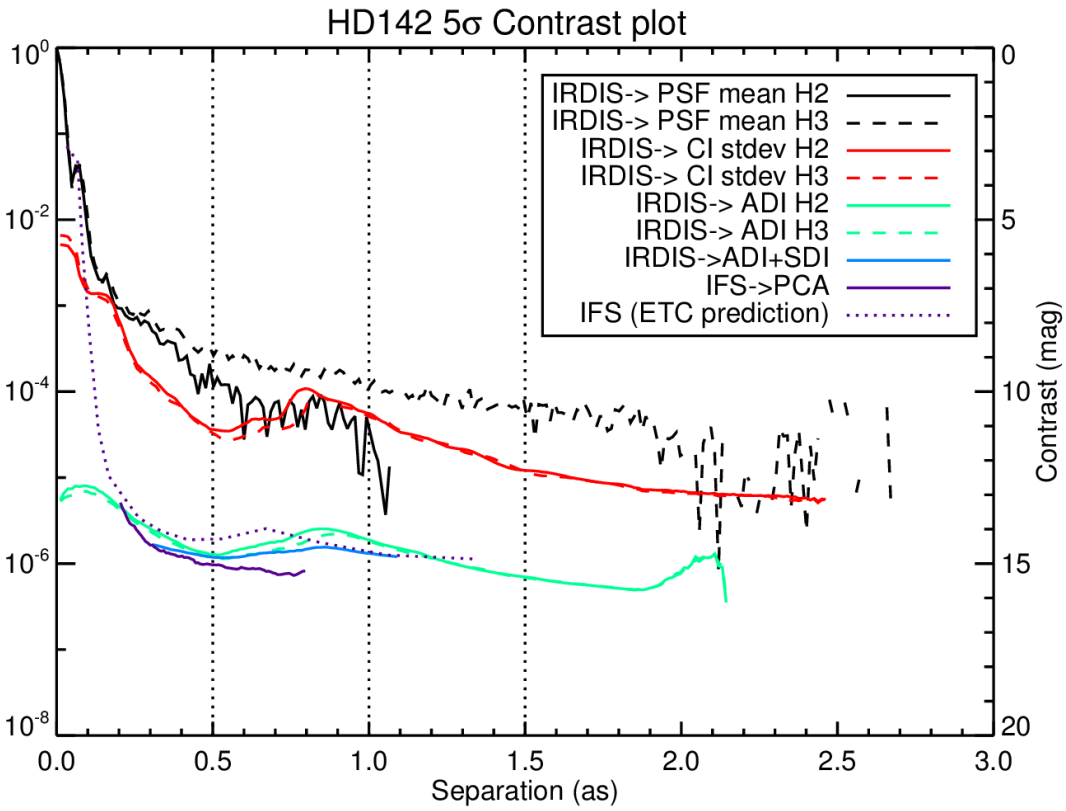

Figure 5.12: 5σ residual noise levels, for the two science modules in IRDIFS mode. The curves refer to the observations of HD 142 A. The mean azimuthal profile of the off-axis PSF (black), the coronagraphic profile (red) are shown for the two IRDIS channels $H2$ (continuous line) and $H3$ (dashed line). The contrast results after the ADI reduction (green), ADI+SDI (light blue) and PCA reduction for IFS (purple), where the self-subtraction effect is considered, are shown. The contrast estimated by the ETC is pessimistic.

Using the QMESS (Bonavita et al. 2012, 2013) Monte Carlo simulation I explored the probability of detection of the object around HD 142 A, in the parameter space of mass vs semi-major axis. The result of the simulation is shown in Fig. 5.13.

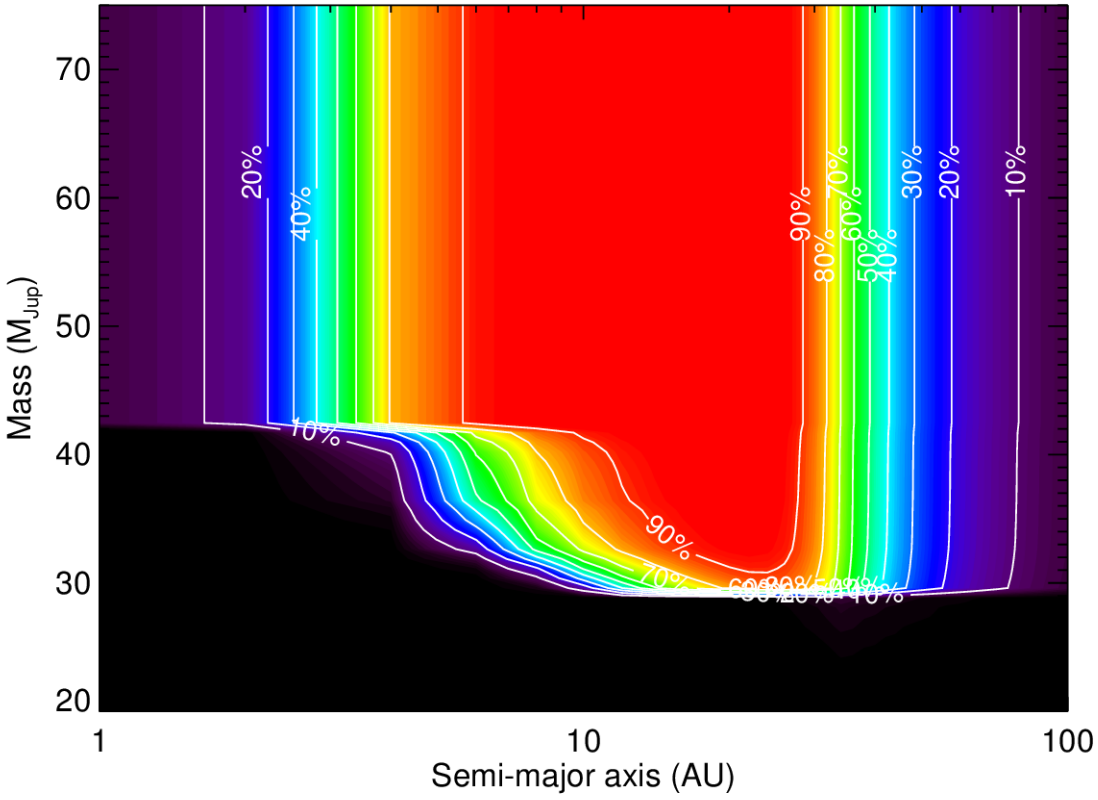

Figure 5.13: Result of QMESS simulation which explores the probability of detection in the parameter space of mass vs semi-major axis for the planet around HD 142 A.

5.4 Conclusions

The possibility of detecting a companion of known dynamical mass through the direct imaging technique is a unique opportunity to prove the evolutionary models that we use to characterize these objects.

For this reason I collected from the literature all the RV planets with a separation and position on the sky such as they are detectable by SPHERE. With this selection I performed a Monte Carlo simulation that includes the parameters of the orbit and explores all the possible inclinations in the range permitted by astrometric constraints.

The result of the simulation is the expected contrast, with respect to its host star, that each object would have in a fixed observation date. We confronted that contrast to see if the object is enough bright to be detectable by SPHERE/IFS. The contrast curve of the instrument has been calculated with the ETC of SPHERE. We found five promising candidates which show a high probability of detection: HIP 74849 b, GJ 676 Ab, GJ 676 Ac, HD 217107 c, and HD 142 c. These objects will be observed during the GTO of SPHERE, and they will give an upper limit on the mass of these planets in case of non-detection. In the case of detection, we will, for the first time, have at the same time the dynamical mass of the object and the estimated mass from the models.

I found an object, that has a stellar mass from the astrometrical constraints, that is easily detectable by SPHERE/IFS: HD 33636 B. This low mass star is also included in the GTO target list to compare the prediction of the mass from the models and the dynamical mass.

I found a companion with a low probability of detection: HD 7449 c. This object will be observed but it will be very challenging have a detection of the planet.

I finally found two targets that are not detectable with SPHERE if we include the tight constraints on the astrometric measurement: HD 39091 b and ϵ Eri b. The latter in particular will be observed by ZIMPOL in visible light to study the controversy nature of this candidate planet.

One of the promising targets, HD 142 c, has been observed during the early-GTO in October, in IRDIFS, the typical observing mode of NIRSUR (see Chapter 2). No detection is found in the two detectors of IRDIS and IFS. This permits anyway to put an upper limit on the mass of its companion, that I calculated to be lower than 30 M_{Jup} using AMES-COND models (Allard et al. 2000) and considering the planet at the expected separation.

Chapter 6

HR 8799

* The intriguing planetary system around HR 8799 is one of the most interesting objects in the field of extrasolar planets. Four giant planets have been detected (HR 8799 bcde; Marois et al. 2008b, 2010b) as well as a double debris belt (Su et al. 2009; Hughes et al. 2011; Matthews et al. 2014).

HR 8799 is a γ Dor-type star (Gray & Kaye 1999), its age has been estimated to be 20-160 Myr (Cowley et al. 1969; Moór et al. 2006; Marois et al. 2008b; Hinz et al. 2010; Zuckerman et al. 2011; Baines et al. 2012), and the distance of the system is 39.4 pc (van Leeuwen 2007). This system is a benchmark for the study of young, gaseous giant planets formation and evolution, and for this reason it has been observed and analyzed in many papers during the last years. The planets are bright enough ($\Delta H \sim 12$ mag) and separated from their host star (15-70 AU) such as they are relatively easy to detect by the current instruments and optimized image processing. For the given range of ages of the system, the measured luminosities of the planets suggest masses around 5-7 M_{Jup} (Marois et al. 2010b; Currie et al. 2011; Sudol & Haghighipour 2012), in agreement with with the upper limits set by dynamical stability studies of the system (Goździewski & Migaszewski 2014).

So far, studies of the atmospheres of HR 8799 bcde were conducted using mostly photometric measurements in the near infrared. The system has been detected by several instruments, providing broad-band photometry and/or astrometry in z, J, H, K, L, M filters (Marois et al. 2008b; Lafrenière et al. 2009; Marois et al. 2010b; Hinz et al. 2010; Janson et al. 2010; Serabyn et al. 2010; Currie et al. 2011; Hinkley et al. 2011a; Galicher et al. 2011a; Soummer et al. 2011; Skemer et al. 2012; Esposito et al. 2013; Skemer et al. 2014). A new generation of high-contrast imaging instruments such as SPHERE, GPI, ScEXAO+CHARIS, Project 1640 (Beuzit et al. 2008; Macintosh et al. 2014b; McElwain et al. 2012; Hinkley et al. 2011b) can now provide the spectra of these objects, allowing a

*An adapted version of this work will be published in Zurlo et al. 2015

deeper study of their chemistry and physical properties. Currently, spectra of the companions have been extracted in JH band for planets b, c, d, and e by Project 1640 (Oppenheimer et al. 2013), in H and K bands using the instruments Keck/OSIRIS (Larkin et al. 2006) for planets b (Barman et al. 2011; Bowler et al. 2010) and c (Konopacky et al. 2013), exploiting GPI for planets c and d (Ingraham et al. 2014), and in 3.88-4.10 μm with VLT/NACO for planet c (Janson et al. 2010).

The state of the art of the analysis of the atmospheres presents a complex picture of the objects of this system, and *ad hoc* models are needed to fit the spectrophotometric data. The planets around HR 8799 show non-equilibrium chemistry in the atmospheres and they appear dustier than field objects at the same effective temperature (Currie et al. 2011). In fact, HR 8799 bcde are brighter at 3.3 μm than the equilibrium chemistry models derived for old brown dwarfs, which suggests that they are not as opaque as expected, because of the lack of CH_4 in the atmosphere (Skemer et al. 2012). To obviate the discrepancies of between models and data, a patchy cloud coverage has been suggested by Currie et al. (2011), Skemer et al. (2012), Marley et al. (2012), and Morley et al. (2012). Madhusudhan et al. (2011b) proposed a set of models which are intermediate between two sets of models, one where in the first the physical extent of the clouds is truncated at a given altitude, and a second one where clouds extend all the way to the top of the atmosphere. The fact that we need thick clouds and non-equilibrium chemistry to fit the observables could be related to the low surface gravities of the planets around HR 8799 (Madhusudhan et al. 2011b; Marley et al. 2012). Finding a good set of parameters to obtain models which fit the spectra of this planetary system is extremely challenging.

In this Chapter I present the data obtained with SPHERE on the system. I measured photometry in J, H and K bands and astrometry for the four planets and extracted YH band spectra for planets d and e. Then I give an updated interpretation of the complex atmospheres of the HR 8799 planets, taking advantage of the exquisite quality of the data obtained.

6.1 Observations

We observed HR 8799 in three different nights during the SPHERE commissioning runs and in four different nights during science verification. I refer the reader to Beuzit et al., in prep. for a detailed description of the sub-systems and the observing modes of SPHERE. Two sequences were acquired with the integral-field spectrometer IFS (Claudi et al. 2008b) and the dual-band imager IRDIS (Dohlen et al. 2008b) in dual-band imaging mode (Vigan et al. 2010b) working in parallel. The last sequence was taken with IRDIS alone in the

Table 6.1: Observations of HR 8799 during SPHERE commissioning and science verification runs.

UT date	IRDIS Filter	IFS Band	IRDIS DIT[a]×NDIT[b]	IFS DIT×NDIT	N. of datacubes	FoV Rotation
2014-07-13	$H2H3$	YJ	4×40	8×20	16	18.1°
2014-08-12	$K1K2$	YH	(30+35)×6	60×3+100×2	16+16	33.8°
2014-08-14	BB_J	-	16×10	-	32	31.2°
2014-12-04	BB_H	-	8×218	-	1	8.7°
2014-12-05	BB_H	-	8×218	-	1	8.7°
2014-12-06	BB_H	-	8×218	-	1	8.5°
2014-12-08	BB_H	-	8×218	-	1	7.9°

[a]Detector Integration Time
[b]Number of frames per dithering position

broad-band imaging mode with the J band filter. Data in different spectral ranges were obtained:

- the first sequence was taken on the 13th of July 2014 in IRDIFS mode (IRDIS in dual-band imaging mode with the $H2H3$ filters, IFS in the YJ mode). The seeing was variable between $0.8 - 1.0''$. Sixteen datacubes were acquired, with a total exposure time of 43 min. The total field of view (FoV) rotation during the observation was 18.1°. The quality of IFS spectra is worse than the YH sequence obtained in August, because of poorer weather conditions;

- an IRDIFS_EXT sequence (IRDIS in dual-band imaging mode with the $K1K2$ filters, IFS in the YH mode) was taken on the 12th of August 2014, with good seeing conditions. Thirty-two datacubes were acquired for each instrument, with a total exposure time of nearly 2 hours. The total field rotation was 33.8° on the sky;

- an IRDIS broad J-band sequence was taken on the 14th of August 2014. Thirty-two datacubes were acquired, for an integration time of $\sim$ 1.4 hours. The total FoV rotation was 31.2°.

- four IRDIS broad H-band sequences were taken between 4th and 8th of December 2014. Integration times for each data set were around 30 minutes, and field rotations were around 8°.

The observations are summarized in Table 6.1.

All the sequences were taken with the same configuration of the apodized Lyot coronagraph (Carbillet et al. 2011) that includes a focal plane mask with a diameter of 185 mas and an inner working angle (IWA) of $0''.09$.

The commissioning sequences were taken with the following observing strategy:

- a coronagraphic image of the star with four satellite spots symmetric with respect to the central star was acquired at the beginning and at the end of each observation by introducing a periodic modulation on the deformable mirror. The purpose of this observation is to accurately determine the star position for the frame registering before the application of the angular differential imaging processing (Marois et al. 2006a) and for the derivation of the astrometry of the detected companions relative to the star (Marois et al. 2006c; Sivaramakrishnan & Oppenheimer 2006);

- non-saturated images of the star shifted from the central axis using a tip-tilt mirror were taken at the beginning and at the end of the observations with a neutral density filter, the ND2.0, with a transmission ∼1% in average on the total bandwidth, to calibrate the flux;

- the coronagraphic images were taken with a 4×4 dithering pattern for IRDIS and no dithering pattern for IFS (laboratory experiments showed that dithering degrades the quality of IFS data). These images were obtained in pupil-stabilized mode to take advantage of the angular differential imaging technique (Marois et al. 2006a).

- At the end of the sequence six sky backgrounds were taken, with the same exposure time for the coronagraphic and unsaturated point spread function (PSF) images.

The broad-band H sequences were acquired with the four satellite spots permanently applied.

All the other calibrations described in Sects. 6.2.1 and 6.2.2 were acquired during the next morning.

For every epochs of observation we also observed a dedicated field in the outer region of the globular cluster 47 Tuc to derive astrometric calibration of the IRDIS image (distortion, plate scale and orientation), using the Hubble Space Telescope (HST) data as a reference (A. Bellini & J. Anderson, private comm., see Bellini et al. 2014, for the methods used to obtain HST measurements). The sequences were acquired during the same observing runs as the science observations reported in this Chapter and with the same instrument setup (filter, coronagraph). Values adopted for the plate scale and for the true North are shown in Table 6.2. Raw data have been corrected for distortion along the vertical dimension of an anamorphism factor of 1.006. Because of its small field of view, calibration for the IFS are obtained from that of IRDIS, applying the relative transformation from one detector to the other derived from observation of the distortion grid available within SPHERE (see Maire et al. in prep. for details).

Table 6.2: Values of the plate scale and the true North for IRDIS observations measured during in each run of the observations. Values of July and August 2014 have been measured for the $H2H3$ filter, while December values refer to BB_H band filter. The measurements for the left and right parts of the IRDIS detector are shown.

Date	Plate scale (mas/px)	True North (deg)
	Left part	
July 2014	12.252 ± 0.006	−1.636 ± 0.013
August 2014	12.263 ± 0.006	−1.636 ± 0.013
December 2014	12.251 ± 0.005	−1.764 ± 0.010
	Right part	
July 2014	12.247 ± 0.006	−1.653 ± 0.005
August 2014	12.258 ± 0.006	−1.653 ± 0.005
December 2014	12.241 ± 0.004	−1.778 ± 0.010

6.2 Data reduction, photometry and astrometry

6.2.1 Broad and dual-band imaging

The IRDIS data were pre-processed with the same strategy: first I subtracted to each datacube the corresponding sky-background taken right after the sequence, I divided for the flat-field, and I applied a procedure of interpolation to remove the bad-pixels. The frames were recentered using the initial star center exposure with the four satellite spots. The master backgrounds and the master flat-field have been obtained with Data Reduction and Handling (DRH, Pavlov et al. 2008) software, official pipeline of the consortium.

The second step of the reduction has been done with three independent pipelines performing the angular differential imaging (ADI; Marois et al. 2006a). I did not performed the spectral differential imaging (SDI, Racine et al. 1999) between the IRDIS filter pairs to avoid photometric calibrations (Maire et al. 2014b). The first data reduction method is based on the principal component analysis (PCA) technique that performs the Karhunen–Loève Image Projection (KLIP) algorithm, following the model of Soummer et al. (2012). This means that for each product of the pre-processing phase I created a PCA library based on all the other collapsed datacubes of the sequence, and I derotated the product of the PCA as a function of the parallactic angle of the reference datacube. The final image was obtained with the median of all the rotated PCA images. In some cases, the data was binned temporally to reduce the number of frames and increase the analysis speed.

The second pipeline is an upgrade of the T-LOCI algorithm presented in Marois et al. (2014). Hence, for each dual-band filter sequence, I calibrated the speckle pattern of each individual frame, rotated the frames to align North up, and median-combined all the frames to obtain the final image.

Table 6.3: IRDIS contrast in magnitudes for HR 8799 bcde. The H-band magnitudes are presented in Apai et al., in prep.

Filter	b	c	d	e
ΔJ	14.39 ± 0.09	13.21 ± 0.13	13.20 ± 0.37	13.01 ± 0.21
$\Delta H2$	12.80 ± 0.14	11.81 ± 0.12	11.74 ± 0.17	11.63 ± 0.20
$\Delta H3$	12.50 ± 0.10	11.50 ± 0.10	11.57 ± 0.16	11.40 ± 0.21
$\Delta K1$	11.91 ± 0.06	10.95 ± 0.05	10.96 ± 0.07	10.88 ± 0.10
$\Delta K2$	11.73 ± 0.09	10.62 ± 0.07	10.60 ± 0.10	10.58 ± 0.11

To perform the reduction of the images in J band, in addition to the other algorithms, we exploited a third pipeline based on the method of the radial ADI (rADI) as illustrated in Chauvin et al. (2012).

The BB_H data was high-pass filtered by subtracting from each images a version of itself smoothed by a median filter with a large 11-pixel wide box width before entering a PCA speckle calibration algorithm.

The final images obtained by these pipelines for all the filters are shown in Fig. 6.1. An image of the combination of $K1K2$ filter with SDI+ADI is also shown, no significant detection is found closer than planet e.

To measure photometry and astrometry we exploited the method of the "fake negative planets" (Lagrange et al. 2010; Marois et al. 2010a; Bonnefoy et al. 2011), as illustrated in Zurlo et al. (2014) and Galicher et al. (2011a). To build models of the planet images accounting for the ADI self-subtraction, we used the median of the unsaturated images of HR 8799 taken right before and after the sequences, and the previously LOCI coefficients or PCA eigenvectors. No unsaturated images of HR 8799 were recorded during science verification, so HR 8799 b served as a PSF to build the planetary system model. We then adjusted the models to the real planet images to estimate the astrometry and the photometry of the planets. The error bars for each reduction account for the flux variations of the unsaturated images of HR 8799, the fluctuations of the results as a function of the PCA/LOCI parameters, and the accuracy of the fitting of the planet image models to the real images.

The contrast in magnitude obtained for the four planets is listed in Table 6.3, while their astrometric positions are shown in Table 6.4.

6.2.2 IFS data reduction and spectra extraction

We obtained IFS data in both YJ (0.95–1.35 μm, spectral resolution $R \sim 54$) and YH (0.95–1.65 μm, $R \sim 33$) modes (Claudi et al. 2008b). Only the YH data are presented in this work because of the poorer quality of the YJ data obtained in July 2014. The IFS raw data

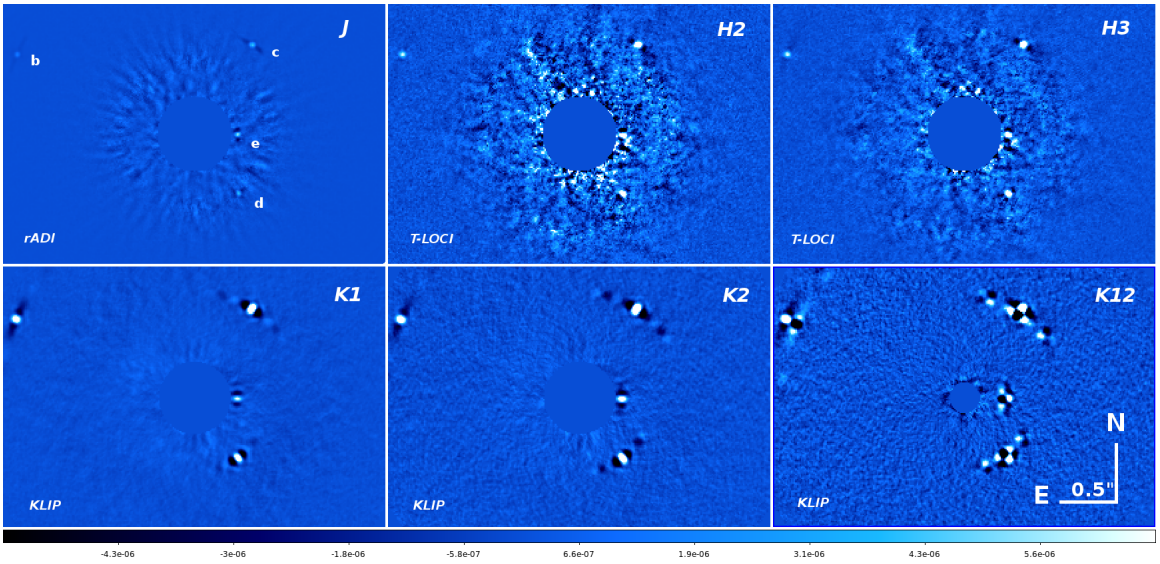

Figure 6.1: IRDIS images for several filters with the four planets around HR 8799 obtained with the rADI, T-LOCI and KLIP pipelines. The color scale is the same for all images. The combination of the $K1K2$ filters, ADI+SDI reduction, is also shown at the bottom-right of the figure.

Table 6.4: Astrometric positions of the planets around HR 8799 in date 2014.53, derived from IRDIS filters $H2H3$, and measurements in date 2014.62, from IFS YH band. The planet positions in broad H-band in date 2014.93 are also shown.

Epoch	Planet	ΔRA (″)	ΔDec (″)
2014.53	HR 8799 b	1.570 ± 0.005	0.707 ± 0.005
	HR 8799 c	−0.522 ± 0.004	0.791 ± 0.004
	HR 8799 d	−0.390 ± 0.005	−0.530 ± 0.005
	HR 8799 e	−0.386 ± 0.009	−0.008 ± 0.009
2014.62	HR 8799 d	−0.391 ± 0.004	−0.529 ± 0.004
	HR 8799 e	−0.384 ± 0.002	−0.005 ± 0.001
2014.93	HR 8799 b	1.574 ± 0.004	0.703 ± 0.004
	HR 8799 c	−0.518 ± 0.004	0.797 ± 0.004
	HR 8799 d	−0.402 ± 0.004	−0.523 ± 0.004
	HR 8799 e	−0.384 ± 0.010	0.014 ± 0.010

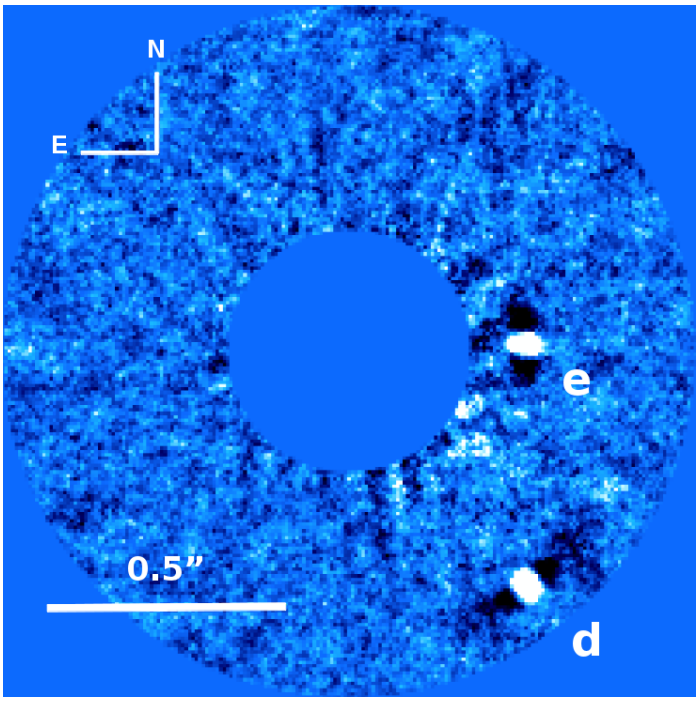

Figure 6.2: Image of the 38th IFS spectral channel (1.63 μm) with planets HR 8799 de obtained with KLIP reduction.

were pre-processed using the DRH software, until the creation of the calibrated spectral datacubes.

The pre-processing consists in background subtraction and flat-field calibration, then the spectra positions is determined by exploiting an image where the Integral Field Unit (IFU) is uniformly illuminated with a white calibration lamp in such a way that the detector is completely filled with spectra. Subsequently we proceed with the wavelength calibration, where the result obtained at the previous step is further refined. For this aim, the IFU is illuminated with four monochromatic lasers with known wavelength. An instrument flat is used to correct for the different response of the lenslets to a uniform illumination; after this last procedure there is the creation of the calibrated spectral datacubes. The final output of this step is a series of datacubes composed of 39 monochromatic images.

An additional step using custom IDL tools has been introduced for a better handling of the bad pixels and spectral cross-talk correction (Mesa et al. 2015). After the creation of the calibrated spectral datacubes, the differential imaging part of the data reduction is performed applying different pipelines written in IDL.

We have adopted two different approaches for searching for additional companions in the HR 8799 system and for extracting the spectrum of the detected planets. Both approaches provided detection of planets d and e with a median signal to noise ratio (S/N)

along the IFS channels of ~ 20.

In the first case, the most relevant solution is to perform KLIP exploiting all the frames at different wavelengths and at different angular positions. No significant signal has been found closer than planet e.

For the extraction of the spectrum of the planets, the first approach is to perform ADI for each individual IFS channel separately. As showed in Table 6.1, for YH observations we took 16 datcubes composed by 3 frames with a DIT of 60 s while for the second one we took 16 datacubes composed by 2 frames with a DIT of 100 s. We decided to use all these 80 frames without performing any binning in time, rescaling the frames of the second data set to take into account the different exposure time. For any single spectral frame I performed the PCA using as a library the frames of the same channel of the other datacubes. To avoid self-subtraction, I selected the frames according to the planet position in each image of the library, and rejected the frames where the planet centroid moved less than $\sim 0.5\lambda/D$ with respect to the reference frame, following the example presented in Pueyo et al. (2014). For each planet the library is composed of a different set of frames. However, we also tried data reductions without performing any selection of the frames. In this case, we used conservative data reductions with small numbers of modes to limit the biases of the PCA. Different number of modes have been used but the result converged rapidly after few modes (2–5 over 80). To retrieve the signal of a planet, we carefully tested the impact of our reductions using synthetic planets injected in the pre-processed datacubes at different positions or the forward modeling (see description in Soummer et al. 2012), assuming the same PCA modes and aperture as employed for the spectral extraction in the science data. For the forward modeling, I used the off-axis PSF obtained after the observing sequence, because of a slight saturation of the off-axis PSF obtained before the observation. An example of the output of this technique is shown in Fig 6.2.

A second approach, where ADI and SDI were used together, was then implemented. For this approach, the single exposures in each of the 32 spectral datacubes were averaged. The PSF library used for the PCA takes all frames into account, both along the temporal and spectral dimensions, where the PSF has moved by more than a separation criteria N_δ. In this scheme, the library is constructed using the frames spatially rescaled according to their respective wavelength. Various tests showed that a value of $N_\delta = 0.8$ FWHM gives good results in terms of SNR for the detection of the planets. To account for the flux losses induced by the speckle subtraction algorithm, forward modeling is attempted by using the off-axis PSF of the star above mentioned as a model for the PSF of the planet. The model is projected on the same PCA modes as the science data, and the flux loss is measured as the attenuation of the flux for the model before and after projection on the PCA modes. The

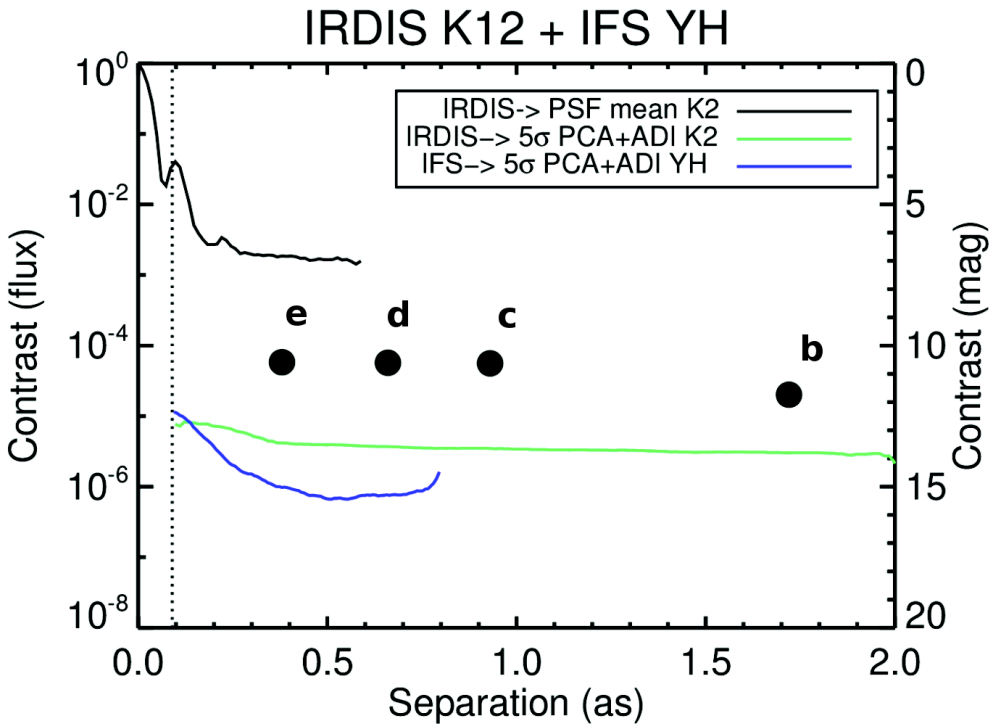

Figure 6.3: Contrast curves for the IRDIFS_EXT dataset. The 5σ contrast for the two instruments are plotted as a function of the angular separation. Planets around HR 8799 are also shown as photometric $K2$ points, the error bars are inside the dimention of the dots. The dotted vertical line indicates the coronagraph IWA.

flux of the planets are measured in the final spectral channels using aperture photometry in an aperture of diameter 0.8 λ/D ($\sim$ 4 pixels). The flux is finally corrected for the flux loss estimated using the forward modeling. The error bars on the photometry were measured in the same way as for the IRDIS data described in Sect. 6.2.1, except that we did not consider the flux variation during the exposure, as one of the two PSFs is slightly saturated.

In this way, we obtained four different spectral extractions from four independent pipelines. For each planet, a final estimate of the flux ratio between the star and the planet was obtained by computing the median of the results.

Astrometric measurements for planets HR 8799 de measured from IFS are shown in Table 6.4.

The 5σ curves of contrast of IRDIS and IFS for the IRDIFS_EXT dataset are shown in Fig. 6.3. Contrast in $K2$ band of the planets around HR 8799 are overplotted. IRDIS contrast curve has been calculated on the KLIP product of filter $K2$, while IFS contrast curve has been obtained on the KLIP result with just ADI (YH band).

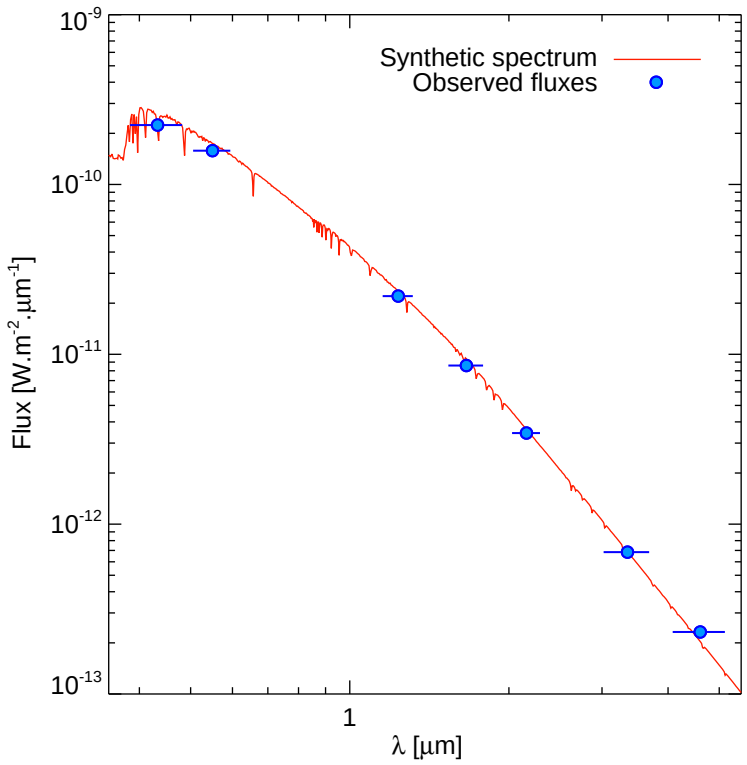

Figure 6.4: Synthetic ATLAS9 spectrum ajusted on the apparent fluxes of HR 8799 A.

6.3 Fluxes of the HR 8799 planets

We converted the flux ratio (IFS spectra, IRDIS photometry) between the HR 8799 planets and their host star into apparent flux, corrected from telluric absorptions, using an ATLAS9 spectrum of the star (Castelli & Kurucz 2004) with T_{eff} = 7500 K, log g=4.5, M/H=0, v_{turb} = 0 km/s scaled in flux to fit the Tycho2 BV, 2MASS JHK_S, and WISE $W1W2$ photometry (Høg et al. 2000; Cutri et al. 2003; Cutri & et al. 2012). This synthetic spectrum was found to provide a good fit to the existing photometry. We chose not to include photometric datapoints longward of 5 μm since the photometry starts to be affected by the disk excess. The scaled spectrum of the star is shown in Fig. 6.4.

We report the fluxes of HR 8799 bcde gathered from the SPHERE/IRDIS measurements and from the literature into Tables 6.5, 6.6, 6.7, and 6.8.

Table 6.5: Currently available fluxes of HR 8799 b at 10 pc gathered from narrow-band and broad-band photometry.

Filter	λ (μm)	FWHM (μm)	Abs. Flux (W.m-2.μm^{-1})	err. Flux + (W.m-2.μm^{-1})	err. Flux - (W.m-2.μm^{-1})	Ref
z- Subaru	1.02	0.10	2.99E-16	9.17E-17	7.02E-17	2
BB_J	1.26	0.20	5.64E-16	9.61E-17	9.61E-17	1
$H2$	1.59	0.05	1.11E-15	2.23E-16	2.23E-16	1
$CH_{4,S}$-Keck	1.59	0.13	1.02E-15	1.73E-16	1.48E-16	3
H- LBT	1.63	0.30	1.10E-15	1.40E-16	1.24E-16	4
$H3$	1.67	0.06	1.30E-15	2.22E-16	2.22E-16	1
$CH_{4,L}$- Keck	1.68	0.14	1.11E-15	1.99E-16	1.69E-16	3
He I B- Keck	2.06	0.03	6.03E-16	4.96E-17	4.96E-17	5
$K1$	2.10	0.10	1.10E-15	1.66E-16	1.66E-16	1
$H2$(v=1-0) - Keck	2.13	0.03	1.01E-15	7.28E-17	7.28E-17	5
K_s- Keck	2.15	0.31	1.04E-15	8.00E-17	7.34E-17	3
$Br_\gamma 2$ - Keck	2.17	0.03	1.06E-15	7.65E-17	7.65E-17	5
$K2$	2.26	0.11	9.62E-16	1.64E-16	1.64E-16	1
$H_2(v$=2-1)	2.26	0.04	8.03E-16	6.44E-17	6.44E-17	5
[3.3]	3.31	0.40	4.38E-16	4.67E-17	4.22E-17	4
L'- Keck	3.78	0.70	4.71E-16	4.54E-17	4.15E-17	6
[4.05]	4.05	0.02	6.87E-16	1.24E-16	1.05E-16	6
M'- Keck	4.67	0.24	1.29E-16	4.10E-17	3.11E-17	7

[1] - This work, [2] - Currie et al. (2011), [3] - Marois et al. (2008b), [4] - Skemer et al. (2012), [5] - Barman et al. (2011), [6] - Currie et al. (2014a), [7] - Galicher et al. (2011b).

6.4 The spectrophotometric properties of HR 8799 bcde

Up to this study, no empirical objects were found to provide a consistent match of HR 8799 bcde spectra and photometry. We took advantage of the new SPHERE data to make a new empirical comparison of the planets spectra and photometric data points to a set of equivalent photometry obtained on field dwarfs, young companions, and peculiar – red – dwarfs at the L/T transition discovered more recently.

We first synthetized the IRDIS colors of M, L, and T dwarfs from the SpeXPrism spectral library* and compared them to those of HR 8799 bcde. For that purpose, we smoothed the low-resolution spectra of the objects to the resolution of the narrowest IRDIS filter, used the IRDIS filter pass-bands, a model of the Paranal atmospheric transmission generated with the ESO `Skycalc` web application† (Noll et al. 2012; Jones et al. 2013), and a

*http://pono.ucsd.edu/~adam/browndwarfs/spexprism/

†http://www.eso.org/observing/etc/bin/gen/form?INS.MODE=swspectr+INS.NAME=SKYCALC

Table 6.6: Same as Table 6.5 but for HR 8799 c.

Filter	λ (μm)	FWHM (μm)	Abs. Flux (W.m-2.μm^{-1})	err. Flux + (W.m-2.μm^{-1})	err. Flux - (W.m-2.μm^{-1})	Ref
z-Subaru	1.02	0.10	<1.51E-15	...	...	2
BB_J	1.26	0.20	1.66E-15	3.16E-16	3.16E-16	1
$H2$	1.59	0.05	2.76E-15	5.26E-16	5.26E-16	1
$CH_{4,S}$-Keck	1.59	0.13	2.41E-15	4.60E-16	3.87E-16	3
H-LBT	1.63	0.30	2.52E-15	4.28E-16	3.65E-16	4
$H3$	1.67	0.06	3.28E-15	5.58E-16	5.58E-16	1
$CH_{4,L}$-Keck	1.68	0.14	2.75E-15	5.27E-16	4.42E-16	3
$K1$	2.10	0.10	2.67E-15	3.76E-16	3.76E-16	1
K_s-Keck	2.15	0.31	2.42E-15	1.86E-16	1.71E-16	3
$K2$	2.26	0.11	2.67E-15	4.56E-16	4.56E-16	1
L_ND1	3.04	0.15	1.34E-15	1.99E-16	1.73E-16	5
L_ND2	3.16	0.08	1.13E-15	2.28E-16	1.89E-16	5
[3.3]	3.31	0.40	1.10E-15	1.17E-16	1.06E-16	4
L_ND3	3.31	0.16	1.13E-15	1.67E-16	1.46E-16	5
L_ND4	3.46	0.16	1.45E-15	2.15E-16	1.87E-16	5
L_ND5	3.59	0.06	1.51E-15	2.23E-16	1.94E-16	5
L'-Keck	3.78	0.70	1.04E-15	8.00E-17	7.35E-17	6
L_ND6	3.78	0.19	1.22E-15	1.81E-16	1.58E-16	5
[4.05]	4.05	0.02	1.50E-15	1.15E-16	1.07E-16	6
M'-Keck	4.67	0.24	3.30E-16	4.54E-17	3.99E-17	7

[1] - This work, [2] - Currie et al. (2011), [3] - Marois et al. (2008b), [4] - Skemer et al. (2012), [5] - Skemer et al. (2014), [6] - Currie et al. (2014a), [7] - Galicher et al. (2011b).

model spectrum of Vega (Bohlin 2007). The same procedure was applied to the continuous 1.1-2.5 μm spectra of the moderately young companions (age < 0.4 Gyr) from Metchev & Hillenbrand (2006); Luhman et al. (2007); Bowler et al. (2013); Rojo et al. 2015, in prep. We also considered spectra of red dwarfs at the L-T transition from Dahn et al. (2002); Chiu et al. (2006); Looper et al. (2008); Burgasser et al. (2010a); Kirkpatrick et al. (2011); Mace et al. (2013); Liu et al. (2013); Schneider et al. (2014); Gizis et al. (2014); Marocco et al. (2014).

Two-color combination enables to discriminate field dwarf objects with different spectral types at the L-T transition. This is shown in Figures 6.5 and 6.6. In these diagrams, the red L6-L8 dwarfs and the young dusty L4-L6 2MASS J01225093-2439505 b companion deviates from the sequence of field dwarfs. These objects have similar colors to HR 8799 bcde planets. The dwarfs WISE0206, WISE0642, and WISE1647 together with the young T2 companion HN Peg B and the T0.5-T1.5 dwarf SDSS1516 seem to be later-type objects than the L6-L8 red dwarfs, but still have redder colors than the sequence of

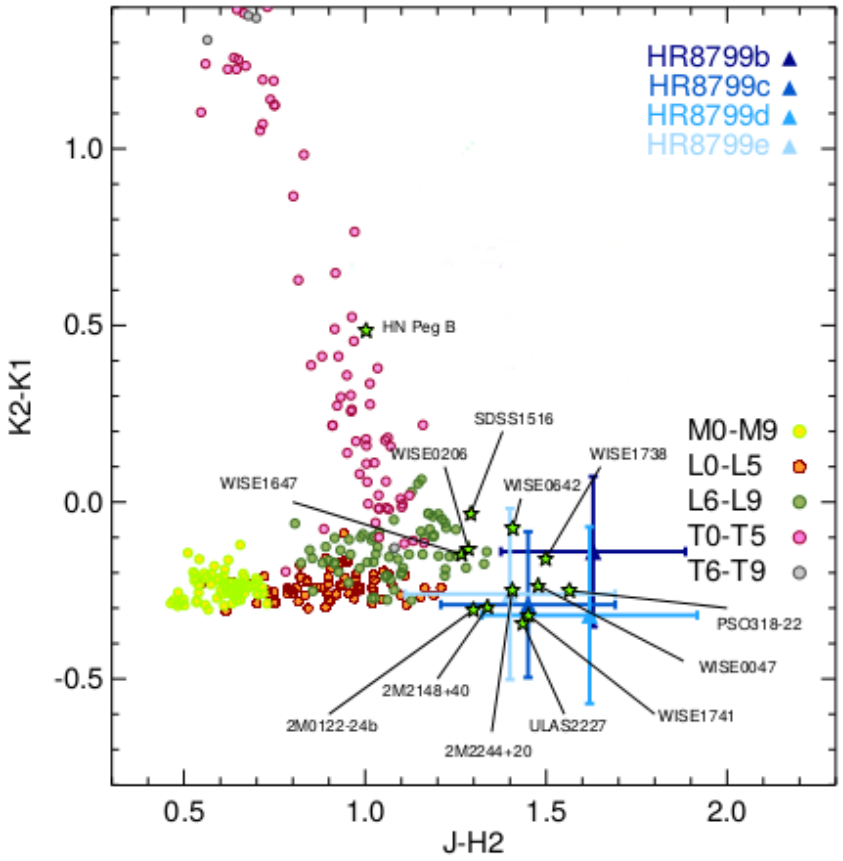

Figure 6.5: Comparison of HR 8799 bcde colors infered from the IRDIS photometry of the system to those of M, L, T field dwarfs (dots), and of young companions and red dwarfs straddling the L/T transition (green stars).

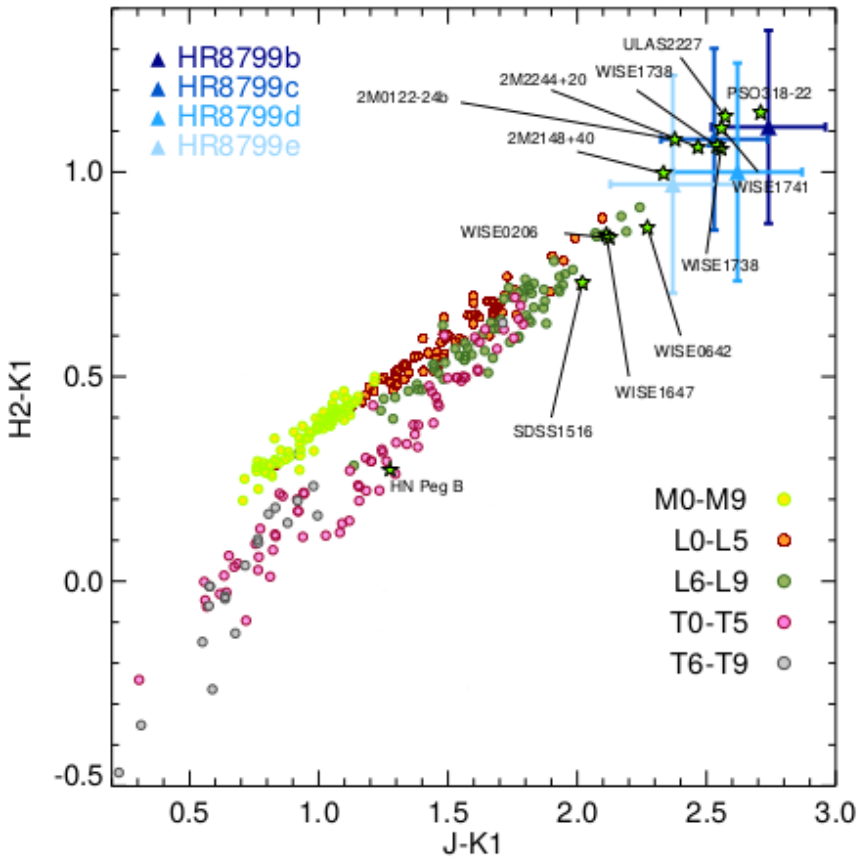

Figure 6.6: Same as Fig. 6.5 but for the $J - K1$ versus $H2 - K1$ colors.

Table 6.7: Same as Table 6.5 but for HR 8799 d.

Filter	λ (μm)	FWHM (μm)	Abs. Flux (W.m-2.μm^{-1})	err. Flux + (W.m-2.μm^{-1})	err. Flux - (W.m-2.μm^{-1})	Ref
z- Subaru	1.02	0.10	<5.76E-15	...	...	2
BB_J	1.26	0.20	1.51E-15	6.03E-16	6.03E-16	1
$H2$	1.59	0.05	2.94E-15	6.87E-16	6.87E-16	1
$CH_{4,S}$-Keck	1.59	0.13	2.95E-15	9.38E-16	7.11E-16	3
H- LBT	1.63	0.30	2.41E-15	5.41E-16	4.42E-16	4
$H3$	1.67	0.06	3.07E-15	6.84E-16	6.84E-16	1
$CH_{4,L}$- Keck	1.68	0.14	1.49E-15	3.50E-16	2.84E-16	3
$K1$	2.10	0.10	2.64E-15	4.24E-16	4.24E-16	1
K_s-Keck	2.15	0.31	2.47E-15	2.89E-16	2.58E-16	3
$K2$	2.26	0.11	2.72E-15	5.78E-16	5.78E-16	1
L_ND1	3.04	0.15	1.34E-15	2.72E-16	2.26E-16	5
L_ND2	3.16	0.08	1.29E-15	3.35E-16	2.66E-16	5
[3.3]	3.31	0.40	1.32E-15	1.41E-16	1.28E-16	4
L_ND3	3.31	0.16	9.83E-16	1.99E-16	1.65E-16	5
L_ND4	3.46	0.16	1.45E-15	2.93E-16	2.44E-16	5
L_ND5	3.59	0.06	1.58E-15	2.34E-16	2.04E-16	5
L'-Keck	3.78	0.70	1.21E-15	1.04E-16	9.60E-17	6
L_ND6	3.78	0.19	1.28E-15	1.90E-16	1.65E-16	5
[4.05]	4.05	0.02	1.65E-15	2.27E-16	2.00E-16	6
M'-Keck	4.67	0.24	4.68E-16	1.78E-16	1.29E-16	7

[1] - This work, [2] - Currie et al. (2011), [3] - Marois et al. (2008b), [4] - Skemer et al. (2012), [5] - Skemer et al. (2014), [6] - Currie et al. (2014a), [7] - Galicher et al. (2011b).

field dwarfs.

We compare in Fig. 6.7 the IFS spectra of HR 8799 d and e to the ones of the aforementioned red dwarfs. The HR 8799 d spectrum is well reproduced by those of the red L7 dwarfs WISE004, PSOJ318-22, 2M2240+20, WISE1741, and by the extremely red object WISE1738. The one of HR 8799 e is also well fitted by those of the L7 objects 2M2240+20, ULAS2227, WISE0047, WISE1741, and WISE1738. Among the sample of 1000 empirical templates from the SpeXPrism library, the HR 8799 d and e spectra are also best represented by those of 2M2148+40 (L6pec) and 2M2240+20 (L7.5pec; consistant with the best fit found with the alternative spectrum of this target published by Stephens et al. 2009). These two objects are candidates members of the 40 Myr old Argus and 50-150 Myr AB Doradus moving groups (Gagné et al. 2014), respectively. Similarly, Gagné et al. (2014) deduces that WISE0047 and PSOJ318-22 are strong candidates of the AB Doradus and β Pictoris moving groups, respectively. WISE1741 is also proposed as potential member of one of these two groups (Schneider et al. 2014). We note that, if truly

Table 6.8: Same as Table 6.5 but for HR 8799 e.

Filter	λ (μm)	FWHM (μm)	Abs. Flux (W.m-2.μm^{-1})	err. Flux + (W.m-2.μm^{-1})	err. Flux - (W.m-2.μm^{-1})	Ref
BB_J	1.26	0.20	2.05E-15	4.56E-16	4.56E-16	1
$H2$	1.59	0.05	3.25E-15	7.60E-16	7.60E-16	1
$H3$	1.67	0.06	3.59E-15	8.79E-16	8.79E-16	1
H- LBT	1.63	0.30	3.33E-15	7.47E-16	6.10E-16	3
$K1$	2.10	0.10	2.84E-15	4.56E-16	4.56E-16	1
$K2$	2.26	0.11	2.77E-15	5.59E-16	5.59E-16	1
K_s- Keck	2.15	0.31	3.02E-15	8.17E-16	6.43E-16	2
[3.3]	3.31	0.40	1.32E-15	2.83E-16	2.33E-16	3
L'- Keck	3.78	0.70	1.22E-15	1.42E-16	1.28E-16	4
[4.05]	4.05	0.02	1.89E-15	3.83E-16	3.18E-16	4
M'- Keck	4.67	0.24	<2.01E-15	...	...	5

[1] - This work, [2] - Marois et al. (2008b), [3] - Skemer et al. (2012), [4] - Currie et al. (2014a), [5] - Galicher et al. (2011b).

member of these groups, all these objects have estimated masses 6-12 M_{Jup} which bracket the present mass estimates of the two planets. The good matches confirm the analysis made in Figures 6.5 and 6.6.

Conversely, a fit to the spectra of the young companions known at the L-T transition, 2M1207 b (Patience et al. 2010), GU Psc B (Naud et al. 2014), HD 203030 B, HN Peg B, and 2M0122 b, does not yield as good fit as the sample of free-floating peculiar L7 dwarfs. This could be due to the lack of a sample of companions at the L/T transition with a good coverage of the spectral-type/age domain.

Ultimately, we compiled all the photometric measurements made on the four planets from 0.96 to 4.67 μm (see Sec. 6.3) and attempted a comparison with the spectral energy distribution (SED) of red L dwarfs built from their flux-calibrated near-infrared spectra and WISE $W1$ (λ_c = 3.35 μm, bandwidth=0.66 μm) and $W2$ (λ_c = 4.60 μm, bandwidth=1.04 μm) photometry, or taken from Stephens et al. (2009). The results are reported in Fig. 6.8. We find that the red L6 dwarf 2M2148+40 dwarf still remain the best fit for HR 8799 e, although it does not appear to provide the best fit to the IFS spectrum of the planet among the sample of known red dwarfs (see Fig. 6.7). The L7pec dwarf WISE0047 appears to be a good alternative fitting solution especially for the IFS part, although its SED has a slightly redder slope. The photometry and spectra of HR 8799 d are equally well represented by those of WISE0047 and WISE1738.

We do not find a good fitting template for the two remaining planets. The empirical analysis of HR 8799 b and c is clearly limited by the lack of young and dusty free-floating

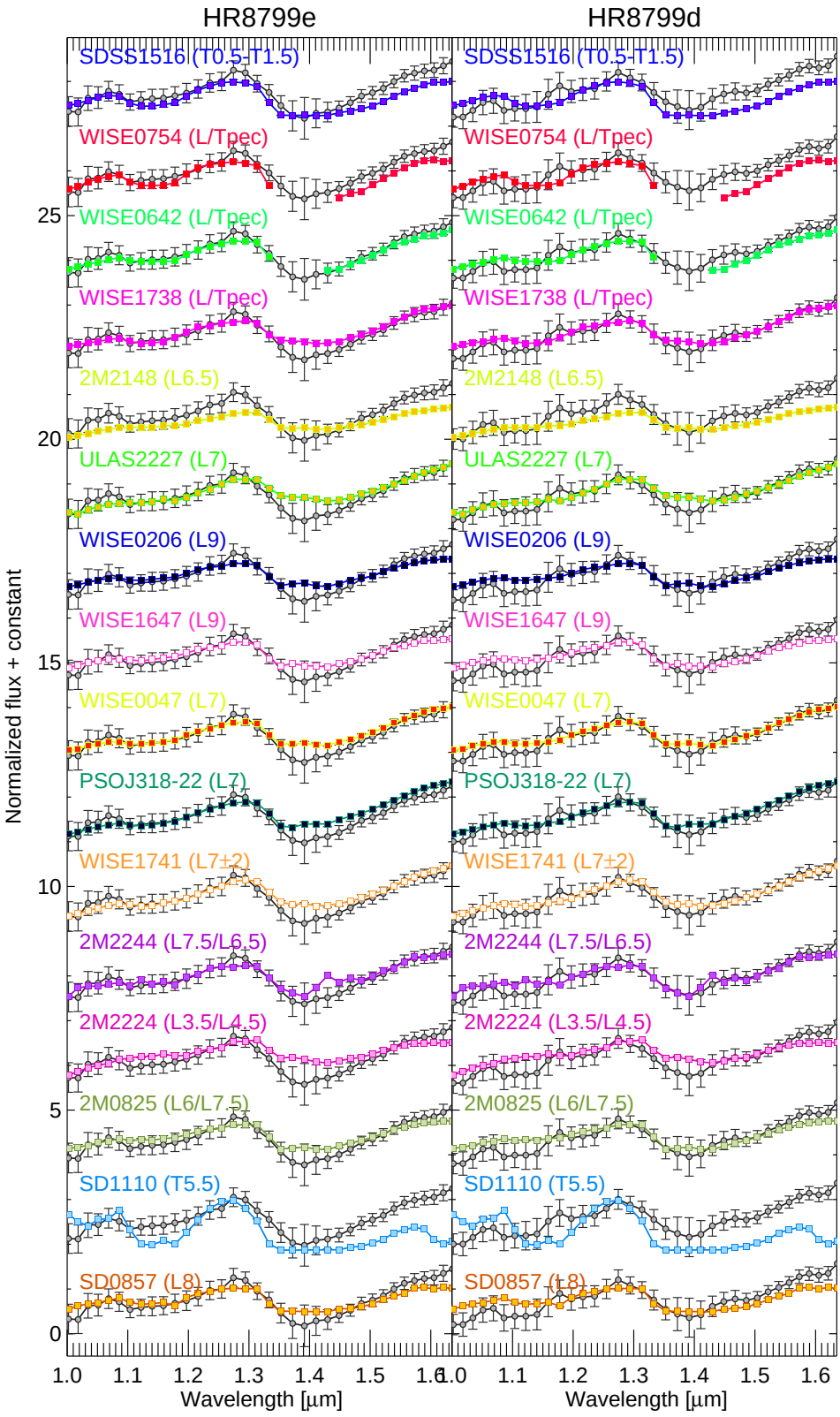

Figure 6.7: Comparison of HR 8799 d and e normalized low-resolution SPHERE YH band spectra to those of red L3.5-T5.5 dwarfs.

objects with spectral types L9-T2. The L/T transition dwarf WISE1741-46 reproduces the presently available SED of HR 8799 c, apart for the strength of the water absorption from 1.9 to 2.0 μm. ULAS2227 and WISE1741 provides a good fit to the Y, J, [3.3], L', and M' band fluxes but failed to reproduce the shape of the OSIRIS HK band spectrum obtained by Barman et al. (2011). The deeper water-bands in the H and K bands (see Fig. 6.8) in the spectrum of these planets suggest that they both have latter spectral types than HR 8799 d and e. The comparison to newly discovered L9pec-T2pec dwarfs in the near-future (e.g. Kellogg & Metchev 2014) may nevertheless solve the issue.
In that sense, neither the reconstructed SED of the extremely red companion 2M1207b (Chauvin et al. 2004; Patience et al. 2010; Skemer et al. 2014), and of the later objects WISE1647, WISE 0206 (Kirkpatrick et al. 2011) yielded better fitting solutions.

This motivates the use of atmospheric models to complement the understanding of the planet properties. To a more detailed empirical analysis of the outer planets of this system we refer the reader to the dedicated paper (Bonnefoy et al., in prep). The solution presented is to adjust the spectra of T-type dwarfs with an extinction factor due to the corundum absorption. This paper will also present a deeper analysis on the comparison of the four planets' SEDs with optimized synthetic models.

6.5 Conclusions

We present in this Chapter the first results of the planet hunter SPHERE on the system around HR 8799. We observed this system during the commissioning and the Science Verification runs of SPHERE, during the months of July, August, and December 2014. The four planets were detected in J, $H2H3$, BB_H, and $K1K2$ bands, with high S/N (reaching $\sim$ 200 in K band). For the first time planet HR 8799 e has been detected in J band.

To obtain the results presented in this work, optimized post-processing methods were exploited. To have robust measurements of photometry, spectrometry, and astrometry we used independent pipelines based on KLIP and T-LOCI, with injection of "fake negative" companions.

We measured the photometry in the four dual- and broad-band filters and spectra in YH band for HR 8799 de have been extracted. The quality of these spectra, with mean S/N $\sim$ 20 along the wavelengths, made them the highest quality spectra ever obtained for these planets in YH band.

The astrometric positions of the four planets are given for the epochs of July and December. For the closest planets d and e we also provide very accurate astrometric positions at August 2014, extracted from IFS data. For this epoch, given the high S/N ratio and the

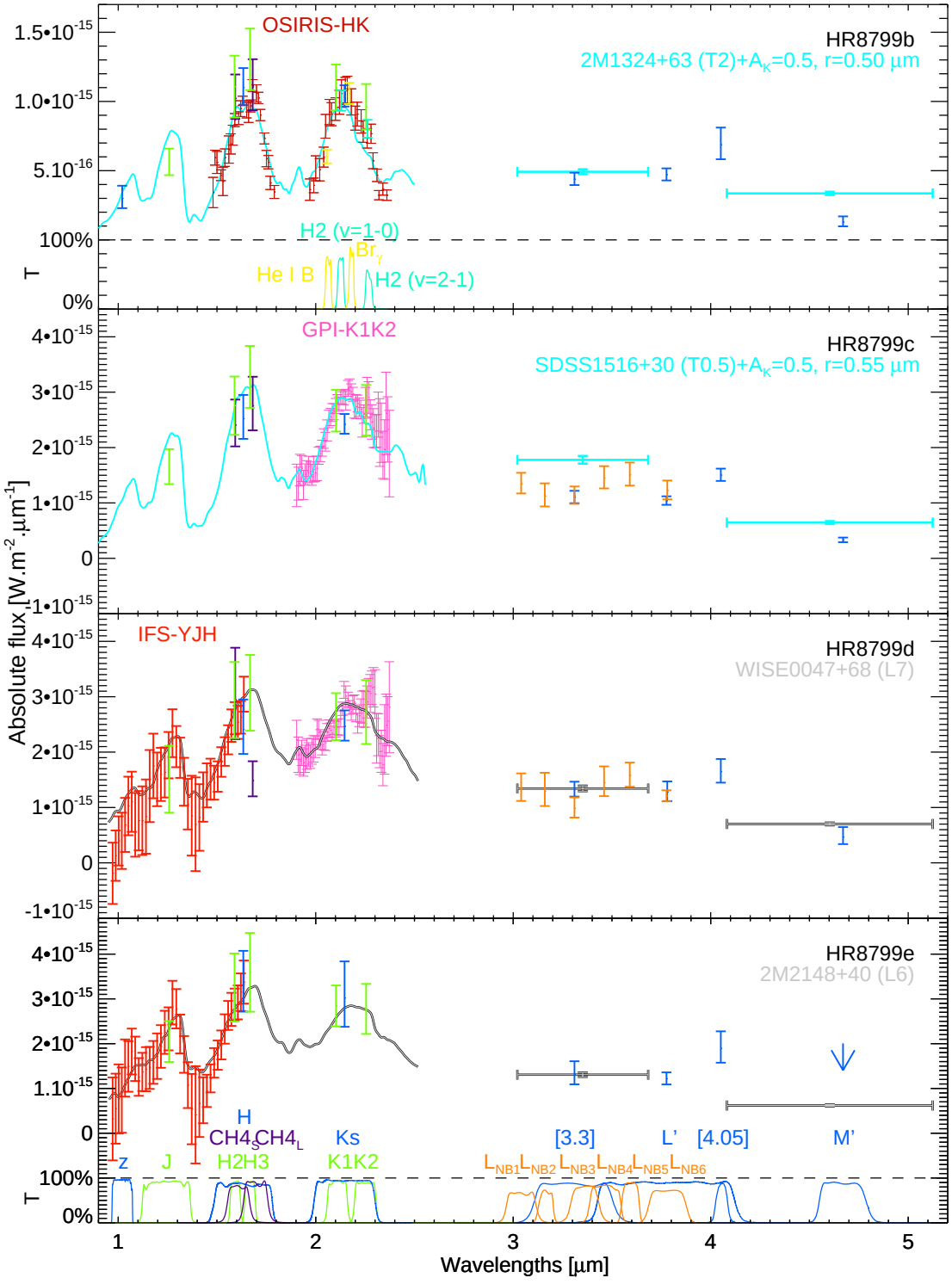

Figure 6.8: Comparison of the current set of spectrophotometric points of HR 8799 b, c, d, and e to the normalized SEDs of red L dwarfs (grey) and to the SED of peculiar early-T dwarfs reddened by additional corundum extinction (light blue). The description of the method applied to obtain planets' b and c spectrum models is described in Bonnefoy et al., in preparation.

small pixel scale of IFS, we are able to obtain astrometric positions with error bars of only 1-2 mas.

We demonstrate for the first time that the overall spectro-photometric properties of HR 8799 d and e are similar to those of dusty L dwarfs with estimated spectral type L6-L7. These objects should have low surface gravities and masses bracketing those of HR 8799 d and e if their presently proposed membership to young nearby associations is confirmed. This suggests that the underlying mechanisms (thicker clouds, non-equilibrium chemistry, variability, chemical enrichments) proposed to explain the spectrophotometric properties of the HR 8799 planets may also apply to these objects, and vice-versa. In addition, we speculate that the lack of a consistent sample of spectra of red – possibly low-gravity – L8-T0 dwarfs may explain why we presently cannot find good empirical templates for the SED of the two outermost planets.

Nevertheless, the deeper water-bands in the *H* and *K* bands in planets' b and c spectra suggest that they both have latter spectral types than the innermost planets. In depth analysis with *ad hoc* synthetic spectra will probably help us in better understanding this complex planetary system.

Chapter 7

Conclusions

Direct imaging is the only technique that permits to separate the light of extrasolar planets from that of the parent star. It allows to explore the outer regions of planetary system, from roughly 10 AU from the host star that cannot be probed by the indirect detection techniques. One of the main advantages of direct imaging is that it permits to acquire the spectra of the planets, giving us information about their composition and chemistry. If enough time coverage is available, direct imaging also allows determination of all the orbital parameters of the detected objects, with greater precision for close-in planets. In Chapters 1 and 2 I present the limitations of this technique and the observational methods and post-processing techniques used to achieve high contrasts with ground-based instruments. The amount of information achievable with this technique was worth the building of a new generation of dedicated instruments. To reach contrasts of the order of 10^6 at small separations ($\sim 0\farcs5$), instruments equipped with ExAO are needed, providing a stable and quasi-diffraction limited beam of light and suppressing the variable speckle pattern.

The two instruments exploited to obtain the results presented in this thesis are NACO and SPHERE both available at VLT telescope, Paranal. NACO can reach high contrast at large separations and it permitted the first detection of an exoplanet by direct imaging, 2M1207 b (see Sec. 1.2.4). In Chapter 3 I present a case of false positive found using NACO: a white dwarf orbiting HD 8049. A promising low-mass companion candidate was detected around the K2-type star in July 2010. Its contrast of $\Delta H = 7.05$ at $1\farcs57$ corresponds to an object with mass of 35 M_{Jup} at a projected separation of 50 AU, for the initially assumed system age and heliocentric distance. A second epoch observation was secured one year later confirming that the companion is gravitationally bound. To constrain the companion orbit and mass, we combined DI information with RV measurements, which spanned 30 yr of observations. These measurements helped also in studying the properties of the host star, in particular the spectral age indicators and the SED. The star shows discrepancies of the age indicators that suggests it might have an older age and that

the moderately high level of chromospheric activity and fast rotation, mimicking the properties of a young star, might rather have been induced by the exchange of mass with the progenitor of a WD. Comparison with space-based UV data and with EFOSC observations of the star in U band confirmed that the companion is actually a quit hot WD and not a low mass companion. This example demonstrates some of the challenges in determining accurate age estimates for stars and in understanding the nature of faint companions. The case presented here alerts us of possible similar errors in future direct imaging campaigns.

Last year, another planet hunter instrument received first light: SPHERE. This instrument is mounted at UT3 of the VLT, in Paranal. SPHERE includes a high order ExAO system (SAXO), a common path providing a very stable beam and various coronagraphic options, and three subsystems: IRDIS, the NIR dual-band imager; IFS, the NIR integral field spectrograph; and ZIMPOL, the visible polarimeter. In this thesis the work is focused on the NIR arm of SPHERE, exploiting the two instruments IRDIS and IFS that may work in parallel. In Chapter 4 we reviewed the expected performance of the two instruments. From laboratory data, obtained before the shipping of the instrument to Paranal, I calculated the expected errors on photometry and astrometry when we exploit the SDI technique. For that I injected 750 synthetic planets in IRDIS and IFS datacubes, with different separations, position angles, and contrasts. I devised *ad hoc* post-processing reduction methods to maximize the speckle pattern subtraction and optimize the SDI technique. In particular, I tested a new PCA technique called KLIP (originally developed by Pueyo et al. 2014), optimized to reduce IFS datacubes. This method permits the creation of a PCA library which includes only the frames where the signal of the faint companion is not present. With respect to a standard PCA where the library includes all the frames, KLIP reduces the self-subtraction effects and provide spectra closer to the ones injected. This work permitted to prepare new routines for the post-processing of IRDIS and IFS data, ready for the on-sky data that soon arrived. From these simulations we expected to detect a bright object such as the white dwarf around the star HD 8049 (presented in Chapter 3), which has an H band contrast of $10^{-2.8}$ and a projected separation of $1''.56$, with a S/N of ~270, an error on photometry of 0.045 mag and an error on the relative position of 0.2 mas. Using VLT/NACO, and exploiting the ADI, I have obtained errors of 0.12 mag on photometry and 7–10 mas on absolute astrometry.

The planet around β Pic is a 12 Myr old planet of ~10 M_{Jup} and orbiting the star with a semi-major axis of 9–10 AU (see Sec. 1.2.4 and Appendix B). With IRDIS, for a H band contrast of 10^{-4} and projected separation of $0''.5$, the S/N would be of ~22, the error on the photometry is 0.16 mag and on the relative astrometric position is of 1.1 mas. With VLT/NACO, typical errors are of the order of 0.2 mag for photometry and ~13 mas for

astrometry. An error of 0.16 mag implies an uncertainty on the determination of the mass of the object of ~0.5 M_{Jup} using COND or DUSTY models (Allard et al. 2000), or of the order of 1–2 M_{Jup} using core accretion models (Fortney et al. 2008). With IFS we would be able to retrieve a spectrum with error bars of the order of 0.15 mag on each channel and astrometric relative position error of 0.6 mas. As we saw in Appendix B the error bars for the IFS spectrum are of the order of 0.02 mag.

For fainter objects, such as the planets around the star HR 8799, SPHERE would be able to detect HR 8799d, 7 M_{Jup} planet at a distance of 27 AU (see Chapter 6), with a relative astrometric error of 3 mas. As we saw in Chapter 6, the error for planet d, including all the on-sky calibrations, is 4 mas. For planet e, which is even closer, the error is 2 mas on the right ascension and 1 mas on the declination.

The work with laboratory data was meant to help us in predicting the performance of the instrument before the survey NIRSUR, which already started, and will dedicate part of the SPHERE GTO to the research of extrasolar planets. A contribution that I gave for the list of targets is presented in Chapter 5. I selected RV planets with long period orbit from the literature, which are observable with SPHERE. For these objects all the orbital parameters given from the RV are available. I performed a Monte Carlo simulation which explored all the possible orbits, having as a free parameter the inclination. The result of the simulation was a plot for each planet, with the separation at a given epoch vs the expected contrast (estimated from the mass). From those we can derive the probability of detection, knowing the expected contrast achieved by IFS. Having a comparison between the dynamical mass of a planet and the estimated one from evolutionary models would be a crucial to test them. SPHERE results for these objects will be very useful in both cases of detection or non-detection: in the first case we will compare dynamical and estimated masses, and in the second case we can give upper limits on the mass of the companion. These objects will be observed during next months, but one of them has been observed already. HD 142 A is a binary star that hosts two planets, the distance of the system is 26.31 pc. The planet which I selected is HD 142 Ac, that has a minimum mass of 5.3 M_{Jup}, a low eccentricity of 0.21, and a period of 6005 days. The system has been observed in October 2014 in IRDIFS mode. No object was detected in the both IRDIS and on IFS data. I gave an upper limit on the mass of its companion, that I calculated to be lower than 30 M_{Jup} using AMES-COND models (Allard et al. 2000) and considering the planet at the expected separation (i.e. 0.″3).

Finally, in Chapter 6 I present the analysis of the planetary system around HR 8799. This system, composed by four planets and a double debris belt, has been discovered in 2010 (see Sec. 1.2.4). It has been observed with SPHERE during the commissioning and Science Verification runs from July to December 2014. It has been one of the first results

obtained with the instrument, and a good test to check the expected performances of IRDIS and IFS.

We obtained photometric measurements from the observations in J, $H2H3$, BB_H, and $K1K2$ bands, with high S/N, reaching a value of $\sim$ 100 in J band and $\sim$ 200 in K band. We detected for the first time planet e in J band (S/N = 26). We calculated the astrometric positions for the four planets from the data-sets of July (in $H23$ band) and December (in broad-band H) and for the two innermost planets with IFS from the observation of August (YH band).

We extracted spectra of planets d and e from IFS YH band data, obtaining the highest quality spectra ever obtained in this wavelength range. The median S/N along the wavelength is $\sim$ 20.

I compared the spectrophotometry information available for each planet to dusty, isolated, and young brown dwarfs in the L/T transition. This is the first time that planets around HR 8799 have been compared to empirical models. We found that the spectra of two inner planets can be fitted to L6-7 dwarfs. Concerning the outer planets, the deeper absorption due to water bands made may suggest a latter-type spectrum. None of the objects used in the comparison can fit these spectra. With a deeper analysis with *ad hoc* synthetic models we will hopefully better understand the nature of these planets.

Appendix A

Celestial mechanics

A.0.1 Kepler's Laws

* In 1619 the astronomer Johannes Kepler published three fundamental laws from the study of celestial mechanics. His laws were purely empirical, directly deduced from Tycho Brahe's observations of our solar system:

1. The planets move in ellipses with the Sun at one focus.
2. A radius vector from the Sun to a planet sweeps out equal areas in equal times.
3. The square of the orbital period of a planet is directly proportional to the cube of its semi-major axis.

Even if the scientist did not explain the physical motivations of the motion of planets they were taken as laws, and just posteriorly proved by the solution of the two-body problem.

If we consider a star and a planet of mass m_1 and m_2, respectively, with position vectors r_1 and r_2 from a common origin O (Fig. A.1), vector $\mathbf{r} = \mathbf{r_2} - \mathbf{r_1}$ gives the relative motion between the planet and the host star.

The gravitational forces acting on the star and the planet are:

$$\mathbf{F_1} = m_1 \ddot{\mathbf{r}}_\mathbf{1} = +G\frac{m_1 m_2}{r^3}\mathbf{r} \tag{A.1}$$

$$\mathbf{F_2} = m_2 \ddot{\mathbf{r}}_\mathbf{2} = -G\frac{m_1 m_2}{r^3}\mathbf{r} \tag{A.2}$$

*Formulas of this Section are taken from Murray & Correia (2011)

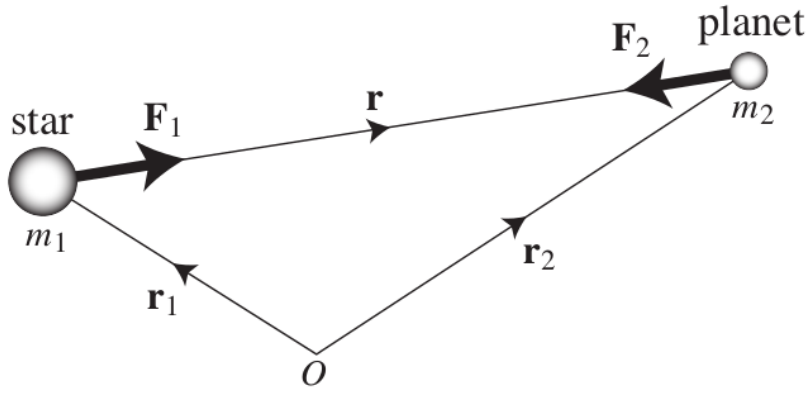

Figure A.1: Two bodies system with respect to the origin O. Image taken from Murray & Correia (2011).

Concerning the motion of the planet with respect to the star. If we write $\ddot{\mathbf{r}} = \ddot{\mathbf{r}}_\mathbf{2} - \ddot{\mathbf{r}}_\mathbf{1}$ and use the gravitational law,

$$\ddot{\mathbf{r}} + G(m_1 + m_2)\frac{\mathbf{r}}{r^3} = 0 \tag{A.3}$$

and if we take the product vector of $\mathbf{r}$ with Eq. A.3 we have $\mathbf{r} \times \ddot{\mathbf{r}} = 0$ which can be integrated to give:

$$\mathbf{r} \times \dot{\mathbf{r}} = \mathbf{h} \tag{A.4}$$

where $\mathbf{h}$ is a constant vector perpendicular to both $\mathbf{r}$ and $\dot{\mathbf{r}}$.

If we want to express these equations in polar coordinates (r, θ), the position vector, the velocity and the acceleration will be:

$$\mathbf{r} = r\widehat{\mathbf{r}} \tag{A.5}$$

$$\dot{\mathbf{r}} = \dot{r}\widehat{\mathbf{r}} + r\dot{\theta}\widehat{\theta} \tag{A.6}$$

$$\ddot{\mathbf{r}} = (\ddot{r} - r\dot{\theta}^2)\widehat{\mathbf{r}} + \left[\frac{1}{r}\frac{\mathrm{d}}{\mathrm{d}t}\left(r^2\dot{\theta}\right)\right]\widehat{\theta} \tag{A.7}$$

where $\widehat{r}$ and $\widehat{\theta}$ are the versors on the direction of the radius and perpendicular to the latter, respectively. Substituting Eq. A.6 into Eq. A.4 gives $\mathbf{h} = r^2\dot{\theta}\widehat{z}$, where $\widehat{z}$ is the versor going out from the plane.

The quantity $r^2\dot{\theta}$ remains constant during the motion.

The area element dA swept out by the star-planet radius vector during the orbital motion in the time interval dt is given by

$$\mathrm{d}A = \int_0^r r\mathrm{d}r\mathrm{d}\theta = \frac{1}{2}r^2\mathrm{d}\theta \tag{A.8}$$

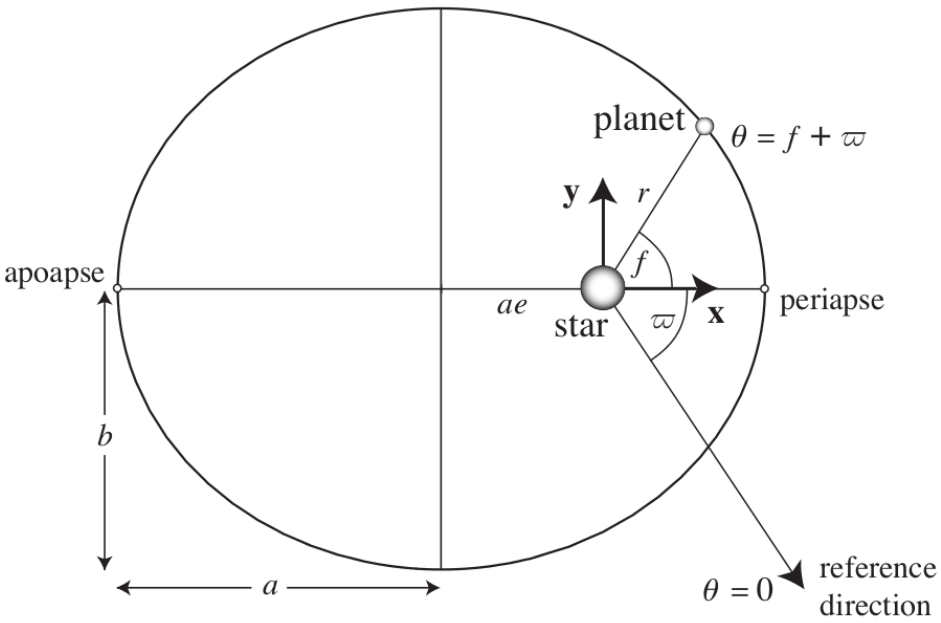

Figure A.2: System star-planet-center of mass, with respect to the star, (a), and to the center of mass, (b). Figure taken from Murray & Correia (2011).

and thus

$$\dot{A} = \frac{1}{2}r^2\dot{\theta} = \frac{1}{2}h = \text{constant}, \tag{A.9}$$

that is Kepler's second law.

To calculate the radius we can use:

$$r = \frac{a(1-e^2)}{1 + e\cos(\theta - \varpi)} \tag{A.10}$$

where θ is called the *true longitude*, a is the *semi-major axis*, e is the eccentricity and ϖ is the *longitude of the periastron*.

The angle $f = \theta - \varpi$ is called the *true anomaly* . The sense of the true anomaly is that if we consider the plane of the orbit and fix the x-axis on the conjunction of the star and the periastron, and the y-axis perpendicular to the latter, f defines the true position of the planet in any time using the cartesian coordinates:

$$x = \cos f \tag{A.11}$$

$$y = \sin f \tag{A.12}$$

Following that, we can then rewrite Eq. A.10 as:

$$r = \frac{a(1-e^2)}{1 + e\cos f}. \tag{A.13}$$

The area of the ellipse traced by the orbit is $A = \pi ab$ and the planet swept out it in a time equal to its period. From Eq. A.9, $A = hT/2$ and so

$$T^2 = \frac{4\pi^2}{G(m_1 + m_2)} a^3 \tag{A.14}$$

that is the Kepler's third law.

A.0.2 Solution of the Kepler problem

If we want to know where a planet is situated at each instant we must solve the so called "Kepler problem". First, we have to find r as a function of time. The expression that connects $\dot{r}$ and r is the following:

$$\dot{r}^2 = n^2 a^3 \left(\frac{2}{r} - \frac{1}{a}\right) - \frac{n^2 a^4 (1 - e^2)}{r^2} \tag{A.15}$$

or

$$\dot{r} = \frac{na}{r} \sqrt{a^2 e^2 - (r - a)^2} \tag{A.16}$$

To solve the differential equation we introduce a new variable, E, known as *eccentric anomaly*:

$$\dot{r} = a(1 - e \cos E) \tag{A.17}$$

and if we derive it in function of the time:

$$\dot{E} = \frac{n}{1 - e \cos E}. \tag{A.18}$$

The solution is

$$n(t - T_P) = E - e \sin E \tag{A.19}$$

where T_P is a constant such that $t = T_P$ when $E = 0$, it is known as *time of periastron passage*. The left term of Eq. A.19 is equal to a new quantity called *mean anomaly*, M. We can finally write the *Kepler's equation*, whose solution permits us to find the position of a planet given the time t:

$$M = E - e \sin E. \tag{A.20}$$

A.0.3 Orbital elements

To summarise all the variables mentioned in previous sections, the so-called *orbital elements* are:

- a, semi-major axis

- i, inclination
- Ω, longitude of the ascending node
- ω, argument of the periastron
- e, eccentricity
- T_P, periastron passage

in addition we also need these important quantities necessary to solve the motion of the planet:

- E, eccentric anomaly
- ϖ, longitude of the periastron
- M, mean anomaly
- f, true anomaly
- K, semi-amplitude of the radial velocity

So far we just considered the problem where the orbit is laying on its plane, but actually the star-planet system belongs to a three dimensional space. In Fig. A.3 a representation of the orbit in a three dimensional space is shown.

The inclination i is defined by the angle between the plane of the sky and the plane where the orbit lies. If the planets move in prograde sense the inclination is defined in the range $0° \leq i \leq 90°$, otherwise the motion is said to be retrograde (Heintz 1978). The intersection from the reference plane and the plane of the orbit is called the *line of the nodes*. The *ascending node* is the intersection between the line traced by the orbit and the reference plane moving from below to above the plane. The *longitude of the ascending node*, Ω, is defined by the angle between the reference line and the ascending node. The angle between this radius vector and the periastron of the orbit is called the *argument of periapse*, ω. The sum of ω and Ω is defined as ϖ, *longitude of periastron* and it is not lying in one plane.

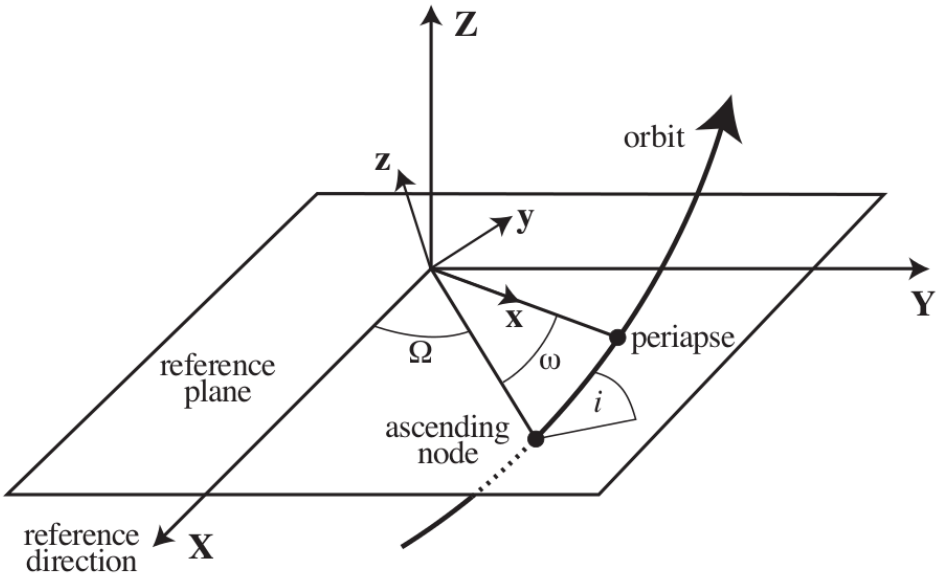

Figure A.3: The orbit in a three dimensional space. Figure taken from Murray & Correia (2011).

A.0.4 Barycentric motion

To predict the observable effects of a planet orbiting around a star we have to study the motion of the barycenter. The position vector of the center of mass of the system is:

$$\mathbf{R} = \frac{m_1\mathbf{r_1} + m_2\mathbf{r_2}}{m_1 + m_2} \tag{A.21}$$

and from Eq. A.1 and A.2 we derive:

$$\ddot{\mathbf{R}} = \frac{m_1\ddot{\mathbf{r}}_1 + m_2\ddot{\mathbf{r}}_2}{m_1 + m_2} = 0 \tag{A.22}$$

so velocity is constant and the barycenter moves from the origin O with a null velocity, stationary case, or with a constant velocity. If $\mathbf{R_1} = \mathbf{r_1} - \mathbf{R}$ and $\mathbf{R_2} = \mathbf{r_2} - \mathbf{R}$, we can write:

$$m_1\mathbf{R_1} + m_2\mathbf{R_2} = 0. \tag{A.23}$$

where R_1 and R_2 are the separation vectors from the two masses (see Fig. A.4) , remembering that the orbit of the planet is an ellipse with semi-major axis a, we have:

$$a_1 = \frac{m_1}{m_1 + m_2}a \tag{A.24}$$

$$a_2 = \frac{m_2}{m_1 + m_2}a \tag{A.25}$$

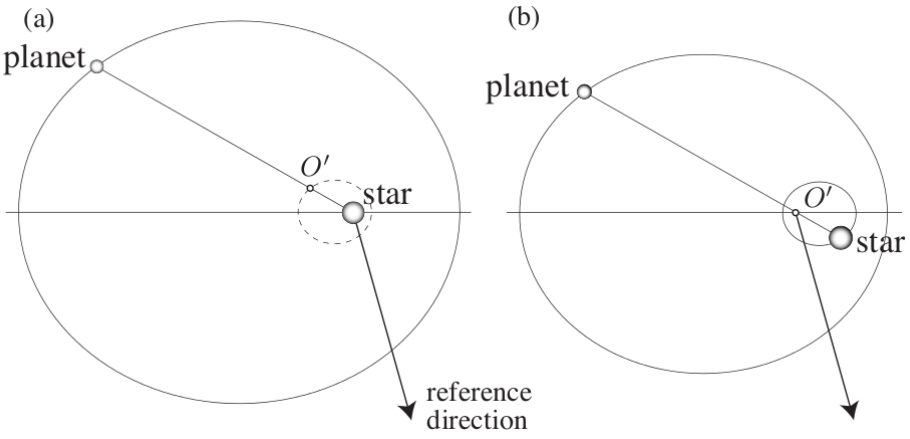

Figure A.4: System star-planet-center of mass, with respect to the star, (a), and to the center of mass, (b). Figure taken from Murray & Correia (2011).

Each mass then moves on its own elliptical orbit with respect to the common center of mass, and the periapses of their orbits differ by π. This is particularly important for an indirect detection method as the radial velocity technique.

As the reference plane is the plane of the sky perpendicular to the line of sight, the Z-axis oriented toward the observer, the radial velocity is given by the projection of the velocity on the line of sight.

$$v_r = \dot{\mathbf{r}}_\mathbf{1}\widehat{\mathbf{Z}} = V_Z + \frac{m_2}{m_1 + m_2}\dot{Z} \tag{A.26}$$

We can write:

$$v_r = V_Z + K(\cos(\omega + f) + e\cos\omega) \tag{A.27}$$

where

$$K = \frac{m_2}{m_1 + m_2}\frac{na\sin i}{\sqrt{1 - e^2}} \tag{A.28}$$

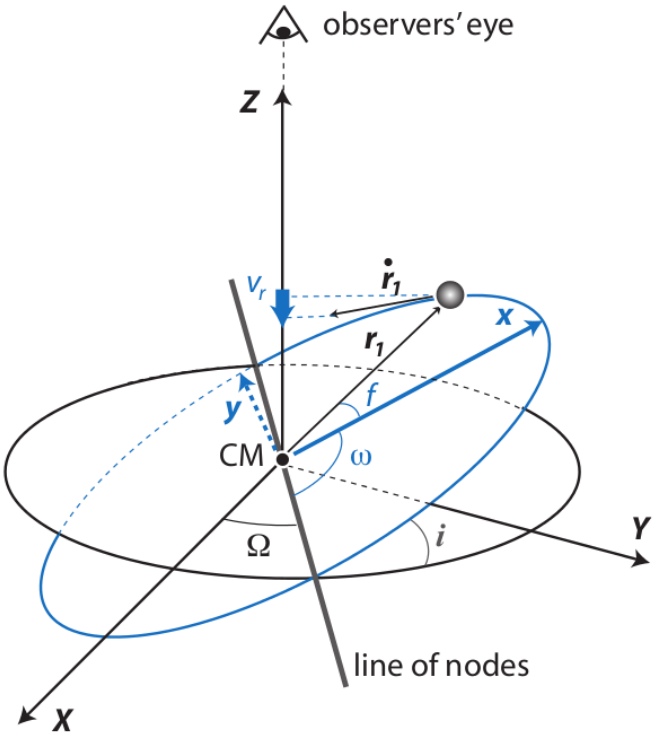

Figure A.5: Radial component of the velocity along the line of sight. Figure taken from Murray & Correia (2011).

Appendix B

Spectrum extraction with KLIP: results on β Pic b

The star β Pictoris host a beautiful debris disk and a giant planet, β Pic b (Lagrange et al. 2009). The system has been presented in Sec. 1.2.4. Here we presents the results obtained with SPHERE. β Pic b was observed during the science verification (SV) phase of SPHERE, in December 2014. The mode was IRDIFS_EXT, to have a wider band range on IFS. I reduced IFS cubes with KLIP routine (presented in Chapter 4). The planet is seen with high S/N in Fig. B.1. Due to the brightness of the companion the spectrum extraction did not show major issues.

I performed the reduction applying the ADI on each singular channel, without exploiting the SDI. The spectrum that I obtained is shown in Fig. B.2.

The capabilities of SPHERE/IFS are demonstrated in this result, that shows a high S/N spectrum of an object that is only $0\farcs4$ separated from its host.

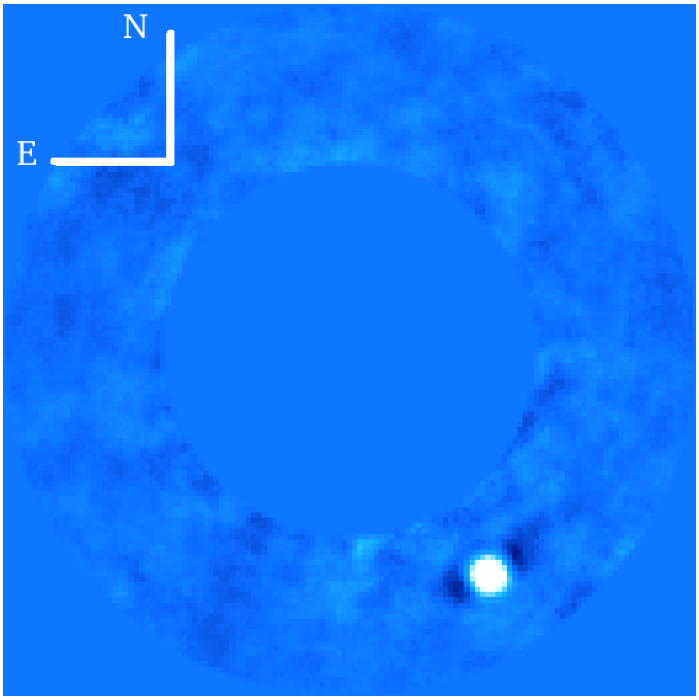

Figure B.1: One of the IFS channels showing β Pic b. The reduction has been made with KLIP routine.

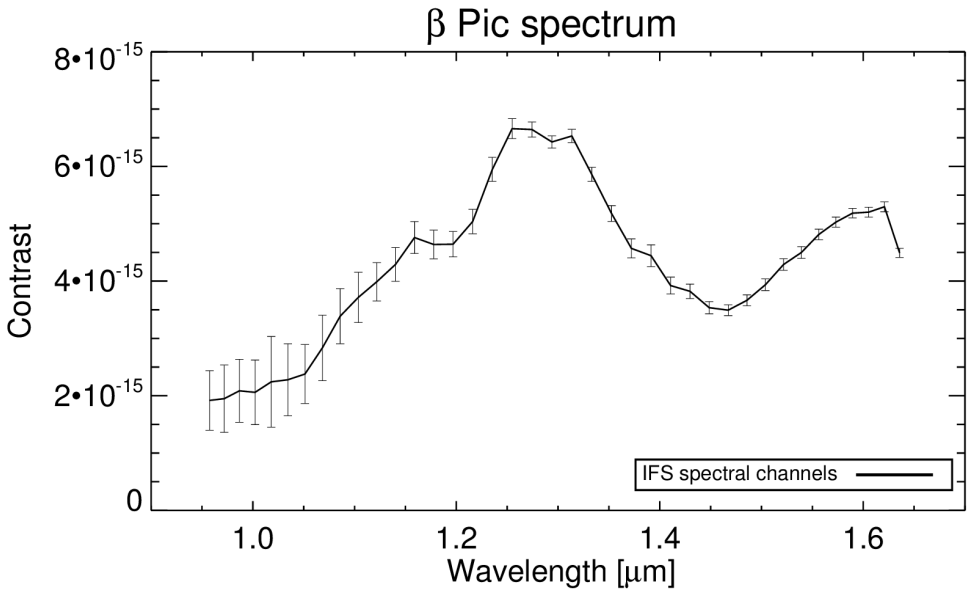

Figure B.2: Spectrum of β Pic b, extracted with KLIP reduction.

Bibliography

Abuter, R., Schreiber, J., Eisenhauer, F., et al. 2006, New A Rev., 50, 398

Ackerman, A. S. & Marley, M. S. 2001, ApJ, 556, 872

Alibert, Y., Mordasini, C., & Benz, W. 2004, A&A, 417, L25

Allard, F., Guillot, T., Ludwig, H.-G., et al. 2003, in IAU Symposium, Vol. 211, Brown Dwarfs, ed. E. Martín, 325

Allard, F., Hauschildt, P. H., Alexander, D. R., Ferguson, J. W., & Tamanai, A. 2000, in Astronomical Society of the Pacific Conference Series, Vol. 212, From Giant Planets to Cool Stars, ed. C. A. Griffith & M. S. Marley, 127

Allard, F., Hauschildt, P. H., Alexander, D. R., Tamanai, A., & Schweitzer, A. 2001, ApJ, 556, 357

Allen, K. W. 1977, Astrophysical quantities.

Amara, A. & Quanz, S. P. 2012, MNRAS, 427, 948

Anglada-Escudé, G. & Tuomi, M. 2012, A&A, 548, A58

Antichi, J., Dohlen, K., Gratton, R. G., et al. 2009, ApJ, 695, 1042

Apai, D., Radigan, J., Buenzli, E., et al. 2013, ApJ, 768, 121

Armitage, P. J. 2007, ArXiv Astrophysics e-prints

Bailey, J. 2014, PASA, 31, 43

Bailey, V., Meshkat, T., Reiter, M., et al. 2014, ApJ *(Letters)*, 780, L4

Baines, E. K., White, R. J., Huber, D., et al. 2012, ApJ, 761, 57

Baraffe, I., Chabrier, G., Allard, F., & Hauschildt, P. H. 2002, A&A, 382, 563

Baraffe, I., Chabrier, G., & Barman, T. 2010, Reports on Progress in Physics, 73, 016901

Baraffe, I., Chabrier, G., Barman, T. S., Allard, F., & Hauschildt, P. H. 2003a, A&A, 402, 701

Baraffe, I., Chabrier, G., Barman, T. S., Allard, F., & Hauschildt, P. H. 2003b, A&A, 402, 701

Baranne, A., Queloz, D., Mayor, M., et al. 1996, A&AS, 119, 373

Barman, T. S., Macintosh, B., Konopacky, Q. M., & Marois, C. 2011, ApJ, 733, 65

Barros, S. C. C., Boue, G., Gibson, N. P., et al. 2013, ArXiv e-prints

Batista, V., Beaulieu, J.-P., Gould, A., et al. 2014, ApJ, 780, 54

Bayo, A., Rodrigo, C., Barrado Y Navascués, D., et al. 2008, A&A, 492, 277

Bean, J. L., McArthur, B. E., Benedict, G. F., et al. 2007, AJ, 134, 749

Bellini, A., Anderson, J., van der Marel, R. P., et al. 2014, ApJ, 797, 115

Benedict, G. F., McArthur, B. E., Gatewood, G., et al. 2006, AJ, 132, 2206

Bergeron, P., Wesemael, F., Dufour, P., et al. 2011, ApJ, 737, 28

Best, W. M. J., Liu, M. C., Magnier, E. A., et al. 2013, ApJ, 777, 84

Beuzit, J.-L., Feldt, M., Dohlen, K., et al. 2006, The Messenger, 125, 29

Beuzit, J.-L., Feldt, M., Dohlen, K., et al. 2008, in Society of Photo-Optical Instrumentation Engineers (SPIE) Conference Series, Vol. 7014, Society of Photo-Optical Instrumentation Engineers (SPIE) Conference Series, 18

Biazzo, K., D'Orazi, V., Desidera, S., et al. 2012, MNRAS, 427, 2905

Bidelman, W. P. 1985, in Astrophysics and Space Science Library, Vol. 114, Cool Stars with Excesses of Heavy Elements, ed. M. Jaschek & P. C. Keenan, 43–45

Biller, B. A. 2007, PhD thesis, The University of Arizona

Biller, B. A., Liu, M. C., Wahhaj, Z., et al. 2013, ApJ, 777, 160

Binks, A. S. & Jeffries, R. D. 2014, MNRAS, 438, L11

Boccaletti, A., Abe, L., Baudrand, J., et al. 2008, in Society of Photo-Optical Instrumentation Engineers (SPIE) Conference Series, Vol. 7015, Society of Photo-Optical Instrumentation Engineers (SPIE) Conference Series

Boccaletti, A., Riaud, P., Baudoz, P., et al. 2004, Publications of the ASP, 116, 1061

Bohlin, R. C. 2007, in Astronomical Society of the Pacific Conference Series, Vol. 364, The Future of Photometric, Spectrophotometric and Polarimetric Standardization, ed. C. Sterken, 315

Boisse, I., Bouchy, F., Hébrard, G., et al. 2011, A&A, 528, A4

Boley, A. C. 2009, ApJ *(Letters)*, 695, L53

Bonavita, M., Chauvin, G., Desidera, S., et al. 2012, A&A, 537, A67

Bonavita, M., de Mooij, E. J. W., & Jayawardhana, R. 2013, Publications of the ASP, 125, 849

Bonnefoy, M., Boccaletti, A., Lagrange, A.-M., et al. 2013, A&A, 555, A107

Bonnefoy, M., Lagrange, A.-M., Boccaletti, A., et al. 2011, A&A, 528, L15

Bonnefoy, M., Marleau, G.-D., Galicher, R., et al. 2014, A&A, 567, L9

Bonnet, H., Abuter, R., Baker, A., et al. 2004a, The Messenger, 117, 17

Bonnet, H., Conzelmann, R., Delabre, B., et al. 2004b, in Society of Photo-Optical Instrumentation Engineers (SPIE) Conference Series, Vol. 5490, Society of Photo-Optical Instrumentation Engineers (SPIE) Conference Series, ed. D. Bonaccini Calia, B. L. Ellerbroek, & R. Ragazzoni, 130–138

Bonnet, H., Ströbele, S., Biancat-Marchet, F., et al. 2003, in Society of Photo-Optical Instrumentation Engineers (SPIE) Conference Series, Vol. 4839, Society of Photo-Optical Instrumentation Engineers (SPIE) Conference Series, ed. P. L. Wizinowich & D. Bonaccini, 329–343

Boss, A. P. 1997, Science, 276, 1836

Bowler, B. P., Liu, M. C., Dupuy, T. J., & Cushing, M. C. 2010, ApJ, 723, 850

Bowler, B. P., Liu, M. C., Shkolnik, E. L., & Dupuy, T. J. 2013, ApJ, 774, 55

Brandt, T. D., McElwain, M. W., Turner, E. L., et al. 2014, ArXiv e-prints

Brown, T. M. 2003, ApJ *(Letters)*, 593, L125

Burbidge, E. M., Burbidge, G. R., Fowler, W. A., & Hoyle, F. 1957, Reviews of Modern Physics, 29, 547

Burgasser, A. J., Cruz, K. L., Cushing, M., et al. 2010a, ApJ, 710, 1142

Burgasser, A. J., Geballe, T. R., Leggett, S. K., Kirkpatrick, J. D., & Golimowski, D. A. 2006, ApJ, 637, 1067

Burgasser, A. J., Kirkpatrick, J. D., Brown, M. E., et al. 2002, ApJ, 564, 421

Burgasser, A. J., Kirkpatrick, J. D., Burrows, A., et al. 2003, ApJ, 592, 1186

Burgasser, A. J., McElwain, M. W., Kirkpatrick, J. D., et al. 2004, AJ, 127, 2856

Burgasser, A. J., Simcoe, R. A., Bochanski, J. J., et al. 2010b, ApJ, 725, 1405

Burrows, A., Marley, M., Hubbard, W. B., et al. 1997, ApJ, 491, 856

Burrows, A., Sudarsky, D., & Hubeny, I. 2006, ApJ, 640, 1063

Burrows, A., Sudarsky, D., & Lunine, J. I. 2003, ApJ, 596, 587

Busso, M., Gallino, R., & Wasserburg, G. J. 1999, ARA&A, 37, 239

Butters, O. W., West, R. G., Anderson, D. R., et al. 2010, A&A, 520, L10

Cameron, A. G. W. 1978, Moon and Planets, 18, 5

Carbillet, M., Bendjoya, P., Abe, L., et al. 2011, Experimental Astronomy, 30, 39

Carpenter, J. M. 2001, AJ, 121, 2851

Castelli, F. & Kurucz, R. L. 2004, ArXiv Astrophysics e-prints

Cegla, H. M., Watson, C. A., Marsh, T. R., et al. 2012, MNRAS, 421, L54

Chabrier, G., Baraffe, I., Allard, F., & Hauschildt, P. 2000, ApJ, 542, 464

Chauvin, G. 2010, in In the Spirit of Lyot 2010

Chauvin, G., Lagrange, A.-M., Beust, H., et al. 2012, A&A, 542, A41

Chauvin, G., Lagrange, A.-M., Bonavita, M., et al. 2010, A&A, 509, A52

Chauvin, G., Lagrange, A.-M., Dumas, C., et al. 2004, A&A, 425, L29

Chauvin, G., Lagrange, A.-M., Dumas, C., et al. 2005, A&A, 438, L25

Chauvin, G., Lagrange, A.-M., Udry, S., & Mayor, M. 2007, A&A, 475, 723

Chauvin, G., Vigan, A., Bonnefoy, M., et al. 2015, A&A, 573, A127

Chauvin, G., Vigan, A., Bonnefoy, M., et al. 2014, ArXiv=1405.1560

Chiu, K., Fan, X., Leggett, S. K., et al. 2006, AJ, 131, 2722

Claudi, R. U., Turatto, M., Gratton, R. G., et al. 2008a, in Society of Photo-Optical Instrumentation Engineers (SPIE) Conference Series, Vol. 7014, Society of Photo-Optical Instrumentation Engineers (SPIE) Conference Series

Claudi, R. U., Turatto, M., Gratton, R. G., et al. 2008b, in Society of Photo-Optical Instrumentation Engineers (SPIE) Conference Series, Vol. 7014, Society of Photo-Optical Instrumentation Engineers (SPIE) Conference Series, 3

Correia, A. C. M., Couetdic, J., Laskar, J., et al. 2010, A&A, 511, A21

Cousins, A. W. J. 1983, South African Astronomical Observatory Circular, 7, 36

Cowley, A., Cowley, C., Jaschek, M., & Jaschek, C. 1969, AJ, 74, 375

Crepp, J. R., Johnson, J. A., Howard, A. W., et al. 2012, ApJ, 761, 39

Crepp, J. R., Pueyo, L., Brenner, D., et al. 2011, ApJ, 729, 132

Currie, T., Burrows, A., Girard, J. H., et al. 2014a, ApJ, 795, 133

Currie, T., Burrows, A., Itoh, Y., et al. 2011, ApJ, 729, 128

Currie, T., Burrows, A., Madhusudhan, N., et al. 2013, ApJ, 776, 15

Currie, T., Daemgen, S., Debes, J., et al. 2014b, ApJ *(Letters)*, 780, L30

Cushing, M. C., Kirkpatrick, J. D., Gelino, C. R., et al. 2011, ApJ, 743, 50

Cushing, M. C., Rayner, J. T., & Vacca, W. D. 2005, ApJ, 623, 1115

Cutri, R. M. & et al. 2012, VizieR Online Data Catalog, 2311, 0

Cutri, R. M., Skrutskie, M. F., van Dyk, S., et al. 2003, 2MASS All Sky Catalog of point sources.

da Silva, L., Girardi, L., Pasquini, L., et al. 2006, A&A, 458, 609

Dahn, C. C., Harris, H. C., Vrba, F. J., et al. 2002, AJ, 124, 1170

D'Angelo, G., Durisen, R. H., & Lissauer, J. J. 2011, Giant Planet Formation, ed. S. Seager, 319–346

Delorme, P., Collier Cameron, A., Hebb, L., et al. 2011, MNRAS, 413, 2218

Desidera, S. & Barbieri, M. 2007, A&A, 462, 345

Desidera, S., Carolo, E., Gratton, R., et al. 2011, A&A, 533, A90

Desidera, S., Covino, E., Messina, S., et al. 2014, ArXiv e-prints

Díaz, R. F., Almenara, J. M., Santerne, A., et al. 2014, MNRAS, 441, 983

Dobbie, P. D., Burleigh, M. R., Levan, A. J., et al. 2005, MNRAS, 357, 1049

Dohlen, K., Langlois, M., Saisse, M., et al. 2008a, in Society of Photo-Optical Instrumentation Engineers (SPIE) Conference Series, Vol. 7014, Society of Photo-Optical Instrumentation Engineers (SPIE) Conference Series

Dohlen, K., Langlois, M., Saisse, M., et al. 2008b, in Society of Photo-Optical Instrumentation Engineers (SPIE) Conference Series, Vol. 7014, Society of Photo-Optical Instrumentation Engineers (SPIE) Conference Series, 3

Dohlen, K., Wildi, F. P., Puget, P., Mouillet, D., & Beuzit, J.-L. 2011, in Second International Conference on Adaptive Optics for Extremely Large Telescopes. Online at ¡A href="http://ao4elt2.lesia.obspm.fr"¿http://ao4elt2.lesia.obspm.fr¡/A¿, id.75

D'Orazi, V., Biazzo, K., Desidera, S., et al. 2012, MNRAS, 423, 2789

Dumusque, X., Lovis, C., Ségransan, D., et al. 2011, A&A, 535, A55

Dumusque, X., Pepe, F., Lovis, C., et al. 2012, Nat, 491, 207

Dupuy, T. J. & Kraus, A. L. 2013, Science, 341, 1492

Dupuy, T. J. & Liu, M. C. 2012, ApJS, 201, 19

Duquennoy, A. & Mayor, M. 1991, A&A, 248, 485

Edvardsson, B., Andersen, J., Gustafsson, B., et al. 1993, A&A, 275, 101

Einstein, A. 1936, Science, 84, 506

Eisenhauer, F., Abuter, R., Bickert, K., et al. 2003, in Society of Photo-Optical Instrumentation Engineers (SPIE) Conference Series, Vol. 4841, Society of Photo-Optical Instrumentation Engineers (SPIE) Conference Series, ed. M. Iye & A. F. M. Moorwood, 1548–1561

Els, S. G., Sterzik, M. F., Marchis, F., et al. 2001, A&A, 370, L1

Esposito, S., Mesa, D., Skemer, A., et al. 2013, A&A, 549, A52

Figueira, P., Marmier, M., Bonfils, X., et al. 2010, A&A, 513, L8

Findeisen, K., Hillenbrand, L., & Soderblom, D. 2011, AJ, 142, 23

Fischer, D. A., Marcy, G. W., Butler, R. P., Vogt, S. S., & Apps, K. 1999, Publications of the ASP, 111, 50

Fischer, D. A. & Valenti, J. 2005, ApJ, 622, 1102

Fitzpatrick, E. L. 1999, Publications of the ASP, 111, 63

Fortney, J. J., Baraffe, I., & Militzer, B. 2011, Giant Planet Interior Structure and Thermal Evolution, ed. S. Seager, 397–418

Fortney, J. J., Marley, M. S., Hubickyj, O., Bodenheimer, P., & Lissauer, J. J. 2005, Astronomische Nachrichten, 326, 925

Fortney, J. J., Marley, M. S., Saumon, D., & Lodders, K. 2008, ApJ, 683, 1104

Forveille, T., Bonfils, X., Lo Curto, G., et al. 2011, A&A, 526, A141

Gagné, J., Lafrenière, D., Doyon, R., Malo, L., & Artigau, É. 2014, ApJ, 783, 121

Galicher, R., Marois, C., Macintosh, B., Barman, T., & Konopacky, Q. 2011a, ApJ *(Letters)*, 739, L41

Galicher, R., Marois, C., Macintosh, B., Barman, T., & Konopacky, Q. 2011b, ApJ *(Letters)*, 739, L41

Galicher, R., Rameau, J., Bonnefoy, M., et al. 2014, A&A, 565, L4

Gammie, C. F. 2001, ApJ, 553, 174

Geballe, T. R., Knapp, G. R., Leggett, S. K., et al. 2002, ApJ, 564, 466

Geballe, T. R., Saumon, D., Leggett, S. K., et al. 2001, ApJ, 556, 373

Giammichele, N., Bergeron, P., & Dufour, P. 2012, ApJS, 199, 29

Gizis, J. E., Allers, K. N., Liu, M. C., et al. 2014, ArXiv e-prints

Goldreich, P. & Tremaine, S. 1980, ApJ, 241, 425

Gould, A., Yee, J. C., Bond, I. A., et al. 2012, ArXiv e-prints

Goździewski, K. & Migaszewski, C. 2014, MNRAS, 440, 3140

Gozdziewski, K., Migaszewski, C., & Musielinski, A. 2008, ArXiv e-prints

Gray, R. O., Corbally, C. J., Garrison, R. F., et al. 2006, AJ, 132, 161

Gray, R. O. & Kaye, A. B. 1999, AJ, 118, 2993

Grether, D. & Lineweaver, C. H. 2006, ApJ, 640, 1051

Guerri, G., Robbe-Dubois, S., Daban, J.-B., et al. 2009, ArXiv e-prints

Guillot, T. 2005, Annual Review of Earth and Planetary Sciences, 33, 493

Guillot, T. & Gautier, D. 2014, ArXiv e-prints

Hagelberg, J. 2010, in In the Spirit of Lyot 2010, 22

Haisch, Jr., K. E., Lada, E. A., & Lada, C. J. 2001, ApJ *(Letters)*, 553, L153

Hamuy, M., Suntzeff, N. B., Heathcote, S. R., et al. 1994, Publications of the ASP, 106, 566

Han, Z., Eggleton, P. P., Podsiadlowski, P., & Tout, C. A. 1995, MNRAS, 277, 1443

Hatzes, A. P., Cochran, W. D., McArthur, B., et al. 2000, ApJ *(Letters)*, 544, L145

Heintz, W. 2000, Visual Binary Stars, ed. P. Murdin

Heintz, W. D. 1978, Geophysics and Astrophysics Monographs, 15

Heinze, A. N., Hinz, P. M., Kenworthy, M., et al. 2010, ApJ, 714, 1570

Hernán-Obispo, M., Gálvez-Ortiz, M. C., Anglada-Escudé, G., et al. 2010, A&A, 512, A45

Hinkley, S., Carpenter, J. M., Ireland, M. J., & Kraus, A. L. 2011a, ApJ *(Letters)*, 730, L21

Hinkley, S., Oppenheimer, B. R., Zimmerman, N., et al. 2011b, Publications of the ASP, 123, 74

Hinz, P. M., Rodigas, T. J., Kenworthy, M. A., et al. 2010, ApJ, 716, 417

Ho, S. & Turner, E. L. 2011, ApJ, 739, 26

Høg, E., Fabricius, C., Makarov, V. V., et al. 2000, A&A, 355, L27

Holberg, J. B. 2009, Journal of Physics Conference Series, 172, 012022

Holberg, J. B. & Bergeron, P. 2006, AJ, 132, 1221

Holmberg, J., Nordström, B., & Andersen, J. 2009, A&A, 501, 941

Hourigan, K. & Ward, W. R. 1984, Icarus, 60, 29

Hubbard, W. B. 1968, ApJ, 152, 745

Hubbard, W. B., Podolak, M., & Stevenson, D. J. 1995, in Neptune and Triton, ed. D. P. Cruikshank, M. S. Matthews, & A. M. Schumann, 109–138

Huélamo, N., Figueira, P., Bonfils, X., et al. 2008, A&A, 489, L9

Hughes, A. M., Wilner, D. J., Andrews, S. M., et al. 2011, ApJ, 740, 38

Hugot, E., Ferrari, M., El Hadi, K., et al. 2012, A&A, 538, A139

Hurley, J. R., Tout, C. A., & Pols, O. R. 2002, MNRAS, 329, 897

Ingraham, P., Marley, M. S., Saumon, D., et al. 2014, ApJ *(Letters)*, 794, L15

Ireland, M. J., Monnier, J. D., Tuthill, P. G., et al. 2007, ApJ, 662, 651

Janson, M., Bergfors, C., Goto, M., Brandner, W., & Lafrenière, D. 2010, ApJ *(Letters)*, 710, L35

Janson, M., Brandt, T. D., Moro-Martín, A., et al. 2013, ApJ, 773, 73

Jeffries, R. D. & Smalley, B. 1996, A&A, 315, L19

Jeffries, R. D. & Stevens, I. R. 1996, MNRAS, 279, 180

Jones, A., Noll, S., Kausch, W., Szyszka, C., & Kimeswenger, S. 2013, A&A, 560, A91

Jones, H. R. A., Paul Butler, R., Tinney, C. G., et al. 2002, MNRAS, 333, 871

Jorissen, A., Van Eck, S., Mayor, M., & Udry, S. 1998, A&A, 332, 877

Kalas, P., Graham, J. R., Chiang, E., et al. 2008, Science, 322, 1345

Kalas, P., Graham, J. R., Fitzgerald, M. P., & Clampin, M. 2013, ApJ, 775, 56

Käppeler, F., Gallino, R., Bisterzo, S., & Aoki, W. 2011, Reviews of Modern Physics, 83, 157

Karovska, M., Hack, W., Raymond, J., & Guinan, E. 1997, ApJ *(Letters)*, 482, L175

Kellogg, K. & Metchev, S. 2014, in American Astronomical Society Meeting Abstracts, Vol. 223, American Astronomical Society Meeting Abstracts #223, 441.21

Kennedy, G. M. & Kenyon, S. J. 2008, ApJ, 673, 502

Kirkpatrick, J. D., Cushing, M. C., Gelino, C. R., et al. 2011, ApJS, 197, 19

Kirkpatrick, J. D., Reid, I. N., Liebert, J., et al. 1999, ApJ, 519, 802

Koen, C., Kilkenny, D., van Wyk, F., & Marang, F. 2010, MNRAS, 403, 1949

Koester, D. 2010, Mem. Soc. Astron. Italiana, 81, 921

Konopacky, Q. M., Barman, T. S., Macintosh, B. A., & Marois, C. 2013, Science, 339, 1398

Kowalski, P. M. & Saumon, D. 2006, ApJ *(Letters)*, 651, L137

Kratter, K. M., Matzner, C. D., & Krumholz, M. R. 2008, ApJ, 681, 375

Kratter, K. M., Matzner, C. D., Krumholz, M. R., & Klein, R. I. 2010a, ApJ, 708, 1585

Kratter, K. M., Murray-Clay, R. A., & Youdin, A. N. 2010b, ApJ, 710, 1375

Kraus, A. L., Ireland, M. J., Cieza, L. A., et al. 2014, ApJ, 781, 20

Kuzuhara, M., Tamura, M., Kudo, T., et al. 2013, ApJ, 774, 11

Lafrenière, D., Jayawardhana, R., & van Kerkwijk, M. H. 2008, ApJ *(Letters)*, 689, L153

Lafrenière, D., Marois, C., Doyon, R., & Barman, T. 2009, ApJ *(Letters)*, 694, L148

Lafrenière, D., Marois, C., Doyon, R., Nadeau, D., & Artigau, É. 2007, ApJ, 660, 770

Lagrange, A.-M., Bonnefoy, M., Chauvin, G., et al. 2010, Science, 329, 57

Lagrange, A.-M., Gratadour, D., Chauvin, G., et al. 2009, A&A, 493, L21

Langlois, M., Vigan, A., Moutou, C., et al. 2013, in Proceedings of the Third AO4ELT Conference, ed. S. Esposito & L. Fini

Lanza, A. F., Bonomo, A. S., Moutou, C., et al. 2010, A&A, 520, A53

Lanza, A. F., De Martino, C., & Rodonò, M. 2008, New A, 13, 77

Larkin, J., Barczys, M., Krabbe, A., et al. 2006, in Society of Photo-Optical Instrumentation Engineers (SPIE) Conference Series, Vol. 6269, Society of Photo-Optical Instrumentation Engineers (SPIE) Conference Series, 1

Leggett, S. K. 1992, ApJS, 82, 351

Leggett, S. K., Allard, F., Geballe, T. R., Hauschildt, P. H., & Schweitzer, A. 2001, ApJ, 548, 908

Leggett, S. K., Geballe, T. R., Fan, X., et al. 2000, ApJ *(Letters)*, 536, L35

Leggett, S. K., Golimowski, D. A., Fan, X., et al. 2002, ApJ, 564, 452

Lenzen, R., Hartung, M., Brandner, W., et al. 2003, in SPIE Conference Series, Vol. 4841, 944–952

Lin, D. N. C. & Papaloizou, J. 1986, ApJ, 309, 846

Liu, M. C., Magnier, E. A., Deacon, N. R., et al. 2013, ApJ *(Letters)*, 777, L20

Lodders, K. & Fegley, Jr., B. 2006, Chemistry of Low Mass Substellar Objects, ed. J. W. Mason, 1

Lodieu, N., Pérez-Garrido, A., Béjar, V. J. S., et al. 2014, A&A, 569, A120

Looper, D. L., Kirkpatrick, J. D., & Burgasser, A. J. 2007, AJ, 134, 1162

Looper, D. L., Kirkpatrick, J. D., Cutri, R. M., et al. 2008, ApJ, 686, 528

Lovis, C., Dumusque, X., Santos, N. C., et al. 2011, ArXiv e-prints

Luhman, K. L., Burgasser, A. J., & Bochanski, J. J. 2011, ApJ *(Letters)*, 730, L9

Luhman, K. L., Patten, B. M., Marengo, M., et al. 2007, ApJ, 654, 570

Mace, G. N., Kirkpatrick, J. D., Cushing, M. C., et al. 2013, ApJS, 205, 6

Macintosh, B., Graham, J. R., Ingraham, P., et al. 2014a, ArXiv e-prints

Macintosh, B., Graham, J. R., Ingraham, P., et al. 2014b, Proceedings of the National Academy of Science, 111, 12661

Madhusudhan, N., Burrows, A., & Currie, T. 2011a, ApJ, 737, 34

Madhusudhan, N., Burrows, A., & Currie, T. 2011b, ApJ, 737, 34

Maire, A.-L., Boccaletti, A., Rameau, J., et al. 2014a, A&A, 566, A126

Maire, A.-L., Boccaletti, A., Rameau, J., et al. 2014b, A&A, 566, A126

Mamajek, E. E. & Hillenbrand, L. A. 2008, ApJ, 687, 1264

Mao, S. & Paczynski, B. 1991, ApJ *(Letters)*, 374, L37

Markwardt, C. B. 2009, in Astronomical Society of the Pacific Conference Series, Vol. 411, Astronomical Data Analysis Software and Systems XVIII, ed. D. A. Bohlender, D. Durand, & P. Dowler, 251

Marley, M. S., Fortney, J. J., Hubickyj, O., Bodenheimer, P., & Lissauer, J. J. 2007, ApJ, 655, 541

Marley, M. S., Saumon, D., Cushing, M., et al. 2012, ApJ, 754, 135

Marocco, F., Day-Jones, A. C., Lucas, P. W., et al. 2014, MNRAS, 439, 372

Marois, C., Correia, C., Véran, J.-P., & Currie, T. 2014, in IAU Symposium, Vol. 299, IAU Symposium, ed. M. Booth, B. C. Matthews, & J. R. Graham, 48–49

Marois, C., Doyon, R., Racine, R., & Nadeau, D. 2000, Publications of the ASP, 112, 91

Marois, C., Lafrenière, D., Doyon, R., Macintosh, B., & Nadeau, D. 2006a, ApJ, 641, 556

Marois, C., Lafrenière, D., Doyon, R., Macintosh, B., & Nadeau, D. 2006b, ApJ, 641, 556

Marois, C., Lafrenière, D., Macintosh, B., & Doyon, R. 2006c, ApJ, 647, 612

Marois, C., Lafrenière, D., Macintosh, B., & Doyon, R. 2008a, ApJ, 673, 647

Marois, C., Macintosh, B., Barman, T., et al. 2008b, Science, 322, 1348

Marois, C., Macintosh, B., & Véran, J.-P. 2010a, in Society of Photo-Optical Instrumentation Engineers (SPIE) Conference Series, Vol. 7736, Society of Photo-Optical Instrumentation Engineers (SPIE) Conference Series, 1

Marois, C., Zuckerman, B., Konopacky, Q. M., Macintosh, B., & Barman, T. 2010b, Nat, 468, 1080

Martin, D. C., Fanson, J., Schiminovich, D., et al. 2005, ApJ *(Letters)*, 619, L1

Martinache, F. & Guyon, O. 2009, in Society of Photo-Optical Instrumentation Engineers (SPIE) Conference Series, Vol. 7440, Society of Photo-Optical Instrumentation Engineers (SPIE) Conference Series, 0

Masciadri, E., Mundt, R., Henning, T., Alvarez, C., & Barrado y Navascués, D. 2005, ApJ, 625, 1004

Mason, B. D., Wycoff, G. L., Hartkopf, W. I., Douglass, G. G., & Worley, C. E. 2001, AJ, 122, 3466

Matthews, B., Kennedy, G., Sibthorpe, B., et al. 2014, ApJ, 780, 97

Mawet, D., Absil, O., Montagnier, G., et al. 2012, A&A, 544, A131

Mawet, D., Serabyn, E., Liewer, K., et al. 2009, Optics Express, 17, 1902

Mayor, M. & Queloz, D. 1995, Nat, 378, 355

McClure, R. D. 1984, Publications of the ASP, 96, 117

McClure, R. D., Fletcher, J. M., & Nemec, J. M. 1980, ApJ *(Letters)*, 238, L35

McClure, R. D. & Woodsworth, A. W. 1990, ApJ, 352, 709

McConnell, R. K. & Gast, P. W. 1972, Moon, 5, 41

McCrea, W. H. 1964, MNRAS, 128, 335

McElwain, M. W., Brandt, T. D., Janson, M., et al. 2012, in Society of Photo-Optical Instrumentation Engineers (SPIE) Conference Series, Vol. 8446, Society of Photo-Optical Instrumentation Engineers (SPIE) Conference Series, 9

McLean, I. S., ed. 1997, Electronic imaging in astronomy. Detectors and instrumentation

Mesa, D., Gratton, R., Berton, A., et al. 2011, A&A, 529, A131

Mesa, D., Gratton, R., Zurlo, A., et al. 2015, ArXiv e-prints

Messina, S., Desidera, S., Lanzafame, A. C., Turatto, M., & Guinan, E. F. 2011, A&A, 532, A10

Messina, S., Desidera, S., Turatto, M., Lanzafame, A. C., & Guinan, E. F. 2010, A&A, 520, A15

Metchev, S. A. & Hillenbrand, L. A. 2006, ApJ, 651, 1166

Metchev, S. A. & Hillenbrand, L. A. 2009, ApJS, 181, 62

Militzer, B., Hubbard, W. B., Vorberger, J., Tamblyn, I., & Bonev, S. A. 2008, ApJ *(Letters)*, 688, L45

Mizuno, H. 1980, Progress of Theoretical Physics, 64, 544

Montes, D., López-Santiago, J., Gálvez, M. C., et al. 2001, MNRAS, 328, 45

Moór, A., Ábrahám, P., Derekas, A., et al. 2006, ApJ, 644, 525

Mordasini, C., Alibert, Y., & Benz, W. 2009, A&A, 501, 1139

Mordasini, C., Alibert, Y., Benz, W., & Naef, D. 2008, in Astronomical Society of the Pacific Conference Series, Vol. 398, Extreme Solar Systems, ed. D. Fischer, F. A. Rasio, S. E. Thorsett, & A. Wolszczan, 235

Morley, C. V., Fortney, J. J., Marley, M. S., et al. 2012, ApJ, 756, 172

Mugrauer, M. & Neuhäuser, R. 2005, MNRAS, 361, L15

Murray, C. D. & Correia, A. C. M. 2011, Keplerian Orbits and Dynamics of Exoplanets, ed. S. Seager, 15–23

Murray, N., Chaboyer, B., Arras, P., Hansen, B., & Noyes, R. W. 2001, ApJ, 555, 801

Nakajima, T., Oppenheimer, B. R., Kulkarni, S. R., et al. 1995, Nat, 378, 463

Naud, M.-E., Artigau, É., Malo, L., et al. 2014, ApJ, 787, 5

Nielsen, E. L., Liu, M. C., Wahhaj, Z., et al. 2013, ApJ, 776, 4

Noll, S., Kausch, W., Barden, M., et al. 2012, A&A, 543, A92

North, P. & Duquennoy, A. 1991, A&A, 244, 335

O'Donovan, F. T., Charbonneau, D., Torres, G., et al. 2006, ApJ, 644, 1237

Ohta, Y., Taruya, A., & Suto, Y. 2005, ApJ, 622, 1118

Oppenheimer, B. R., Baranec, C., Beichman, C., et al. 2013, ApJ, 768, 24

Oppenheimer, B. R. & Hinkley, S. 2009, ARA&A, 47, 253

Oppenheimer, B. R., Kulkarni, S. R., Matthews, K., & Nakajima, T. 1995, Science, 270, 1478

Papaloizou, J. C. B. & Nelson, R. P. 2005, A&A, 433, 247

Patience, J., King, R. R., de Rosa, R. J., & Marois, C. 2010, A&A, 517, A76

Pavlov, A., Feldt, M., & Henning, T. 2008, in Astronomical Society of the Pacific Conference Series, Vol. 394, Astronomical Data Analysis Software and Systems XVII, ed. R. W. Argyle, P. S. Bunclark, & J. R. Lewis, 581

Pepe, F., Lovis, C., Ségransan, D., et al. 2011, A&A, 534, A58

Pepper, J., Gould, A., & Depoy, D. L. 2003, Acta Astron., 53, 213

Perryman, M. 2014, The Exoplanet Handbook

Perryman, M. A. C., Lindegren, L., Kovalevsky, J., et al. 1997, A&A, 323, L49

Peters-Limbach, M. A., Groff, T. D., Kasdin, N. J., et al. 2013, in Society of Photo-Optical Instrumentation Engineers (SPIE) Conference Series, Vol. 8864, Society of Photo-Optical Instrumentation Engineers (SPIE) Conference Series

Petit, C., Sauvage, J.-F., Sevin, A., et al. 2012, in Society of Photo-Optical Instrumentation Engineers (SPIE) Conference Series, Vol. 8447, Society of Photo-Optical Instrumentation Engineers (SPIE) Conference Series

Pickles, A. J. 1998, VizieR Online Data Catalog, 611, 863

Podolak, M. & Cameron, A. G. W. 1974, Icarus, 22, 123

Pojmanski, G. 2002, Acta Astron., 52, 397

Pollacco, D. L., Skillen, I., Collier Cameron, A., et al. 2006, Publications of the ASP, 118, 1407

Pollack, J. B., Hubickyj, O., Bodenheimer, P., et al. 1996, Icarus, 124, 62

Porto de Mello, G. F. & da Silva, L. 1997, ApJ *(Letters)*, 476, L89

Press, W. H. & Rybicki, G. B. 1989, ApJ, 338, 277

Pueyo, L., Soummer, R., Hoffmann, J., et al. 2014, ArXiv e-prints

Queloz, D., Henry, G. W., Sivan, J. P., et al. 2001, A&A, 379, 279

Racine, R., Walker, G. A. H., Nadeau, D., Doyon, R., & Marois, C. 1999, Publications of the ASP, 111, 587

Rameau, J., Chauvin, G., Lagrange, A.-M., et al. 2013a, ApJ *(Letters)*, 772, L15

Rameau, J., Chauvin, G., Lagrange, A.-M., et al. 2013b, A&A, 553, A60

Ramírez, I., Meléndez, J., & Asplund, M. 2014, A&A, 561, A7

Rayner, J. T., Cushing, M. C., & Vacca, W. D. 2009, ApJS, 185, 289

Reffert, S. & Quirrenbach, A. 2011, A&A, 527, A140

Rohloff, R.-R., Blümchen, T., Feldt, M., et al. 2008, in Society of Photo-Optical Instrumentation Engineers (SPIE) Conference Series, Vol. 7018, Society of Photo-Optical Instrumentation Engineers (SPIE) Conference Series

Rouan, D., Riaud, P., Boccaletti, A., Clénet, Y., & Labeyrie, A. 2000, Publications of the ASP, 112, 1479

Rousset, G., Lacombe, F., Puget, P., et al. 2003, in SPIE Conference Series, ed. P. L. Wizinowich & D. Bonaccini, Vol. 4839, 140–149

Ruiz, M. T., Leggett, S. K., & Allard, F. 1997, ApJ *(Letters)*, 491, L107

Sahlmann, J., Lazorenko, P. F., Ségransan, D., et al. 2013, A&A, 556, A133

Sahu, K. C., Bond, H. E., Anderson, J., & Dominik, M. 2014, ApJ, 782, 89

Salaris, M., Serenelli, A., Weiss, A., & Miller Bertolami, M. 2009, ApJ, 692, 1013

Salter, G. S., Tinney, C. G., Wittenmyer, R. A., et al. 2014, in IAU Symposium, Vol. 299, IAU Symposium, ed. M. Booth, B. C. Matthews, & J. R. Graham, 66–67

Santos, N. C., Mayor, M., Bouchy, F., et al. 2007, A&A, 474, 647

Saumon, D., Chabrier, G., & van Horn, H. M. 1995, ApJS, 99, 713

Saumon, D. & Guillot, T. 2004, ApJ, 609, 1170

Saumon, D., Hubbard, W. B., Burrows, A., et al. 1996, ApJ, 460, 993

Scargle, J. D. 1982, ApJ, 263, 835

Schneider, A. C., Cushing, M. C., Kirkpatrick, J. D., et al. 2014, AJ, 147, 34

Schneider, J., Dedieu, C., Le Sidaner, P., Savalle, R., & Zolotukhin, I. 2011, A&A, 532, A79

Ségransan, D., Mayor, M., Udry, S., et al. 2011, A&A, 535, A54

Serabyn, G., Mawet, D., & Burruss, R. 2010, in Bulletin of the American Astronomical Society, Vol. 42, American Astronomical Society Meeting Abstracts #215, 377.06

Setiawan, J., Henning, T., Launhardt, R., et al. 2008, Nat, 451, 38

Simmerer, J., Sneden, C., Ivans, I. I., et al. 2003, AJ, 125, 2018

Sivaramakrishnan, A. & Oppenheimer, B. R. 2006, ApJ, 647, 620

Skemer, A. J., Hinz, P. M., Esposito, S., et al. 2012, ApJ, 753, 14

Skemer, A. J., Marley, M. S., Hinz, P. M., et al. 2014, ApJ, 792, 17

Skrutskie, M. F., Cutri, R. M., Stiening, R., et al. 2006, AJ, 131, 1163

Smith, G. H. & Redenbaugh, A. K. 2010, Publications of the ASP, 122, 1303

Soummer, R., Brendan Hagan, J., Pueyo, L., et al. 2011, ApJ, 741, 55

Soummer, R., Pueyo, L., & Larkin, J. 2012, ApJ *(Letters)*, 755, L28

Sozzetti, A. 2014, ArXiv e-prints

Sparks, W. B. & Ford, H. C. 2002, ApJ, 578, 543

Spiegel, D. S. & Burrows, A. 2012, ApJ, 745, 174

Steffen, M. 1985, A&AS, 59, 403

Stephens, D. C. & Leggett, S. K. 2004, Publications of the ASP, 116, 9

Stephens, D. C., Leggett, S. K., Cushing, M. C., et al. 2009, ApJ, 702, 154

Su, K. Y. L., Rieke, G. H., Stapelfeldt, K. R., et al. 2009, ApJ, 705, 314

Sudol, J. J. & Haghighipour, N. 2012, ApJ, 755, 38

Tanaka, H., Takeuchi, T., & Ward, W. R. 2002, ApJ, 565, 1257

ten Brummelaar, T., Mason, B. D., McAlister, H. A., et al. 2000, AJ, 119, 2403

ten Brummelaar, T. A., Mason, B. D., Bagnuolo, Jr., W. G., et al. 1996, AJ, 112, 1180

Testi, L., D'Antona, F., Ghinassi, F., et al. 2001, ApJ *(Letters)*, 552, L147

Thalmann, C., Schmid, H. M., Boccaletti, A., et al. 2008, in Society of Photo-Optical Instrumentation Engineers (SPIE) Conference Series, Vol. 7014, Society of Photo-Optical Instrumentation Engineers (SPIE) Conference Series

Thatte, N., Abuter, R., Tecza, M., et al. 2007, MNRAS, 378, 1229

Tingley, B., Grundahl, F., & Kjeldsen, H. 2009, in IAU Symposium, Vol. 253, IAU Symposium, ed. F. Pont, D. Sasselov, & M. J. Holman, 506–507

Todorov, K., Luhman, K. L., & McLeod, K. K. 2010, ApJ *(Letters)*, 714, L84

Tomkin, J., Lambert, D. L., Edvardsson, B., Gustafsson, B., & Nissen, P. E. 1989, A&A, 219, L15

Toomre, A. 1964, ApJ, 139, 1217

Torres, C. A. O., Quast, G. R., da Silva, L., et al. 2006, A&A, 460, 695

Torres, G., Fressin, F., Batalha, N. M., et al. 2011, ApJ, 727, 24

Tremblay, P.-E., Bergeron, P., & Gianninas, A. 2011, ApJ, 730, 128

van den Bos, W. H. 1929, Circular of the Union Observatory Johannesburg, 80, 59

van Leeuwen, F. 2007, A&A, 474, 653

Vennes, S. 1999, ApJ, 525, 995

Vennes, S., Kawka, A., & Németh, P. 2011, MNRAS, 410, 2095

Ventura, P., D'Antona, F., Mazzitelli, I., & Gratton, R. 2001, ApJ *(Letters)*, 550, L65

Vigan, A., Langlois, M., Moutou, C., & Dohlen, K. 2008, A&A, 489, 1345

Vigan, A., Moutou, C., Langlois, M., et al. 2010a, MNRAS, 407, 71

Vigan, A., Moutou, C., Langlois, M., et al. 2010b, MNRAS, 407, 71

Vigan, A., Moutou, C., Langlois, M., et al. 2010c, in SPIE Conference Series, Vol. 7735, SPIE Conference Series

Vigan, A., Patience, J., Marois, C., et al. 2012a, A&A, 544, A9

Vigan, A., Patience, J., Marois, C., et al. 2012b, A&A, 544, A9

Voges, W., Aschenbach, B., Boller, T., et al. 1999, A&A, 349, 389

Vogt, S. S., Butler, R. P., Marcy, G. W., et al. 2005, ApJ, 632, 638

Vogt, S. S., Butler, R. P., Marcy, G. W., et al. 2002, ApJ, 568, 352

Wang, J. J., Rajan, A., Graham, J. R., et al. 2014, in Society of Photo-Optical Instrumentation Engineers (SPIE) Conference Series, Vol. 9147, Society of Photo-Optical Instrumentation Engineers (SPIE) Conference Series

Williams, P. M. 1975, MNRAS, 170, 343

Winn, J. N. 2011, Exoplanet Transits and Occultations, ed. S. Seager, 55–77

Wittenmyer, R. A., Tinney, C. G., O'Toole, S. J., et al. 2011, ApJ, 727, 102

Wright, J. T. & Gaudi, B. S. 2013, Exoplanet Detection Methods, ed. T. D. Oswalt, L. M. French, & P. Kalas, 489

Zhu, Z., Hartmann, L., Nelson, R. P., & Gammie, C. F. 2012, ApJ, 746, 110

Zorotovic, M. & Schreiber, M. R. 2012, ArXiv e-prints

Zuckerman, B., Rhee, J. H., Song, I., & Bessell, M. S. 2011, ApJ, 732, 61

Zurlo, A., Vigan, A., Hagelberg, J., et al. 2013, A&A, 554, A21

Zurlo, A., Vigan, A., Mesa, D., et al. 2014, A&A, 572, A85